

University of Alberta

ULTRAFAST MAGNETIC RELAXATION IN NANOCOMPOSITE MATERIALS

by

Kristen S. Buchanan



A thesis submitted to the Faculty of Graduate Studies and Research in partial fulfillment of the requirements for the degree of **Doctor of Philosophy**.

Department of Physics

Edmonton, Alberta
Fall 2004



Library and
Archives Canada

Bibliothèque et
Archives Canada

Published Heritage
Branch

Direction du
Patrimoine de l'édition

395 Wellington Street
Ottawa ON K1A 0N4
Canada

395, rue Wellington
Ottawa ON K1A 0N4
Canada

Your file *Votre référence*

ISBN: 0-612-95911-2

Our file *Notre référence*

ISBN: 0-612-95911-2

The author has granted a non-exclusive license allowing the Library and Archives Canada to reproduce, loan, distribute or sell copies of this thesis in microform, paper or electronic formats.

L'auteur a accordé une licence non exclusive permettant à la Bibliothèque et Archives Canada de reproduire, prêter, distribuer ou vendre des copies de cette thèse sous la forme de microfiche/film, de reproduction sur papier ou sur format électronique.

The author retains ownership of the copyright in this thesis. Neither the thesis nor substantial extracts from it may be printed or otherwise reproduced without the author's permission.

L'auteur conserve la propriété du droit d'auteur qui protège cette thèse. Ni la thèse ni des extraits substantiels de celle-ci ne doivent être imprimés ou autrement reproduits sans son autorisation.

In compliance with the Canadian Privacy Act some supporting forms may have been removed from this thesis.

Conformément à la loi canadienne sur la protection de la vie privée, quelques formulaires secondaires ont été enlevés de cette thèse.

While these forms may be included in the document page count, their removal does not represent any loss of content from the thesis.

Bien que ces formulaires aient inclus dans la pagination, il n'y aura aucun contenu manquant.

Canada

Acknowledgements

Acknowledgements

Thank you to my supervisors Al Meldrum and Mark Freeman for advice and support throughout my degree. Al, thank you for taking the time to train me on the TEM and furnace and for always providing excellent editorial comments. Mark, thank you for your assistance in the laser labs and for helpful discussions of my approach and results. I appreciate your combined efforts to help me to finish from a distance – I was continually impressed by how seamlessly I could remain actively involved from 1500 miles away.

There are a number of people that contributed to the research discussed in this thesis that I would like to acknowledge. I am grateful to C. W. White (Oak Ridge National Laboratory) for providing the implanted specimens discussed in this thesis. SEM images of the masks used for patterning were taken with the assistance of George Braybrook. Time-resolved MOKE measurements were made in collaboration with Alexander Krichevsky. Thank you to Miro Belov for training at the University of Alberta Nanofab. Photoconductive switches were designed and fabricated with the assistance of Lindsay LeBlanc and Mark Roseman. Training on MBE film growth was provided by Marek Malac, who also was helpful in demonstrating more advanced TEM techniques. Low temperature AC magnetic susceptibility measurements were made in collaboration with Mark Roseman. Thank you to Xiaobin Zhu for discussion of measurements made on similar specimens after I completed my experimental work, to John Beamish for lending me his nailpolish, to Colm Ryan for ion milling several specimens, to Jason Sorge for measuring in-plane hysteresis loops for some implanted samples, to B. C. Choi for initial training on the time-resolved scanning Kerr effect microscopy system, to Aaron Hryciw for discussions on the use of the Ocean Optics spectrometers, and to Dave Fortin for his ideas on optimizing LabView programs. I am also grateful to Grey Arnup for his assistance with backing up simulation results and printing transparencies.

I would like to thank the technicians from the Department of Physics – Don Mullin, Greg Popowich, Ken Marsh, and Tony Walford, who I am greatly in debt to for their assistance in setting up and fixing apparatus in the laboratory. In addition to the department's technical staff, I would also like to thank Jim MacKinnon and Jay Haverstock for solving any computing issues that arose, especially those associated with working remotely, and the support staff.

The lithography and some of the thin film growth were carried out at the University of Alberta Nanofab. I would like to thank the Nanofab staff for providing training, advice, and technical support: Ken Westra, Stephanie Bozic, Keith Franklin, Mirwais Aktary, and Nicole Morin.

I would also like to acknowledge funding from NSERC, iCORE, the Alberta Heritage Foundation, and the Killam Trust.

To my committee and external examiner, I thank you for serving on my committee and for your helpful feedback on my work.

Last but not least, I would like to acknowledge my family for their support. I would especially like to thank my husband, Norm, for his encouragement throughout my degree. Thank you Norm, for everything!

Table of Contents

1	Introduction and background	1
1.1	Introduction	1
1.2	Magnetic nanoparticles	2
1.2.1	Ferromagnetic domains	2
1.2.2	Single domain particles	4
1.2.3	Hysteresis in single-domain nanostructures	5
1.2.4	Coercivity of small particles	7
1.2.5	Superparamagnetism	8
1.3	Magneto-optical effects	11
1.4	Time-resolved scanning Kerr effect microscopy	13
1.5	Ion implantation	15
1.6	Outline	17
2	Theory	19
2.1	Dipolar interactions	19
2.2	Ferromagnetic resonance	23
2.2.1	Basic FMR theory	24
2.2.2	Generalized resonance formula	25
2.3	Magnetic resonance for an array of nanoclusters	28
2.3.1	Striped magnetization	29
2.3.2	Uniform magnetization	32
2.3.3	From striped to uniform	34
2.3.4	Kittel demagnetization coefficients	36
2.4	FMR of nanocluster array, out-of-plane bias field	37
2.4.1	High out-of-plane bias fields	38
2.4.2	Low out-of-plane bias fields	39
2.5	Micromagnetics simulations	41
2.5.1	Exchange energy	42
2.5.2	Anisotropy energy	43
2.5.3	Zeeman energy	43
2.5.4	Demagnetization energy	44
2.5.5	Other energy terms	44
3	Experimental Setup	46
3.1	Sample preparation	46
3.2	Patterning of nanocomposites	47
3.3	Hysteresis measurements (MOKE)	50
3.4	TR-SKEM measurements	55
3.4.1	Photoconductive switches	61
3.4.2	Transient field generated by a transmission wire	65

4	Microstructure and hysteresis	69
4.1	TEM results	70
4.2	Patterning results	76
4.3	Optical properties	79
4.4	Hysteresis measurements	82
4.4.1	Large Faraday rotation	95
5	Magneto-dynamics of Fe implanted SiO₂	98
5.1	Results, 10 ns pulse	98
5.2	Photoconductive switch data	103
5.2.1	Dynamic response of the specimens	103
5.2.2	Rise time trend	105
5.2.3	Variation of temporal response with position	108
5.3	AC Susceptibility as a function of temperature	111
5.4	Effective medium approximation	113
6	Micromagnetics simulation results	120
6.1	The models	121
6.2	Initial states	124
6.3	Hysteresis	127
6.3.1	Temperature dependence of AC Susceptibility	129
6.4	Temporal response to a square magnetic field pulse	131
6.4.1	In-plane transient field	131
6.4.2	Out-of-plane transient field	138
6.5	Temporal response to a photoconductive switch pulse	138
6.5.1	Regular array response as a function of in-plane bias field	140
6.5.2	Regular array response as a function of inter-particle separation	142
6.5.3	Regular array response as a function of scale	149
6.5.4	Regular array response as a function of pulse angle	150
6.5.5	Regular array response as a function of out-of-plane bias field	154
6.5.6	Irregular array response as a function of in-plane bias field	155
6.5.7	Comparison of data and simulations	158
7	Discussion	163
7.1	Comparison of experimental and simulation results	163
7.2	Technological implications	169
7.2.1	Ultrafast current probe	169
7.2.2	Considerations in MRAM development	172
8	Conclusions	175
A	FMR equation summary	179
B	Details of patterning technique	181
C	Magneto-optical hysteresis loop measurements	183
D	Preparation of photoconductive switches	187
	Bibliography	194

List of Tables

1.1	Verdet constants V and total Faraday rotation θ_F for selected materials.	12
2.1	Demagnetization factors for a sphere, an infinite sheet in the $x-z$ plane, and a cylinder aligned along the z axis.	25
2.2	Demagnetization factors for a two-dimensional array of magnetic dipole for a striped configurations (stripes parallel to z axis) and for uniform alignment along the z axis.	37
3.1	Ion implantation parameters for SiO ₂ substrates.	47
3.2	Candidate masking materials.	48
3.3	Ion stopping and range for 80 keV iron ions [1].	49
4.1	Summary of Fe implanted SiO ₂ samples including implantation energy, annealing temperature, and whether or not a coating was used.	70
4.2	Sample thicknesses.	83
4.3	Table of coercivities H_c and corresponding errors ΔH_c for Fe implanted SiO ₂ obtained from in-plane Faraday hysteresis measurements.	86
5.1	Exponential fit parameters for in-plane temporal data.	101
5.2	Optical and magneto-optical parameters for bulk iron.	116
5.3	Values for the refractive index η , the magneto-optical Voigt parameter Q , and the Kerr and Faraday rotation, ϕ_K and ϕ_F , calculated using effective medium approximations.	117
6.1	Exponential fit parameters for simulated response to a 48 kA/m (600 Oe) in-plane transient magnetic field.	135

List of Figures

1.1	Spheroidal particle showing the definitions of the angles θ and α used in the Stoner-Wohlfarth theory.	6
1.2	Stoner-Wohlfarth hysteresis curves for a single-domain ferromagnetic particle [2] including the definitions of saturation magnetization, remnant magnetization, and coercivity.	7
1.3	Dependence of intrinsic coercivity on particle diameter [2].	9
1.4	Kerr-effect configurations: a) polar, b) longitudinal, and c) transverse (after Freiser, 1968).	12
1.5	Illustration of how ion implantation process is used to fabricate nanoparticles.	16
2.1	Magnetic dipoles.	20
2.2	Energy as a function of angle for the interaction of two magnetic dipoles.	21
2.3	Magnetic field will be found for particle at $i = j = 0$ for an array of magnetic dipoles with a minimum inter-particle spacing of a	21
2.4	Energy and resonance frequency vs. in-plane bias field for a regular array of magnetic dipoles.	36
2.5	Values of the summations as a function of array size k_{max}	37
3.1	Diagram illustrating the masking procedure used for creating patterned nanocomposites.	48
3.2	Histograms of predicted ranges and lateral spread of 80 keV Fe ⁺ ions implanted in SiO ₂	50
3.3	Photograph and diagram showing set-up used to measure static hysteresis loops.	52
3.4	View of sample positioned between the magnet pole pieces for in-plane hysteresis measurements.	53
3.5	Configurations used to measure in-plane and out of plane hysteresis loops.	53
3.6	Extinction curve with Fe implanted SiO ₂ sample in place.	54
3.7	Illustration of the pump-probe concept.	55
3.8	Transmission wire set-up.	56
3.9	Diagram of the apparatus used in TR-MOKE measurements where an electronic pulser is used to generate a transient magnetic field.	57
3.10	Diagram showing how the polar Kerr effect is exploited to measure M_z	59
3.11	Diagram showing how the longitudinal Kerr effect is exploited to measure the in-plane components of the magnetization.	60
3.12	Illustration of the transmission wire and photoconductive switch arrangement.	62
3.13	Diagram of the TR-SKEM apparatus modified to employ a photoconductive switch for generating the transient magnetic field.	64
3.14	Cross-sectional diagram of a current-carrying transmission wire.	67
3.15	Magnetic field generated by a 1 A current pulse traveling through a set of 10 μm transmission wires separated by 10 μm	68
4.1	Plan view and cross-sectional TEM micrographs of Fe nanoclusters in SiO ₂ (80 kV, 1.5×10^{17} ions/cm ² , as-implanted and annealed at 600°C).	72
4.2	Cross-sectional (a and b) and plan view (c) TEM micrographs of Fe nanocrystals fabricated by implanting 80 keV ions into SiO ₂ and annealing at 800°C.	73
4.3	Cross-sectional TEM micrographs of 80 keV Fe-implanted specimens that were coated with 200 nm of SiO ₂ prior to annealing at 600°C, 800°C, and 1000°C.	75

4.4	TEM micrographs of Fe nanoclusters fabricated by implanting 150 kV Fe ions into SiO ₂ . a) plan view and b) cross-sectional images of as-implanted specimen.	76
4.5	Mo mask (760±10 nm thick) on SiO ₂ before implantation.	77
4.6	A 380-nm-thick Mo mask on SiO ₂ before (left) and after (right) implantation with 80 kV Fe ⁺ ions to a fluence of 5 × 10 ¹⁶ ions/cm ²	78
4.7	Optical microscope picture of patterned implanted sample after removing the Mo mask.	78
4.8	Transmission, reflection and absorption of iron nanocomposite specimens.	81
4.9	Comparison of in-plane magnetic hysteresis curves for the 80 kV Fe as-implanted SiO ₂ sample (u1m) obtained using a vibrating sample magnetometer and through Faraday rotation.	84
4.10	In-plane magnetic hysteresis curves for the u series measured in transmission.	85
4.11	In-plane magnetic hysteresis curves for the c series measured in transmission.	87
4.12	In-plane magnetic hysteresis curves for the d series measured in transmission.	88
4.13	In-plane magnetic hysteresis curves for the d series measured in reflection.	90
4.14	Example of a typical background signal (no sample) in measuring the out-of-plane magnetic hysteresis curves.	90
4.15	Out-of-plane magnetic hysteresis curves for the u series measured in transmission.	91
4.16	Out-of-plane magnetic hysteresis curves for the c series measured in transmission.	92
4.17	Out-of-plane magnetic hysteresis curves for the d series measured in transmission.	94
5.1	In-plane response of sample u1 to 10 ns current pulse.	100
5.2	Out-of-plane response of sample u1 to 10 ns current pulse.	102
5.3	Response of sample u1 to photoconductive switch transient pulse.	104
5.4	Response of sample u2 to photoconductive switch transient pulse.	105
5.5	Response of sample u2 to photoconductive switch transient pulse, reflection suppressed.	106
5.6	Comparison of the proposed fit functions for determining rise times.	108
5.7	Rise time as a function of in-plane bias field for samples u1 and u2.	109
5.8	Temporal scans as a function of position between wires.	109
5.9	Intensity scans showing the position of temporal measurements.	110
5.10	Spatial Kerr images corresponding to the previous figure.	110
5.11	Diagram of the arrangement of the specimen and coil over a cold finger.	112
5.12	AC susceptibility as a function of temperature for Fe/SiO ₂	114
5.13	Effective medium approximation for the complex refractive indices and the magneto-optical Voigt parameter for Fe spheres in SiO ₂ as a function of volume fraction of iron.	118
5.14	Predicted Faraday and Kerr rotation for Fe spheres in SiO ₂ vs. volume fraction of iron.	118
6.1	Illustration of two types of models used in to approximate the nanocomposite specimen: a) a regular array and b) an irregular array.	122
6.2	Total and demagnetization energy as a function of iteration for a regular array in zero bias field.	123
6.3	Initial state for a regular array of Fe cubes with no bias field.	125
6.4	Initial state for a regular array of Fe cubes subject to an in-plane bias field of 8 kA/m (100 Oe).	125
6.5	Initial state for a random array of Fe cubes with no bias field.	126
6.6	Initial state for a random array of Fe cubes subject to an in-plane bias field of 8 kA/m (100 Oe).	126
6.7	Initial state for a three dimensional random array of 10 nm Fe cubes subject to zero bias field.	127
6.8	Initial state for a three dimensional random array of Fe cubes with sizes ranging from 2.5 to 17.5 nm subject to zero bias field.	128
6.9	Simulations of the in-plane hysteresis curves along the <i>x</i> -direction (easy axis of the cube) and at an angle of 63° in-plane for a single 10 nm cube.	130
6.10	Simulations of the in-plane hysteresis curves along the <i>x</i> -direction and at an angle of 63° in-plane for a) a regular array with 5 nm separation, and b) an irregular array of 10 nm cubes.	130
6.11	Simulations of the out-of-plane hysteresis curves for the same regular and random arrays as in Figure 6.10.	131
6.12	Simulations of the out-of-plane hysteresis curve over a smaller field range for temperatures ranging from 0 to 300 K.	132
6.13	Magnetization as a function of time, <i>x</i> component, for a regular array of 10 nm cubes separated by 5 nm, a random array of 10 nm cubes, and both of the three-dimensional models.	133

6.14	Average in-plane magnetization M_x as a function of time for the model in response to in-plane transient magnetic fields (x direction) of 4.8 and 48 kA/m.	134
6.15	Magnetization as a function of time, x component, for randomly selected individual cubes in a regular array in response to a 48 kA/m (600 Oe) in-plane transient field with zero bias field.	137
6.16	Magnetization as a function of time, z component, for a regular array of 10 nm cubes separated by 5 nm, and both two and three-dimensional random arrays of 10 nm cubes.	139
6.17	Magnetization as a function of time for a regular array of cubes subjected to a transient out-of-plane magnetic field in the presence of an in-plane bias.	143
6.18	Interpolated image of the magnetization (z component) as a function of time and in-plane bias field for a regular array of cubes subjected to a transient out-of-plane magnetic field.	144
6.19	a) Rise time and b) resonance frequency as a function of out-of-plane bias field for a regular array of Fe cubes.	145
6.20	Histograms of local effective fields at each cube due to the dipolar fields of all of the other cubes in the model for in-plane bias fields of a) 0 Oe, b) 8 kA/m, c) 20 kA/m, and d) 120 kA/m.	146
6.21	Magnetization as a function of time, y and z components, for a single cube from an area with stripes parallel to the x axis.	147
6.22	Magnetization (z component) vs. time for a regular array of cubes with inter-particle separations ranging from 2.5 to 15 nm for in-plane bias fields of a) 0 kA/m and b) a 120 kA/m.	148
6.23	a) Rise times and b) peak frequencies measured from the M_z response for a regular array as a function of inter-particle separation (0 and 120 kA/m bias fields).	149
6.24	Initial state for a regular array of cubes, 2×2 cells, separated by 1 cell, cell size 2 nm.	150
6.25	Initial state for a regular array of cubes, 2×2 cells, separated by 1 cell, cell size 1 nm.	151
6.26	The a) z , and b) y components of the magnetization for a regular array of Fe cubes with cell sizes ranging from 1 to 10 nm where the cubes.	151
6.27	Magnetization (M_y and M_z) as a function of time for a regular array of cubes subjected to a transient magnetic field with a static bias field of 140 kA/m applied in the x direction.	153
6.28	Initial state for a regular array of Fe cubes subject to a 320 kA/m out-of-plane bias field.	155
6.29	Magnetization vs. time for a regular array of cubes subjected to a transient magnetic field in the presence of an out-of-plane bias fields a) below and b) above the saturation field.	156
6.30	a) Rise time and b) resonance frequency as a function of out-of-plane bias field for a regular array of Fe cubes.	157
6.31	The a) z and b) y components of magnetization as a vs. time for a random array of cubes subjected to a transient out-of-plane magnetic field for a range of in-plane bias fields.	159
6.32	a) Rise time and b) resonance frequency as a function of in-plane bias field for a random array of Fe cubes.	160
6.33	Histograms of local effective fields at each cube due to the other cubes in the model (random array) for in-plane bias fields of a) 0 kA/m, b) 8 kA/m, c) 20 kA/m, and d) 120 kA/m.	161
6.34	Comparison of simulations and data measured using a photoconductive switch showing a) M_z as a function of time for zero bias field and b) rise time as a function of bias field.	162
7.1	Diagram illustrating how the nanoparticles respond to a transient out-of-plane field.	165
7.2	Illustration of how an ion implanted SIL lens can be used as an ultrafast current probe.	172
7.3	Diagram illustrating a possible plan for precession-limited fast MRAM [3].	173
B.1	Design of mask for optical lithography for creating patterned nanocomposites.	182
D.1	Diagram (to scale) showing the design of the wires with photoconductive switches.	188
D.2	Calibration curve for Nanofab mask writer (July, 2002).	193

List of Symbols

A_1, A_2	amplitude constants used in two-exponential fit	$h_x^{rf}, h_y^{rf}, h_z^{rf}$	Cartesian components of an rf magnetic field
A_{ex}	exchange energy (2.1×10^{-11} J/m for iron)	$\hat{i}, \hat{j}, \hat{k}$	Cartesian unit vectors
A, B, C, A_U	summations for an array of dipoles (dimensionless)	J	constant describing magnitude of exchange interaction
a, b, p, q	empirical constants describing coercivity trend	K	anisotropy constant
a	size of unit cell in the context of exchange interactions	K_1	cubic crystalline anisotropy constant (4.7×10^4 J/m ³ for iron)
a	center to center minimum inter-particle separation	K_u	uniaxial crystalline anisotropy constant
c	speed of light	k_B	Boltzman constant
\vec{B}	magnetic induction (T)	k_n	number of nearest neighbours in the crystal structure
c	cell size in simulations	l	sample thickness
D_c	critical diameter for a single domain particle	\vec{M}	magnetization or magnetic moment per unit volume (A/m)
D	diameter of a spherical particle	\vec{m}	magnetic moment (A·m ²)
E_a	anisotropy energy barrier	m	reduced magnetization $m = M/M_s$ for Stoner-Wohlfarth model
e	charge of an electron	M_s	saturation magnetization (1.714×10^6 A/m for iron)
f	frequency	M_x, M_y, M_z	Cartesian components of magnetization (A/m)
f	volume fraction	\vec{M}_0	constant part of the magnetization in ferromagnetic resonance derivation
f_o	resonance frequency	m_e	mass of an electron
g	spectroscopic splitting factor	m_x, m_y	Cartesian components of time dependent part of the magnetization (A/m)
\vec{H}	magnetic field (A/m)	N_x, N_y, N_z	demagnetization factors ($N_x + N_y + N_z = 1$ in SI units)
\vec{H}_{eff}	effective magnetic field (A/m)	p	ratio of axes of a prolate spheroid (≥ 1)
\vec{H}_{ext}	external magnetic field (A/m)	Q	magneto-optical Voigt parameter (complex)
H_c	normally coercivity (A/m), also used in ferromagnetic resonance formula for an array of dipoles as $H_c = M_s V / (4\pi a^3)$	\hat{r}	unit position vector
H_x, H_y, H_z	Cartesian components of magnetic field (A/m)	r	magnitude of the position vector
H	Hamiltonian	R	radius
\vec{H}_o	constant part of the magnetic field in ferromagnetic resonance derivation, also effective field in Larmour equation	S_i, S_j	quantum mechanical spin operator
h	reduced applied field $h = HM_s / 2K_u$ for Stoner-Wohlfarth model	T	temperature
$h(t)$	profile of transient magnetic field pulse	t	time
h_c	critical reduced field in Stoner-Wohlfarth model	t_{rise}	10/90% rise time
		U	energy (J)
		V	volume

V	Verdet constant	τ_1, τ_2	time constants used in two-exponential fit
x_p, z_p	Cartesian coordinates of a point	ϕ_x, ϕ_y	small angles used in ferromagnetic resonance derivation
x_w, z_w	Cartesian coordinates of a point on a transmission wire	ϕ	polar angle from the z axis ($0 \leq \phi \leq \pi$)
α	damping constant (0.0023 for iron [4])	ϕ_K	Kerr rotation
$\alpha_1, \alpha_2, \alpha_3$	direction cosines of the magnetization ($-1 \leq \alpha_i \leq 1$)	ϕ_F	Faraday rotation
α, θ	angles used in Stoner-Wohlfarth model	ϕ_{Ks}	Kerr rotation for s-polarized light
γ	gyromagnetic field, $1.76 \times 10^{11} \text{ Hz} \cdot \text{T}^{-1}$ ($1.76 \times 10^7 \text{ Hz} \cdot \text{Oe}^{-1}$) for iron	ϕ_{Fs}	Faraday rotation for s-polarized light
γ	magneto-optical constant $\gamma = -i\epsilon_{xy} = Q\epsilon_{xx}$	ϕ_1, ϕ_2	small angles used in ferromagnetic resonance derivation
γ_e	effective magneto-optical constant	χ	magnetic susceptibility (dimensionless, 4π (SI) = 1 (cgs))
ϵ	energy per unit volume (J/m^3)	ω	angular frequency $\omega = 2\pi f$
ϵ_a	anisotropy energy per unit volume	ω_o	angular resonance frequency
ϵ_{ext}	Zeeman energy per unit volume		
ϵ_{dem}	demagnetization energy per unit volume for a magnetic particle in an array		
ϵ_o	energy (per unit volume) at an equilibrium position		
ϵ_{ij}	second derivative energy where i and j can each represent x or y in cartesian coordinates, θ or ϕ in spherical coordinates		
ϵ_{yy}	energy (per unit volume) at an equilibrium position		
ϵ_p	dielectric constant of particle (diagonal)		
ϵ_m	dielectric constant of matrix (diagonal)		
ϵ_e	effective dielectric constant (diagonal)		
ϵ_1 OR ϵ_{xx}	dielectric constant (diagonal)		
ϵ_2 OR ϵ_{xy}	dielectric constant (off-diagonal)		
ϵ_{xy}	dielectric constant (off-diagonal)		
η	index of refraction		
η_o	index of refraction (subscript emphasizes it is for zero field)		
η^\pm	indices of refraction for right and left circularly polarized light		
θ	azimuthal angle in the $x - y$ plane ($0 \leq \theta < 2\pi$)		
θ	Faraday rotation angle		
θ_c	critical angle in Stoner-Wohlfarth model		
θ_H, ϕ_H	spherical coordinates of the external magnetic field		
λ	wavelength		
μ_o	permeability of free space ($4\pi \times 10^{-7} \text{ N}/\text{A}^2$)		
ξ	used in calculating critical diameter of single domain particle		
τ_c	carrier lifetime		
τ_r	time constant describing rising edge of transient magnetic field pulse		

Chapter 1

Introduction and background

1.1 Introduction

Magnetism is a rich and interesting field of study from a fundamental perspective, especially as experimental capabilities progress to smaller scales. There is also currently great interest in magnetic nanoparticles, loosely defined as magnetic particles with dimensions smaller than a micrometer, due to their potential applications. Magnetic nanoparticles may find important applications in ultra-high-density magnetic recording technologies. For individual bits with particle size and separation smaller than 50 nm (i.e., single nanoparticles) recording media with areal densities approaching 1 terabit per square inch might be obtained [5]. This would represent a substantial improvement over current technology, in which the storage densities are at about 60 gigabits per square inch in high-end commercially available products and 100 gigabits per square inch in the lab [6]. While the properties of isolated single domain magnetic nanoparticles are reasonably well understood [2], the effects of inter-particle interactions on the behavior of an ensemble of nanoparticles continues to be an active area of research [7–9]. As the limits of access speed are also being explored, improvements in the understanding of the dynamic properties of magnetic nanoparticles and the role that magnetic interactions play will be relevant to the advancement of data storage technology.

In addition to magnetic storage and magneto-electronics applications, the medical community is interested in tailoring magnetic nanoparticles for use as contrast agents for magnetic resonance imaging, targeted drug delivery and for use as tracking agents in the body [10]. Also, many permanent magnets are made up of a collection of small,

single-domain magnetic particles [11]. The desired properties for each of these applications are, however, not necessarily the same. A fundamental understanding of the underlying physics of small magnetic particles is thus important.

The magneto-optical properties of these small particles are also of interest [12–14]. These properties have been less well studied to date, but interest in this area is increasing at present as magneto-optical investigations provide useful insights into electronic properties of materials [15,16]. The magneto-optical properties of nanostructured Fe thin films are found to be different than those of bulk iron [17]. The Kerr rotation for granular films has been shown to depend on both the particle density and the particle/matrix interface [16]. Other studies indicate that the magneto-optical properties of Fe nanocomposites agree reasonably well with effective medium approximations for particle sizes larger than 4 nm [18]. In addition to being a useful probe, studying the magneto-optical properties of materials can lead to technological advancement. Devices such as Faraday isolators, magneto-optical storage devices, magneto-optic modulators, and magnetic field or current sensors are important technologies that rely on optically active magnetic materials [19].

In this study, the static and dynamic magnetic and magneto-optical properties of a thin layer of strongly interacting Fe nanocrystals were examined. Magnetic hysteresis curves were measured using Faraday rotation and the dynamics of the nanocomposite were investigated using ultrafast time-resolved scanning Kerr effect microscopy (TR-SKEM), a powerful tool that combines picosecond temporal and sub-micrometer spatial resolution [20,21]. The TR-SKEM technique has been applied to permalloy microstructures [22] and has provided insights into magnetic switching dynamics [23]. This technique has, however, not yet been applied to nanocomposite materials.

1.2 Magnetic nanoparticles

1.2.1 Ferromagnetic domains

Magnetic domains were hypothesized to exist in 1906 by Weiss but the idea remained virtually unexplored until 1949 when researchers at Bell Telephone Laboratories observed domains in silicon-iron single crystals. A domain wall is defined as the interface between regions in which the spontaneous magnetization has different directions. Domain theory

is now an important part of the study of magnetism [2].

Ferromagnetism is commonly described by the Heisenberg Hamiltonian

$$\mathcal{H} = -|J| \sum_{ij} \mathbf{S}_i \cdot \mathbf{S}_j \quad (1.1)$$

where J describes the magnitude of the exchange interaction and \mathbf{S}_i and \mathbf{S}_j are spin operators. This Hamiltonian term describes the exchange energy of a material. This is the energy that arises from interactions between the atomic spins. The lowest energy state occurs when all of the spins of adjacent particles are aligned. In bulk materials, however, spins are only observed to align in small areas known as domains. There are several energy contributions not taken into account by the Heisenberg Hamiltonian – contributions due to anisotropy and demagnetization, for example. A bulk ferromagnetic sample will spontaneously divide into domains to minimize its total energy. As a particle becomes smaller, however, there comes a point where the single-domain state is energetically more favourable.

If a magnetic field is applied to a bulk ferromagnetic material, the magnetization of the material will increase through either the motion of domain walls or the rotation of the domains themselves. In the presence of a sufficiently large magnetic field, all of the domains will tend to align along the direction of the applied field and a corresponding saturation value of the magnetization will be observed. The response is generally not reversible, which gives rise to the observation of hysteresis behaviour for ferromagnets [2].

The response of a small particle to a magnetic field can be quite different than that of a bulk material, however. As the size of a ferromagnetic particle is reduced, a critical size is reached such that the magnetostatic energy of the particle becomes less for the single-domain state than for a multi-domain configuration. In contrast to the multi-domain state, the magnetization of a single-domain particle is usually described by a single magnetic moment vector that reverses through coherent rotation [2].*

*This is a simplified view - larger magnetic particles can also reverse through nucleation and curling [24].

1.2.2 Single domain particles

Single-domain magnetic particles are of great theoretical and practical interest. They exhibit different behaviour than larger particles, one example being superparamagnetism, which is characterized by the apparent loss of ferromagnetism in a collection of small particles, depending on the time scale of the measurement [24]. The first questions that arise about these particles are how small is this critical size and upon what does it depend? This can be answered by considering the energy of the particle. The particle is expected to be single-domain when the energy for that state is smaller than for a multi-domain arrangement. In determining the energy, it is important to take into account the shape of the particle and the magnetic anisotropy of the crystal. If the particle is embedded in a host material then the interactions with the host material may also be important.

Often it is only possible to put broad limits on the value of the critical size [24]. A simple expression for the lower bound on the critical diameter D_c for the single domain state of a prolate spheroid particle (in m) is given (neglecting anisotropy) by

$$D_c \approx \frac{2q}{M_s} \sqrt{\frac{A_{ex}}{\mu_o N_z}} \quad (1.2)$$

where M_s is the saturation magnetization, A_{ex} is the exchange constant, and N_z is the demagnetization factor along z . For a prolate spheroid, the factor q is given by

$$q = 1.84120 + 0.48694/p - 0.11381/p^2 - 0.50149/p^3 + 0.54072/p^4 - 0.172/p^5 \quad (1.3)$$

where $p = c/a \geq 1$ is the ratio of ellipsoidal axes; for a sphere $p = 1$, while $p = \infty$ represents the limit of an infinite cylinder. The demagnetization factor for a prolate spheroid is given by

$$N_z = \frac{1}{p^2 - 1} \left[\frac{1}{2\xi} \ln \left(\frac{1 + \xi}{1 - \xi} \right) - 1 \right] \quad (1.4)$$

where $\xi = \sqrt{p^2 - 1}/p$. For a sphere, $q \approx 2.0816$ and $N_z = 1/3$. Using the constants for bulk iron, $M_s = 1.714 \times 10^6$ A/m and $A_{ex} = 2.1 \times 10^{-11}$ J/m [25], which yields a critical diameter of 17 nm.

The anisotropy constant, which is a constant that describes the dependence of the magnetic properties on a preferred direction, is sufficiently large for iron ($K_1 = 4.7 \times 10^4$ J/m³ [25]) that the calculation above is expected to underestimate the critical diameter.

An estimate for the upper limit on the critical diameter for a spherical particle, which does incorporate the crystalline anisotropy, can be expressed as

$$D_c = \frac{18}{8 \times 10^{-7}(3\sigma - 2)M_s^2} \sqrt{A_{ex}(K_1 + 8 \times 10^{-7}\pi\sigma M_s^2)} \quad (1.5)$$

where $\sigma = 0.785398$ [24]. Thus the transition from a single to a multi-domain equilibrium state for an iron sphere occurs for a diameter of somewhere between 17 and 238 nm.

1.2.3 Hysteresis in single-domain nanostructures

Hysteresis in bulk materials is often related to the nucleation, annihilation, and motion of domain walls. Small magnetic structures can exhibit hysteresis even if they are small enough that domains do not form. The Stoner-Wohlfarth theory [2] is a simple model that predicts the shape of a hysteresis curve for either an individual single domain particle or else a collection of non-interacting particles. These particles are assumed to be prolate spheroids with uniaxial anisotropy. A magnetic field, H is applied at an angle α to the easy axis of the magnetic particle, which is assumed to be aligned with the semi-major axis of the spheroid (Figure 1.1). The energy per unit volume of the system is given by

$$\varepsilon = K_u \sin^2 \theta - \mu_o M_s H \cos(\alpha - \theta) \quad (1.6)$$

where K_u is the uniaxial anisotropy constant, M_s is the saturation magnetization and θ is the angle between M_s and the easy axis. To find the equilibrium position of M_s , the energy should be minimized with respect to θ

$$\frac{d\varepsilon}{d\theta} = 2K_u \sin \theta \cos \theta - \mu_o M_s H \sin(\alpha - \theta) = 0. \quad (1.7)$$

The magnetization resolved in the direction of the applied field is

$$M = M_s \cos(\alpha - \theta). \quad (1.8)$$

Reduced magnetization and applied field parameters can be defined as $m = M/M_s$ and $h = \mu_o M_s H / 2K_u$, respectively. The relationship $m = h$ then describes the hysteresis for $\alpha = 90^\circ$ (i.e., the coercivity is zero).

For arbitrary α , the relevant equations reduce to

$$\sin \theta \cos \theta - \sin(\alpha - \theta) = 0, \quad (1.9)$$

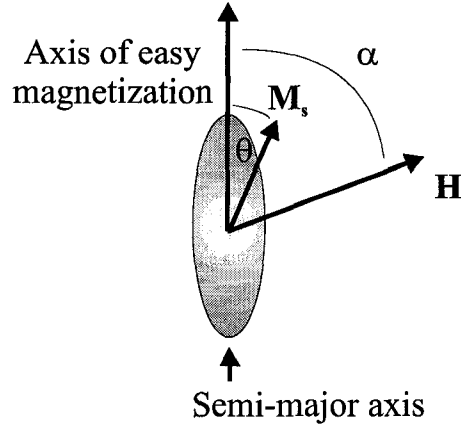


Figure 1.1: Spheroidal particle showing the definitions of the angles θ and α used in the Stoner-Wohlfarth theory.

$$m = \cos(\alpha - \theta). \quad (1.10)$$

In a hysteresis curve, there is a critical point where the energy minimum is unstable and the magnetization will flip. This can be found using

$$\frac{d^2 \varepsilon}{d\theta^2} = \cos^2 \theta - \sin^2 \theta + h \cos(\alpha - \theta) = 0. \quad (1.11)$$

Solving (1.9) and (1.11) simultaneously leads to the definition of the critical angle θ_c and critical reduced field h_c

$$\tan^3 \theta_c = -\tan \alpha, \quad (1.12)$$

$$h_c^2 = 1 - \frac{3}{4} \sin^2(2\theta_c). \quad (1.13)$$

The hysteresis curves predicted from this model are shown in Figure 1.2. For $\alpha = 90^\circ$ there is no hysteresis while for $\alpha = 0^\circ$ the coercivity is maximized and the hysteresis curve is square.

The Stoner-Wohlfarth model can also be used to predict the hysteresis curves for a collection of non-interacting nanoparticles. If the anisotropy axes of the particles are randomly oriented then the prediction is made by averaging the curves for all orientations. The importance of dipolar interactions in understanding the magnetic properties of collections of nanoparticles has often been overlooked in the past. In interpreting magnetic hysteresis curves in particular, non-interacting models have been favored for their simplicity. It is only more recently [8,26] that the inter-particle interactions have been shown

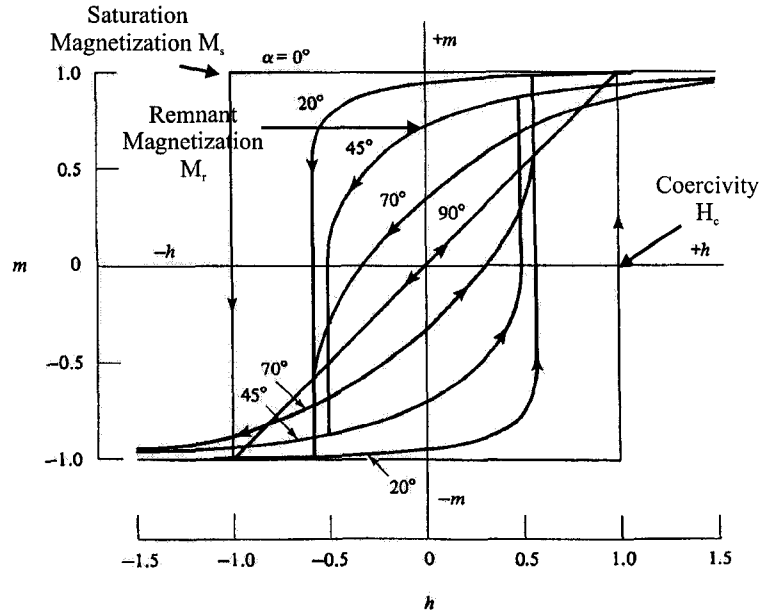


Figure 1.2: Stoner-Wohlfarth prediction of the hysteresis curves for a single-domain ferromagnetic particle (after Cullity, 1972 [2]). The diagram also illustrates the definition of saturation magnetization, remnant magnetization, and coercivity.

to be necessary for a full understanding of the hysteresis curves for these types of materials and have also been shown to lead to dipolar-based anisotropy effects depending on detailed arrangement of nanoparticles [27].

1.2.4 Coercivity of small particles

Coercivity is a value that is often considered in magnetic studies because it describes how easily a material can lose its magnetization. This is of particular importance for permanent magnets and magnetic storage devices where maintaining magnetization is desirable. The intrinsic coercivity, H_c is the value of the applied field required to reduce the magnetization to zero. Cullity [2] presents a good summary of the variation of coercivity with size.

For multi-domain particles, the coercivity is found experimentally to follow the relation

$$H_c = a + \frac{b}{D} \quad (1.14)$$

where a and b are constants and D is the particle diameter. This relation is empirical and is not fully understood.

For single-domain particles the relation becomes

$$H_c = p - \frac{q}{D^{3/2}} \quad (1.15)$$

where p and q are also constants. This is derived starting from the energy U of the nanoparticle placed in a field anti-aligned with its magnetic moment

$$U = V(K \sin^2 \theta + \mu_o M_s H \cos \theta) \quad (1.16)$$

where θ is the angle between \vec{M} and the easy axis of the particle, and V is the volume of the particle. The energy barrier for magnetic reversal is found through subtracting the maximum and minimum values of U , which are defined by the zeros of

$$V \sin \theta (2K \cos \theta - \mu_o M_s H) = 0. \quad (1.17)$$

The energy barrier has a single maximum corresponding to $\cos \theta = \mu_o M_s H / 2K$ and two minima corresponding to $\sin \theta = 0$ with energies $U = \pm \mu_o V M_s H$. Subtracting the minimum from the maximum energy value yields a barrier energy of

$$\Delta U = KV \left(1 + \left(\frac{\mu_o M_s H}{2K} \right)^2 \right) \quad (1.18)$$

If the energy barrier is set equal to the thermal energy available to the particle then $H = H_c$. Solving for H_c and noting that $V \propto D^3$ yields an expression of the form of Equation (1.15).

As D is reduced, a critical diameter is reached, below which the coercivity drops to zero. This is the region of superparamagnetism. These relationships describing the dependence of coercivity on particle size are illustrated in Figure 1.3.

1.2.5 Superparamagnetism

The magnetic moment of a single-domain particle will tend to align along an easy axis due to magnetic anisotropy. A certain amount of energy is required to re-orient the magnetic moment (1.18). When the thermal energy available to the particle is larger than this energy

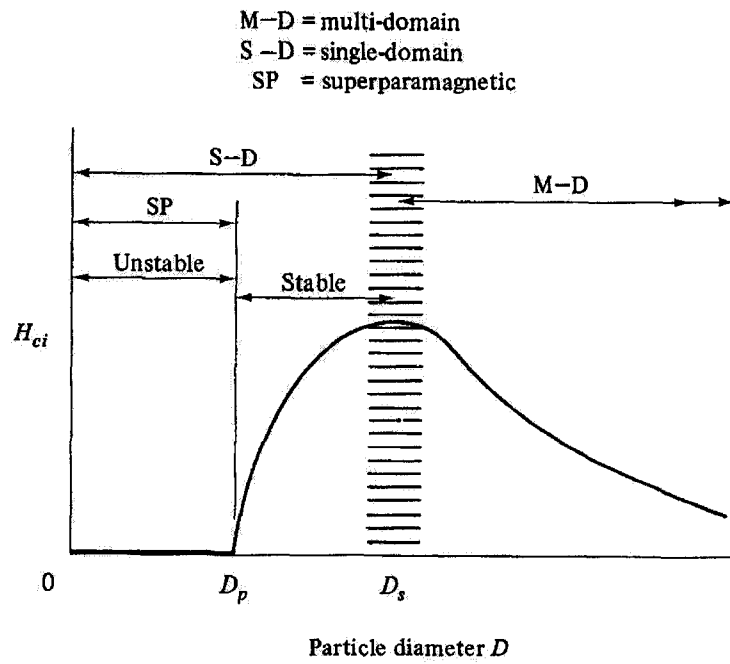


Figure 1.3: Dependence of intrinsic coercivity on particle diameter (after Cullity, 1972 [2]). The stack of horizontal lines is meant to illustrate that the boundary between single and multi-domain particles is not necessarily sharply defined.

barrier the magnetic moment of the particle can flip freely and can undergo coherent rotations (all spins rotate as one). An ensemble of single-domain particles with sufficient thermal energy will thus exhibit paramagnetic-like behaviour, a phenomenon known as superparamagnetism [24].

The Neel-Arrhenius law describes the relaxation time τ for a collection of non-interacting single domain nanocrystals [24]

$$\tau = \tau_o \exp(E_a/k_B T), \quad (1.19)$$

where $f_o = \tau_o^{-1}$ is an attempt frequency with typical values of between 10^9 and 10^{10} s^{-1} , k_B is the Boltzmann constant ($1.38 \times 10^{-23} \text{ J/K}$), T is temperature, and E_a is the anisotropy energy barrier that must be overcome in order for the particle to reverse. For uniaxial anisotropy $E_a = K_u V$, where K_u can include both crystalline and shape anisotropy contributions. For cubic anisotropy the expression is actually the same but with K_u replaced with $K_1/4$. Reducing the size of a particle will reduce the energy barrier, thereby reducing the onset temperature for superparamagnetism, also known as the blocking temperature. The blocking temperature for 3 nm nickel particles, for example, is around 20 K [28,29]. For spherical iron nanoparticles (using $K_1 = 4.7 \times 10^4 \text{ J/m}^3$, $f_o = 10^9 \text{ s}^{-1}$), a radius r of 11.5 nm corresponds to a relaxation time of 0.07 s but when r is increased to 14.0 nm, τ increases to $1.5 \times 10^5 \text{ s}$ at room temperature. Radii of 5 and 10 nm correspond to relaxation times of $\tau = 4.4 \text{ ns}$ and $\tau = 146 \text{ } \mu\text{s}$, respectively. This time dependence leads to the concept of dynamic coercivity – at fast time scales a collection of nanoparticles will often have a larger coercivity than at slow time scales. As a “rule of thumb”, superparamagnetism will generally be observed if $\tau \leq 0.01 \tau_{obs}$ where τ_{obs} is the observation time.

Magnetostatic interactions have been found to increase the energy barrier (and the relaxation time) in Co [30] and Ni [31] nanoclusters and the functional form of the relaxation also deviates from the Neel-Arrhenius expression. The Vogel-Fulcher law, for example, was proposed for interacting particles $\tau = \tau_o \exp(E_a/k_B(T - T_o))$, but is only valid for $T_o \ll T_B$. Dormann *et al.* [32] tested various proposed laws on data obtained for Fe nanocrystals over a wide frequency and temperature range and suggest an alternative model that incorporates the magnetic interactions into the energy barrier.

1.3 Magneto-optical effects

Plane polarized light incident on a magnetized material will undergo a rotation in polarization known as the Faraday effect in transmission and the Kerr effect in reflection. This is due to the inter-relationship between electromagnetism and light. With a simple optical set-up, these effects can be used to measure hysteresis loops magneto-optically. The particulars of one such set-up are discussed in detail below.

In 1845 Faraday first recorded evidence of the interaction of light with magnetic force [33]. He discovered that when a linearly polarized beam of light is propagated through a piece of lead glass[†] with a magnetic field applied parallel to the beam path, the light undergoes a rotation in polarization. This effect is commonly described in terms of the complex dielectric tensor ϵ . In an isotropic medium in the presence of a magnetic field along the z-axis, this tensor has the form

$$\epsilon = \begin{pmatrix} \epsilon_1 & \epsilon_2 & 0 \\ -\epsilon_2 & \epsilon_1 & 0 \\ 0 & 0 & \epsilon_1 \end{pmatrix}. \quad (1.20)$$

For a transparent, non-absorbing medium, ϵ_1 is real and ϵ_2 is imaginary. For an absorbing medium, both may be complex. Right and left circularly polarized light experience different indices of refraction $\eta^\pm = (\epsilon_1 \pm i\epsilon_2)^{1/2}$, which results in the observed polarization rotation for linearly polarized light.

The Faraday effect is a non-reciprocal effect, which means that the sign of the polarization rotation is in the same direction for a given magnetization direction independent of the direction of propagation of the light. The direction of rotation is reversed upon reversal of the magnetization. These properties are exploited in magneto-optical devices such as the Faraday isolator, designed to prevent back reflections from destabilizing lasers.[‡]

In diamagnetic and paramagnetic materials ϵ is proportional to the magnitude of the applied magnetic field H . For normal incidence where the magnetic field is applied per-

[†]Lead glass is glass that contains a high proportion of lead oxide [34].

[‡]A Faraday isolator is made up of a permanent magnetic, a magneto-optical material and a polarizer. The laser output passes through a polarizer that is aligned for maximum transmission and then through the magneto-optical material, which is tuned to rotate the polarization of the beam through an angle of 45 degrees. Beams reflected from other optical components undergo a rotation of an additional 45 degrees when they pass through the isolator on the return path, resulting in a total rotation of 90 degrees and maximum rejection by the polarizer.

1.3. MAGNETO-OPTICAL EFFECTS

Material	V (deg/A)	θ_F (deg/mm)	λ (nm)	Ref.
SiO ₂	3.48×10^{-4}	-	-	[35]
Flint Glass	6.64×10^{-4}	-	-	[35]
Air	1.32×10^{-7}	-	-	[35]
YIG*	-	24	1200	[36]
EuS doped TiO ₂ *	0.19 deg/cm/Oe	-	700	[37]
YIG indicator*	38	1.05×10^3	633	IBM
Ce _x Y _{3-x} Fe ₅ O ₁₂ *	17.7	1.78×10^3	633	[38]
α Fe*	-	3.5×10^4	-	[19]

Table 1.1: Verdet constants V and total Faraday rotation θ_F for selected materials. Entries marked with an asterisk are (ferro- or ferri-) magnetic so the Verdet constants listed are only valid up to saturation for these materials.

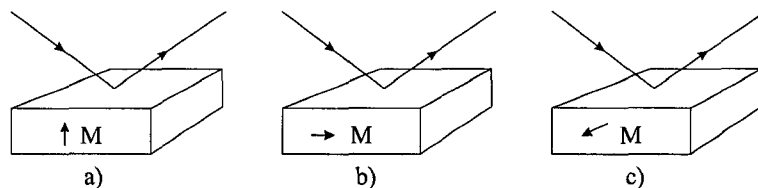


Figure 1.4: Kerr-effect configurations: a) polar, b) longitudinal, and c) transverse (after Freiser, 1968).

pendicular to the sample face, the rotation in polarization θ can be described as

$$\theta = V l H \quad (1.21)$$

where l is the sample thickness, and V is the Verdet constant of the medium. The Verdet constants for selected materials are listed in Table 1.1.

The rotation is proportional to the magnetization of the sample rather than the applied magnetic field, a property that can be exploited to measure hysteresis loops for ferromagnetic materials. Faraday rotation values for magnetic materials are usually listed as the polarization rotation achieved when saturation magnetization is reached.

When linearly polarized light is incident on a magnetized sample it will undergo a rotation in polarization upon reflection, an effect known as the magneto-optical Kerr effect [33]. Discovered by Kerr in 1888, this effect can be explained by the same physics responsible for the Faraday effect. There are three geometries associated with the Kerr

1.4. TIME-RESOLVED SCANNING KERR EFFECT MICROSCOPY

effect (Figure 1.4) [36]. The polar geometry occurs when the magnetization of the sample is perpendicular to the sample surface. This effect is strongest at normal incidence. The longitudinal Kerr effect occurs when the sample magnetization lies in the plane of the sample, parallel to the plane of incidence. The longitudinal effect is zero at normal incidence. The case where the magnetization vector lies in-plane but perpendicular to the plane of incidence is known as the transverse geometry. The transverse effect manifests itself as a change in reflectivity of p-polarized light (\vec{E} parallel to plane of reflection) related to the magnetization rather than a rotation in polarization. In general, linearly polarized light will undergo a change in polarization based on the component of the magnetization that is parallel or antiparallel to its direction of propagation.

The polar and longitudinal Kerr effects are exploited for measuring hysteresis loops and also for time-resolved scanning Kerr effect microscopy (TR-SKEM). For measuring out of plane hysteresis curves, the polar geometry is used while for in-plane measurements the longitudinal effect is employed. The same geometries apply whether the measurements are carried out in reflection (Kerr) or transmission (Faraday).

1.4 Time-resolved scanning Kerr effect microscopy

The dynamics of magnetic microstructures can be examined experimentally using an ultrafast microscopy technique known as time-resolved scanning Kerr effect microscopy (TR-SKEM). Time-resolved scanning Kerr effect microscopy is a powerful tool that combines picosecond temporal and sub-micrometer spatial resolution [20,21]. Both the polar and longitudinal Kerr effects can be measured simultaneously, allowing reconstruction of all three spatial components of the sample magnetization. The TR-SKEM technique has been applied to permalloy microstructures [22] and has recently provided insights into switching dynamics [23]. This technique, however, has not yet been applied to nanostructured materials.

The TR-SKEM technique works on a pump-probe principle. A current pulse is sent down a lithographically patterned transmission line to provide a transient magnetic field. The system is then probed using a laser at a later time and the temporal dynamics are reconstructed by varying the lag time between pump and probe pulses. Spatially the pic-

1.4. TIME-RESOLVED SCANNING KERR EFFECT MICROSCOPY

ture is constructed by scanning the probe laser over the sample surface. This is achieved in practice by varying the position of the sample using a piezo translation stage. By performing full spatial scans at a number of progressively longer lag times, magnetic “movies” showing the change in the spatial magnetization profile with time can be constructed. These movies provide valuable insight into switching dynamics. Other techniques, such as magnetic force microscopy (for example [39]), provide superior spatial resolution but are not capable of providing fast-time information [20].

The dynamics of nanocomposite materials were measured in response to a transient magnetic field produced by a current pulse propagating through a lithographically patterned transmission wire. Initial measurements were carried out using a current pulse generated by an electronic pulser. For this arrangement, typical pulse duration and time resolution were around 10 ns and 200 ps, respectively. The temporal resolution can be improved by at least an order of magnitude by employing photoconductive switches in TR-MOKE measurements [22,40]. In these studies, an optical pulse is used to excite the photoconductive switch providing a current pulse with a rise-time on the order of a few picoseconds. Photoconductive switches have also proven useful in shaping ultrafast current pulses for exploring precession-limited switching dynamics in permalloy microstructures [41,3]. Here, photoconductive switches were employed to generate a magnetic field pulse with a much faster rise time (on the order of a few picoseconds) to explore the dynamic response of iron nanocomposites on a faster time-scale.

Other researchers have used optical pulses directly rather than a current pulse to excite the magnetization of the sample on an ultrafast time-scale but the results are significantly more complicated to interpret [42–45]. The optical pulse can be used to thermally disrupt the magnetization of the specimen and probe the subsequent spin-relaxation dynamics. Alternately, if a circularly polarized pump beam is used, it can be used to transfer angular momentum to the magnetic moments of the specimen (“optically induced magnetization”) through what is sometimes known as the inverse Faraday effect [46].

1.5 Ion implantation

Magnetic nanoparticles can be created through a number of techniques including chemical synthesis [47,48,10], co-sputtering [49,37,16], pulsed laser deposition [50,51], sol-gel techniques[§] [52], electron-beam lithography [53,5], and ion implantation [7,12,28,13,54–57]. The nanoparticles examined in this study were created through ion implantation of Fe⁺ ions into optical quality fused quartz substrates.

Ion implantation is a versatile technique that can be used to modify surface properties (typically at fluences less than 10¹⁶ ions/cm²) or to create buried layers of nanoparticles (fluences > 10¹⁶ ions/cm²) [12]. Figure 1.5 illustrates how ion implantation is used to create nanoparticles. An element is ionized and accelerated (energies on the order of a few keV to several MeV) into a host material, resulting in a supersaturated solid solution in the near-surface of the host. Annealing a specimen generally promotes aggregation and crystallization of the implanted material resulting in the formation of nanoparticles (clusters of atoms with diameter on the order of 10⁻⁹ to 10⁻⁸ m), although nanocrystals have also been observed in as-implanted specimens [58].

Typical nanocomposite materials consist of a layer of nanoscale clusters of implanted material located within a layer that is typically a few tens of nanometers to a micron or more in thickness, depending on the implantation energy. These precipitates are formed below the surface and become an integral part of the host material. Thus nanocomposites formed through implantation are durable because they are protected from the surrounding environment, and the surface of the resulting composite remains flat enough to meet current data storage device specifications. The host also provides protection from oxidation and hydration under normal atmospheric conditions (protection from hydration lessens for higher energy/fluence implantations [59]). A wide variety of ferromagnetic nanoparticles can be created with different shapes, orientations, and magnetic properties through varying the host material, the implanted element, and the conditions under which the sample is annealed [39,13,7,60–63,28,54].

There are several disadvantages associated with ion implantation, however. One is that, so far, there is invariably a wide distribution of particle sizes. Another significant

[§]The sol-gel process, which can be used to fabricate a wide variety of ceramic and glass materials, involves the transition of a system from a liquid “sol” (mostly colloidal) into a solid “gel” phase.

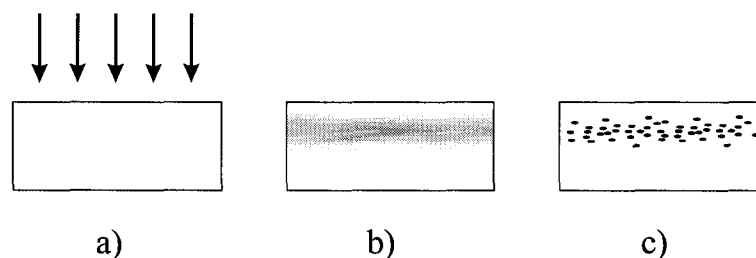


Figure 1.5: Ions are first implanted into a host material (a), resulting in a solid solution of ions in the near-surface region (~ 100 nm depth) (b). Subsequent annealing of the sample results in the formation of nanoparticles (c).

limitation of the technique is the inability to effectively implant into a small (micron or less), well-defined lateral region. Focused ion beams have some promise for patterning with “manufacturer-claimed” beam diameters of < 10 nm at the specimen surface [64]. Focused ion beam devices currently available, however, have been developed mainly as cutting or thinning tools and are very limited in both source type (mainly Ga) and energy range (5 to 30 kV) [65]. At this low energy, sputtering processes dominate [12].

An alternate method for achieving micron-scale lateral control on implantation employs lithographic masking. This method has been extensively used in the microelectronics industry for spatial selection of regions to be doped using ion implantation [66], and it has recently been applied to the patterning of the magnetic properties of Co/Pt magnetic multilayers through ion irradiation [67]. Until now, however, it has not been used to create patterned nanocomposite implanted materials. The details of the patterning technique will be discussed further in Chapter 3. Experimentally, patterning of microscale structures facilitates the use of scanning microscopy techniques for examining the properties of the nanostructured materials. Individual nanoparticles are not distinguishable using conventional optical microscopy techniques (the particles are tens of nanometers in size, which is small compared to the sub-micrometer beam diameter). Therefore, a microscale pattern is useful for ensuring proper focus. An additional advantage is that both implanted and unimplanted parts of the same specimen can be examined simultaneously.

Single-nanocrystal-per-bit data recording would represent an important advance in the information storage capacity of magnetic recording media [68]. Nevertheless, several quite stringent requirements must be met in order to achieve device-quality performance.

For single-particle bits to be written individually, the precipitates must be discrete, magnetically isolated, ferromagnetic nanoparticles that are larger than the superparamagnetic limit and whose coercivity, size, orientation, and position can be controlled [5]. Ferromagnetic nanoclusters produced by ion implantation can be formed as single domain particles that are larger than the superparamagnetic limit. The crystallographic orientation (and therefore, the magnetic anisotropy directions) can also be controlled by using single-crystal hosts [13]. However, the effects of magnetic interactions cannot always be neglected [8], size distributions are relatively wide, and there has been no effective in-plane control over the spatial distribution of the magnetic nanoclusters. In this thesis, a patterning technique will be developed to provide micrometer and sub-micrometer control over the in-plane location of implanted areas and the effects of inter-particle interactions in high-dose implanted specimens will be explored.

1.6 Outline

This thesis will focus on the microstructural, magnetic, and magneto-optical properties of nanocomposite materials. Nanoparticles were created through ion implantation of iron into SiO₂. A masking process was developed where ions were implanted through a metallic mask to create micro-scale patterned arrays of nanostructured areas. These patterned samples were found to be quite useful for microscopy-based characterization of implanted materials.

Both the static and dynamic magnetic properties of these nanocomposite samples were studied. The static magnetic properties were examined by measuring hysteresis loops using the magneto-optical Faraday effect. In some cases the observed Faraday rotation was found to be very large, which may be useful for technological applications. Dynamic measurements were made using time-resolved scanning Kerr effect microscopy (TR-SKEM) [21]. This is the first time this technique has been applied to these types of nanocomposite materials. An electronic pulser was used to generate transient magnetic fields 10 ns long with a rise-time of around 200 ps. Photoconductive switches were employed to generate a magnetic field pulse with a rise-time on the order of a few picoseconds to explore the dynamic response of iron nanocomposites at even faster time-scales. Finally, the results

of the dynamic measurements and hysteresis curves will be discussed in the context of ferromagnetic resonance predictions and complimentary micromagnetics simulations.

Chapter 2 develops the theoretical ferromagnetic resonance predictions of the ferromagnetic resonance behaviour for arrays of interacting magnetic nanoparticles and gives some basic background on micromagnetics simulation techniques. Chapter 3 provides a detailed description of sample preparation methods as well as the techniques used in characterizing their static and dynamic magnetic properties. Characterization results showing the microstructural, optical and hysteresis behaviour of the samples are presented in Chapter 4 along with an evaluation of the success of the patterning technique. The dynamic magnetic properties for selected samples are presented in Chapter 5 and corresponding micromagnetics simulations are detailed in Chapter 6. The results presented in the thesis as a whole are synthesized in Chapter 7 and some potential technological applications are discussed. Finally the results are summarized in Chapter 8.

Chapter 2

Theory

Dipolar interactions can influence the initial magnetization state of a nanocomposite specimen. They also play an important role in determining the ferromagnetic resonance frequency. Numerical simulations will be used to explore the details of dynamic processes for both regular arrays of nanoclusters as well as disordered arrangements containing distributions of separations and/or cluster sizes and to evaluate the validity of the analytical ferromagnetic resonance expressions. This chapter will outline the theory of dipolar interactions and ferromagnetic resonance of arrays of nanoclusters. Finally, the general theory of micromagnetics simulations will be discussed.

2.1 Dipolar interactions

The magnetic field generated by a dipole can be written as

$$\vec{B} = \frac{\mu_0}{4\pi r^3} [3(\vec{m} \cdot \hat{r})\hat{r} - \vec{m}] \quad (2.1)$$

where \vec{m} is the magnetization vector, μ_0 is the permeability of free space ($4\pi \times 10^{-7}$ N/A² in SI units), \hat{r} points from the dipole to the point where the field is being calculated, and r is the magnitude of this distance [69,70]. The magnetic field generated by a uniformly magnetized sphere is identical to that of a point dipole located at its center with dipole

moment $\vec{m} = M_s V \hat{m} = M_s \frac{4}{3} \pi R^3 \hat{m}$, where M_s is the saturation magnetization, V is the dipole volume, R is the dipole radius, and \hat{m} is a unit vector.

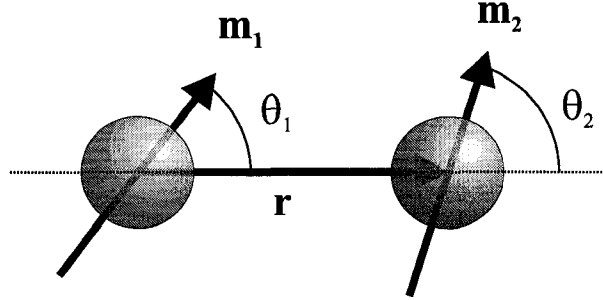


Figure 2.1: Magnetic dipoles.

Energy of a magnetic dipole in a magnetic field B is

$$U = -\vec{m} \cdot \vec{B} \quad (2.2)$$

The interaction of two magnetic dipoles (figure 2.1) with their separation described by the vector \vec{r} is given by

$$U = \frac{\mu_0}{4\pi r^3} (\vec{m}_1 \cdot \vec{m}_2 - 3(\vec{m}_1 \cdot \hat{r})(\vec{m}_2 \cdot \hat{r})) \quad (2.3)$$

where \vec{m}_1 and \vec{m}_2 are the magnetic dipole vectors. The energy of interaction for two magnetic dipoles is shown as a function of their orientation angles in Figure 2.2. Minima occur when the dipoles are aligned in the same direction either parallel or anti-parallel to \vec{r} . Saddle points occur for an anti-parallel arrangement with the dipole vectors orthogonal to \vec{r} . These saddle points represent the minimum energy configuration if one of the dipoles is fixed orthogonal to \vec{r} .

Based on energy considerations, the zero-field equilibrium state for a one dimensional array of magnetic dipoles would find all of the magnetization vectors aligned in the same direction, along the length of the line. A two dimensional array of spherical particles would be expected to form stripe-like patterns in zero external field as illustrated in Figure 2.3. Here alignment along the rows minimizes the dipolar interaction energy in the x direction while the alternating orientations of adjacent rows minimizes the energy between rows. Note that for a finite array size, smaller domain-like regions may form with vertical or horizontal striped patterns to minimize the demagnetization energy at the edges of the specimen.

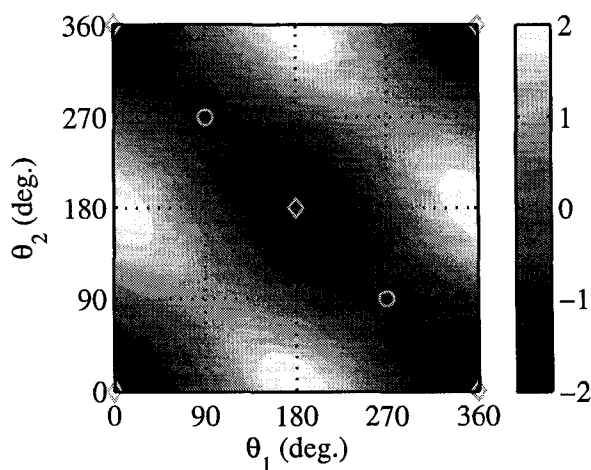


Figure 2.2: Energy, in units of $\mu_o M_s V / (4\pi r^3)$, as a function of angle for the interaction of two magnetic dipoles where the angles are defined in Figure 2.1. Diamonds mark the energy minima (corners and center) and circles show the saddle points that are minima if one of the dipoles is fixed such that it is orthogonal to the vector connecting the two.

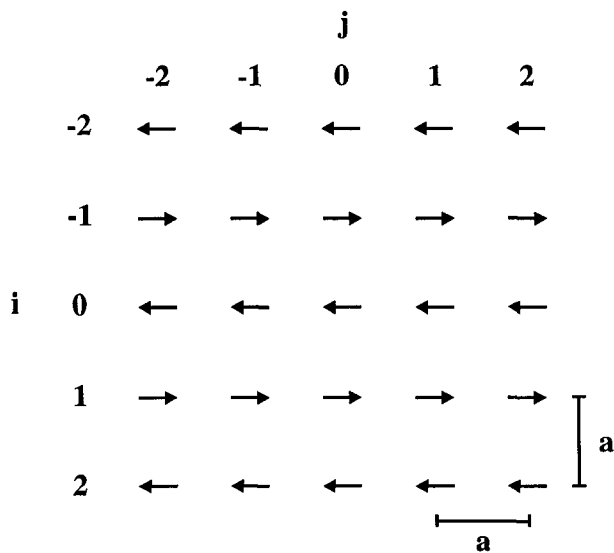


Figure 2.3: Magnetic field will be found for particle at $i = j = 0$ for an array of magnetic dipoles with a minimum inter-particle spacing of a .

2.1. DIPOLAR INTERACTIONS

It is informative to calculate the magnetic field for a given spherical particle generated by an infinite array of magnetic spheres in a striped magnetization configuration. The indices i and j can be taken as zero at an arbitrary particle, the location for which the magnetic field will be found. The magnetic field \vec{H} ($\vec{B} = \mu_o(\vec{H} + \vec{M})$), neglecting the self-demagnetization field, can be expressed as an infinite sum

$$\vec{H} = \frac{M_s V}{4\pi} \sum_{i,j} \frac{1}{r_{ij}^3} (3(\hat{m}_{ij} \cdot \hat{r}_{ij})\hat{r}_{ij} - \hat{m}_{ij}), \quad (2.4)$$

where the sums in i and j extend from negative to positive infinity, excluding the case where $i = j = 0$. The x direction is chosen to be parallel to the direction of the stripes. The magnetization for a given particle is $\hat{m}_{ij} = (-1)^{i+1}\hat{i}$ and the vector \vec{r}_{ij} is $ja\hat{i} + ia\hat{j}$ where a is the smallest distance between the centers of adjacent particles. The expression for \vec{H} reduces to

$$\vec{H} = \frac{M_s V}{4\pi a^3} \sum_{i,j} \frac{(-1)^{i+1}(2j^2 - i^2)\hat{i} + 3(-1)^{i+1}ij\hat{j}}{(j^2 + i^2)^{\frac{5}{2}}} \quad (2.5)$$

The summations come out to zero for the y component and -5.098873 in the x direction.* The same calculation centered on a particle with its magnetization oriented in the positive x direction yields an identical result except the magnetic field is positive.

If a large enough external magnetic field is applied then the magnetization vectors of the individual particles will become oriented along the direction of the applied field. Considering the same array in the saturated state with all of the magnetization vectors oriented in the negative x direction, $\hat{m}_{ij} = -\hat{i}$ for all ij and Equation 2.5 becomes

$$\vec{H} = \frac{M_s V}{4\pi a^3} \sum_{i,j} \frac{(i^2 - 2j^2)\hat{i} - 3ij\hat{j}}{(j^2 + i^2)^{\frac{5}{2}}}. \quad (2.6)$$

The y component again vanishes for an array of arbitrary size (a y component would be present near the edge of an array). The x summation, however, converges slowly to -4.51681[†]. The magnetic field for a given particle is in the same direction as the magnetization of that dipole.

For an array of 10-nm-diameter spherical particles of iron ($M_s = 1.714 \times 10^6$ A/m (SI), 1714 emu/cm³ (cgs)) separated by 15 nm (centre to centre), the magnetic field due to

* H_x summation is equivalent to evaluating $4 \sum_{i=1}^{\infty} \sum_{j=1}^{\infty} (-1)^{i+1} (2j^2 - i^2) / (j^2 + i^2)^{5/2} - 2 \sum_{i=1}^{\infty} (-1)^{i+1} / i^3 - 4 \sum_{j=1}^{\infty} 1/j^3$.

[†] H_x summation is equivalent to evaluating $4 \sum_{i=1}^{\infty} \sum_{j=1}^{\infty} -(2j^2 - i^2) / (j^2 + i^2)^{5/2} - 2 \sum_{i=1}^{\infty} 1/i^3$.

all of the other particles can be calculated. In the case of a striped array, the magnitude of this field is 107.9 kA/m (equivalent to $B = 0.1356$ T or 1356 G). If all of the particles are aligned in the same direction then the magnetic field at a given particle for an infinite array of particles is slightly smaller: 95.49 kA/m ($B = 0.1200$ T or 1200 G). In both cases, the magnetic field is oriented in the same direction as the magnetization vector of the particle where the field is found. For the striped configuration, the field generated by all four nearest neighbours is in the same direction as the magnetization vector of a given particle, whereas for the uniform array the dipolar fields from the two neighbours that are aligned end to end with the central particle generate a local field aligned with the magnetization but the fields generated by the other nearest neighbours are opposite in sign (but smaller in magnitude). If the array is limited to 20 particles in either direction then these fields reduce to 107.8 kA/m and 92.63 kA/m, respectively. If the spherical particles are replaced with 10 nm cubes, the fields increase to 205.9 kA/m (0.2588 T) and 176.9 kA/m (0.2223 T), respectively, due to the increase in volume.

2.2 Ferromagnetic resonance

Basic background on ferromagnetic resonance can be found in Kittel [71,72] and a more thorough treatment is developed in Lax and Button [73]. The total magnetic moment vector of an atom will precess about the direction of an applied field in a manner analogous to the precession of a spinning top about the direction of gravitational pull. The approach taken here to derive the resonance frequency is purely classical but a full quantum mechanical treatment has been shown to yield the same results [74].

In a traditional ferromagnetic resonance experiment, a magnetic specimen is subjected to an external static bias magnetic field. A sinusoidal oscillating field is then applied in a direction transverse to the bias field. When the frequency of the oscillating field matches the resonance frequency of the specimen, strong absorption of the energy of the oscillating field will be observed. Alternatively, the frequency can be held constant and absorption monitored as a function of bias field. With TR-SKEM measurements, a fast transient current pulse is used to excite the sample and the temporal response is recorded. As long as the bandwidth of the pulse is sufficiently high, the resonance frequency will

be excited and will appear as strong oscillations in the temporal response. The frequency can be measured from the period of the oscillations or obtained using Fourier methods.

2.2.1 Basic FMR theory

The resonance frequency ω_o can be obtained starting with the expression for torque on a classical magnetic moment,

$$\frac{d\vec{M}}{dt} = \gamma(\vec{M} \times \mu_o \vec{H}_{eff}), \quad (2.7)$$

where γ is the gyromagnetic field, and \vec{H}_{eff} is the effective magnetic field. The latter contains contributions due to anisotropy, external magnetic fields, and demagnetization fields. An external static bias field applied in the z direction, $H_{ext}\hat{k}$ and an rf field is applied with time dependence $\exp(i\omega t)$. The external field is assumed to be large enough to fully magnetize the specimen. For a ferromagnetic specimen, the demagnetization field – that is, the field generated by the magnetic moment of the specimen itself – cannot be neglected. The demagnetization contribution is always in the opposite direction from the magnetization of the specimen and can be expressed in terms of demagnetization factors $H_d = -N_i M_i$, for example. The exchange field of a ferromagnet does not play a role in the uniform mode of resonance (“ $k = 0$ spin wave”) as it is always parallel to the magnetization and thus does not exert any torque. It is important for higher order spin waves, which will not be covered here.

The components of the time-dependent magnetic field are:

$$H_x = h_x^{rf} - N_x M_x \quad (2.8)$$

$$H_y = h_y^{rf} - N_y M_y \quad (2.9)$$

$$H_z = h_z^{rf} - N_z M_z \quad (2.10)$$

where \vec{h}^{rf} is the rf applied field. The components of equation (2.7) can be expressed as

$$\frac{dM_x}{dt} = \gamma\mu_o(M_y H_z - M_z H_y) = \gamma\mu_o(H_o + (N_y - N_z)M_s)M_y, \quad (2.11)$$

$$\frac{dM_y}{dt} = \gamma\mu_o(M_z H_x - M_x H_z) = -\gamma\mu_o(H_o + (N_x - N_z)M_s)M_x. \quad (2.12)$$

The magnetization vector is assumed to lie along the direction of the applied field $M_z = M_s$, an assumption that is reasonable for high applied fields, and not to change with time

Shape	N_x	N_y	N_z
sphere	1/3	1/3	1/3
plane	0	1	0
cylinder	1/2	1/2	0

Table 2.1: Demagnetization factors for a sphere, an infinite sheet in the $x - z$ plane, and a cylinder aligned along the z axis (in SI units – multiply by 4π to obtain factors in cgs units).

$dM_z/dt = 0$. The other magnetization components are proportional to $\exp(i\omega t)$ as is the time-varied rf magnetic field. If there is no crystalline anisotropy, $H_o = H_{ext}$.

The resonance frequency can be found by solving

$$\begin{vmatrix} i\omega & \gamma\mu_o(H_o + (N_y - N_z)M_s) \\ \gamma\mu_o(H_o + (N_x - N_z)M_s) & i\omega \end{vmatrix} = 0. \quad (2.13)$$

The solution is known as the Kittel formula

$$\omega_o^2 = (\gamma\mu_o)^2 (H_o + (N_y - N_z)M_s)(H_o + (N_x - N_z)M_s) \quad (2.14)$$

where $\omega_o = 2\pi f_o$ is the resonance angular frequency, γ is related to the spectroscopic splitting factor g through the relation $\gamma = -g\mu_B\mu_o/\hbar$. For iron, g is close to 2, which yields a value for gamma of 1.76×10^{11} Hz·T⁻¹ (1.76×10^7 Hz/Oe in cgs). The demagnetization coefficients for several specimen shapes are summarized in Table 2.1 [72]. For a sphere, this expression reduces to the Larmor equation $\omega_o = \gamma\mu_o H_o$.

Additional effective demagnetization factors can be included to incorporate the effects of crystalline or induced anisotropy, however, it is only very recently that a general method for deriving effective demagnetization factors has been published [75]. For both cubic and uniaxial anisotropy, if the field and magnetization are aligned along the easy axis, the effective field due to the anisotropy is $H_a = 2K/(\mu_o M_s)$ where K is either the uniaxial or first order cubic anisotropy coefficient depending on the situation. In this case, H_a simply adds to the external field $H_o = H_{ext} + H_a$.

2.2.2 Generalized resonance formula

A more general method, originally developed by Smit and Beljers [76], exists for calculating the resonance frequency for highly anisotropic crystals in the presence of an external

bias field at an arbitrary angle. Recently, this method was applied to Fe films grown on GaAs to explore the evolution of a number of anisotropy constants with film thickness. In this study, the theory was used to fit experimentally determined values of the applied field required for resonance at a constant frequency as a function of the angle at which it was applied [77]. Another study employed similar methods to determine the anisotropy constants for a magnetic video recording tape [78]. This method has the advantage of generality but the formulae are not as compact as the Kittel relations.

The method is based on the free energy of the system ε , which can be expressed as

$$\varepsilon = \varepsilon_{ext} + \varepsilon_a \quad (2.15)$$

where $\varepsilon_{ext} = -\mu_o \vec{M} \cdot \vec{H}$ is the Zeeman energy (due to the interaction of the external field \vec{H}_{ext} with the magnetization of the specimen \vec{M}) and ε_a is the crystalline anisotropy energy.

Following the derivation in Ref. [73], a theoretical solution to the resonance problem can be found by minimizing the total magnetic energy of the system with respect to the equilibrium position of the magnetization vector. For the purpose of this derivation, the z direction is initially chosen along the direction of the equilibrium magnetization. If the magnetization is deflected by a small angle from equilibrium ϕ_x in the x direction and similarly by ϕ_y in the y direction, the motion of the magnetization vector can be described by

$$\frac{dM_x}{dt} = \gamma\mu_o \frac{\partial \varepsilon}{\partial \phi_y}, \quad \frac{dM_y}{dt} = -\gamma\mu_o \frac{\partial \varepsilon}{\partial \phi_x}. \quad (2.16)$$

The magnetization is assumed to rest in an equilibrium position so the first derivatives of the energy are zero. Expanding the energy as a Taylor series in small angles about the equilibrium position yields

$$\varepsilon = \varepsilon_o + \frac{1}{2}\varepsilon_{xx}\phi_x^2 + \varepsilon_{xy}\phi_x\phi_y + \frac{1}{2}\varepsilon_{yy}\phi_y^2 + \dots \quad (2.17)$$

where ε_o is the energy at the equilibrium position and $\varepsilon_{ij} = \partial^2\varepsilon/\partial\phi_i\partial\phi_j$ are the second derivatives of the energy evaluated at equilibrium.

The time dependent components of the magnetization can be expressed as

$$m_y = M_s\phi_x e^{i\omega t}, \quad m_x = M_s\phi_y e^{i\omega t}. \quad (2.18)$$

Using these components, equation 2.16 yields

$$-i\omega M_s \phi_y = \gamma\mu_o(\varepsilon_{xx}\phi_x + \varepsilon_{xy}\phi_y), \quad i\omega M_s \phi_x = \gamma\mu_o(\varepsilon_{xy}\phi_x + \varepsilon_{yy}\phi_y) \quad (2.19)$$

The resonance frequency ω_o can be obtained by solving

$$\begin{vmatrix} \gamma\mu_o\varepsilon_{xx} & \gamma\mu_o\varepsilon_{xy} + i\omega M_s \\ \gamma\mu_o\varepsilon_{xy} - i\omega M_s & \gamma\mu_o\varepsilon_{yy} \end{vmatrix} = 0, \quad (2.20)$$

which yields,

$$\omega_o = \frac{\gamma\mu_o}{M_s}(\varepsilon_{xx}\varepsilon_{yy} - \varepsilon_{xy}^2)^{\frac{1}{2}}. \quad (2.21)$$

This equation can be reformulated for the more general case where the magnetization direction does not coincide with the z axis, which can be expressed in spherical coordinates θ and ϕ as

$$\omega_o = \frac{\gamma\mu_o}{M_s \sin \theta}(\varepsilon_{\theta\theta}\varepsilon_{\phi\phi} - \varepsilon_{\theta\phi}^2)^{\frac{1}{2}}. \quad (2.22)$$

The crystalline anisotropy energy ε_a for a cubic crystal can be expressed as

$$\varepsilon_a = K_1(\alpha_1^2\alpha_2^2 + \alpha_2^2\alpha_3^2 + \alpha_3^2\alpha_1^2) \quad (2.23)$$

where α_i are the direction cosines of the magnetization, K_1 is the cubic anisotropy constant (in emu/cm³). If K_1 is positive, as it is for example for iron, then the directions of the easy axes are along the cube faces (x , y , and z axes). The easy axes lie along the diagonals of the cube for $K_1 < 0$. For iron, $K_1 = 4.7 \times 10^4$ J/m³ (4.7×10^5 emu/cm³) [25].

In spherical coordinates, the free energy for a spherical specimen (no demagnetization contribution) with crystalline anisotropy is

$$\varepsilon = -\mu_o M_s H_{ext}(\cos \theta_H \cos \theta + \sin \theta_H \sin \theta \cos(\phi - \phi_H)) + K_1(\sin^2 \theta \cos^2 \theta + \sin^4 \theta \cos^2 \phi \sin^2 \phi) \quad (2.24)$$

where θ_H and ϕ_H describe the direction of the applied magnetic field H_{ext} .

The direction of the magnetization vector at equilibrium is found by setting the first derivatives of the energy with respect to θ and ϕ to zero. These conditions can be expressed as

$$\begin{aligned} \frac{\partial \varepsilon}{\partial \theta} = 0 = & -\mu_o M_s H_{ext}(\cos \theta \sin \theta_H \cos(\phi - \phi_H) - \sin \theta \cos \theta_H) \\ & + \frac{K_1}{2}(8 \sin^3 \theta \cos \theta \cos^2 \phi \sin^2 \phi + \sin(4\theta)), \end{aligned} \quad (2.25)$$

and

$$\frac{\partial \varepsilon}{\partial \phi} = 0 = \mu_o M_s H_{ext} \sin \theta \sin \theta_H \sin(\phi - \phi_H) + \frac{K_1}{2} \sin^4 \theta \sin(4\phi). \quad (2.26)$$

Analytical solutions exist for particular cases where constraints are placed on the direction of the magnetic field but for the general case considered here, the equilibrium position must be found numerically. One way to approach the problem is to find the minima of the function $f(\theta, \phi) = (\partial \varepsilon / \partial \theta)^2 + (\partial \varepsilon / \partial \phi)^2$, which will occur when both of the partial derivatives are zero and the second derivative ε_{xx} and ε_{yy} are positive. The minimization can be carried out using any type of numerical method; in this case the minima were found using a grid-search method. In the case of multiple minima, the lowest energy minimum was kept.

The second derivatives are:

$$\varepsilon_{ext,\theta\theta} = \mu_o M_s H_{ext} (\cos \theta_H \cos \theta + \sin \theta_H \sin \theta \cos(\phi - \phi_H)) \quad (2.27)$$

$$\varepsilon_{ext,\phi\phi} = \mu_o M_s H_{ext} \sin \theta \sin \theta_H \cos(\phi - \phi_H) \quad (2.28)$$

$$\varepsilon_{ext,\theta\phi} = \mu_o M_s H_{ext} \cos \theta \sin \theta_H \sin(\phi - \phi_H), \quad (2.29)$$

and

$$\varepsilon_{a,\theta\theta} = 2K_1 ((6 \sin^2 \theta \cos^2 \theta - 2 \sin^4 \theta) \cos^2 \phi \sin^2 \phi + \cos(4\theta)) \quad (2.30)$$

$$\varepsilon_{a,\phi\phi} = 2K_1 \sin^4 \theta \cos(4\phi) \quad (2.31)$$

$$\varepsilon_{a,\theta\phi} = 2K_1 \sin^3 \theta \cos \theta \sin(4\phi). \quad (2.32)$$

Substituting these expressions into Equation 2.21 yields the resonance frequency.

2.3 Magnetic resonance for an array of nanoclusters

Following the same general methods as [73] and [71] used for a single ferromagnetic body, the expected resonance frequencies for an array of nanoclusters will be derived, first for the zero-field case and then for high bias fields where the specimen can be considered to be uniformly magnetized along the direction of the applied field.

Considering a single nanocluster that is part of a larger array, naively it seems reasonable to assume that Kittel's formula should apply directly. For a single domain spherical

2.3. MAGNETIC RESONANCE FOR AN ARRAY OF NANOCCLUSERS

nanocluster, the resonance would be given by $f = \gamma\mu_o H_{eff}$ where the effective field H_{eff} contains contributions from the external bias magnetic field, the fields generated by the other dipoles, and the anisotropy field. For a sphere with cubic anisotropy with all of the fields oriented along an easy axis, the anisotropy contribution is $H_a = 2K_1/(\mu_o M_s)$.

In Chapter 6, simulations of (cubic rather than spherical) nanoclusters arranged in a regular array with inter-particle distances of 15 nm and clusters of 10 nm will be shown. The frequencies predicted by this formula agree reasonably well with the peak frequency found in response to a transient out-of-plane field at high bias fields (uniform magnetization along direction of applied field). Significant disagreement, however, is observed at low fields when the equilibrium state is predominantly a striped pattern, somewhat like a macroscopic antiferromagnet. Derivation of a new formula for the resonance frequency is of particular interest for this configuration.

2.3.1 Striped magnetization

At low bias fields the equilibrium magnetization state is a striped array, as discussed in Section 2.1. The expression for the magnetic field at a given cluster when the array is in a striped magnetization configuration for a cluster oriented in the $-x$ direction is given by Equation 2.5. A transient field applied in the z direction will cause the magnetization vectors of the positive and negative sublattices to precess about the x axis in opposite directions. In the in-plane orientation, the vectors will be tilted by a small (positive) angle ϕ_1 such that the magnetization vectors directed along the positive and negative x each gain small y components of opposite sign. The magnetization unit vector for a spin oriented in the positive x direction is $\hat{n}_{ij} = (-1)^i(\hat{i} \cos \phi_1 + \hat{j} \sin \phi_1)$. The magnetic field experienced by the cluster at $i = j = 0$ is given by

$$\vec{H} = \frac{M_s V}{4\pi a^3} \left(\hat{i} \cos \phi_1 \sum_{i,j} \frac{(-1)^i (2j^2 - i^2)}{(j^2 + i^2)^{\frac{5}{2}}} + \hat{j} \sin \phi_1 \sum_{i,j} \frac{(-1)^i (2i^2 - j^2)}{(j^2 + i^2)^{\frac{5}{2}}} \right), \quad (2.33)$$

or

$$\vec{H} = \frac{M_s V}{4\pi a^3} (\hat{i} \cos \phi_1 A + \hat{j} \sin \phi_1 B), \quad (2.34)$$

where the sums have been evaluated for all i and j , excluding $i = j = 0$, yielding $A = 5.0989$ (the same value as for Equation 2.5) and $B = -6.0343$. Terms proportional to ij

2.3. MAGNETIC RESONANCE FOR AN ARRAY OF NANOCCLUSERS

have been omitted as they sum to zero. Notice that the y component of the magnetic field is directed in the opposite direction as compared to the y component of the magnetization vector at $i = j = 0$.

When the magnetization vectors rotate such that they are tilted out-of-plane by a small angle ϕ_2 , the magnetization vector is $\hat{m}_{ij} = (-1)^i \cos \phi_2 \hat{i} + \sin \phi_2 \hat{k}$; vectors oriented in both the positive and negative x directions collectively tilt in the positive z direction. The magnetic field becomes

$$\vec{H} = \frac{M_s V}{4\pi a^3} \left(\hat{i} \cos \phi_2 \sum_{i,j} \frac{(-1)^i (2j^2 - i^2)}{(j^2 + i^2)^{\frac{5}{2}}} + \hat{k} \sin \phi_2 \sum_{i,j} \frac{-1}{(j^2 + i^2)^{\frac{3}{2}}} \right), \quad (2.35)$$

or

$$\vec{H} = \frac{M_s V}{4\pi a^3} (\hat{i} \cos \phi_2 A + \hat{k} \sin \phi_2 C), \quad (2.36)$$

The first summation is identical to A for the in-plane case and the second is $C = -9.03362$. Again, the magnetic field in the z direction is oriented in the opposite direction to the z component of the magnetization.

The starting point for the derivation of the resonance frequency is again the expression for free precession (2.7). The magnetization vector \vec{M} and the effective magnetic field \vec{H}_{eff} can be broken down into a sum of constant (\vec{M}_o and \vec{H}_o) and time-dependent parts (\vec{m} and \vec{h}); $\vec{M} = \vec{m} + \vec{M}_o$ and $\vec{H} = \vec{h} + \vec{H}_o$. The equilibrium magnetization vector and the static effective magnetic field are both oriented in the same direction.

Choosing the z -axis along the direction of static magnetization, the time-dependent magnetization can be expressed as $\vec{m} = [M_s \cos(\omega t) \sin \phi_1, -M_s \sin(\omega t) \sin \phi_2, 0]$. The time derivative of the magnetization is then

$$\frac{d\vec{M}}{dt} = \frac{d\vec{m}}{dt} = -M_s \omega (\hat{i} \sin(\omega t) \sin \phi_1 + \hat{j} \cos(\omega t) \sin \phi_2) \quad (2.37)$$

As the magnetization rotates with time, the magnetic field also changes with time. Rotating the solution for an in-plane tilt in the magnetization, the corresponding magnetic field is $\vec{h} = H_c [B \sin \phi_1, 0, A \cos \phi_1]$, where $H_c = M_s V / (4\pi a^3)$. For an out-of-plane tilt of the magnetization the magnetic field is $\vec{h} = H_c [0, C \sin \phi_2, A \cos \phi_2]$. As ϕ_1 and ϕ_2 are both small angles, $\cos \phi \approx 1$, and the z component is essentially constant. The time-dependent

2.3. MAGNETIC RESONANCE FOR AN ARRAY OF NANOCCLUSERS

field can then be expressed as $\vec{h} = H_c[B \cos(\omega t) \sin \phi_1, -C \sin(\omega t) \sin \phi_2, 0]$.[†] In the absence of an external bias field, $\vec{H}_o = [0, 0, H_a + H_c A]$ and $\vec{M}_0 = M_s[0, 0, \cos \phi] \approx [0, 0, M_s]$. Assuming cubic anisotropy with an easy axis aligned along the z axis, the anisotropy field is $H_a = 2K_1/(\mu_o M_s)$, where K_1 is the first order crystalline anisotropy constant.

Breaking \vec{M} and \vec{H}_{eff} down into their constant and time-dependent parts, Equation 2.7 becomes

$$\frac{\partial \vec{m}}{\partial t} = \gamma \mu_o (\vec{M}_o \times \vec{h} + \vec{m} \times \vec{H}_o). \quad (2.38)$$

Note that $\vec{M}_o \times \vec{H}_o = 0$ and has not been included. The cross products are

$$\vec{M}_o \times \vec{h} = -\hat{i} M_s h_y + \hat{j} M_s h_x, \quad (2.39)$$

and

$$\vec{m} \times \vec{H}_o = -\hat{i} M_s \sin(\omega t) \sin \phi_2 (H_a + H_c A) - \hat{j} M_s \cos(\omega t) \sin \phi_1 (H_a + H_c A). \quad (2.40)$$

Assembling the x component yields

$$-\omega M_s \sin(\omega t) \sin \phi_1 = \gamma \mu_o (M_s H_c C \sin(\omega t) \sin \phi_2 - M_s \sin(\omega t) \sin \phi_2 (H_a + H_c A)), \quad (2.41)$$

which can be simplified to obtain

$$\omega = \gamma \mu_o (H_a + H_c (A - C)) \frac{\sin \phi_2}{\sin \phi_1}. \quad (2.42)$$

Similarly, the y component can be expressed as

$$-\omega M_s \cos(\omega t) \sin \phi_2 = \gamma \mu_o (M_s H_c B \cos(\omega t) \sin \phi_1 - M_s \cos(\omega t) \sin \phi_1 (H_a + H_c A)), \quad (2.43)$$

which simplifies to

$$\omega = \gamma \mu_o (H_a + H_c (A - B)) \frac{\sin \phi_1}{\sin \phi_2}. \quad (2.44)$$

The two equations 2.42 and 2.44 can be solved to obtain

$$\frac{\sin \phi_1}{\sin \phi_2} = \sqrt{\frac{(H_a + H_c (A - C))}{(H_a + H_c (A - B))}} \quad (2.45)$$

and

$$\omega_o = \gamma \mu_o ((H_a + H_c (A - C))(H_a + H_c (A - B)))^{\frac{1}{2}}. \quad (2.46)$$

[†]Note that no externally applied time-dependent magnetic field has been included. The analysis assumes that there is an initial out-of-plane pulse that introduces an angle between the direction of magnetization and the direction of the constant field which has sufficient bandwidth to excite the resonance frequency.

2.3. MAGNETIC RESONANCE FOR AN ARRAY OF NANOCCLUSERS

Using the constants for iron and considering a square array of 10 nm diameter spheres, 15 nm apart, a frequency of 10.8 GHz is obtained. If the 10 nm spheres are replaced with 10 nm cubes, a frequency of 19.2 GHz is predicted. Note that these frequencies are slightly more than a factor of 2 higher than those predicted using the Kittel formula for a sphere (5.3 and 8.8 GHz, respectively). The coordinated oscillation of dipoles in a striped array thus results in a significant enhancement of the resonance frequency over that predicted by simply considering the magnitude of the effective magnetic field at equilibrium for a given particle.

When an in-plane bias field is applied, the initial state begins to change from a striped state to a uniform state. It is difficult to predict the resonance frequencies for the transition states because the initial states become more complex. It is expected that the resonance should become less sharp as the effective fields for any remaining oppositely oriented stripes and for the uniformly magnetized areas will not necessarily be the same everywhere. Once the in-plane field is sufficiently large to saturate the sample an analytic expression for the resonance frequency as a function of in-plane bias field can be found, which will be derived in the next section.

2.3.2 Uniform magnetization

For higher in-plane magnetic fields, the magnetization vectors of all of the individual clusters tend to align along the direction of the bias field. Following the same procedure as for the striped initial state, the ferromagnetic resonance formula will be derived using the same method as above.

The expression for the magnetic field at a given particle when the array is uniformly magnetized in the $-x$ direction is given in Equation 2.6. Now consider the same array except with magnetization vectors for each of the particles oriented in the $+x$ direction but tilted slightly in the y direction by a small, positive angle ϕ_1 . The magnetization vector for a given cluster is described by $\hat{m}_{ij} = \cos \phi_1 \hat{i} + \sin \phi_1 \hat{j}$. The magnetic field experienced by a cluster at $i = j = 0$ is

$$\vec{H} = \frac{M_s V}{4\pi a^3} (\hat{i} \cos \phi_1 + \hat{j} \sin \phi_1) \sum_{i,j} \frac{(2j^2 - i^2)}{(j^2 + i^2)^{\frac{5}{2}}}, \quad (2.47)$$

where the summation is for all i and j , excluding $i = j = 0$. The summation $A_U =$

2.3. MAGNETIC RESONANCE FOR AN ARRAY OF NANOCCLUSERS

$\sum_{i,j}(2j^2 - i^2)/(j^2 + i^2)^{\frac{5}{2}} = 4.51681$ is the same as the x summation in Equation 2.6. Unlike the striped case, the y component of the magnetic field is in the same direction as the magnetization vector \hat{m}_{00} .

When the magnetization vectors rotate such that the net magnetization is tilted out of plane by an angle ϕ_2 , the magnetization vector is $\hat{m}_{ij} = \cos \phi_2 \hat{i} + \sin \phi_2 \hat{k}$ and the magnetic field becomes

$$\vec{H} = \frac{M_s V}{4\pi a^3} \left(\hat{i} \cos \phi_2 \sum_{i,j} \frac{(2j^2 - i^2)}{(j^2 + i^2)^{\frac{5}{2}}} + \hat{k} \sin \phi_2 \sum_{i,j} \frac{-1}{(j^2 + i^2)^{\frac{3}{2}}} \right). \quad (2.48)$$

The first summation is equal to A_U and the second is the same as the constant $C = -9.03362$ from the striped array case. The z component of the magnetic field is in the opposite direction as compared to that of \hat{m}_{00} .

The derivation of the resonance frequency is similar to that of the striped case. The vectors \vec{M}_o , \vec{m} , and $d\vec{m}/dt$ are the same. The magnetic fields are different, however, with a constant field of $\vec{H}_o = [0, 0, H_a + H_{ext} + H_c A_U]$, where H_{ext} is the magnitude of the externally applied bias magnetic field, and a time-dependent field of

$$\vec{h} = H_c [A_U \cos(\omega t) \sin \phi_1, -C \sin(\omega t) \sin \phi_2, 0]. \quad (2.49)$$

The cross products are

$$\vec{M}_o \times \vec{h} = \hat{i} M_s H_c C \sin(\omega t) \sin \phi_2 + \hat{j} M_s H_c A_U \cos(\omega t) \sin \phi_1 \quad (2.50)$$

and

$$\vec{m} \times \vec{H}_o = -\hat{i} M_s \sin(\omega t) \sin \phi_2 (H_a + H_{ext} + H_c A_U) - \hat{j} M_s \cos(\omega t) \sin \phi_1 (H_a + H_{ext} + H_c A_U), \quad (2.51)$$

which can be used to solve for

$$\frac{\sin \phi_1}{\sin \phi_2} = \sqrt{\frac{(H_a + H_{ext})}{(H_a + H_{ext} + H_c(A_U - C))}} \quad (2.52)$$

and

$$\omega_o = \gamma \mu_o ((H_a + H_{ext}) (H_a + H_{ext} + H_c(A_U - C)))^{\frac{1}{2}} \quad (2.53)$$

This expression yields slightly smaller values for the frequency than those predicted by the Kittel equation for a sphere $\omega_o = \gamma \mu_o (H_a + H_{ext} + H_c A_U)$ at low fields and higher values

2.3. MAGNETIC RESONANCE FOR AN ARRAY OF NANOCCLUSERS

at greater fields. The results converge for very large external fields ($H_{ext} \gg H_c A_U$). The oscillations of a uniformly magnetized array is coordinated as it also was for the striped array, however, in this case the coordination of the array has a much smaller effect on the resonance frequency.

2.3.3 From striped to uniform

Thus far expressions have been derived for the ferromagnetic resonance frequencies of a regular array of magnetic dipoles for two special cases: in the limit of zero bias field, and in the limit of high bias field. Now the expected resonance behaviour in the transitional region will be examined. For zero bias field the initial state was assumed to consist alternating rows of dipoles aligned in either the positive or negative x directions to minimize the dipolar energy. At high fields the array was assumed to be uniformly magnetized in the positive x direction, which was also the direction of the externally applied magnetic field, to minimize the Zeeman energy. At intermediate fields both the Zeeman and dipolar contributions to the energy are important. It is expected that progressively more of the individual dipoles will re-orient along the direction of the bias field as it is increased but that the stripe patterns, that is, uniform magnetization along individual rows with the occasional row of opposite orientation, will persist until the bias field is sufficiently high that the Zeeman energy term dominates.

In the intermediate state, any number of striped patterns are possible. To illustrate the general implications of the widening of the stripes in the positive x direction, a repeating array with a unit pattern of N rows will be considered where the magnetization of rows $n = 1$ to $n = N - 1$ are oriented along the positive x direction and the magnetization of the N^{th} row is oriented anti-parallel to the others. For $N = 1$ the array is in the zero-field striped pattern, while in the limit of $N \rightarrow \infty$, the array approaches uniform magnetization. The energy due to the external field and the demagnetization energy from inter-particle interactions is

$$\epsilon_N = -\frac{1}{N} \sum_{n=1}^N \mu_o M_s \hat{m}_n \cdot \vec{H}_{ext} - \frac{1}{2N} \sum_{n=1}^N \mu_o M_s \hat{m}_n \cdot |H_{dem}|. \quad (2.54)$$

This expression can be simplified using the fact that all of the stripes but one will be aligned along the direction of the external field for a unit of the pattern, and also consid-

2.3. MAGNETIC RESONANCE FOR AN ARRAY OF NANOCCLUSERS

ering that the demagnetization field is always in the same direction as the magnetization vector. This yields

$$\varepsilon_N = -\frac{N-2}{N}\mu_o M_s H_{ext} - \frac{\mu_o M_s H_c}{2N} \sum_{n=1}^N A_{N,n}. \quad (2.55)$$

The summation $A_{N,n}$ is given by

$$A_{N,n} = \sum_{i,j} (2 \operatorname{sgn}|\operatorname{rem}(i+n, N)| - 1) \frac{(2j^2 - i^2)}{(j^2 + i^2)^{\frac{5}{2}}}, \quad (2.56)$$

where $\operatorname{sgn}(x)$ is the signum function (1 for $x > 0$, -1 for $x < 0$, and 0 for $x = 0$), and $\operatorname{rem}(i+n, N)$ is the remainder of $(i+n)$ divided by N . For the single striped case ($N = 2$), the energy is

$$\varepsilon_2 = -\frac{1}{2}\mu_o M_s H_c A, \quad (2.57)$$

and for a uniformly magnetized array, the energy is

$$\varepsilon_\infty = -\mu_o M_s H_{ext} - \frac{1}{2}\mu_o M_s H_c A U. \quad (2.58)$$

The energy as a function of H_{ext} is shown for a regular array of 10 nm cubes with interparticle separation of $a = 15$ nm in Figure 2.4a. This figure shows that the lowest energy state goes through the transition from striped to uniform at a field of around 12 kA/m.

The resonance formulae developed in the previous sections can be generalized into the following form:

$$\omega_o = \gamma\mu_o ((H_a + H_{ext} + H_c(A_{N,n} - B_{N,n})) (H_a + H_{ext} + H_c(A_{N,n} - C)))^{\frac{1}{2}} \quad (2.59)$$

keeping in mind that H_{ext} is positive except for the case when $n = N$. The summation C is unchanged but the summation $B_{N,n}$ is

$$B_{N,n} = \sum_{i,j} (2 \operatorname{sgn}|\operatorname{rem}(i+n, N)| - 1) \frac{(2i^2 - j^2)}{(j^2 + i^2)^{\frac{5}{2}}}. \quad (2.60)$$

With the exception of the two limiting cases already considered, this formula yields multiple resonance frequencies for the dipoles at different locations n , which actually violates the assumption of oscillation at a coherent frequency used in deriving it. One possible result is that the array may oscillate at the average of these frequencies, another is that

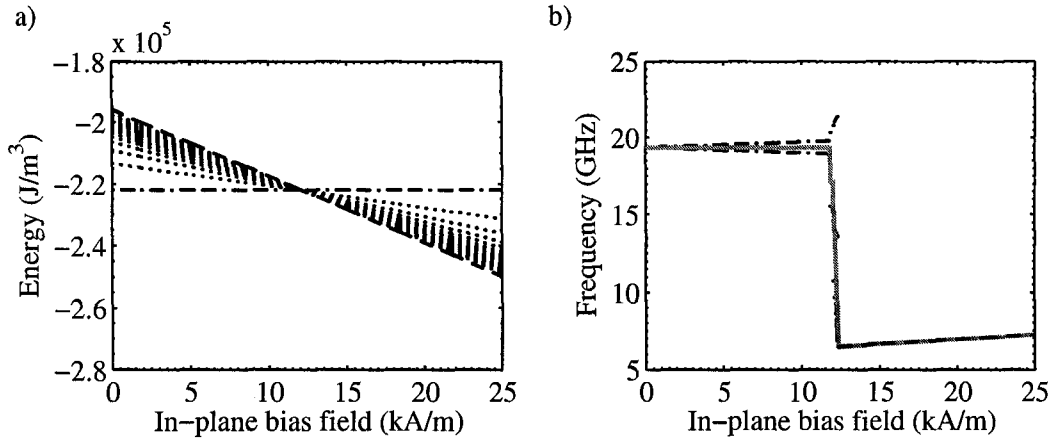


Figure 2.4: a) Energy as a function of in-plane bias field for a regular array of magnetic dipoles (10 nm cubes, $a = 15$ nm). The dash-dot line represents the striped state, the dashed the uniform state, and the dotted lines show the intermediate states with successively higher N . b) Predicted frequency as a function of in-plane bias field for the lowest energy arrangement. At intermediate frequencies, the lowest values correspond to uniformly magnetized areas of thicker stripes, which have higher degeneracy as compared to higher resonance frequencies. The solid gray line shows the average frequency for each bias field.

this expression gives a range of possible oscillation frequencies. The individual and average frequencies found using this expression are shown as a function of bias field in Figure 2.4b. There is a sharp change in resonance frequency at around 12 kA/m (150 Oe) for this example and the average frequency approaches the solution for the uniform array at higher fields.

2.3.4 Kittel demagnetization coefficients

Comparing equations (2.46) and (2.53) to Kittel's general formula (2.14), the demagnetization coefficients for a two-dimensional array of particles in both the low-field and high-field can be extracted by inspection. These coefficients are not for a continuous body so the condition $N_x + N_y + N_z = 1$ (4π in cgs) does not apply, and the coefficients are also not required to be positive. They are summarized in Table 2.2 and can be compared to the well-known values in Table 2.1. Recalling that B and C are negative, it is interesting to note that some of the demagnetization coefficients are actually negative in magnitude.

2.4. FMR OF NANOCUSTER ARRAY, OUT-OF-PLANE BIAS FIELD

Configuration	N_x	N_y	N_z
striped	$-H_c B/M_s$	$-H_c C/M_s$	$-H_c A/M_s$
uniform	$-H_c A_U/M_s$	$-H_c C/M_s$	$-H_c A_U/M_s$

Table 2.2: Demagnetization factors for a two-dimensional array of magnetic dipole for a striped configurations (stripes parallel to z axis) and for uniform alignment along the z axis. The y -axis is perpendicular to the plane.

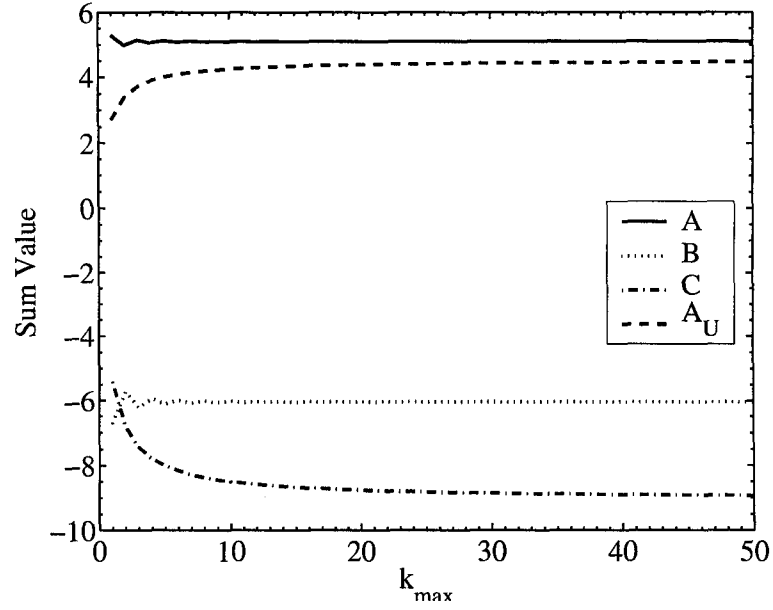


Figure 2.5: Values of the summations as a function of array size k_{max} .

For both arrays, N_z is negative and for the uniform array, N_x is also negative.

The values for the various constants as a function of array size k_{max} are shown in Figure 2.5. The summations for uniform magnetization states (C and A_U) are slower to converge than the summations involving stripes of alternating magnetization.

2.4 FMR of nanocluster array, out-of-plane bias field

Ferromagnetic resonance theory for an array of nanoclusters in the presence of an out-of-plane bias field can be divided into two categories: high field theory and low-field theory,

which describe the resonance of the clusters above and below saturation, respectively. At low fields an out-of-plane transient field can still be used to excite the array, however, at high out-of-plane fields (above saturation) an in-plane excitation will be required. In general, as long as there is a component of the transient field that is perpendicular to the direction of magnetization and the transient excitation is small the array will resonate at the same frequency (the direction will, however, affect the initial phase of the excitation).

2.4.1 High out-of-plane bias fields

For high out-of-plane bias fields, the magnetization vectors of all of the cubes will be in the $+z$ -direction and the effective field will also be in the $+z$ -direction. In this case, the anisotropy field reduces to $2K_1/(\mu_o M_s)$ and the resonance frequency, if the contribution from the array of cubes only contributes by reducing the applied field, should be described by the following expression:

$$f_o = \frac{\gamma\mu_o}{2\pi} \left(H_{ext} + H_{dem} + \frac{2K_1}{\mu_o M_s} \right). \quad (2.61)$$

In Section 2.3.1, the expression for the magnetic field (Equation 2.36) experienced by a spherical nanocluster oriented in the $+x$ direction in a striped array tilted by a small angle ϕ_2 out-of-plane was found to be

$$\vec{H} = \frac{M_s V}{4\pi a^3} (\hat{i} \cos \phi_2 A + \hat{k} \sin \phi_2 C), \quad (2.62)$$

The values of the constants are $A = 5.0989$ and $C = -9.03362$. For $\phi_2 = 90^\circ$ (particles tilted fully out-of-plane) this expression reduces to $H = M_s V C / (4\pi a^3) = H_c C$, directed in the negative out-of-plane direction. Substituting this expression into equation 2.61 yields

$$f_o = \frac{\gamma\mu_o}{2\pi} \left(H_{ext} + H_c C + \frac{2K_1}{\mu_o M_s} \right). \quad (2.63)$$

This expression is developed under the assumption that the array only contributes to determining the resonance frequency through the static field it generates, which neglects the effects of the resonance of the particles on each other (“small angle approximation”).

In the presence of a large out-of-plane bias field, the initial magnetization of all of the particles is in the out-of-plane direction and all of the particles resonate coherently.

2.4. FMR OF NANOCUSTER ARRAY, OUT-OF-PLANE BIAS FIELD

Following the same arguments as in Section 2.3.2, the resonance formula is found to be

$$f = \frac{\gamma\mu_o}{2\pi} \left(H_{ext} + H_c(C - A_U) + \frac{2K_1}{\mu_o M_s} \right). \quad (2.64)$$

The maximum in-plane angles in both directions are the same, indicating that the resonance path is circular. The constant C is negative and A_U is positive, resulting in a smaller frequency as compared to that predicted using Equation 2.63.

2.4.2 Low out-of-plane bias fields

For smaller out-of-plane bias fields, the striped initial state is an important consideration but the out-of-plane tilt angle is also significant. To determine the resonance frequency properly, the generalized method described in Section 2.2.2 should be used with the addition of the expression for the demagnetization energy for a single nanocrystal in the striped array. To simplify the calculations, the stripes will be considered to be oriented along the y -axis and all calculations will be done for a static bias field directed in the $+x$ -direction ($\theta_H = 90^\circ$, $\phi_H = 0^\circ$). This ensures that the equilibrium orientation will be confined to the $x - y$ plane, which is desirable because the method of Smit and Beljers [76] becomes less stable when the magnetization is oriented along the z -axis. The resonance formula will be derived for a cube with its magnetization predominantly in the $+y$ -direction but the results are applicable to all cubes in the array.

First an expression for the demagnetization energy of the array ε_{dem} (neglecting the demagnetization energy of a particle on itself) must be found. In Section 2.3.1 the magnetic field was found at a given particle oriented in the $+x$ direction (stripes along x -axis, out-of-plane direction along z -axis) due to all of the other particles in the array for both small perturbations in y and z . Combining these two expressions, the magnetic field for a particle (i, j) in a regular array that has been perturbed in both z and y such that $\hat{m}_{ij} = (-1)^i(\alpha_1\hat{i} + \alpha_2\hat{j}) + \alpha_3\hat{k}$ can be expressed as

$$\vec{H}_{ij} = H_c((-1)^i(\hat{i}\alpha_1A + \hat{j}\alpha_2B) + \hat{k}\alpha_3C) \quad (2.65)$$

where α_i are the direction cosines of the magnetization. The demagnetization energy can be written as

$$\varepsilon_{dem} = -\frac{1}{2} \frac{\mu_o M_s}{N^2} \sum_{i=1}^N \sum_{j=1}^N \hat{m}_{ij} \cdot \vec{H}_{ij} \quad (2.66)$$

2.4. FMR OF NANOCUSTER ARRAY, OUT-OF-PLANE BIAS FIELD

$$= -\frac{1}{2}\mu_o M_s H_c (A\alpha_1^2 + B\alpha_2^2 + C\alpha_3^2) \quad (2.67)$$

where the factor of 1/2 has been included to account for double counting. Since A is positive and B and C are negative, the minimum energy occurs for $\alpha_2 = \alpha_3 = 0$, as expected. This solution can be rotated such that the out-of-plane direction lies along the x -axis and the stripes are oriented along the y -axis. The demagnetization energy, expressed in spherical coordinates, becomes

$$\varepsilon_{dem} = -\frac{1}{2}\mu_o M_s H_c (A \sin^2 \theta \sin^2 \phi + B \cos^2 \theta + C \sin^2 \theta \cos^2 \phi) \quad (2.68)$$

The free energy for a striped array in the presence of an out-of-plane bias field is

$$\begin{aligned} \varepsilon = & -\mu_o M_s H_{ext} \sin \theta \cos \phi - \frac{1}{2}\mu_o M_s H_c (A \sin^2 \theta \sin^2 \phi + B \cos^2 \theta \\ & + C \sin^2 \theta \cos^2 \phi) + K_1 (\sin^2 \theta \cos^2 \theta + \sin^4 \theta \cos^2 \phi \sin^2 \phi) \end{aligned} \quad (2.69)$$

The direction of the magnetization vector at equilibrium is found by setting the first derivatives of the energy with respect to θ and ϕ to zero. These conditions can be expressed as

$$\begin{aligned} \frac{\partial \varepsilon}{\partial \theta} = 0 = & -\mu_o M_s H_{ext} \cos \theta \cos \phi - \frac{1}{2}\mu_o M_s H_c (A \sin^2 \phi - B + C \cos^2 \phi) \sin 2\theta \\ & + \frac{K_1}{2} (8 \sin^3 \theta \cos \theta \cos^2 \phi \sin^2 \phi + \sin(4\theta)), \end{aligned} \quad (2.70)$$

and

$$\begin{aligned} \frac{\partial \varepsilon}{\partial \phi} = 0 = & \mu_o M_s H_{ext} \sin \theta \sin \phi + \frac{1}{2}\mu_o M_s H_c (C - A) \sin^2 \theta \sin 2\phi \\ & + \frac{K_1}{2} \sin^4 \theta \sin(4\phi). \end{aligned} \quad (2.71)$$

The second derivatives for the external field energy ε_{ext} are

$$\varepsilon_{ext,\theta\theta} = \mu_o M_s H_{ext} \sin \theta \cos \phi \quad (2.72)$$

$$\varepsilon_{ext,\phi\phi} = \mu_o M_s H_{ext} \sin \theta \cos \phi \quad (2.73)$$

$$\varepsilon_{ext,\theta\phi} = \mu_o M_s H_{ext} \cos \theta \sin \phi, \quad (2.74)$$

and those for the demagnetization energy from the array ε_{dem} are

$$\varepsilon_{dem,\theta\theta} = -\mu_o M_s H_c (A \sin^2 \phi - B + C \cos^2 \phi) \cos 2\theta \quad (2.75)$$

$$\varepsilon_{dem,\phi\phi} = \mu_o M_s H_c (C - A) \sin^2 \theta \cos 2\phi \quad (2.76)$$

$$\varepsilon_{dem,\theta\phi} = \frac{1}{2}\mu_o M_s H_c (C - A) \sin 2\theta \sin 2\phi. \quad (2.77)$$

The second derivatives for the anisotropy contribution of the energy are the same as those in Equation 2.32. In the limit of zero bias field, this method agrees with the analytic solution (Equation 2.46). At the high-field solution there is a sharp discontinuity at the saturation point, above which the high-field theory must be used because the assumption of striped resonance no longer holds. At the saturation point, the two theories agree.

A summary of the ferromagnetic resonance predictions and related variables and constants can be found in Appendix A. In Chapter 6 these theories will be compared to simulation results.

2.5 Micromagnetics simulations

The starting point for most micromagnetic simulations is the Landau-Lifshitz Gilbert equation

$$\frac{d\vec{M}}{dt} = -\gamma\mu_0\vec{M} \times \vec{H}_{eff} + \frac{\alpha}{M_s}(\vec{M} \times \frac{d\vec{M}}{dt}), \quad (2.78)$$

which provides a semi-classical description of the time-evolution of a magnetic system [79]. The gyromagnetic ratio γ is equal to $g|e|/(\mu_0 2m_e c)$ where the spectroscopic splitting factor g is 2 for a free electron, e is the charge of an electron, m_e is the mass of an electron, and c is the speed of light, which yields a value of $\gamma = 1.76 \times 10^{11} \text{ Hz}\cdot\text{T}^{-1}$ ($1.76 \times 10^7 \text{ Hz}\cdot\text{Oe}^{-1}$ in cgs units). This value is often used for the 3d transition metals, which have g factors close to 2 (g varies for 4f ferromagnets) [71]. The dimensionless damping parameter α is around 0.008 for permalloy [21], and 0.0023 for iron [4] and the saturation magnetization M_s is $1.714 \times 10^6 \text{ A/m}$ (1714 emu/cm^3) for bulk iron [25]. The vector \vec{M} is the magnetization, t is time, and \vec{H}_{eff} is the effective magnetic field, which contains contributions from the external field, the demagnetization field, effective anisotropy fields, and exchange fields. A software package, the “LLG Micromagnetics Simulator” [25], was used to carry out numerical simulations on simplified models of the nanocomposite specimens.

Micromagnetics simulations are often used to model the temporal response of a magnetic specimen to a transient stimulus. They are also used to simulate equilibrium magnetization states by using a larger damping parameter ($\alpha \leq 1$) and allowing the system to relax under static conditions. Hysteresis curves can be simulated by allowing the model

to relax under successively applied magnetic fields, although this is by no means the only method that has been used to model hysteresis behaviour. Monte Carlo simulations, for example, have been used to simulate hysteresis for interacting Fe nanoparticle arrays [27,8]. It is, however, more straightforward to simulate temporal dynamics using LLG simulations as compared to Monte Carlo methods.

A brief description of the contributions to the effective field will be provided below. These contributions will be discussed in terms of their energies. In micromagnetics simulations, the effective field \vec{H}_{eff} is typically found by exploiting the fact that it can be determined by calculating the energy variational with magnetization

$$\vec{H}_{eff} = \frac{\delta \varepsilon}{\delta \vec{M}}. \quad (2.79)$$

More complete discussions of the details of the numerical methods involved in micromagnetics simulations can be found in Refs. [80],[79] and [81].

2.5.1 Exchange energy

Exchange energy is quantum mechanical in origin and is directly responsible for the existence of magnetism, in general. The exchange energy is described by the Heisenberg Hamiltonian

$$\varepsilon_{ex} = - \sum J_{ij} \vec{S}_i \cdot \vec{S}_j \quad (2.80)$$

where J is known as the exchange integral, and \vec{S} are vector spin operators. For a ferromagnetic material, J is positive, while a negative J results in an antiferromagnetic ground state. Exchange interactions are short range thus are often evaluated only between nearest neighbour cells.

In micromagnetics simulations, this quantum mechanical effect is incorporated into the classical framework of the simulations by representing discrete exchange as a continuous effect. The exchange energy density is approximated as

$$\varepsilon_{ex} = A_{ex}(\nabla m_x^2 + \nabla m_y^2 + \nabla m_z^2) \quad (2.81)$$

where A_{ex} is an exchange constant equal to JS^2k_n/a , k_n is the number of nearest neighbours in the crystal structure, and a is the size of the unit cell. This energy is summed over all of the magnetic cells in the simulation.

For single domain nanoparticles, exchange interactions are responsible for keeping all of the magnetization vectors oriented in the same direction within a given nanoparticle. In the collections of nanoparticles discussed here, exchange interactions are important within a given particle, however, the individual particles will be modeled as physically separated entities and thus are exchange-decoupled.

2.5.2 Anisotropy energy

This energy term describes the tendency for the magnetization to align along certain directions in a perfect crystal. As mentioned earlier in this chapter, the crystalline anisotropy energy ε_a for a cubic crystal can be expressed as

$$\varepsilon_a = K_1(\alpha_1^2\alpha_2^2 + \alpha_2^2\alpha_3^2 + \alpha_3^2\alpha_1^2) \quad (2.82)$$

where α_i are the direction cosines of the magnetization, K_1 is the cubic anisotropy constant. If K_1 is positive, as it is for iron, then the directions of the easy axes are along the cube faces (x , y , and z axes). The easy axes lie along the diagonals of the cube for $K_1 < 0$. For uniaxial anisotropy, the energy expression reduces to

$$\varepsilon_a = K_u \sin^2 \theta \quad (2.83)$$

where θ is the angle between the anisotropy axis and the magnetization.

2.5.3 Zeeman energy

The Zeeman energy describes the interaction of the magnetization with an external magnetic field. This term will be smallest when the magnetization vectors are aligned along the direction of the external field.

$$\varepsilon_{ext} = -\mu_o \vec{H}_{ext} \cdot \vec{M}. \quad (2.84)$$

In a micromagnetics simulation, the interaction energy of the magnetization of each cell with the external field must be included.

2.5.4 Demagnetization energy

An individual spin in a magnetic specimen can be thought of as a point dipole, which not only reacts to any field external to itself but also generates a magnetic field of its own (Equation 2.1). The energy U_{ij} between a given dipole i and another dipole j is given by Equation 2.3. Summing the contributions from a number of dipoles in a collection results in an energy of the form

$$\varepsilon_{dem} = -\frac{1}{2} \sum_j U_{ij} \quad (2.85)$$

for a given spin i . In a uniformly magnetized specimen, the magnetic fields generated by the other spins will result in each spin experiencing a net magnetic field opposite to its own direction. The dipolar interactions between adjacent spins are typically a thousand times smaller than exchange interactions between nearest neighbours [82]. Dipolar interactions, however, are much longer range (fall off as the inverse cube of separation) than exchange interactions (fall off exponentially as a function of separation). For a large enough specimen, magnetic domains will form to minimize this energy, which is the reason it is often referred to as the “demagnetization” energy.

This is a long-range contribution and is the most computationally expensive part of micromagnetics simulations because the energy at a given point in a specimen depends on the magnetization everywhere else in the specimen. As a result, most micromagnetics simulations use a volume averaging method [83] to compute a demagnetization tensor and use Fourier methods on a regular grid to increase the computation speed.

2.5.5 Other energy terms

The energy terms discussed in the preceding sections are the contributions that are most commonly included in simulations. Other terms can, however, be added as necessary. For example, the effects of temperature are often represented using a stochastic thermal magnetic field term, the standard deviation of which scales as a function of temperature. Other possible contributions to the energy of the system include surface anisotropy and magnetostriction effects. Surface anisotropy arises from the fact that spins near the surface have neighbouring spins on one side but not the other, which leads to exchange that is not equivalent to the bulk [84,85]. The properties of the material adjacent to the surface

2.5. MICROMAGNETICS SIMULATIONS

can further modify the environment of the surface spins. For nanostructures these effects may be important as the surface to volume ratio is high. There are still open questions, however, as to how to treat this contribution [24]. Magnetostriction refers to the connection between elastic and magnetic properties. Magnetization of a ferromagnet causes the it to shrink (or expand) in the direction of the magnetization. Similarly, pressure can have an influence on magnetization. This term is complicated and is generally neglected [24]. For the simulations presented here, contributions from exchange, crystalline anisotropy, demagnetization, Zeeman interactions, and thermal fluctuations were included.

Chapter 3

Experimental Setup

3.1 Sample preparation

Iron nanocomposite samples were prepared using ion implantation, a versatile technique for fabricating nanocomposite materials [12]. Samples were prepared by implanting an optical quality fused quartz wafer (Esco Products type A1) with Fe^+ ions. The energies and fluences used are presented in Table 3.1. The specimens were clipped into a supporting plate and were not heat sunk. The beam current was maintained at less than $25 \mu\text{A}$ in order to minimize local heating effects. Implantations were carried out at Oak Ridge National Laboratory. These samples were then annealed at temperatures ranging from 600°C to 1000°C in a reducing atmosphere (Argon with 10% hydrogen at an overpressure of 2 to 4 psi) for 1 hour.

The microstructure of the samples was characterized using a JEOL 2010 transmission electron microscope with a LaB_6 gun. Bright field imaging as well as energy dispersive x-ray spectroscopy (EDXS) and electron diffraction techniques were used. The optical reflectivity, transmission and absorbance were measured using a fiber optic spectrometer for wavelengths ranging from UV to the near infrared (Ocean Optics USB2000 Miniature Fiber Optic Spectrometers: one is optimized for UV-VIS $\lambda = 200 - 800 \text{ nm}$, the other is optimized for VIS-NIR $\lambda = 530 - 1100 \text{ nm}$, the LS-1 Tungsten Halogen Light Source

3.2. PATTERNING OF NANOCOMPOSITES

Element	Energy (keV)	Fluence (ions/cm ²)	Notes
Fe	80	1.5×10^{17}	High dose
Fe	80	5.0×10^{16}	Low dose, used in testing masks
Fe	150	1.5×10^{17}	High dose, higher energy

Table 3.1: Ion implantation parameters for SiO₂ substrates.

$\lambda = 360 \text{ nm}$ - $2 \mu\text{m}$ and the DT-MINI Deuterium Tungsten Halogen Light Source ($\lambda = 200$ - 1100 nm).

3.2 Patterning of nanocomposites

The goal of creating patterned arrays of nanoparticles was realized by using ion implantation combined with lithographic masking. These patterned samples allow for convenient differentiation between signals arising from the matrix and the nanocrystals when using scanning microscopy techniques. Patterned samples have proven useful for TR-SKEM applications [56] as well as for creating micro-pixelated luminescent arrays of silicon nanoparticles [86].

The procedure used for creating patterned nanocomposites is outlined in Figure 3.1. A metallic thin film is grown on top of the substrate, which is then patterned using standard lithographic methods (spin photoresist, expose pattern, develop photoresist, etch metal, remove photoresist). During ion implantation, the mask shadows the substrate. The procedure is completed by removing the mask. Any further processing required to create the nanoparticles can be carried out on the patterned specimen.

A good masking material should adhere well to the substrate, have a high stopping power and a low sputtering yield, and should be easily etched through a process that will not affect the host material or implanted layer. It must also withstand high-dose ion implantation without significant physical degradation. Materials with higher sputtering yield or lower stopping power are less desirable as thicker masking films would be required. It becomes more difficult to lithographically define small structures as the film thickness is increased. A low sputtering yield is also desirable to minimize contamination.

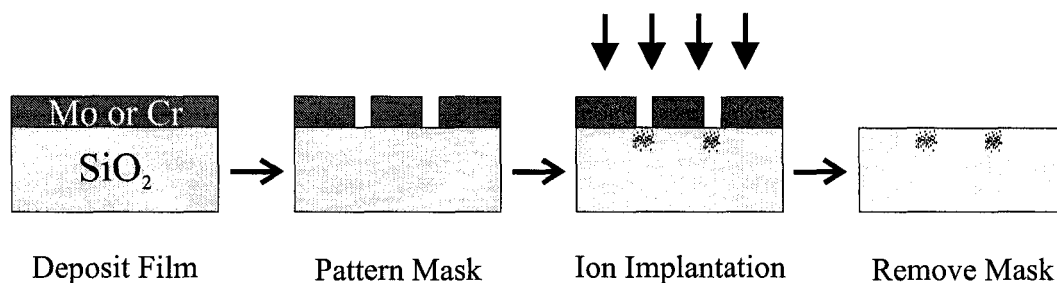


Figure 3.1: Diagram illustrating the masking procedure used for creating patterned nanocomposites.

Element	Growth Techniques	Etchant	SBE (eV)
Mo	sputter, e-beam	H ₂ O ₂	6.83
Cr	sputter, e-beam	Chrome etch (standard)	4.12
Cu	sputter, thermal	PC board etch (FeCl ₃)	3.52

Table 3.2: Candidate masking materials. The methods commonly used to grow and etch these materials are listed along with the surface binding energies (SBE's) of the films (sputter = sputtering, thermal = thermal evaporation, and e-beam = electron beam evaporation).

Based on these requirements, Mo, Cu, and Cr were selected as potential masking materials. Thin films of all of these metals can be grown directly on the host material using sputtering techniques, or alternatively, thermal (Cu) or e-beam (Mo, Cr) evaporation, and all adhere well to oxide substrates such as SiO₂. Standard deep UV lithography was used to transfer the pattern from a specially designed mask with features ranging from 10.0 to 0.5 μm , followed by wet chemical etching and removal of photoresist. The etchants for these metals are relatively mild and should not adversely affect SiO₂. Table 3.2 lists the candidate masking materials along with growth techniques, etchants, and surface binding energies (SBE). Materials with higher SBE's will exhibit lower sputtering yields, which is desirable for this application. Table 3.3 lists the projected ranges of 80 kV Fe ions in the candidate masking materials as well as in the SiO₂ host [1]. Based on only the projected ranges, a mask of < 100 nm in thickness would be expected to stop the vast majority of the ions. The masks made for testing purposes were made thicker (from 380 to 760 nm) to allow for sputtering losses and to err on the side of caution.

3.2. PATTERNING OF NANOCOMPOSITES

Substrate	Projected Range (nm)	Longitudinal Stragglng (nm)	Lateral Stragglng(nm)
Cu	25.3	13.3	9.3
Cr	28.8	13.6	9.5
Mo	25.3	16.0	11.4
SiO ₂	64.9	18.7	14.2

Table 3.3: Ion stopping and range for 80 keV iron ions [1].

The feature sizes explored here are a micrometer or larger but it should be possible to extend this technique to smaller scales. One of the considerations in determining the minimum feature size possible with this technique is the lateral straggle of the ions as they come to rest in the host material. Figure 3.2 shows histograms of projected range and lateral straggle for 80 keV Fe⁺ ions in an SiO₂ host. The predictions were made using a software package SRIM 2003 [1]. For 50,000 events, the mean range was 67 nm with the deepest ion found at 189 nm. The standard deviation of both the x and y lateral spreads was 17 nm, with a maximum lateral range of 99 nm. The lateral straggle would thus be expected to increase the implanted area by about 34 nm over the size of the hole in the contact mask. This is quite small in comparison to the features explored here but places an approximate lower limit on the feature size for patterning using this technique. Optical lithography techniques are limited in resolution to a few hundred nanometers so other methods would have to be used to fabricate a mask with features this small. Electron beam lithography, for example, can be used to fabricate structures on the order of 50 nm in size. Another factor that would have to be taken into consideration in developing smaller structures is the etching process. Wet chemical etching tends to etch outwards to some degree as the features are etched downwards, which can result in sloping walls and/or enlargement of features. Using thinner masks will make it possible to obtain more sharply defined lithographic features, however, in order to obtain smaller features, anisotropic etching techniques would have to be employed to produce steeper walls. Alternatively, another type of masking template could be considered, for example, anodized aluminum*

*Anodized aluminum, also known as porous aluminum oxide, is synthesized by electrochemical oxidation (anodization) of Al in acid electrolytes, which, under the right conditions, causes uniform nano-sized cylindrical pores to form perpendicular to the surface and self-organized into a hexagonal lattice [87].

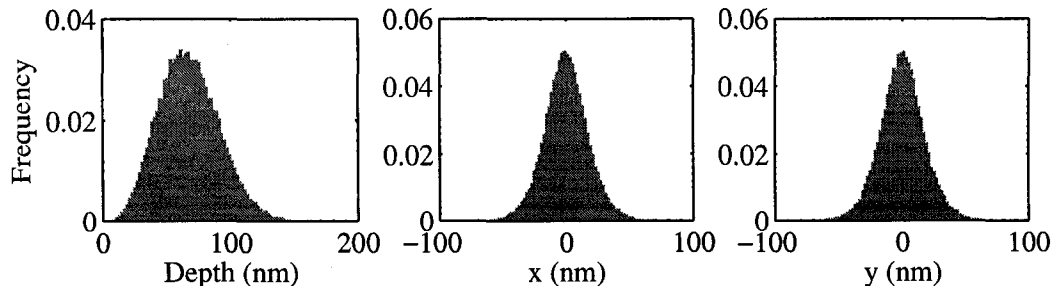


Figure 3.2: Histograms of predicted ranges and lateral spread (x and y) of 80 keV Fe^+ ions implanted in SiO_2 (50,000 events).

[88].

Masks have been patterned with 5-10 μm Cu pillars or else with square holes ranging from 0.5 μm to 10 μm in diameter in all three metals. All masks were created using standard deep UV lithography techniques at the U of A Nanofab. A diagram of the mask design can be found in Appendix B. To test the patterning technique, iron[†] was implanted through the contact masks to create patterned, buried nanoparticle layers [55]. An energy of 80 keV was used, with fluences of 1.5×10^{17} and 5×10^{16} ions/ cm^2 . Before and after implantation the masks were examined using a scanning electron microscope to determine if the implantation process damaged the mask. The masks were then removed and the magnetic properties, both static and dynamic, of the resulting nanocomposite samples were examined using magneto-optical methods.

3.3 Hysteresis measurements (MOKE)

The magneto-optical Faraday and Kerr effects can both be exploited to measure magnetic hysteresis loops for transparent samples. The experimental set-up is illustrated in Figure 3.3. A laser beam ($\lambda = 532$ nm) is split into reference and probe beams. The probe beam is directed through a long focal length lens and a polarizer prior to the sample, which is situated between the poles of an electromagnet (Figure 3.4). The probe beam

[†]Silicon was also implanted to produce patterned luminescent nanoparticle regions but the properties of these specimens were studied by other researchers. Masks implanted with silicon ions survived the implantation process at least as well as the Fe implanted specimens.

3.3. HYSTERESIS MEASUREMENTS (MOKE)

then passes through a second polarizer, or analyzer, that is oriented a few degrees from the extinction point and is detected by a photovoltaic detector. The reference beam is subtracted from the probe beam resulting in a differential signal that is proportional to the magnetization of the sample. The applied magnetic field can be swept over a given range and the differential signal is monitored as a function of magnetic field, which is measured using a Hall probe. The system can be easily modified to measure Kerr hysteresis loops by moving both the analyzer and signal detector into the path of the reflected beam as suggested in Figure 3.4.

A close up view of the sample position between the pole pieces of the magnet is shown in Figure 3.5. For in-plane measurements the sample (and magnet) are tilted such that the beam is incident at ~ 20 degrees from normal. For the out-of-plane measurements, small mirrors are mounted between the pole pieces of the magnet and the sample face is aligned perpendicular to the magnetic field such that normal incidence is achieved within 1° . Using a 2 Ampere power supply (Kepco BOP 100-2M), fields of around 750 kA/m (9.4 kOe) can be obtained for the in-plane measurements (pole piece separation around 1 cm). The out-of-plane configuration required a larger pole piece separation to accommodate the mirrors, typically 2 cm, which resulted in a maximum field of ~ 6 kG.

When two polarizers are placed one after the other in the path of a beam, the intensity I of the transmitted light follows Malus's law

$$I(\theta) = I(0) \cos^2 \theta \quad (3.1)$$

where θ is the angle between the transmission axis of the second polarizer, often called the analyzer, and the first [35]. Maximum transmittance occurs when this angle is 0° ; minimum transmittance, known as the extinction point, occurs when the axes are perpendicular. When linearly polarized light passes through a magnetized sample it undergoes a rotation in polarization. If the beam passes through a magnetized sample in between the polarizer and the analyzer a change in intensity will be observed identical to the change in intensity that would occur if the sample were removed and the analyzer rotated by the Faraday rotation angle of the sample. If the extinction curve for the set-up and the angle of the analyzer with respect to the first polarizer are known then the change of intensity observed with the magnetized sample in place can be converted to a Faraday rotation.

The extinction curve for this set-up with a Fe implanted SiO_2 sample ($190 \mu\text{m}$

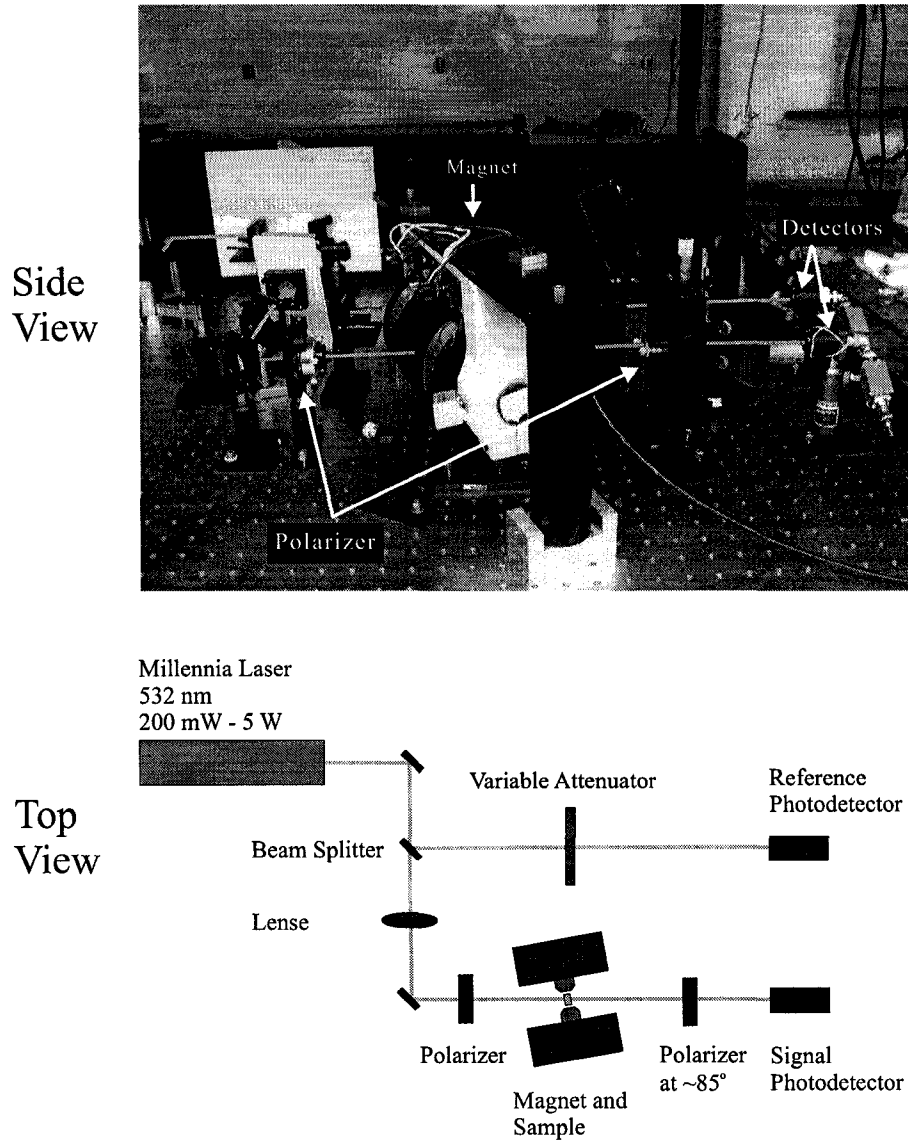


Figure 3.3: Photograph and diagram showing set-up used to measure static hysteresis loops using the Faraday effect.

3.3. HYSTERESIS MEASUREMENTS (MOKE)

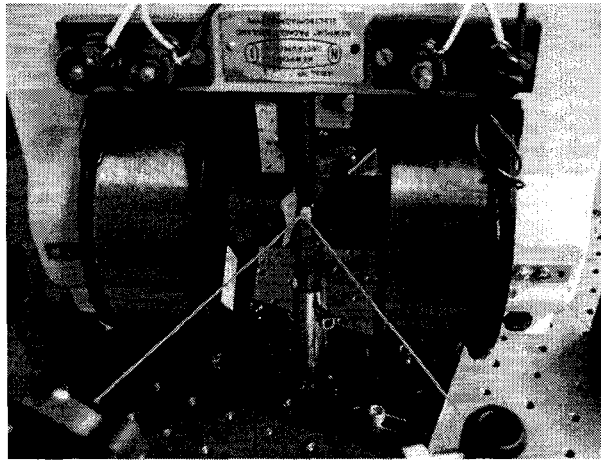


Figure 3.4: Close up view of a sample positioned between the pole pieces of the magnet for in-plane hysteresis measurements. Typically the transmitted beam is collected by the signal photodetector but both the second polarizer and the photodetector can be moved to measure hysteresis loops from the reflected beam also.

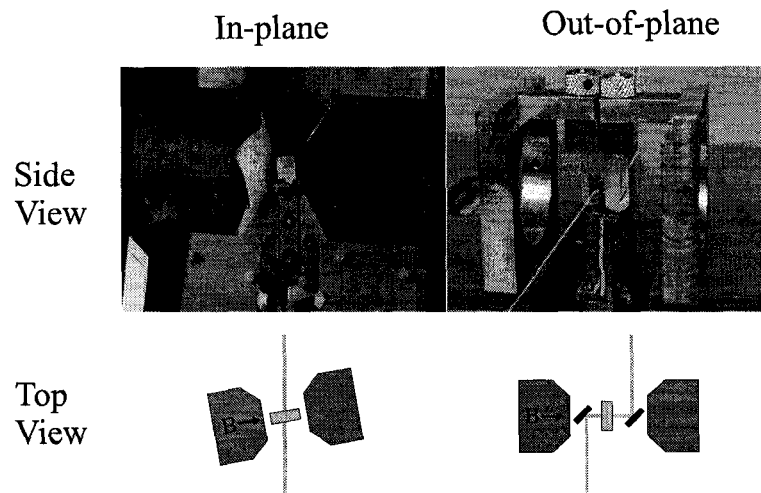


Figure 3.5: Configurations used to measure in-plane and out-of-plane hysteresis loops. Both the magnet and sample in the in-plane configuration are tilted by an angle of $\sim 20^\circ$ with respect to the beam path. The mirrors used in the out-of-plane set-up were mounted directly onto the pole pieces of the magnet.

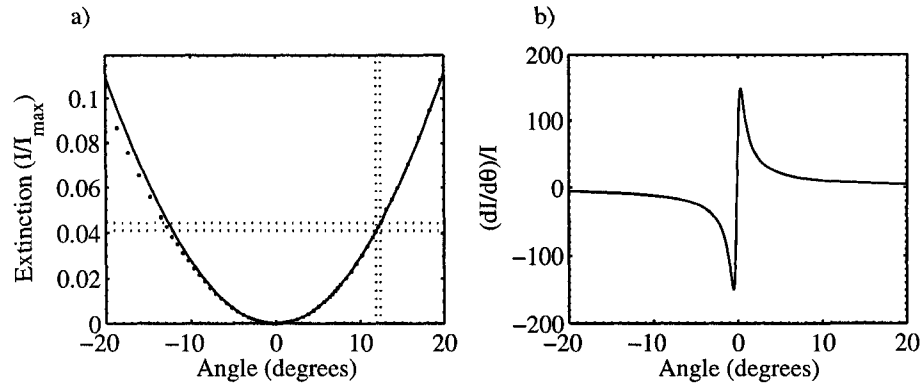


Figure 3.6: a) Extinction curve with Fe implanted SiO_2 sample in place (out-of-plane configuration, negligible applied magnetic field, sample was $\sim 200 \mu\text{m}$ thick). The solid line is a $\cos^2(\theta)$ fit to the data. The vertical dotted lines show the angle the polarizer must be rotated by with an applied magnetic field of $+476 \text{ kA/m}$ or -455 kA/m to preserve transmitted intensity. The horizontal dotted lines show the change of intensity when a field is applied if the polarizer angle is maintained at 12° from extinction. b) First derivative of the extinction curve normalized by the intensity.

thick) in place is shown in Figure 3.6a to illustrate this concept. The vertical dotted lines show the change in angle on the analyzer required to maintain constant intensity when a magnetic field of $+476 \text{ kA/m}$ (5.98 kOe) or -455 kA/m (5.72 kOe) is applied to the sample. The difference between the two recorded angles is a direct measure of the Faraday rotation. The horizontal dotted lines indicate the change in intensity observed under the same applied magnetic fields with the analyzer angle held constant at 12° from the extinction point. Both sets of measurements intersect along the extinction curve as expected. The second method is used to measure hysteresis loops because no mechanical movement is involved, making it relatively easy to automate the process. The best angle to work at can be selected by choosing a point where the extinction curve that has a large slope-to-intensity ratio, which should correspond to a high signal-to-noise ratio (Figure 3.6b). Care must be taken to ensure that the angle is chosen far enough away from the extinction point that a linear mapping from intensity to angle is valid. For in-plane hysteresis curves, angles of 2 or 3° were used, while for out-of-plane hysteresis curves, which can result in larger Faraday rotations, angles closer to 10° were chosen. A more detailed account of how hysteresis curves were measured can be found in Appendix C.

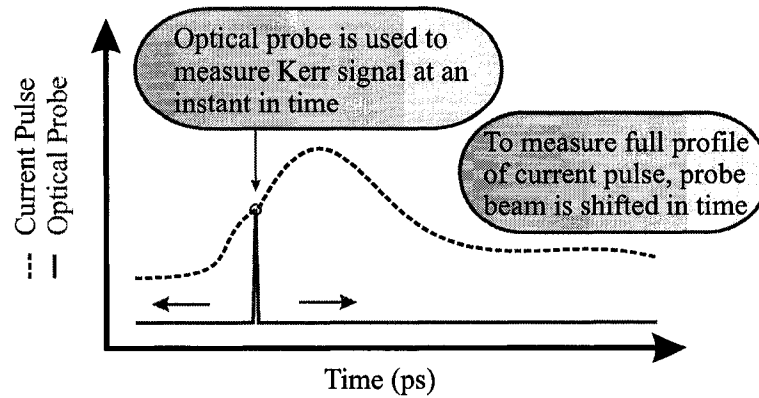


Figure 3.7: Illustration of the pump-probe concept.

3.4 TR-SKEM measurements

Time resolved scanning Kerr effect microscopy (TR-SKEM) was used to quantitatively characterize the dynamic magnetic response of the Fe/SiO₂ nanocomposites. This stroboscopic pump-probe method is capable of locally probing the change in magnetization state with sub-micrometer spatial resolution and picosecond temporal resolution [89]. An overview of the technique will be given below; for a more detailed description, refer to Hiebert [21].

The general concept of a pump-probe system is illustrated in Figure 3.7. In the magnetodynamics experiments, a pump beam triggers a current pulse, which is hundreds of picoseconds to tens of nanoseconds in length, and the magnetization responds to the transient magnetic field that it creates. A probe beam (100 fs pulse) is used to examine the magnetization state at a given instant in time with respect to the pump beam. The full temporal profile can be reconstructed by varying the time lag between the pulses. The pump-probe works under the assumption that the response of the system to the pump is the same each time the sample is excited. For a stochastic process the best that a pump-probe experiment can do is to capture the average behaviour or in some cases the deviations from the average behaviour [90].

Figure 3.8 shows a cross-sectional view of the sample position with respect to lithographically patterned transmission wires. The u-shaped gold wires used here were 10 μm wide and were separated by 10 μm . They were fabricated by first sputtering 30 nm of

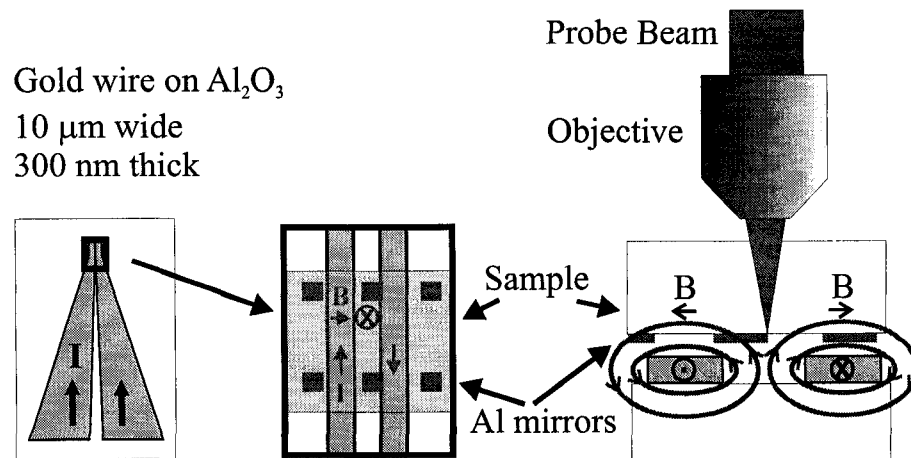


Figure 3.8: Transmission wire set-up showing how the sample is positioned, directions of the field, and the positioning of the probe beam. Diagram is not to scale.

titanium followed by 300 nm of gold onto a sapphire substrate. The wires were then patterned using standard deep UV lithography and wet etching techniques. Small aluminum mirrors, 10 nm thick and $< 10 \mu\text{m}$ on a side, were similarly fabricated on the implanted surface of the nanocomposite specimen. The nanocomposites tend to transmit more light than they reflect so this allows the signal reflected from the mirrors, which should be higher in intensity, to be compared to that from the bare nanocrystals. The specimen was then mounted directly on top of the transmission wires with the implanted (and mirrored) face as close to the transmission wires as possible. [‡] The spacing between the nanocrystals and the write wires was estimated to be on the order of $10 \mu\text{m}$ based on the difference in focus distance for the gold wires and mirrors patterned on the implanted face of the nanocomposite specimen.

A diagram illustrating the apparatus used to probe the dynamic magnetic response of the sample is shown in Figure 3.9. A pulsed laser beam (mode-locked Ti-sapphire beam, wavelength 800 nm, repetition rate of 740-760 kHz) is split into a pump and a probe beam.

[‡]A variety of methods for fastening the specimen in place were tested. UV cure epoxy was found to hold the sample very well but it was difficult to re-use the transmission wire or the implanted specimen because it is not easily removed. TEM wax provided a less permanent solution (dissolves in acetone) but usually resulted in a large air gap between the wires and the implanted surface (measured as $40 \mu\text{m}$ in one case using a calibrated optical microscope). It also had the disadvantage that it needed to be heated, which sometimes caused the patterned wires to bubble. The best solution was a small amount of clear nailpolish applied along the edges of the specimen. It takes longer to cure than the first two methods but adheres well and can be removed with acetone.

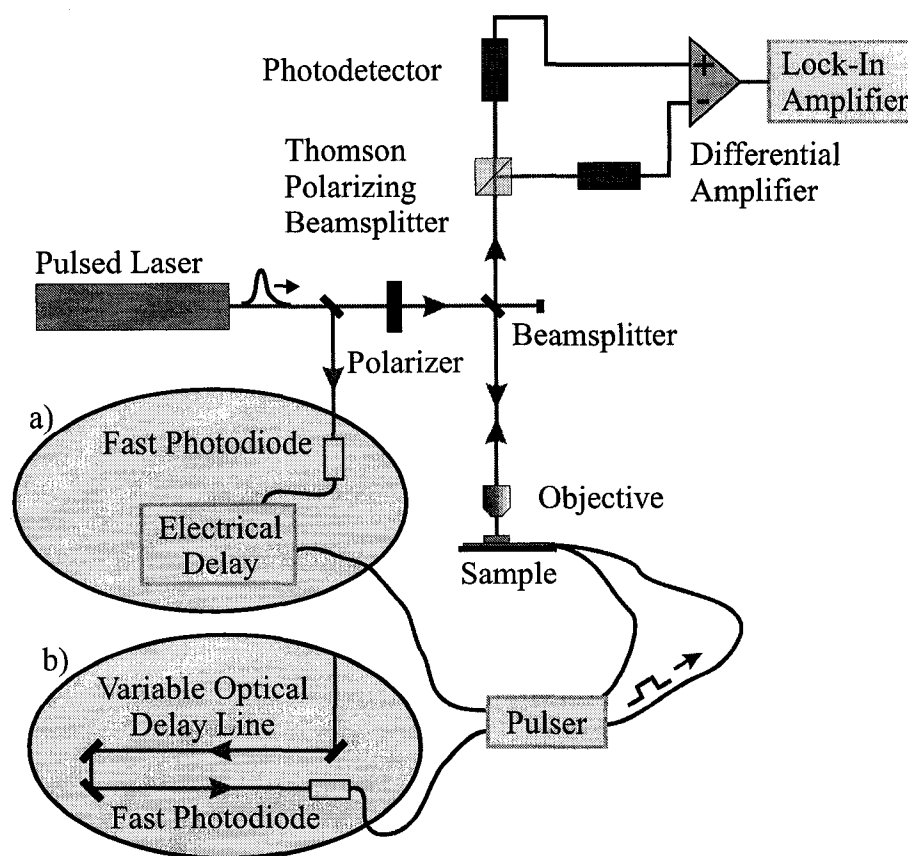


Figure 3.9: Diagram of the apparatus used in TR-MOKE measurements where an electronic pulser is used to generate a transient magnetic field. For maximum flexibility in the length of temporal scans, an electrical delay line (a) can be used to control the delay between the pump and probe. For measurements requiring improved temporal resolution, the electrical delay line is replaced with b) an optical delay line.

The probe beam (average power between 20 and 40 μW) was focused using an objective lens through the silicon dioxide substrate onto the layer of implanted nanoparticles. The focused laser spot was estimated to be 1.2 μm in diameter. The objective was mounted on a precision translation stage, allowing it to move through a range of two millimeters, forming a scanning optical microscope.

The pump beam is aimed at a fast photodiode, which is used to trigger a current pulse that propagates down the transmission wire. The corresponding pulsed magnetic field is predominantly an in-plane field over the wire and an out-of-plane field between the wires. Two separate pulse source/delay line combinations were used, as shown in Figures 3.9a

and b. The first was a 50 V pulser with a 250 ps rise-time (Picosecond Pulse Labs 2000D Turbo) in combination with an electronic delay line with a characteristic jitter of 220 ps. The second was a 10 V pulser with a 50 ps rise-time (PSPL 4050B) in combination with a jitter-free optical delay line. The first setup provides stronger signal and a long scan range of 120 ns, at the expense of temporal resolution. The second set-up has excellent temporal resolution but is limited to shorter 4 ns scans and weaker magnetic field pulse. In addition, constant in-plane bias magnetic fields ranging from 0 to more than 80 kA/m (1 kOe) were applied.

The probe beam, after reflection from the magnetic specimen, is split using a Glan Thomson beamsplitting cube such that the emerging beams are polarized $+45^\circ$ and -45° with respect to the initial polarization state. Figure 3.9 shows a simplified version of the detection scheme. Using a quadrant detection scheme, it is possible to measure the change in magnetization for all three components simultaneously. The z component of the magnetization is detected using the polar Kerr effect (Figure 3.10). A change in the M_z state of the sample will result in equal but opposite changes in the intensity of the beams incident on the two photodetectors. The difference of the intensities measured by the two photodetectors is proportional to the change in M_z .

The longitudinal Kerr effect is exploited to measure the in-plane components of the magnetization. The longitudinal Kerr effect is zero for normal incidence. The beam, however, is tightly focused by the objective so the full beam contains a range of angles of incidence. Figure 3.11 illustrates how the quadrant detectors were used to monitor the change in M_x and M_y . The in-plane response is illustrated using a sample that is magnetized in-plane and to the right. A beam normally incident on the left side of the objective will result in an increased intensity on half of one detector and an equal but opposite decrease in intensity on half of the other detector. A beam starting from right side of the objective will result in an intensity difference between the opposite halves of the opposite detectors. The total intensity observed by both detectors is the same and thus does not affect the polar Kerr measurement of M_z . The longitudinal Kerr rotation is recorded by subtracting the intensities from the left and right sides of each detector and summing them such that the signal is doubled. If the left and right directions are chosen to correspond to the positive and negative x directions then the y component can be similarly

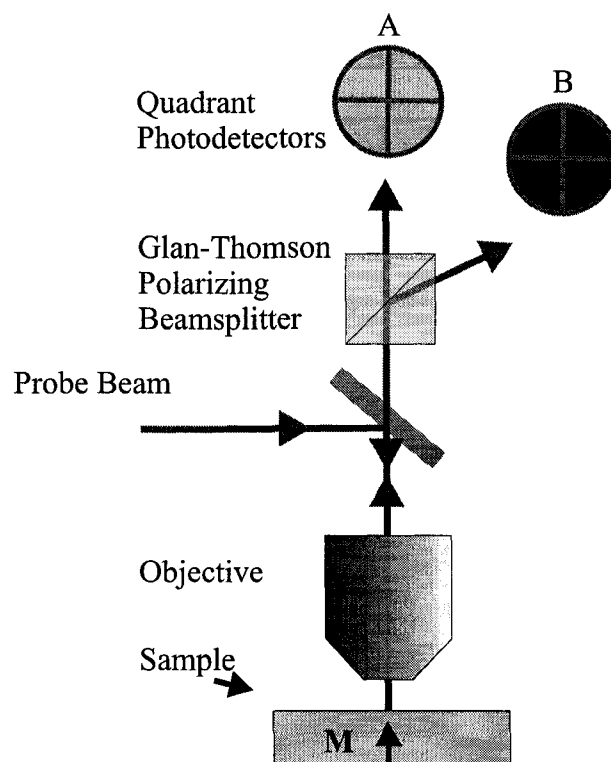


Figure 3.10: The polar Kerr effect is exploited to measure the z component of the magnetization. This effect results in an intensity difference between detectors A and B.

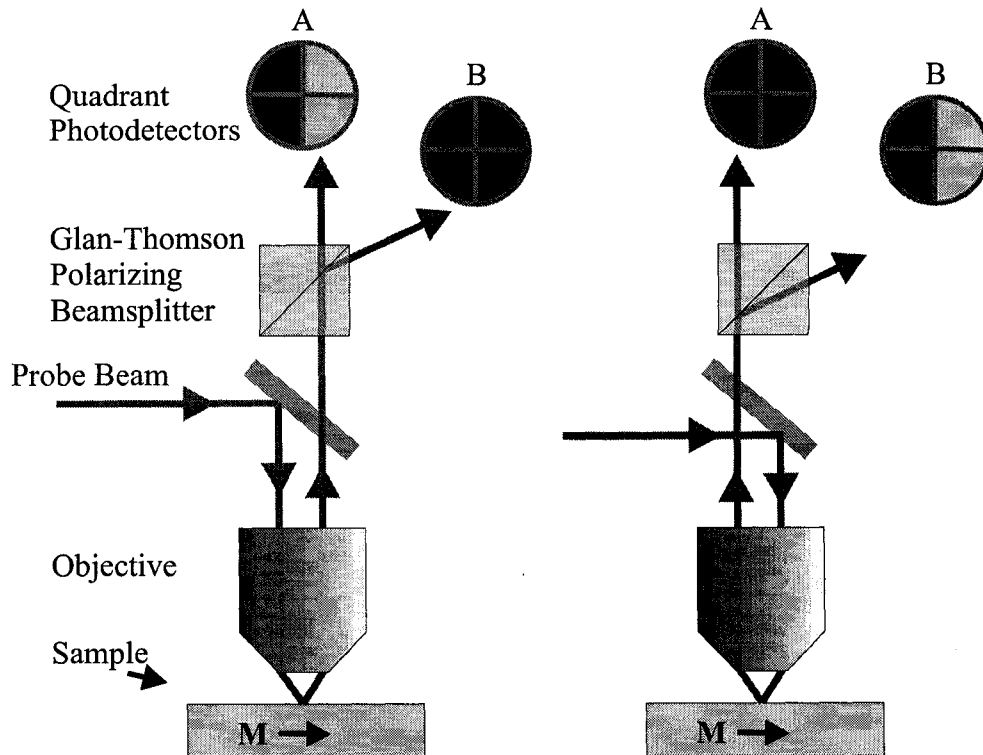


Figure 3.11: The longitudinal Kerr effect is sensitive to the in-plane components of the magnetization. For a sample magnetized to the right, a beam traveling from the left side of the objective will result in an increased intensity on one half of one detector and a decreased intensity on half of the other detector. A beam starting from right side of the objective will result in the opposite change in intensity on the other half of each detector. The total intensity observed by detectors A and B is the same. The longitudinal rotation can be measured with quadrant detectors by subtracting the intensities from the left and right sides of each detector and summing them such that the signal is doubled.

monitored using the intensities from the top and bottom of the two detectors.

To boost the small magneto-optical signals, the M_x , M_y , and M_z signals are fed into lock-in amplifiers. A function generator was used to provide a reference signal at a frequency of 2.3 kHz, chosen to be well below the repetition rate of the laser and different from common electrical noise frequencies (e.g., 60 Hz). To build up signal with the lock-in amplifier, the sample must be excited during half of a given period and probed in its equilibrium state the remainder of the time. In practice this is achieved by varying the delay between the photodiode and the trigger input for the pulser. During half of the period the delay is set so that the probe beam measures a baseline value before the current pulse

has been triggered. During the other half of the period the probe beam is incident at the desired pump/probe delay time.

3.4.1 Photoconductive switches

The TR-SKEM technique discussed in the previous section was used to study the dynamics of the nanoparticle assemblies but even using the optical delay line, the temporal resolution is limited by the bandwidth of the interconnection between the pulser and the transmission wires, which results in a current pulse with a rise-time of approximately 150 ps. The temporal resolution can be improved by an order of magnitude by incorporating photoconductive switches into the experimental design [22,40]. This was done by making a few modifications to the set-up described in the previous section.

First, the transmission wires were redesigned to include a photoconductive switch. The design for the transmission wire/photoconductive switches used in this experiment is illustrated in Figure 3.12 (a scale diagram can be found in Figure D.1). The wires consist of two long leads that taper into narrow transmission wires 10 μm wide, separated by 10 μm , with a photoconductive switch on the end. The impedance of the transmission line is approximately 100 Ω [91]. The wires connecting the narrow transmission wire area to the photoconductive switches were designed to be 2 mm long. This distance was chosen to be as short as possible to minimize dispersion of the current pulse while still allowing for sufficient space so that the objective lens used to focus the probe beam does not obstruct the switch. A version was also designed with the photoconductive switch further from the transmission wires for versatility but was not used in these experiments.

Photoconductive switches were designed based on work by Gerrits *et al.* [40,92]. The design involves two copper layers on GaAs – a semiconductor with a direct band gap of 1.41 eV. A simple photoconductive switch involves two conductive leads patterned on the GaAs substrate separated by a gap a few microns wide. When GaAs is illuminated with light with sufficient energy, electrons are excited into the conduction band and current will flow across a biased switch. In this particular design, two layers of copper are used as conductors. The lower layer of copper is designed to be 10 nm thick and to have a slightly larger footprint than the upper, which is 250 nm thick. The gap between the fingers of the

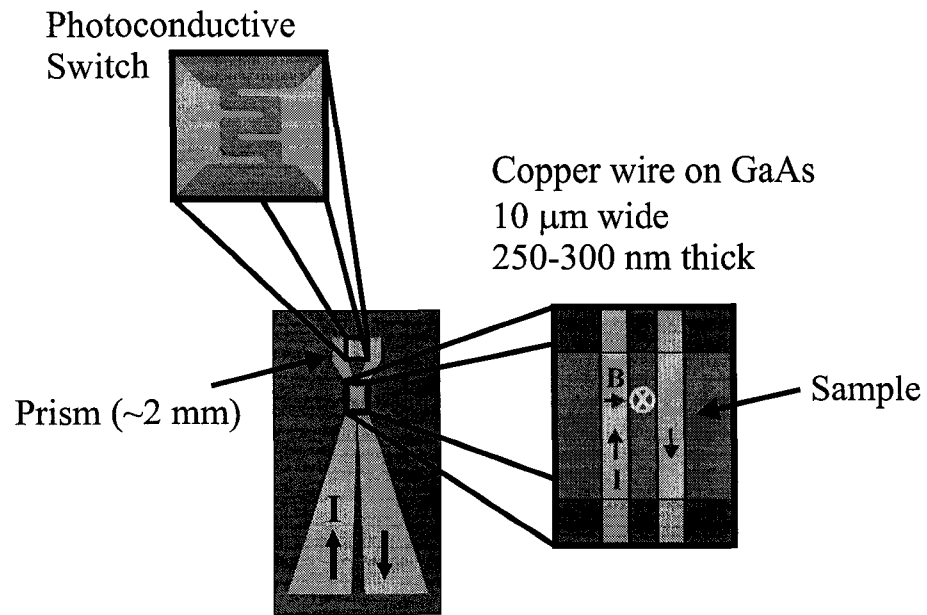


Figure 3.12: Illustration of the transmission wire and photoconductive switch arrangement. The specimen is fastened on top of the transmission wire with the implanted face directly above the surface of the wire. A photograph of an actual photoconductive switch as seen through an optical microscope is shown.

switch was $15\ \mu\text{m}$ for the upper layer but only $5\ \mu\text{m}$ for the lower layer. The underlayer is expected to improve the efficiency of the switches. It is thick enough that the conduction layer is extended if the beam is incident on the switch at an angle, which helps to avoid shadowing effects. It is also thin enough that carriers can still be excited under the layer in areas where there is no shadowing. The wires were fabricated using a two-step liftoff process and the copper layers were grown using electron-beam evaporation. The details of the process used to fabricate the switches are described in Appendix D.

The sample was attached directly above the narrow transmission wires with the implanted face closest to the wires and the probe beam (mode-locked Ti-sapphire beam, wavelength $800\ \text{nm}$, repetition rate $80\ \text{MHz}$, average power 4 to $5\ \text{mW}$) was focused through the transparent SiO_2 substrate onto the nanocomposite face. Figure 3.13 illustrates how the overall set-up was modified to incorporate the photoconductive switch. The main difference lies in how the current pulse was triggered. The photodiode and electronic pulser have been removed and instead the pump beam ($100\ \text{mW}$ average power, $80\ \text{MHz}$ repetition rate) is used to trigger the photoconductive switch directly. A $2\ \text{mm}$ prism was fastened onto the photoconductive switch such that the pump beam, which traveled parallel to the wires, was deflected onto the fingers of the switch through total internal reflection. The beam was focused onto the fingers of the switch using a lens (focal length approximately $5\ \text{cm}$). An optical delay line was used to vary the time delay between the pump and probe beams, the minimum step size of which corresponds to a delay change of $0.8\ \text{ps}$. A rheostat was used to monitor the position of the optical delay line so that data taken in different runs could be compared on the same time scale.

The current pulse in this set-up is triggered directly by the beam instead of first being converted to an electrical signal, which triggers an electronic pulser. As a result, electronic gating of the pulse trigger can no longer be used for locking. As an alternative, a mechanical chopper can be used to modulate the beam at a low frequency (kHz range) or else the bias voltage across the photoconductive switch can be made to vary with time. In practice a $10\ \text{V}$ AC bias was applied between the two leads and a pump beam with an average

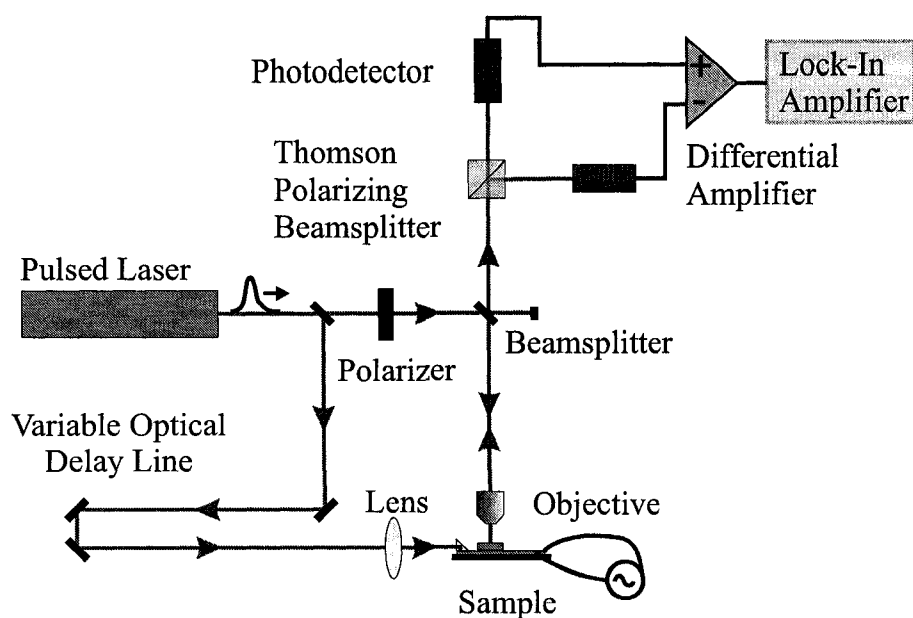


Figure 3.13: Diagram of the TR-SKEM apparatus modified to employ a photoconductive switch for generating the transient magnetic field. The pump beam is focused using a lens and then redirected using total internal reflection in a 2 mm glass prism onto the fingers of the photoconductive switch. An optical delay line is used to control the delay between pump and probe.

power of 100 mW was used (repetition rate 80 MHz).[§] The resulting current pulse has a fast rise-time of a few picoseconds and an exponential decay, the time constant of which is related to the carrier lifetime of the GaAs substrate. Gerrits *et al.* [94] report typical rise-times of 10 ps and decay times of 400 ps. An inductive current probe was attached to one of the leads connected to the photoconductive switch to obtain an estimate of the current pulse amplitude. Measured amplitudes of 36 mA were typical, although the actual peak amplitude is expected to be significantly higher as the bandwidth of the oscilloscope is the limiting factor in the measurement (300 MHz). Also, the current probe was centimeters away from the measurement location and dispersion of the pulse is expected.

To facilitate the investigation of the effects of an in-plane bias field on the magnetization response, a strong magnet was securely mounted on a stepper motor track. The magnetic field was measured using a gaussmeter (Walker Scientific MG-3D Precision Hall Effect Gaussmeter) positioned as close to the sample as possible without interfering with the Kerr measurements. Using the output from the gaussmeter, the measurements could be automated for low fields. At fields above 40 kA/m (500 Oe), the translation stage had to be manually adjusted for each measurement due to attraction of the apparatus to the magnet. A centering algorithm was utilized for fine adjustment of the position to ensure that data were collected as close to midway between the wires as possible for all fields. Using this set-up, in-plane bias fields of between zero and 135 kA/m (1700 Oe) were obtained.

3.4.2 Transient field generated by a transmission wire

The magnetic field generated by a current traveling through the transmission wires can be calculated using the Biot-Savart law [69,70]. The transmission lines are much thinner than they are wide ($0.3 \mu\text{m}$ as compared to $10 \mu\text{m}$ so they can be treated as thin films carrying a surface current $\vec{K} = [I/2a]\hat{j}$ where I is the total current and $2a$ is the width of the current

[§]The voltage of the photoconductive switch was modulated using a sinusoidal wave form. A square wave pulse could have been used instead, although the out-of-plane response was found to be a linear function of current pulse amplitude, suggesting that it should not make a difference in the overall measurement. The result of using square wave versus a sinusoidally varying voltage were compared for another sample (Fe/Au layers on GaAs made at Simon Fraser University) and were found to yield the same signal shape [93].

carrying film. Working in S.I. units, the magnetic field \vec{B} can be found using

$$\vec{B} = \frac{\mu_o}{4\pi} \int \frac{\vec{K} \times \hat{r}}{r^2} da = \frac{\mu_o}{4\pi} \int \frac{\vec{K} \times \vec{r}}{r^3} da. \quad (3.2)$$

Figure 3.14 shows a diagram of a transmission wire in cross-section. The transmission wire is centered on zero in the x and z directions and extends to $\pm a$ in x . It is assumed to extend to infinity in both the positive and negative y directions from the point of interest $(x_p, 0, z_p)$. The vector \vec{r} extends from a point on the transmission wire $(x_w, y_w, 0)$ to the point $(x_p, 0, z_p)$: $\vec{r} = (x_p - x_w)\hat{i} - y_w\hat{j} + z_p\hat{k}$. The cross product of the surface current with \vec{r} is then $\vec{K} \times \vec{r} = I/2a(z_p\hat{i} - (x_p - x_w)\hat{k})$, which can be used to obtain the following expression for the magnetic field generated by a single transmission wire

$$\vec{B}(x_p, 0, z_p) = \frac{\mu_o I}{8\pi a} \int_{-a}^a dx_w \int_{-\infty}^{\infty} dy_w \frac{z_p\hat{i} - (x_p - x_w)\hat{k}}{((x_p - x_w)^2 + z_p^2 + y_w^2)^{3/2}} \quad (3.3)$$

$$= \frac{\mu_o I}{8\pi a} \int_{-a}^a dx_w \frac{z_p\hat{i} - (x_p - x_w)\hat{k}}{((x_p - x_w)^2 + z_p^2)}. \quad (3.4)$$

Integration in x_w yields the following components of the magnetic field at point $(x_p, 0, z_p)$

$$B_x = \frac{\mu_o I}{4\pi a} \left(\tan^{-1} \left(\frac{x_p + a}{z_p} \right) - \tan^{-1} \left(\frac{x_p - a}{z_p} \right) \right) \quad (3.5)$$

$$B_y = 0 \quad (3.6)$$

$$B_z = \frac{\mu_o I}{8\pi a} \ln \left(\frac{z_p^2 + (x_p - a)^2}{z_p^2 + (x_p + a)^2} \right). \quad (3.7)$$

The magnetic field generated by a 1 A current pulse traveling through a set of 10 μm transmission wires separated by 10 μm is shown in Figure 3.15. The current for the transmission wire on the right flows into the page while the current for the other wire flows out of the page. The in-plane magnetic field directly over the wires is 60 mT ($H = 48$ kA/m) while the out-of-plane magnetic field between the wires is 40 mT ($H = 32$ kA/m). Both fields are quite uniform except within around 1 μm of the edges where the field over the wire gains a significant out-of-plane component (around 60 mT) and the field between the wires gains an in-plane component. At a distance of 10 μm above the wire (the approximate separation between the nanocomposite and the wires), the fields are reduced to 19.1 and 14.6 mT ($H = 15$ and 12 kA/m) for the out-of-plane and in-plane configurations, respectively.

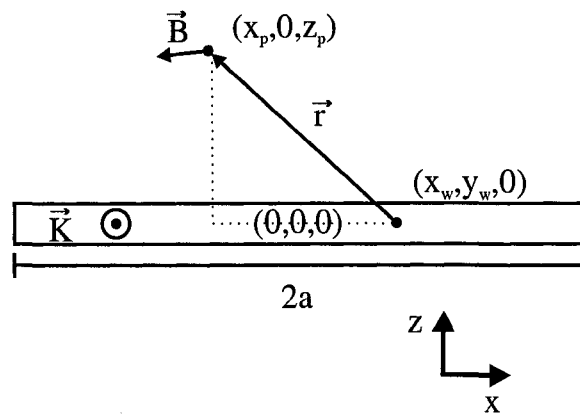


Figure 3.14: Cross-sectional diagram of a current-carrying transmission wire (surface current \vec{K} , width $2a$) showing the magnetic field at a point $(x_p, 0, z_p)$ generated at point $(x_w, y_w, 0)$ on the wire.

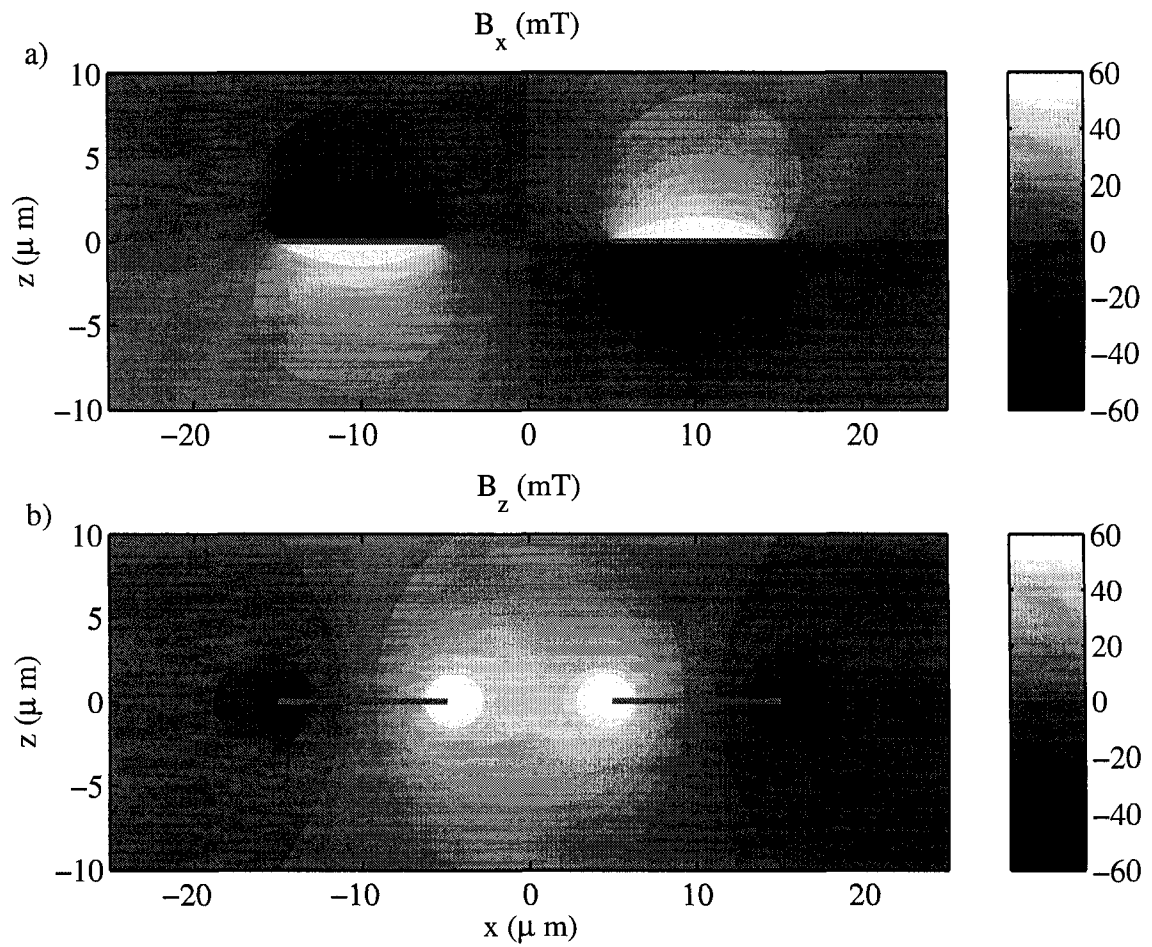


Figure 3.15: Magnetic field generated by a 1 A current pulse traveling through a set of 10 μm transmission wires separated by 10 μm (located at $z = 0 \mu\text{m}$). The x component is shown in a) and the z component in b).

Chapter 4

Microstructure and hysteresis

This chapter will show the microstructural and optical properties of the ion implanted specimens. In addition, the results of the patterning study will be summarized. Finally, hysteresis measurements for both the bulk and patterned implanted specimens will be presented and the magnitude of the Faraday rotation will be discussed.

All of the samples studied were fabricated by implanting Fe^+ ions into fused quartz wafers. The ion implanted samples can be divided into three categories: samples that were implanted with 80 kV ions that were uncoated (u series), those that were implanted with 80 kV ions and then coated with 200 nm of SiO_2 prior to annealing (c series), and finally, samples that were implanted with 150 kV ions (d series). Table 4.1 shows a summary of the ion implanted samples that were characterized in terms of their microstructural, optical and magnetic properties (hysteresis). All samples were implanted to a fluence of 1.5×10^{17} ions/ cm^2 . This relatively high fluence was chosen to ensure a high concentration of nanoparticles, which will increase the likelihood of having both a large magneto-optical signal and significant inter-particle interactions. The 150 kV ions penetrate deeper and occupy a broader depth range than the 80 kV ions. For each series, the effects of annealing the implanted wafer at temperatures of 600, 800 and 1000°C for 1 hour in a reducing atmosphere ($\text{Ar} + 10\% \text{H}_2$) were explored. As-implanted specimens from each series were also examined and compared to their annealed counterparts.

Sample ID	Energy (kV)	Temperature (°C)	Coating
u1	80	NA	none
u2	80	600	none
u3	80	800	none
u4	80	1000	none
c1	80	NA	200 nm SiO ₂
c2	80	600	200 nm SiO ₂
c3	80	800	200 nm SiO ₂
c4	80	1000	200 nm SiO ₂
d1	150	NA	none
d2	150	600	none
d3	150	800	none
d4	150	1000	none

Table 4.1: Summary of Fe implanted SiO₂ samples including implantation energy, annealing temperature (“NA” signifies that the sample was not annealed), and whether or not a coating was used. All samples were implanted to a fluence of 1.5×10^{17} ions/cm² and annealed for 1 hour.

4.1 TEM results

Transmission electron microscopy (TEM) was performed on the ion implanted samples using a JEOL 2010 LaB₆ electron microscope. Both plan view and cross sectional specimens were prepared. Energy dispersive x-ray spectroscopy (EDX) and electron diffraction were used to identify the composition and crystal structure. Table 4.1 shows a summary of the ion implanted samples that were characterized in terms of their microstructural, optical, and magnetic properties (hysteresis). The dynamic properties of selected samples were also examined, the results of which will be covered in the next chapter.

The u series is composed of Fe/SiO₂ samples implanted at 80 kV. Figures 4.1a and c show cross-sectional and plan-view TEM micrographs of the as-implanted sample from this series, which was found to contain nanoclusters prior to annealing. Although the substrates were implanted at room temperature, the dose and flux were quite high, which could cause local heating. Radiation induced diffusion has also been known to promote particle growth [95]. Bright-field images show spherical nanoclusters of iron with diameters of around 10 nm (size range 5 to 12 nm) concentrated within the top 62 ± 2 nm from the

specimen surface. Electron diffraction results, recorded for the cross-sectional image, are shown in Figure 4.1a. This image reveals the presence of crystalline iron in the bcc crystal form (the common ferromagnetic form). This sample (u1) in particular is noteworthy for its relatively high Faraday rotation, which will be discussed later in this chapter.

In viewing plan view micrographs of these nanocomposite specimens it is important to consider the sample preparation technique and the role that it can play in influencing what is seen in the micrograph. These specimens are thinned by hand and then ion milled from the substrate side until they are electron transparent. The final stage of the preparation process is to ion mill from both sides at once to clean any sputtered material from the TEM specimen. The thinnest areas will provide the best TEM images but it is difficult to know the exact thickness or the depth of the imaged portion of the specimen with respect to the total implanted layer thickness. It is also possible for sputtered material to be redeposited on the specimen. The density of nanoparticles looks much higher in cross-section as compared to the plan view for the as-implanted sample so it is likely that this specimen (u1) represents only a limited depth-range of the total implanted thickness. Conversely, it is important to remember that the plan view specimens have a finite thickness and nanocrystals from all depths will appear to overlap even though they may be physically separated in reality.

The sample that was annealed at 600°C for 1 hour (Figures 4.1b and d) contains larger nanocrystals, ranging in size from 5 to 20 nm in diameter, that are spherical in shape. The electron diffraction from the plan view specimen indicates that the nanocrystals are bcc iron. The majority of the nanoclusters are concentrated in the top 70-80 nm of the specimen but a few larger (up to 25 nm), widely spaced nanoclusters can be found as deep as 220 nm. Deep stray particles have been observed previously in SiO₂ that had been implanted with both Zn and S ions and annealed in a reducing (Ar + 4% H₂) atmosphere at 800°C for 1 hour [96]. In that experiment, the majority of the particles were ZnS, however, the deeper stray particles were found to be zinc silicides (γ -Zn₂SiO₄). Diffraction patterns were not obtained specifically for the stray particles in this Fe/SiO₂ sample so there is a possibility that these particles are of a different crystalline form.

The filling factors can be estimated (very approximately) from the plan view micrographs of the specimens. The filling factors for the as-implanted and annealed samples

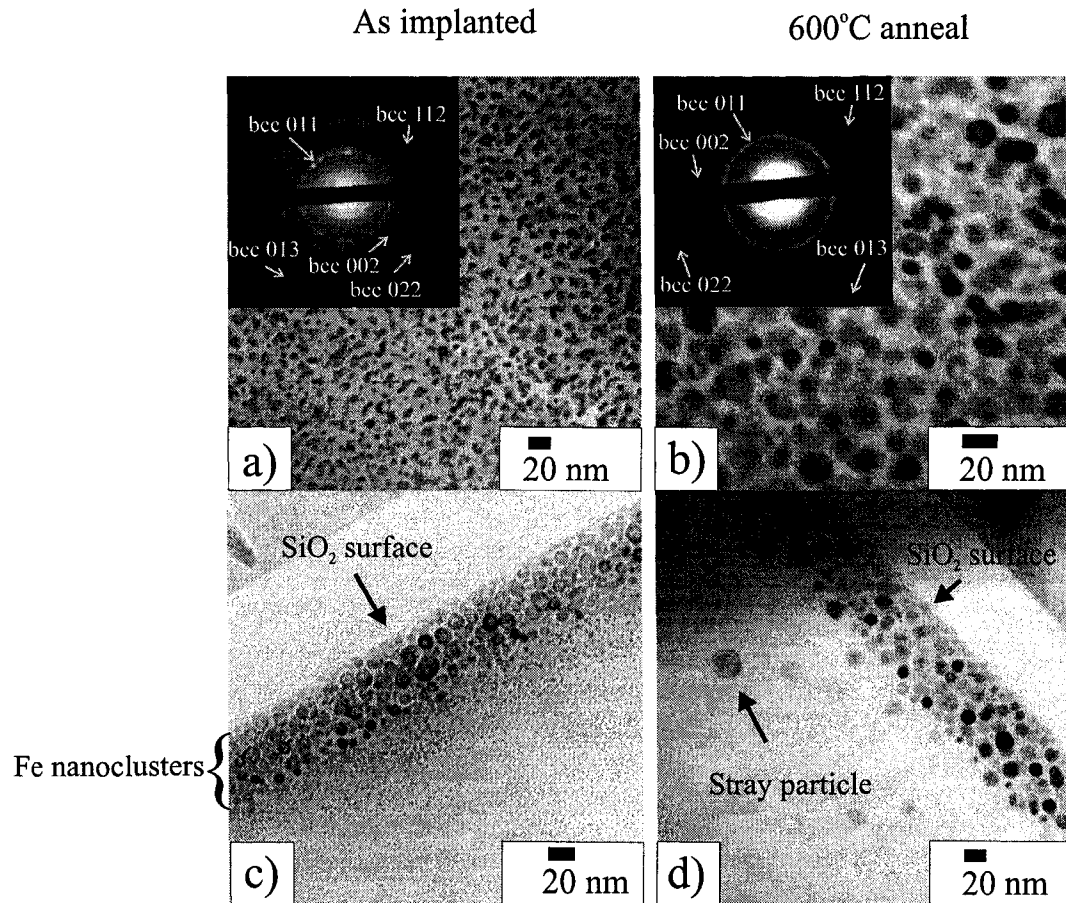


Figure 4.1: Plan view (a and b) and cross-sectional (b and d) TEM micrographs of Fe nanoclusters in SiO_2 . Fe ions (80 kV) were implanted to a fluence of 1.5×10^{17} ions/ cm^2 into the SiO_2 substrate, which was held at room temperature during implantation. Images a) and c) show the as-implanted specimen while micrographs b) and d) show the specimen that was annealed at 600°C for 1 hour. The insets of Figures a) and b) show the diffraction patterns for these samples.

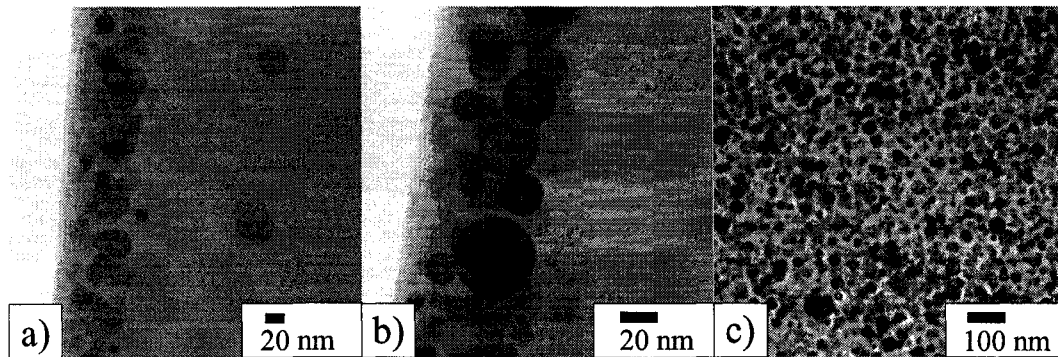


Figure 4.2: Images a) and b) show a cross-sectional view of Fe nanocrystals fabricated by implanting 80 keV ions into SiO₂ after annealing for 1 hour at 800°C, while c) shows a plan-view micrograph of the same sample.

(600°C) are estimated to fall in the 40 to 50% range. Both should contain approximately the same amount of iron and they should have similar filling factors. The filling factor could be slightly lower for the annealed sample as a small amount of iron may diffuse out of the sample on annealing and the nanocrystals are distributed over a larger depth range. Out-diffusion of iron has been observed previously on annealing where it tended to form small islands on the surface [97]. It is these two materials (u1 and u2) for which dynamic measurements were carried out.

Figure 4.2 shows TEM micrographs for the uncoated 80 keV sample after annealing at 800°C for 1 hour. The nanocrystals extend from the surface to 90-100 nm in depth and are larger than for the sample annealed at 600°C (u2), with diameters ranging from 5 to 45 nm. Like the other annealed sample (u2), larger stray particles with diameters of up to 55 nm were observed at depths of up to 200 nm. The particles at all depths are roughly spherical in shape and are randomly distributed in-plane. The diffraction pattern is not shown but is consistent with bcc iron as determined from the plan-view specimen. For this sample, the top 10 nm appears distorted – it does not have the smooth appearance of the SiO₂ below the nanocrystal layer and few nanocrystals are observed in this region – which could indicate that some of the iron diffused out of the sample during annealing. A study of diffusion of iron in SiO₂ layers on Si shows that for annealing temperatures of 900 to 1000°C, diffusion is significant [98].

The possibility of containing the iron by coating the specimens with a thin layer of

SiO₂ after implantation was explored (c series). A 200 nm thick layer of SiO₂ was deposited onto an 80 kV as-implanted wafer using e-beam evaporation. The wafer was then diced and the pieces were annealed. A coated version of the as-implanted material was fabricated for optical and hysteresis measurements but not examined with TEM as the coating process was not expected to affect the nanocrystals already present in the material. Cross-sectional micrographs of the coated sample that was annealed at 600°C are shown in Figure 4.3a and b. In Figure 4.3a, the full coating, which is 180-205 nm thick, is intact, while Figure 4.3b shows a closer view highlighting three distinct layers of nanoparticles. The thickest layer extends from the former surface of the SiO₂ host to approximately 65 nm below the surface and contains particles that range in size from 6 to 25 nm. The other two layers are located 20 to 60 nm from either surface of the thicker layer and contain slightly larger particles. The layer above the former surface supports the hypothesis that some of the iron may have diffused out of the uncoated samples on annealing. As in the uncoated specimen there are a few stray particles found as deep as 200 nm (400 nm from coating surface). This specimen is similar to its uncoated counterpart from the initial surface and down with slightly larger particles (maximum size 25 nm vs. 20 nm) observed in the main layer.

The coated sample that was annealed at 800°C (sample c3, Figure 4.3c) contains larger crystals as compared to the uncoated specimen annealed at the same temperature. Typically the bcc iron particles were around 60 nm in diameter but crystals as large as 250 nm and as small as 5 nm were observed. The crystals are concentrated near the interface of the substrate and the coating. Most of the particles are found within 350 nm of the new surface with a few located as deep as 540 nm. There are also some small (10-20 nm) particles located right at the coating surface. The coating of this sample appeared cloudy after annealing, which suggests that the the SiO₂ film quality may not be ideal for this sample.

The coated specimen that was annealed at 1000°C (sample c4, Figure 4.3d) actually contains a narrower distribution of particle sizes that form a more uniform single layer as compared to the sample annealed at 800°C. With this specimen, no stray particles were observed deeper than the main layers. Most of the particles are found in a layer that extends approximately 65 nm from the previous surface. The majority of the particles in this layer are between 50 and 65 nm in diameter. Thinner layers containing smaller 10-

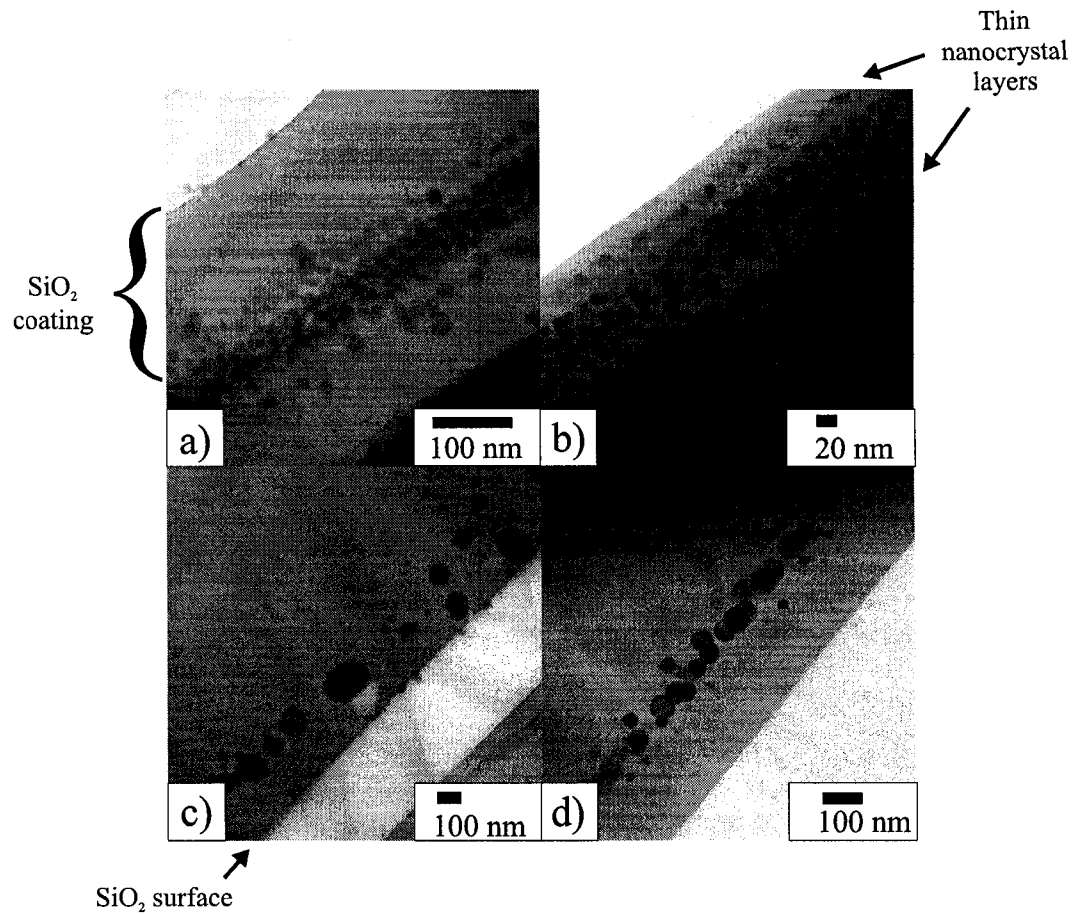


Figure 4.3: Cross-sectional TEM micrographs of 80 keV Fe-implanted specimens that were coated with 200 nm of SiO₂ prior to annealing at a) 600°C (showing the full SiO₂ coating), b) 600°C (at higher magnification), c) 800°C, and d) 1000°C.

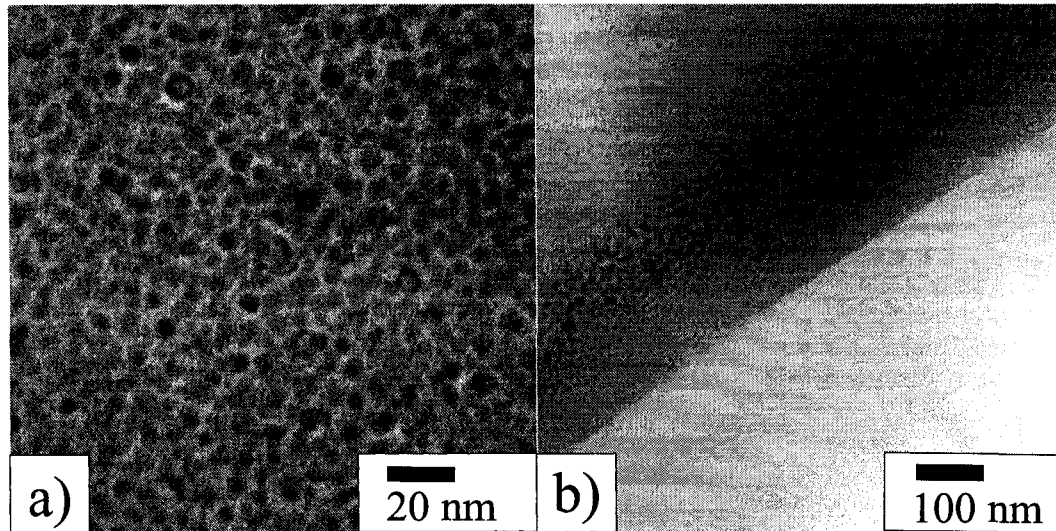


Figure 4.4: TEM micrographs of Fe nanoclusters fabricated by implanting 150 kV Fe ions into SiO₂. a) plan view and b) cross-sectional images of as-implanted specimen.

30 nm diameter particles are found 80 to 120 nm below the original surface and 5 to 35 nm above it. The diffraction patterns from the cross-sectional, annealed specimens from the c series were all found to match that of bcc iron.

The final series that will be discussed is the series implanted with 150 kV iron ions (d series, Figure 4.4). Increasing the energy of the ions was expected to increase the depth of penetration as well as the thickness of the implanted layer. A cross-sectional view of the as-implanted sample from this series (Figure 4.4b) shows that the implanted iron is found at depths ranging from 40 to 140 nm so the implanted layer is both thicker and deeper than for the 80 kV sample. The particles are mainly 4 to 6 nm in diameter with some as large as 8 nm. The cross-sectional sample reveals that there are smaller particles found near the edges of the layer, especially at the top edge.

4.2 Patterning results

A representative SEM image of a mask is shown in Figure 4.5 before implantation. The masked substrates were implanted with 80 kV Fe⁺ to fluences of either 1.5×10^{17} ions/cm² or 5×10^{16} ions/cm². Scanning electron microscopy (SEM) images of a representative

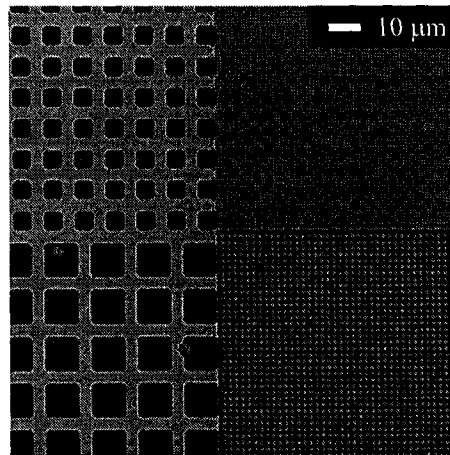


Figure 4.5: Mo mask (760 ± 10 nm thick) on SiO_2 before implantation.

mask before and after implantation are shown in Figure 4.6. Mask sputtering tends to clean the bottoms of holes in the mask that were incompletely etched before implantation. The overall structure of the mask, however, remains intact. This ion-cleaning effect is illustrated in Figure 4.6, where there is relatively little residual material in the mask holes.

An optical microscope image of a patterned sample after removal of the mask (Figure 4.7) shows that the pattern has been effectively transferred. Areas that were covered by the mask remain transparent while the unmasked areas show increased reflectivity due to the implanted iron. Examination of the implanted specimen under an optical microscope shows that even the $0.5 \mu\text{m}$ structures are well preserved in the implanted SiO_2 wafer. One interesting item worth noting is, the Fe implanted areas are recessed with respect to the unimplanted substrate by between 16 and 89 nm, as measured using a profilometer. All of the masks tested resulted in effective pattern transfer, however, the Mo masks were found to be less susceptible to oxidation as compared to the other metals tested (Cr and Cu) and was determined to be the preferred masking material for this application.

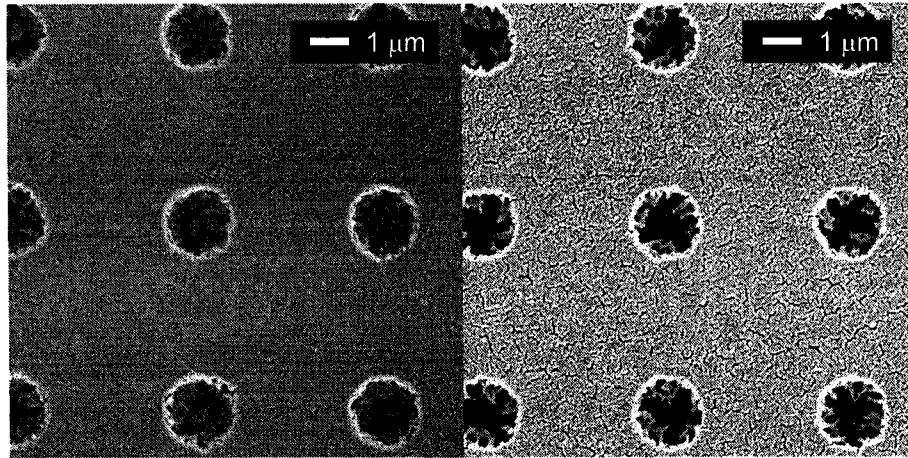


Figure 4.6: A 380-nm-thick Mo mask on SiO₂ before (left) and after (right) implantation with 80 kV Fe⁺ ions to a fluence of 5×10^{16} ions/cm². The hole-bottoms contain residual material, which is partially removed by the implantation process.

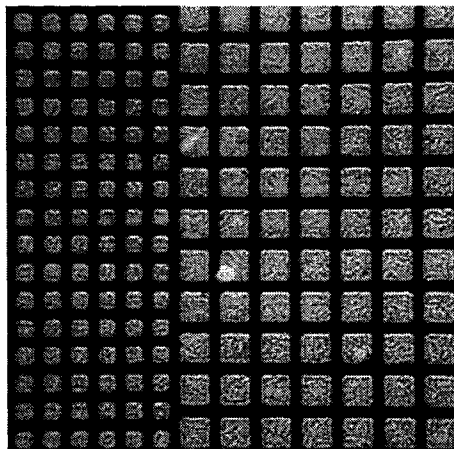


Figure 4.7: Optical microscope picture of patterned implanted sample after removing the Mo mask (Fe implanted SiO₂). Implanted areas appear lighter in this image.

4.3 Optical properties

The reflection, transmission and absorption of the nanocomposite specimens were characterized using fiber optic spectrometers. The transmission and reflection spectra were recorded separately and then the internal absorption was obtained from the results. For each transmission or reflection measurement, corresponding reference and dark spectra were also recorded without disturbing the position of the optical fibers. For transmission measurements, the reference measurement was taken with no sample (i.e., through air), which is assumed to have a transmission coefficient of 1. Alternately, a bare SiO₂ wafer could be used. The samples, however, were thinned down to approximately 200 μm and the choice of reference was determined to have no discernible effect on the results. A broadband mirror (Newport 10D10AL.2 UV Enhanced Aluminum mirror) for which the reflectivity as a function of wavelength was known was used as a reference for the reflectivity measurements.

The integration time was optimized for each of the sample and reference spectra. Separate dark spectra were recorded for each integration time to account for detector noise. The transmission coefficient T for a given wavelength λ was found using the following expression

$$T = \frac{(\text{Sample}_{int1} - \text{Dark}_{int1})/t_{int1}}{(\text{Reference}_{int2} - \text{Dark}_{int2})/t_{int2}} \quad (4.1)$$

where t_{int} is the integration time. The same expression was used to find the reflection coefficient except that a small correction was made to account for the reference mirror not being 100% reflective (the reflectivity ranged from 85 to 92% depending on wavelength).

As a wave travels through a material, its intensity I is exponentially attenuated with distance x :

$$I = I_0 e^{-\alpha x} \quad (4.2)$$

where I_0 is the interface and α is the absorption coefficient. The internal absorption $A = \alpha x$ was determined using the expression $A = -\log(T/(1 - R))$ (no units). To obtain the absorption coefficient α the absorption must be divided by the thickness of the nanocrystal layer.

Figure 4.8 shows the transmission, reflection and absorption measurement results for the iron nanocomposites. The SiO₂ host is virtually transparent (transmits 100% of the

light, reflects little) so no correction for the host material was made to these data. In general, the samples are most transmissive at long wavelengths. Also, the absorption is lower at 800 nm than it is for the visible spectrum. The 80 kV as-implanted specimens, both coated and uncoated, are less transmissive and also more absorptive than the annealed samples from their respective groups (ignoring sample c3, which was cloudy in appearance and thought to be compromised). The transmission and absorption from the annealed samples are comparable, however, even though the particle sizes change significantly depending on the annealing temperature. The main difference between the annealed vs. the as implanted samples is that the iron is distributed over a thicker area after annealing (i.e., the iron is less densely packed), which could improve transmission. For spherical nanocrystals, effective medium approximations for the optical properties scale with the volume fraction of particles but do not depend on the actual particle sizes [18]. Annealing may also promote development of a thin oxide shell which could also affect the optical properties.

For the 150 kV specimen, the transmission and absorption results are almost independent of the annealing treatment. The particles are already distributed over a wider thickness band so any changes in the local density of iron should not be as dramatic as for the 80 kV samples. The reflection spectra for this series, unlike the 80 kV implanted specimens, show minima at around 450 nm and maxima around 900 nm. The oscillations in the reflection spectra are caused by interference in the SiO₂ layer between the sample surface and the top of the nanocrystal layer, which is located deeper below the surface as compared to the 80 kV specimen. The reflection spectra for the coated 80 kV samples show similar oscillations with minima at around 400 and 800 nm, which would be expected for the 200 nm SiO₂ coating (destructive interference for increasing index of refraction occurs when the thickness is an integer multiple of $\lambda/4$). The thickness of the coating, however, is not perfectly uniform over the entire area of the sample so the peaks and troughs of the oscillations do not necessarily occur at the same wavelengths, even for the same specimen measured at a different location.

At the wavelength at which dynamic measurements were performed (800 nm), the 80 keV as-implanted nanocomposite was found to be 48% transmissive and 28% reflective. The remaining 24% of the input intensity was absorbed by the nanocrystals. Assum-

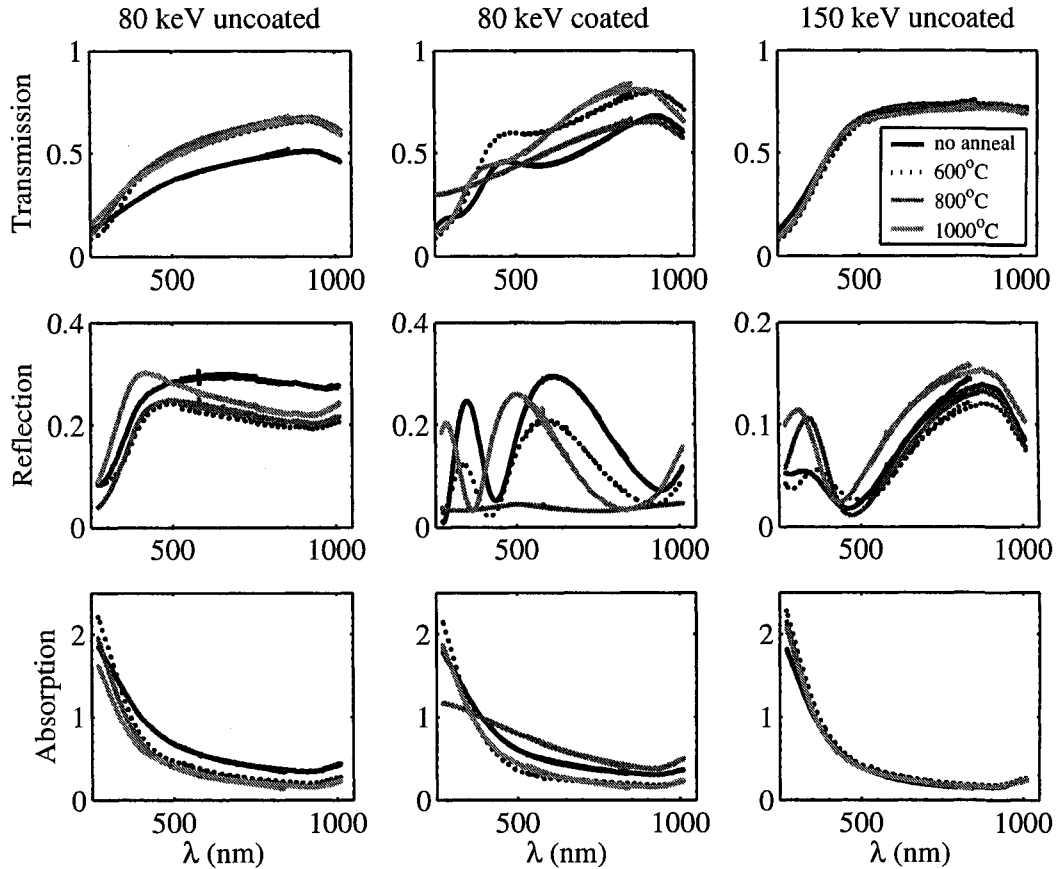


Figure 4.8: Transmission, reflection and absorption of iron nanocomposite specimens.

ing a thickness of 62 ± 2 nm, which was measured from cross-sectional TEM micrographs, this corresponds to an absorption coefficient of $6.5 \pm 0.3 \mu\text{m}^{-1}$. The sample annealed at 600°C is 63% transmissive and 20% reflective. The remaining 17% was absorbed, corresponding to an absorption coefficient of $3.2 \pm 0.5 \mu\text{m}^{-1}$. The absorption coefficient for bulk iron is around $80 \mu\text{m}^{-1}$ at 532 nm and $60 \mu\text{m}^{-1}$ at 800 nm so the nanocrystals are an order of magnitude less absorptive than their bulk counterpart. Yttrium iron garnet (YIG) films, which are often used for magneto-optical applications, have absorption coefficients as low as $3 \times 10^{-6} \mu\text{m}^{-1}$ in the near infrared (1.3-5.5 μm wavelengths), and as high as $4 \times 10^{-3} \mu\text{m}^{-1}$ at 800 nm [99]. The nanocomposites are at least three orders of magnitude more absorptive.

4.4 Hysteresis measurements

Hysteresis curves for the nanocomposites were measured magneto-optically in both the in-plane and out-of-plane configurations. Each hysteresis loop represents an average of 10 to 20 runs, which were obtained over the course of 10 to 15 minutes. Due to some problems with the stability of the laser power supply the drift in the laser intensity was not insignificant but since the drift frequency was lower than the repetition rate of the runs it was possible to correct for this problem. Both smooth and linear drift corrections were used to account for any low frequency drift in the laser intensity; the corrected data were quite similar so only the best curves are shown for each case. Curves that were measured in transmission were also corrected for the Faraday rotation due to the SiO₂ host. To reduce the effects of the SiO₂ substrate on the measurement, the samples were polished from the backside, reducing their thicknesses from 1 mm to around 200 μm. Sample thicknesses, which were measured using a calibrated optical microscope, are summarized in Table 4.2. The thicknesses were measured near each of the corners of the samples and the standard deviation of these measurements was taken as the uncertainty. It is estimated that the applied magnetic field is parallel to the sample face within 1 or 2 degrees for the in-plane configuration (uncertainty in measuring azimuthal angle on sample holder). For the out-of-plane arrangement, the applied magnetic field is within 1 or 2 degrees from perpendicular in the azimuthal direction and within 5 degrees in the polar direction.

The in-plane hysteresis loop for the Fe implanted SiO₂ (80 kV, as-implanted) sample is shown in Figure 4.9 as measured using both a vibrating sample magnetometer (VSM) and the Faraday set-up (beam incident at approximately 22°). For the Faraday curves, the solid line represents the mean of a number of runs and the shaded region shows the standard deviation between runs after drift correction. The measurements were carried out at room temperature for the same implanted specimen (u1m). The curves are similar in appearance with coercivities of 0.6 kA/m (8 Oe) and 1.0±0.4 kA/m (13±5 Oe), which agree within error. The VSM measurements are made over a period of several hours whereas the Faraday measurements represent an average of 10 or 20 curves obtained over the course of approximately 10 to 15 minutes. The sample contains a range of particle sizes, some of which will be superparamagnetic and others that remain blocked at room temperature. This range of particles contributed to the rounded hysteresis loops observed

4.4. HYSTERESIS MEASUREMENTS

Sample	Thickness (μm)
st	1000 ± 1
s	193 ± 20
u1	205 ± 5
u2	227 ± 35
u3	191 ± 33
u4	213 ± 47
c1	176 ± 35
c2	176 ± 12
c3	201 ± 22
c4	207 ± 18
d1	207 ± 22
d2	223 ± 9
d3	198 ± 34
d4	180 ± 17

Table 4.2: Sample thicknesses as determined by the difference in focus points for the top and bottom surfaces of the substrate using a calibrated optical microscope. Samples “s” and “st” are unimplanted SiO_2 .

and may also explain why the coercivity measured with the Faraday set-up is slightly higher than that obtained with the VSM. Although the coercivity is around 0.8 kA/m (10 Oe), the approach to saturation is gradual and a field of several hundred Oersteds is necessary to attain saturation. This particular sample was measured using the VSM in order to cross-check the magneto-optical measurements. A few of the other samples were also measured with this instrument, however, the magnetic signal was smaller and it was difficult to obtain good signal-to-noise.

The in-plane hysteresis loops for the Fe implanted SiO_2 80 kV series are shown in Figure 4.10. Table 4.3 summarizes the in-plane coercivities for these samples as well as for the other two sets. The in-plane coercivity for the as-implanted sample (u1) measured here, which is $1.8 \pm 0.2 \text{ kA/m}$ ($22 \pm 2 \text{ Oe}$), is larger than both the magneto-optical and the VSM coercivities shown in Figure 4.9. This sample (u1) and the other (u1m) were implanted on two separate occasions at Oak Ridge National Laboratory so the discrepancy between these measurements may be due to slight differences in the implantation conditions. Samples u1m and u1p were from the first set of implantations, while the others

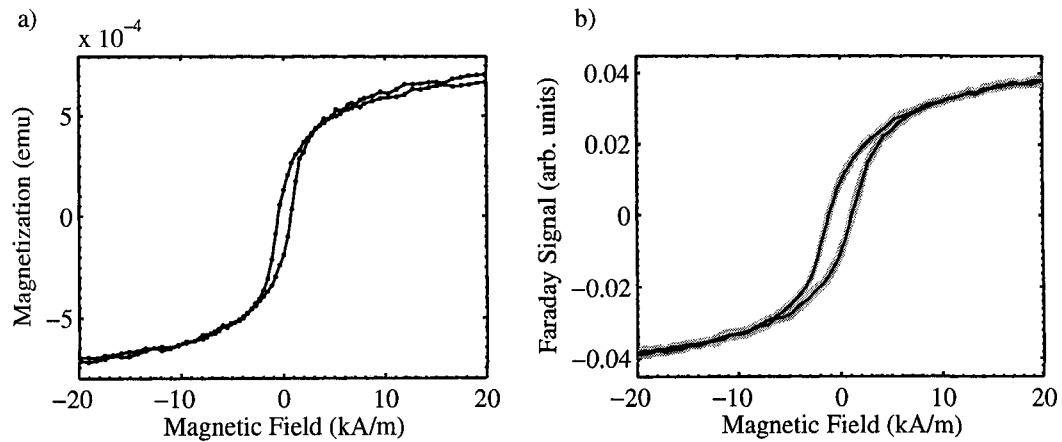


Figure 4.9: Magnetic hysteresis curve for the 80 kV Fe implanted SiO_2 sample before annealing (u1m) obtained at room temperature using a vibrating sample magnetometer (left) and through Faraday rotation (right). The shaded area represents one standard deviation about the mean of the measured Faraday rotation. The magnetic field was applied parallel to the sample surface.

listed in Table 4.3 were implanted in the second run. The coercivities measured from the patterned sample and from u1m all agree within error. In general, the coercivities increase with annealing temperature, a trend that corresponds to the increasing particle sizes observed in the TEM images.

The curve from the sample annealed at 1000°C (u4) shows a different shape as compared to the others. It is made up of a ferromagnetic hysteresis curve similar to the other samples in this series as well as a secondary signal that looks paramagnetic and saturates at a field of around 400 kA/m (5 kOe). This secondary signal may be related to small, superparamagnetic particles in the sample, however, with the trend of increasing particle sizes with temperature it would be surprising if there were more small particles in this sample as compared to the others. Another possibility is that annealing at this temperature results in particles that are coated with a thick oxide layer. This interpretation is supported by a study on discontinuous sputter-deposited iron/ ZrO_2 multilayers that showed that annealing resulted in increasing amounts of iron being found in an oxidized state at thin film interfaces [100].

Figures 4.11 shows the in-plane hysteresis curves that were measured from the coated 80 kV samples. The curves for the as-implanted specimen and for the specimen annealed

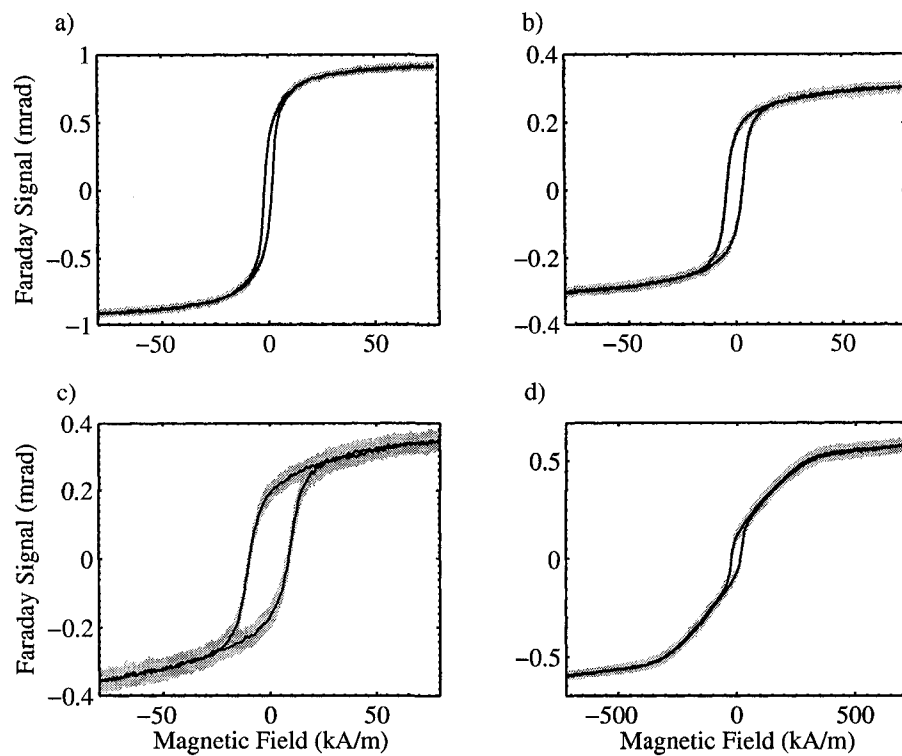


Figure 4.10: In-plane magnetic hysteresis curves for the u series measured in transmission. The panels show curves for the a) as-implanted sample, and samples annealed at b) 600°C, c) 800°C, and d) 1000°C.

Sample	Temp (°C)	Transmission	Reflection	Notes
		H_c (kA/m)	H_c (kA/m)	
u1	NA	1.8±0.2	2.0±0.4	
u2	600	3.7±0.5	3.7±0.5	
u3	800	9±1	9.9±0.8	
u4	1000	19±4	21±2	
u1m	NA	1.0±0.4	-	u1 with mirrors
u1p10	NA	0.9±0.5	-	u1 pattern, 10 μm squares
u1p5	NA	1.0±0.4	-	u1 pattern, 5 μm squares
u1b	NA	0.8±0.5	-	u1 pattern, bulk area
c1	NA	1.5±0.2	1.7±0.6	
c2	600	4.9±0.6	5.4±0.5	
c3	800	8±48	-	surface cloudy, no signal
c4	1000	40±40	40±40	large uncertainty
d1	NA	0±32	0.2±4.9	
d2	600	3±6	2±3	odd shaped curve
d3	800	2.8±0.8	9±1	
d4	1000	5±1	12±1	

Table 4.3: Table of coercivities H_c and corresponding errors ΔH_c for Fe implanted SiO_2 obtained from in-plane Faraday hysteresis measurements (see Table 4.1 for definition of sample names, except for the last few, which are defined in the “Notes” column). The errors are based on the width of the shaded standard deviation area on the hysteresis plots. The patterned sample and the bulk sample with the mirrors were both measured with the time-resolved magneto-optical Kerr effect setup. The bulk sample with mirrors (u1m) is the same sample that was measured using the Vibrating Sample Magnetometer, which yielded a coercivity of 0.6 kA/m (8 Oe).

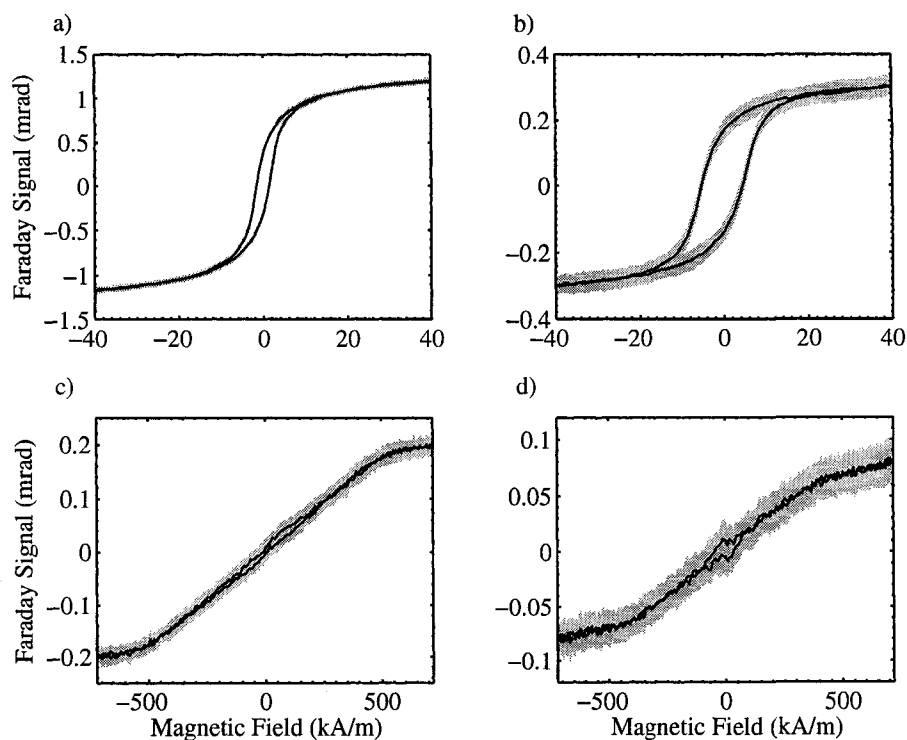


Figure 4.11: In-plane magnetic hysteresis curves for the c series measured in transmission. The panels show curves for the a) as-implanted sample, and samples annealed at b) 600°C, c) 800°C, and d) 1000°C.

at 600°C are quite similar in appearance to their uncoated counterparts. The coercivities agree within error for the as-implanted sample, which is not unexpected as the coating process should not affect the magnetic properties. For the 600°C samples the coercivities were similar but the value for the coated specimen was found to be slightly larger as compared to the uncoated specimen -4.9 ± 0.6 kA/m (61 ± 7 Oe) as compared to 3.7 ± 0.5 kA/m (46 ± 6 Oe). In the TEM micrographs, particle sizes range up to 25 nm for the coated sample but the largest particles observed in the uncoated sample were only 20 nm in diameter, which could explain the observed difference in coercivities.

For the samples annealed at 1000°C, the curves were found to be predominantly paramagnetic in shape with a field of approximately 480 kA/m (6 kOe) required to reach saturation. Both the coated and uncoated samples are similar in shape with a small ferromagnetic component superimposed on the otherwise linear curve. The Faraday rotation

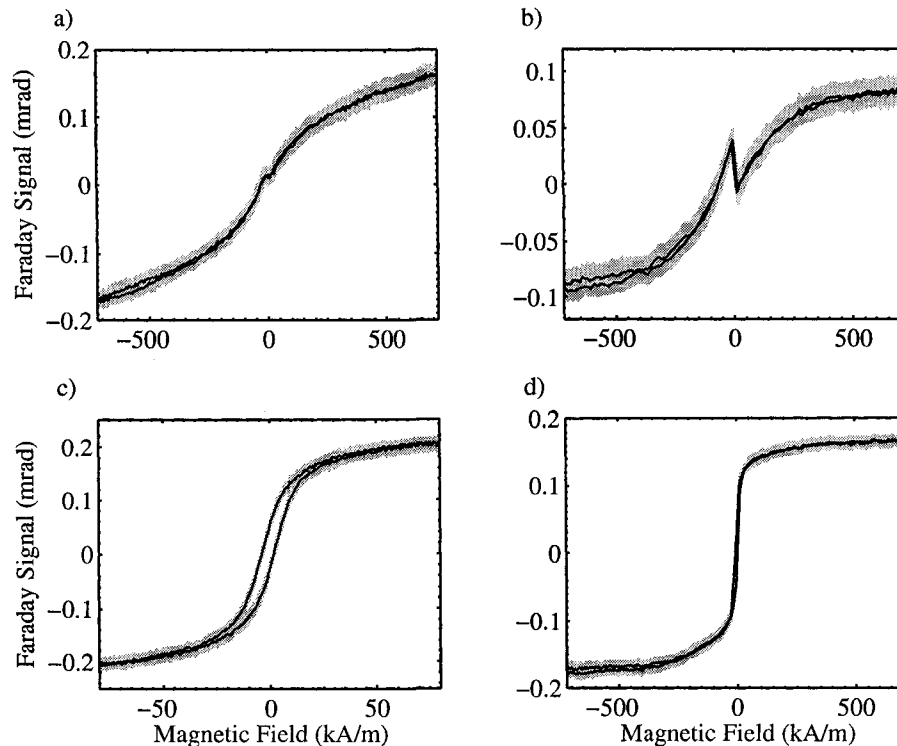


Figure 4.12: In-plane magnetic hysteresis curves for the d series measured in transmission. The panels show curves for the a) as-implanted sample, and samples annealed at b) 600°C, c) 800°C, and d) 1000°C.

(signal-to-noise) for the coated sample, however, was smaller (lower). The results for the coated sample annealed at 800°C this particular sample are thought to be questionable.

Figure 4.12 shows the in-plane hysteresis curves for the d series as measured in transmission. The as-implanted specimen has no coercivity within the error of the measurement, indicating that the implanted iron is superparamagnetic at room temperature. The particles for this sample, as measured from TEM images, were mainly 4 to 6 nm with all particles found being 8 nm or smaller. In Chapter 1 the relaxation time for an 8 nm diameter iron sphere was estimated to be 146 μs , which is much faster than the observation time. As with the other samples, the annealed specimens generally show an increase in coercivity with annealing temperature. This is true for the samples annealed at 800°C and 1000°C. The hysteresis curve for the sample annealed at 600°C, however, shows no coercivity and has an inverted “kink” at zero field that is not observed for any other sample.

Figure 4.13 shows the hysteresis curves for the d series as measured in reflection. Signal amplitudes are in units of mrad for Faraday curves, unnormalized intensities (mV) for reflection. Comparing Figure 4.13b and Figure 4.12b, the magnitude of the negative-sloped “kink” is larger in measured in reflection, which suggests that it may originate from particles closest to the implanted surface. The negative slope coupled with the difference in magnitude between reflection and transmission could indicate that there are two separate contributions to the magneto-optical signal and that one results in negative rotation while the other causes positive rotation as a function of magnetization. The in-plane hysteresis curves were measured in reflection for all of the samples, which yielded similar curve shapes for most of the other samples (no usable signal was obtained from sample c3).^{*} The coercivities were found to be the same, with the exception of samples d3 and d4, which displayed higher coercivities in reflection.

Hysteresis curves were also measured in the out-of-plane configuration. With these measurements, an additional source of uncertainty was present, related to the use of mirrors to direct the beam along the direction of the applied field. The signal measured from the mirrors alone is shown in Figure 4.14. The mirrors were mounted on the pole pieces of the magnet and as the field is increased, the pole pieces are attracted to one another. The small motion (not visible to the eye) results in the beam hitting slightly different parts of the mirrors, which leads to the curved signal shown in Figure 4.14. This signal is always even as a function of magnetic field but the amplitude varies depending on the exact arrangement of the mirrors, the beam, and the sample and can be negative or positive. For samples exhibiting a large Faraday signal this mechanical noise is not significant, however, for lower-signal samples its signature can be observed. The curves were corrected for the contribution of the SiO₂ but it was not possible to correct for the mechanical noise. A better mounting system for the mirrors could eliminate this problem.

The out-of-plane hysteresis loops for the u series are shown in Figure 4.15. There are three curves shown in each panel - the topmost curve corresponds to the best estimate for the corrected hysteresis curve, while the other curves show the outer ranges of possible curves based on the uncertainty in the correction for the SiO₂ host. All of the hysteresis curves for this series are close to linear in shape. No coercivity is observed within the

^{*}Reflection hysteresis measurements shown here were performed by J. Sorge.

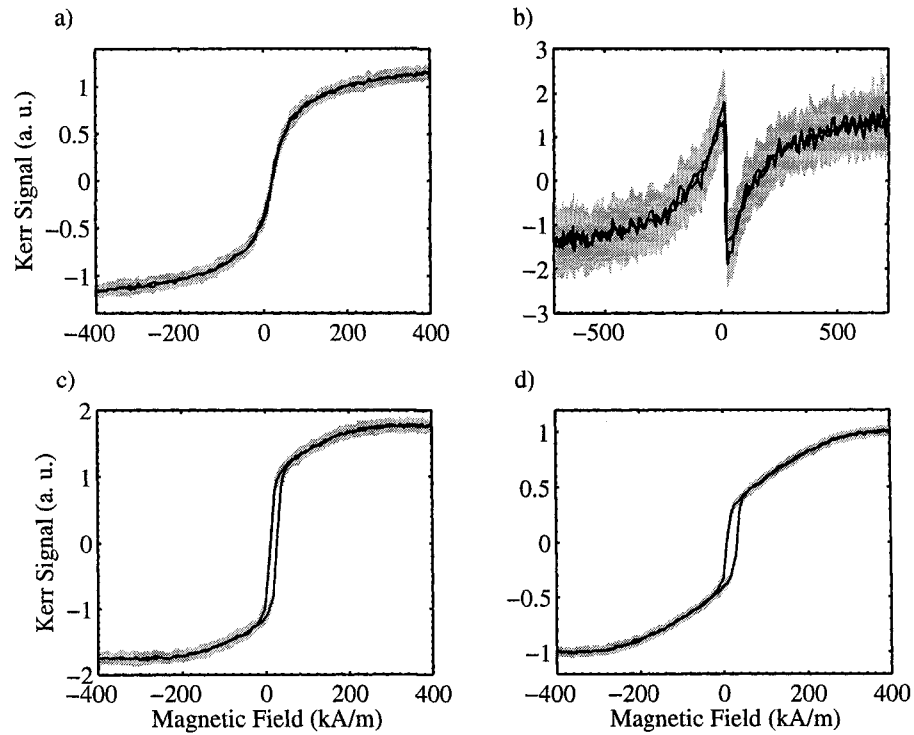


Figure 4.13: In-plane magnetic hysteresis curves for the d series measured in reflection. The panels show curves for the a) as-implanted sample, and samples annealed at b) 600°C, c) 800°C, and d) 1000°C.

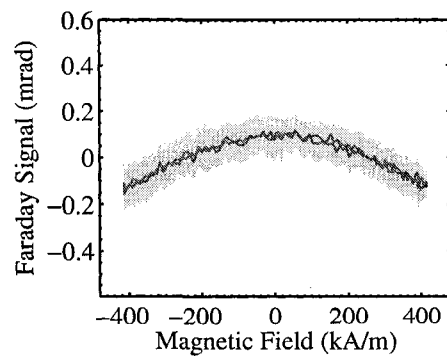


Figure 4.14: Example of a typical background signal (no sample) in measuring the out-of-plane magnetic hysteresis curves.

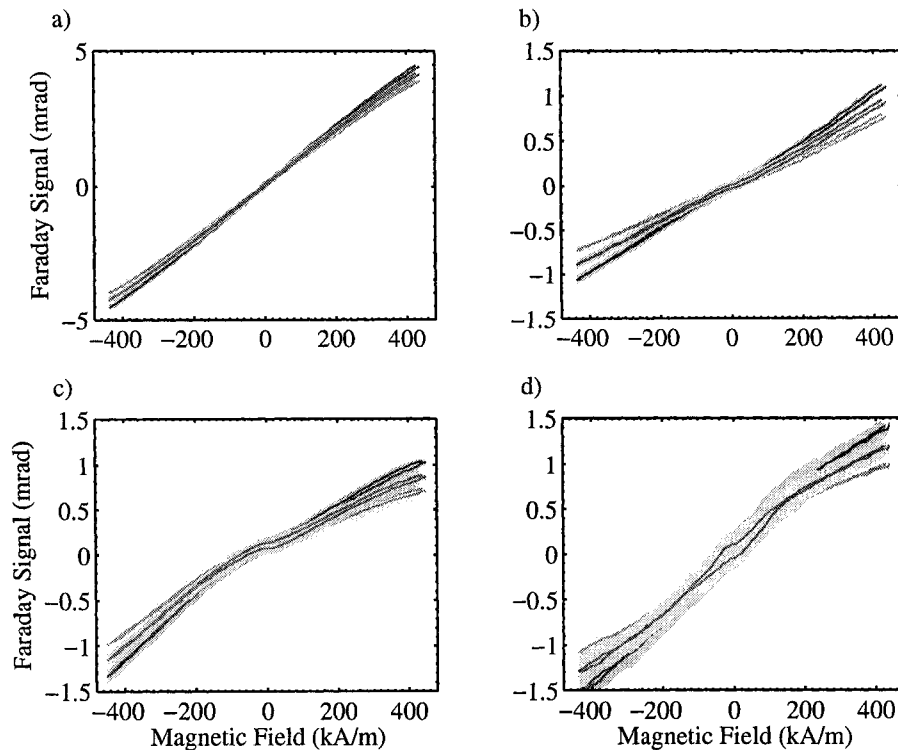


Figure 4.15: Out-of-plane magnetic hysteresis curves for the u series measured in transmission. The panels show curves for the a) as-implanted sample, and samples annealed at b) 600°C, c) 800°C, and d) 1000°C. Curves are shown that have been normalized by the measured intensity as well as plus or minus the uncertainty in this value.

resolution of the measurements, although the samples annealed at 800 and 1000°C look as if they might possess some coercivity. The maximum magnetic field (480 kA/m or 6 kOe) is not sufficient to saturate any of the samples. These curves are significantly different as compared to the in-plane curves, indicating that strong demagnetizing fields originating from the thin, dense layers of nanoclusters in these samples results in an induced in-plane anisotropy. The Faraday signal from the as-implanted sample from this series is significantly larger than for the annealed samples, a phenomenon that will be discussed later in this chapter.

The out-of-plane hysteresis loops for the coated samples (c series) are shown in Figure 4.16. The Faraday signal for the as-implanted sample is almost identical to that of its uncoated counterpart, both in magnitude and shape. The other hysteresis curves for

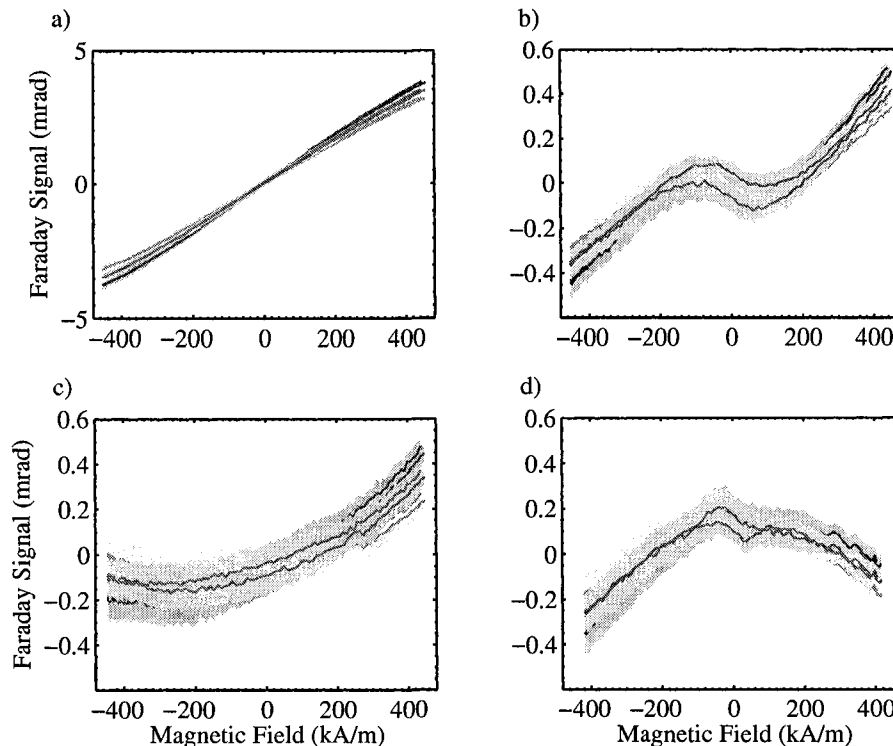


Figure 4.16: Out-of-plane magnetic hysteresis curves for the c series measured in transmission. The panels show curves for the a) as-implanted sample, and samples annealed at b) 600°C, c) 800°C, and d) 1000°C.

this series, however, are approximately a factor of ten or more smaller in magnitude. The signal-to-noise for the sample annealed at 600°C is better than for the other annealed samples, which have signals that are comparable both in shape and in magnitude to the mechanical noise (Figure 4.14). Sample c2 also has a non-zero coercivity; however, the coercive and linear parts of the curve have opposite slopes. The linear rotation is consistent with that for the uncoated sample u2, although it is slightly smaller.

The out-of-plane hysteresis loops for the samples implanted at 150 kV (d series) are shown in Figure 4.17.[†] Keeping in mind that the slopes at high magnetic fields that are even in magnetic field ($\propto H^2$) are probably related to the mechanical noise discussed ear-

[†]It is interesting to note that the out-of-plane magneto-optical signal for this whole series (d) is opposite in sign to the Faraday rotation in SiO₂ as compared to samples from the other series (u and c) where the rotation has the same sign as the host material. The longitudinal signal (in-plane curves) has the same sign as the other samples. This is thought to be related to the thicknesses of the SiO₂ above the nanocrystal layer and the thickness of the nanocrystal layer itself.

lier, these curves all show a linear slope between saturation fields with no measurable coercivity. The as-implanted and 600°C annealed samples start to approach saturation at around 320 kA/m (4 kOe), while the samples annealed at higher temperatures show signs that they are saturated at fields closer to 80 kA/m (1 kOe). This suggests that the inter-particle interactions are stronger for the first two (d1 & d2) than for the second two samples (d3 & d4). The magneto-optical signal is small for samples d1, d3, and d4 but larger for sample d2. The lower magneto-optical signal for the first sample could indicate that some of the iron occurs as isolated atoms in a solid solution, which would not necessarily contribute to the magneto-optical signal for the sample and would also be difficult to identify in TEM micrographs. The in-plane and out-of-plane signals for this sample are actually quite similar so the shape of the out-of-plane loop is more likely a reflection of strong superparamagnetism rather than strong interactions in this case. Neglecting the “kink” in the in-plane curve for sample d2, the same can be said for this sample. Looking at the higher temperature annealed samples, their out-of-plane hysteresis curves are also similar to their in-plane curves indicating that the dipolar interactions for this whole series are smaller than for series u or c. This is to be expected as the same amount of iron was implanted, however, when it was implanted at 150 keV it was distributed over more than 100 nm as compared to only 62 nm at 80 keV.

The shapes of the in-plane magnetic hysteresis curves are consistent with the shape of the Stoner Wohlfarth prediction for a collection of non-interacting, randomly oriented, magnetic nanoparticles (with the exception of the kink for sample d2). The out-of-plane curves, however, demonstrate that the inter-particle interactions are significant for some of the implanted sample (u series, as-implanted c and d samples). For these samples, the interactions are strong enough to result in an overall in-plane anisotropy. Numerical simulations of hysteresis curves for samples containing collections of nanoparticles have shown that dipolar interactions result in hysteresis curves that are similar in appearance to those predicted through non-interacting models. The interactions, however, are necessary to explain the suppression of coercivity for out-of-plane curves and also were found to result in an increase in the field required to saturate the sample and a reduction of the overall coercivity as compared to non-interacting model predictions [8].

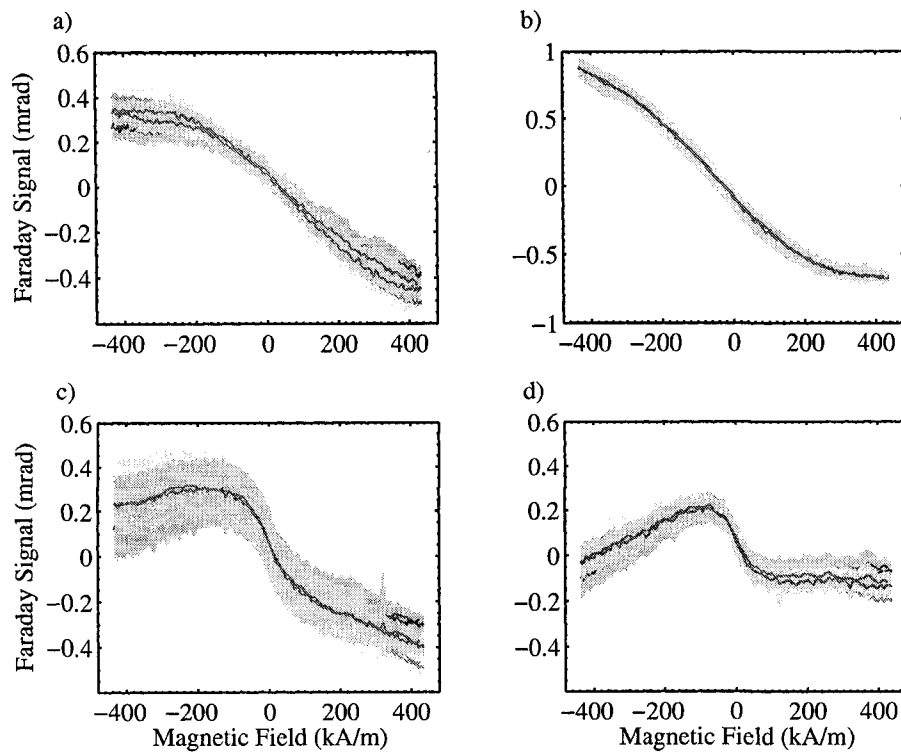


Figure 4.17: Out-of-plane magnetic hysteresis curves for the d series measured in transmission. The panels show curves for the a) as-implanted sample, and samples annealed at b) 600°C, c) 800°C, and d) 1000°C.

4.4.1 Large Faraday rotation

The Faraday signal from the 80 keV as-implanted sample is quite large, especially considering that the Fe nanoparticles are concentrated in a layer that is only 62 ± 2 nm thick. The Verdet constant measured for this material (out-of-plane configuration) is 7.9 ± 0.5 deg/A (6.3 ± 0.4 deg/cm/Oe) measured at a wavelength of 532 nm (compare to Table 1.1). Part of the uncertainty of this measurement is attributed to statistical fluctuations in the rotation measurement and there is also some uncertainty in defining the exact thickness of the implanted layer. For an applied field of 480 kA/m (6 kOe), a Faraday rotation θ_F (as compared to zero field) of $3.8 \pm 0.2 \times 10^3$ deg/mm was observed. This value was cross-checked against a direct measurement of the Faraday rotation as illustrated in Figure 3.6 with excellent agreement.

To put this into context, the Faraday rotation for yttrium iron garnet (YIG) of 24 deg/mm has been measured at a wavelength of 1200 nm [36]. A Verdet constant for a EuS-doped TiO₂ film of 0.19 deg/A (0.15 deg/cm/Oe) is reported at $\lambda = 700$ nm, a value that is larger by two orders of magnitude than other rare-earth containing glasses [37]. A YIG indicator film exhibits linear behavior with a Verdet constant of 38 deg/A (30 deg/cm/Oe) for $\lambda = 633$ nm between applied magnetic fields of ± 28 kA/m (± 350 Oe) (saturation field) [101]. This yields a total Faraday rotation of 1.05×10^3 deg/mm. Other reports of giant Faraday rotation include epitaxial Ce_xY_{3-x}Fe₅O₁₂ films with $V = 17.7$ deg/A (14.1 deg/cm/Oe) and $\theta_F = 1.78 \times 10^3$ deg/mm at $\lambda = 633$ nm at room temperature [38]. Dilute magnetic semiconductors can exhibit very large Faraday rotation at low temperatures. A maximum Verdet constant of 35 deg/A (28 deg/cm/Oe) was measured for Zn_{1-x}Fe_xSe at 4.5 K for at $\lambda = 443$ nm, a class of Fe based dilute magnetic semiconductors that exhibit particularly large Faraday rotation [102].

Recently, a high Faraday rotation was reported for γ -Fe₂O₃ (maghemite) thin films: 4×10^3 deg/mm and 2.5×10^3 deg/mm at wavelengths of 645 and 1550 nm, respectively [103]. These values are comparable to the Faraday rotation measured for the Fe nanocomposite. In that study, they attributed the large rotation in the visible/near IR to the Fe²⁺ oxidation state of the iron. A study of Faraday and Kerr rotation in Fe/Al₂O₃ co-sputtered films [49,104] also suggested that the Fe²⁺ oxidation state was responsible for the magneto-optical signal in the visible and near infrared for these films. Although the

samples contained iron nanocrystals, the oxidized state was thought to occur at the interface between the Fe particles and the oxide host. For the implanted nanocomposites it is possible that the nanoparticles have a thin oxide coating that similarly contributes to the magneto-optical signal.

One study of the Faraday and Kerr effect of Fe clusters in amorphous Al_2O_3 created by cosputtering [49,104] suggests that Faraday measurements are sensitive to thin oxide shells around metallic Fe nanoclusters. Another independent study of Fe nanoparticles in Al_2O_3 , created by pulsed laser deposition, also reports evidence for a surface layer of Fe oxide [50]. Based on analysis of the magnetic moment per unit atom, the presence of a surface oxide layer of 0.4 nm thickness for 2.7 nm diameter α -Fe clusters is deduced. This oxide shell is assumed to be antiferromagnetic or paramagnetic. It is possible that monolayer oxide shells surround the ion implanted Fe nanoclusters examined here.

It is important to note that for some technological applications, for example for Faraday isolators, absorption is also an important consideration. The Faraday rotation θ_F for bulk Fe, for example, is 3.5×10^4 deg/mm for a wavelength of 633 nm but its figure of merit ($Q = V/\alpha$, where α is the absorption coefficient) is only 0.1 deg/dB compared to 267 deg/dB reported for a bismuth-substituted gadolinium iron garnet at $\lambda = 1300$ nm, which is considered to be quite good [19]. The absorption coefficient of this implanted sample at a wavelength of 532 nm (29% reflective and 39% transmissive) is $10.1 \pm 0.7 \mu\text{m}^{-1}$, which yields a figure of merit of 0.043 ± 0.005 deg/dB. Both the absorption and the Faraday rotation are similar to those reported for γ - Fe_2O_3 (maghemite) [103]. Although the nanocomposite film possesses high absorption, the reflectivity is much higher than for yttrium iron garnet, which could be a useful property for some applications.

The Faraday rotation observed for the annealed samples from the u series is significantly smaller than that observed for the as-implanted sample (u1). The rotation is reduced by roughly a factor of five, as observed in Figure 4.15. There are several factors that might contribute to this decrease. The first is that some of the iron, especially at the highest temperatures, may diffuse out of the sample thereby decreasing the overall magnetic moment of the specimen [98]. The Kerr rotation has been found to decrease as a function of decreasing volume fraction for granular Fe/SiO₂ films containing similar sized iron particles below the percolation threshold [16]. Another mechanism for the reduction of

the magnetic moment per atom is through oxidation at the Fe/SiO₂ interfaces. Annealing of discontinuous sputter-deposited iron/ZrO₂ multilayers has been shown to result in oxidized iron at thin film interfaces [100]. Prior to annealing, 20% of the iron atoms were in the Fe²⁺ oxidation state, a figure that increased to 40% after annealing at 600°C for 20 minutes under vacuum. An x-ray diffraction pattern consistent with bcc iron was reported, suggesting that these surface oxides were amorphous and thus indistinguishable from the SiO₂ host in the diffraction pattern. This latter mechanism would reduce the magnetic moment but not necessarily the overall magneto-optical rotation as large Faraday rotations have been reported for iron oxides [103].

In addition to the reduction of the magnetic moment per atom, it is also possible that the annealed samples exhibit a smaller Kerr rotation per magnetic moment. Kerr rotation has been observed to decrease as a function of particle size for the same volume fraction, which was attributed to the decrease in surface-to-volume ratio [16]. The coercivity and particle sizes were observed to increase on annealing for the u series so this effect would result in a reduction in magneto-optical signal on annealing as well.

Chapter 5

Magneto-dynamics of Fe implanted

SiO₂

The dynamics of the magnetic nanocomposites were examined experimentally using time-resolved scanning Kerr effect microscopy (TR-SKEM). The as-implanted Fe/SiO₂ (80 keV, 1.5×10^{17} ions/cm²) specimen was focused on initially because of its large Faraday rotation and also because the hysteresis curves suggest that the dipolar interactions in this sample are significant. The dynamics of bulk and patterned specimens were probed first using an electronic pulser. A follow-up experiment was designed employing photoconductive switches to improve the temporal resolution and further explore the dynamics of both the as-implanted sample and a specimen that was annealed at 600°C for an hour in a reducing atmosphere (Ar+10%H₂). Finally, the TR-SKEM setup was modified to work at low temperatures and the AC susceptibility was measured as a function of temperature.

5.1 Results, 10 ns pulse

Magneto-dynamic measurements were made on an Fe implanted SiO₂ nanocomposite (80 keV, 1.5×10^{17} ions/cm², no annealing). Using the pulser/electrical delay line com-

combination discussed in Section 3.4, the magnetic signal from both patterned and unpatterned implanted samples was measured in response to in-plane and out-of-plane magnetic fields.* With the 50 V pulser, the current pulse has a rise time of approximately 250 ps and an amplitude of 1 Amp. As discussed in Section 3.4.2, the field directly above the wire is 48 kA/m (600 Oe) in-plane and between the wires the field is 32 kA/m (400 Oe) out-of-plane. The nanocomposite specimens were mounted with the implanted face as close as possible to the transmission wires. The separation between the nanoparticles and the wire was estimated to be on the order of 10 μm using a calibrated optical microscope, which suggests that the magnetic fields experienced by the nanocomposite were closer to 12 kA/m (150 Oe) in-plane directly over the wire and 15 kA/m (190 Oe) out-of-plane mid-way between the wires.

For transient magnetic fields applied in the plane of the sample, the magnetic response of the nanocomposite is relatively slow (Fig. 5.1). The x (in-plane, perpendicular to the direction of current flow) magnetization component changes almost linearly from the time that the magnetic pulse begins until it ends (10 ns). Once the transient pulse ends, the magnetization of the sample slowly relaxes back to its original state over the course of more than 80 ns. Data taken with bias fields ranging from 0 to 16 kA/m (200 Oe) show the same behavior. The responses of both the patterned and unpatterned implanted samples were found to be spatially quite uniform.

Focusing on the data starting from the end of the transient pulse, a two-exponential function $f(t) = A_1 \exp(-(t - t_2)/\tau_1) + A_2 \exp(-(t - t_2)/\tau_2)$, where t_2 is the end-time of the pulse, was found to provide a good fit. This function was chosen because the slow relaxation of the magnetization back to equilibrium appears exponential in nature but is not well described by a single time constant.† A standard nonlinear least-squares fitting method was used (Gauss-Newton method), yielding the values for the two time constants shown in Table 5.1. The fit parameters for both the data taken at zero bias field and a bias field of 16 kA/m (200 Oe) agree within error; both exhibit a relatively fast relaxation of $\tau_1 = 10$ ns and a slower time constant of $\tau_2 \approx 300$ ns. The time constant τ_1 found for

*Data presented in this section were taken in collaboration with A. Krichevsky.

†The function $f(t) = A[\exp(-(t - t_2)/\tau_1) + \exp(-(t - t_2)/\tau_2)]$ also provides a good fit but there is no theoretical justification for assuming that the amplitudes of the two exponentials should be the same. A stretched exponential fit $f(t) = A \exp(-((t - t_2)/\tau_1)^\beta)$ was also tried, however, the fit was generally not as good, especially for fits to simulation results that show a very fast initial response followed by a much slower relaxation.

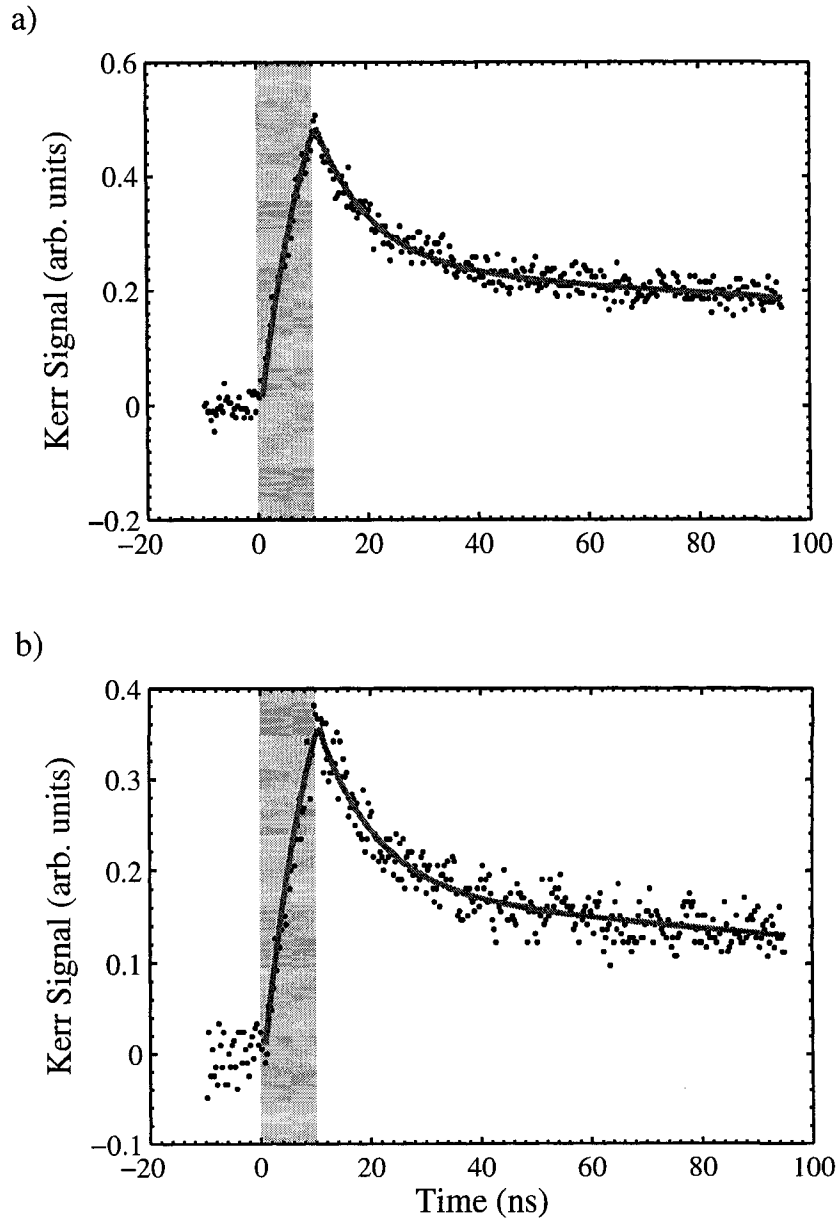


Figure 5.1: Response of the Fe implanted SiO_2 to an in-plane magnetic field generated by a 10 ns current pulse (shaded region) in the presence of a) zero in-plane bias field, and b) a 20 kA/m (250 Oe) in-plane field. Solid lines show a double-exponential fit to data after the falling edge of the pulse.

Bias Field (kA/m)	τ_1 (ns)	τ_2 (ns)	A_1/A_2
0	10 ± 2	280 ± 80	0.88 ± 0.09
16	10 ± 2	300 ± 100	1.0 ± 0.1

Table 5.1: Exponential fit parameters for in-plane temporal data. Uncertainties represent a 95% confidence interval on the fitting parameters.

the falling edge also provides a good match to the data taken during the pulse when substituted into the exponential function $f(t) = (A_1 + A_2)(1 - \exp(-(t - t_1)/\tau_1))/(1 - \exp(-(t_2 - t_1)/\tau_1))$, where t_1 is the pulse-on time. The duration of the pulse is short compared to τ_2 so adding the second exponential term makes no difference in the quality of the fit to the data during the pulse.

When a transient magnetic pulse is applied in the out-of-plane (plane perpendicular) direction a much different response is observed (Fig. 5.2). The out-of-plane response was measured first using the 50 V pulser/electrical delay line combination (not shown) and then using the 10 V pulser/optical delay line combination (pulse amplitude approximately 3.2 kA/m (40 Oe)). In both cases the response followed the profile of the current pulse and was sufficiently fast that the measurement was limited by the rise time of the pulser. In addition, the shape of the response was unaffected by the presence or absence of an in-plane bias field of up to approximately 80 kA/m (1 kOe). A spatially uniform response was observed within the resolution limits of the system for both the patterned and bulk implanted samples. Measurements of the patterned implanted samples confirm that the signal is spatially correlated with the implanted areas and that there is no signal from the host material.

In this particular semi-transparent sample (44% transmissive, 28% reflective at a wavelength of 800 nm), the magneto-optical response is a combination of Kerr and Faraday effects for reflected and transmitted light, respectively. In order to demonstrate the effect of Faraday rotation as compared to a Kerr polarization shift, the beam was focused on the layer of implanted nanoparticles on top of an aluminum micro-mirror and the signal was compared to the magneto-optical response at a point adjacent to the mirror. Figure 5.2 shows a comparison of these responses in the absence of any bias magnetic field.

The black curve represents the (mostly) Kerr signal from the bare sample. The magneto-

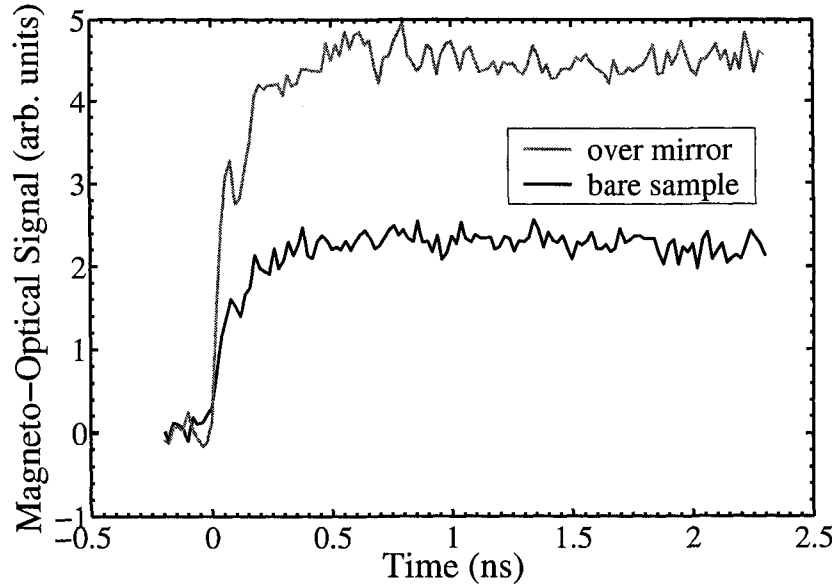


Figure 5.2: Kerr versus Faraday magneto-optical response of the implanted nanoparticles. The stronger Faraday signal (gray line) has opposite polarity as compared to the Kerr signal and has been inverted to allow for direct comparison.

optical signal measured from the mirror region was approximately double that reflected from only the nanoparticles and the rotation was also opposite in direction. The polarized beam incident on the mirrors travels twice through the nanocomposite, resulting in double the Faraday rotation, but the overall rotation is also reduced by the Kerr effect originating from the portion of the beam that is reflected directly by the nanocomposite. Henceforth these effects will be referred to simply as magneto-optical effects, since the same underlying physics applies whether the light is reflected or transmitted. The relative magnitudes and signs of these signals will be discussed further in Section 5.4.

The magneto-optical response recorded over the mirrors is very similar in shape (within the noise level) as compared to the signal measured from the bare nanocomposite. For both samples, the time it takes to reach the maximum change in magnetization is around 150 ps (measured from 10 to 90% of the maximum amplitude). The apparent rise time of the pulse has been degraded by a reflection from impedance mismatched short indium wires connecting the lithographic line to a 50 Ohm coaxial cable. Faster temporal resolution is necessary to determine the exact response time of the sample.

To summarize the results of the dynamic measurements so far, the iron nanocrystals respond very slowly to both the leading and falling edges of an in-plane transient magnetic field pulse. In contrast, they show a very fast response to an out-of-plane magnetic field. For both the in-plane and out-of-plane measurements, the responses were found to be independent of the magnitude of an in-plane bias field. For the in-plane measurements, the maximum field applied was 16 kA/m (200 Oe); for the out-of-plane measurements higher fields of more than 80 kA/m were applied.

5.2 Photoconductive switch data

The temporal resolution of the TR-SKEM set-up used to study the switching dynamics of the nanoparticles in the previous section is limited by the rise time of the current pulse, which is around 150 ps. The temporal resolution can be improved by an order of magnitude by employing photoconductive switches [22,40], which were used to explore the ultrafast out-of-plane response in more detail. Modifications to the TR-SKEM set-up made to accommodate the switches were discussed in Section 3.4.1 and measurement results will be presented here.

5.2.1 Dynamic response of the specimens

The polar Kerr response, which is sensitive to the out-of-plane component of the magnetization, was measured in response to a transient magnetic pulse applied in the out-of-plane (plane perpendicular) direction. Figure 5.3 shows the response of the as-implanted (80 kV implanted) iron nanocomposite in the presence of in-plane bias fields ranging from 0 to 135 kA/m (1700 Oe). Overall, the temporal response mirrors the expected pulse shape with small oscillations superimposed. For all bias fields the response time is faster than 150 ps, in agreement with previous measurements [56], but slower than the anticipated rise time of the pulse. The sharp drop in the Kerr signal observed at 270 ps was determined to be an actual feature of the current pulse. It corresponds to the negative reflection of the current pulse from the impedance mismatch at the end of the leads, which is verified by the fact that shortening the leads results in this feature occurring sooner in time.

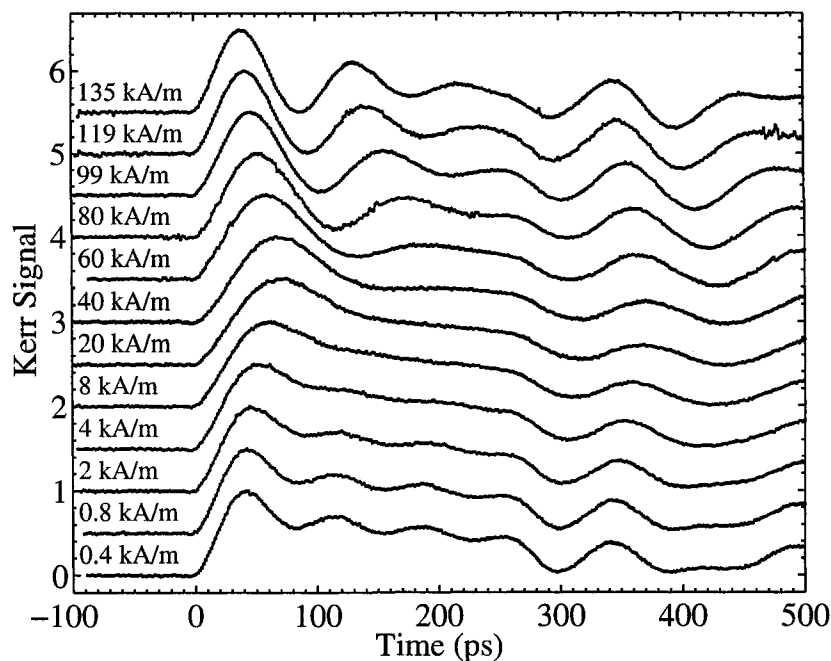


Figure 5.3: Response of the unannealed Fe implanted SiO_2 to an out-of-plane magnetic field generated by a photoconductive switch for in-plane bias fields ranging from 0.4 to 135 kA/m (5 to 1700 Oe).

The 10/90% drop time (time between 10% and 90% of amplitude change) on the reflection is the same as the 10/90% rise time for a given bias field, which confirms that the rise time is limited by the material rather than by the rise time of the current pulse. Any dispersive loss of the highest frequencies of the pulse are above the highest response frequency of the material.

Several trends with bias field can be observed in these data. The rise time of the response varies smoothly from fast to slow and then fast again as the field is increased from 0 to 135 kA/m (1700 Oe). The data taken at bias fields of 8 and 40 kA/m (100 to 500 Oe) have slower rise times and also exhibit fewer oscillations as a function of time. Zero and high-field measurements, on the other hand, show oscillations superimposed on the profile of the pulse. The high bias field data show the strongest oscillations with the first peak being the largest.

Figure 5.4 shows temporal Kerr measurements made on the 80 kV implanted specimen that was annealed at 600°C . These data are remarkably similar to the measurements made

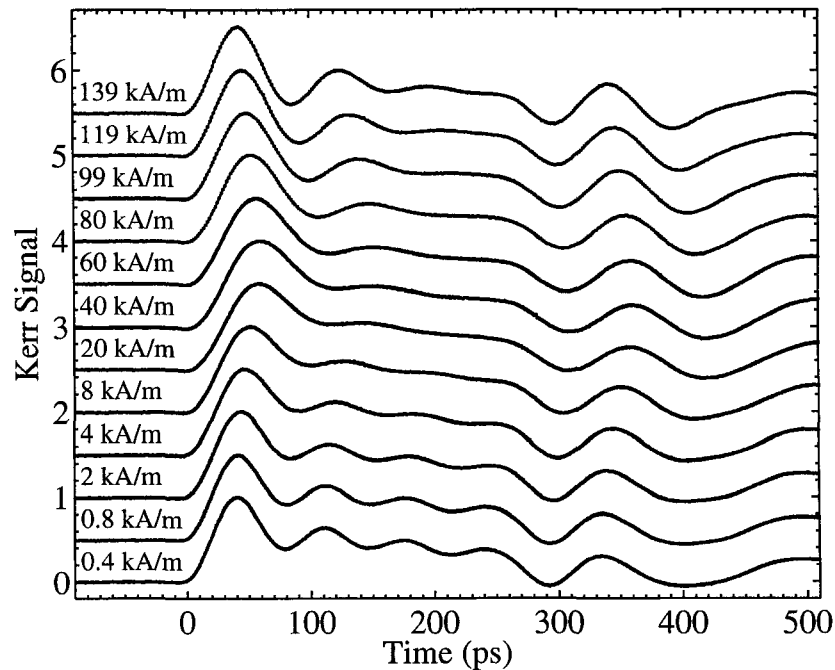


Figure 5.4: Response of the Fe implanted SiO_2 specimen that was annealed at 600°C to an out-of-plane magnetic field generated by a photoconductive switch for in-plane bias fields ranging from 0.4 to 140 kA/m (5 to 1750 Oe).

on the as-implanted sample. They exhibit a similar rise-time trend and also show the suppression followed by the reappearance of oscillations as the bias field is increased from zero to 140 kA/m (1750 Oe). The high-field oscillations and the mid-field suppression of oscillations are both less pronounced than for the as-implanted nanocomposite. These data were re-measured using a dielectric material over the transmission wires to suppress the reflected current pulse (Figure 5.5).[†] The sharp drop at 270 ps is no longer visible, further confirming that it was caused by a reflection, and the change in the characteristics of the oscillations as a function of bias field are easier to observe.

5.2.2 Rise time trend

A method for determining the rise times of the data was developed by first finding a function that provides a good fit to the shape of rising edge of the response. Figure 5.6

[†]These data were taken by Xiaobin Zhu.

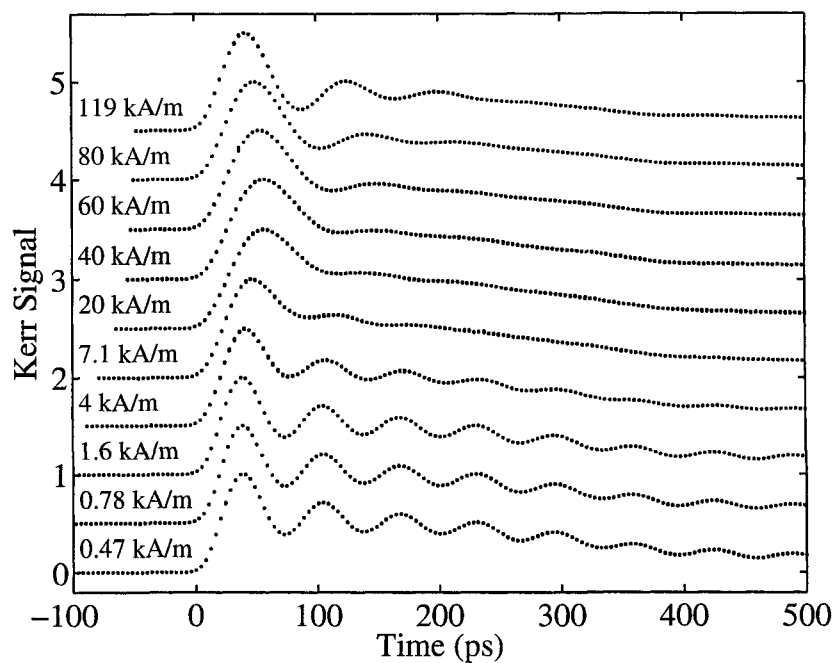


Figure 5.5: Response of the Fe implanted SiO_2 specimen that was annealed at 600°C to an out-of-plane magnetic field generated by a photoconductive switch where the reflected current pulse has been suppressed (measured by X. Zhu).

shows the results of fitting the rising edge of a representative dataset using a tanh function $f_t(t) = A(\tanh((t-t_{mid})/B)+1)/2$, a sum of 10 Chebyshev polynomials, and a shifted sine function with the formula $f_{ss}(t) = A \sin(\omega t + \phi) + f_o$, with a minimum value of f_o imposed. The fit parameters were then used to solve for the time difference between the 10 and 90% maximum amplitude points. The Chebyshev polynomial fit was carried out using a linear least-squares method and provides a reasonable fit. For the other functions, a standard nonlinear fitting method was used (Gauss-Newton method) to determine the best values for the parameters and the related uncertainty. The shifted sine function provides the best fit overall and was ultimately used to determine the rise times of the data. The uncertainty in rise time was found by propagating the error in the fit parameters using standard error propagation techniques [105]. A minimum uncertainty in rise time of $\sqrt{2}(0.8)$ ps was imposed, which is the uncertainty due to the minimum time step of the optical delay line. The rise time in this example was found to be 27 ± 1 ps using both the Chebyshev and the shifted sine fits. The rise time was also determined directly by taking the time at 10% and 90% of the maximum amplitude (minus the baseline) for comparison. It was difficult to extract the peak frequencies from Fourier transforms of these data as the response is not mono-frequency and the pulse shape is complicated and difficult to remove from the FFT. As a result, the resonance frequencies will not be shown.[§]

The rise time as a function of in-plane bias field has been determined for both the as-implanted and annealed specimens and is shown in Figure 5.7. For both samples there is a smooth increase in rise time up to 20 kA/m (250 Oe) for the as-implanted specimen and between 20 and 40 kA/m (250 and 500 Oe) for the annealed specimen. The rise time then increases in an almost linear manner as the bias field is increased up to 1700 Oe. The fastest rise time recorded was 26 ± 1 ps and the slowest was 44 ± 2 ps.[¶] The zero-field rise times were 27 ± 1 and 26 ± 1 ps for the as-implanted and annealed nanocomposites, respectively, which agree within error. The change in rise time with bias field is more

[§]From later measurements made by Xiaobin Zhu on the annealed specimen, it is possible to see a small peak in the FFT's of the low and high frequency data where there are coherent oscillations. For these measurements, a dielectric coating over the wires was used to help absorb reflections of the current pulse in the transmission wires. For the few datasets where it is possible to see this peak, the frequency predicted based on the rise time measurements is generally between 0.5 and 2.5 GHz higher than the peak.

[¶]Rise times as fast as 15 ps have been recorded for a Fe implanted yttrium stabilized zirconia (80 kV, 1.5×10^{17} ions/cm²) since these measurements were made, confirming that the rise times measured in this experiment are not limited by the rise time of the current pulse.

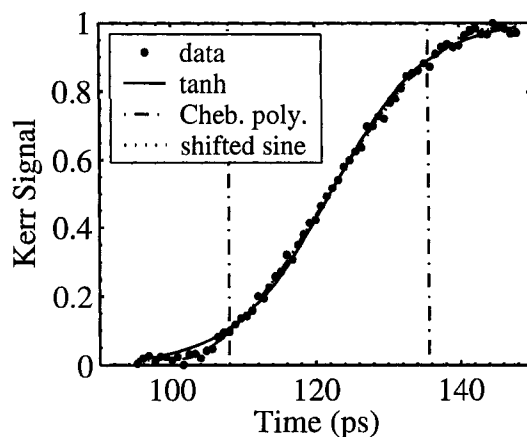


Figure 5.6: Figure demonstrating the proposed fit functions for determining rise times and a representative dataset.

dramatic for the as implanted specimen as compared to the annealed specimen. For this sample, the maximum rise time is slower and the rise time increases as a function of bias field in the high-field region faster than it does for the annealed specimen.

5.2.3 Variation of temporal response with position

To test the uniformity of the M_z response with position, a series of temporal scans were carried out at different positions between the wires. These temporal scans are shown in Figure 5.8 and the locations of each scan are illustrated in Figure 5.9. On the intensity images, the white areas are the reflective copper wire and the dark area is between the wires. The temporal scans were obtained at the central position (white circle) for each position of the piezo stage. Note that the reflective aluminum mirrors were actually less reflective than the copper wire in this image and the mirrors ended up being positioned mostly over the copper wire in this situation. The $10\ \mu\text{m}$ mirrors in the intensity image are located at the top and bottom right side. On the Kerr image (Figure 5.10) these areas show a stronger Kerr signal as compared to other areas of the image. When the central position is changed by more than a small amount and the scan range is kept constant, the stage will reach its limit on one edge of the scan. In the spatial scan this will result in having the values repeated at the limited edge.

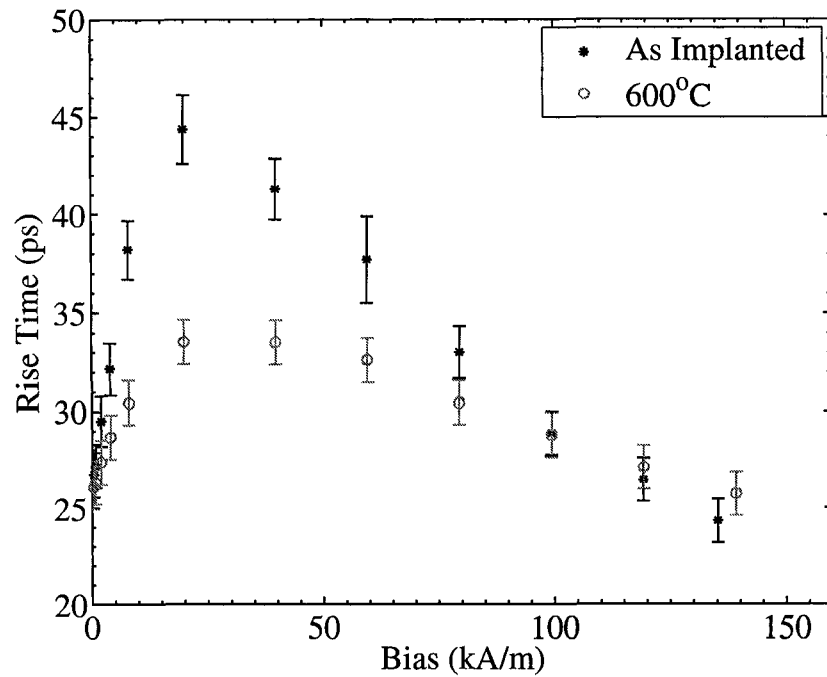


Figure 5.7: Rise time as a function of in-plane bias field for Fe implanted SiO_2 , both as-implanted and annealed specimens.

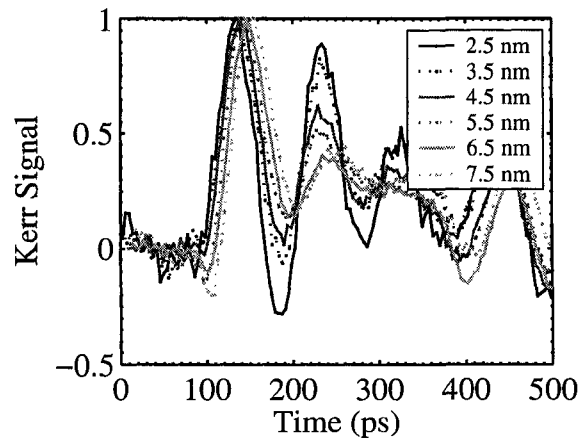


Figure 5.8: Temporal scans with different values of initial x placement on piezo stage (listed in legend). The location of the temporal scan for each placement are illustrated in Figure 5.9.

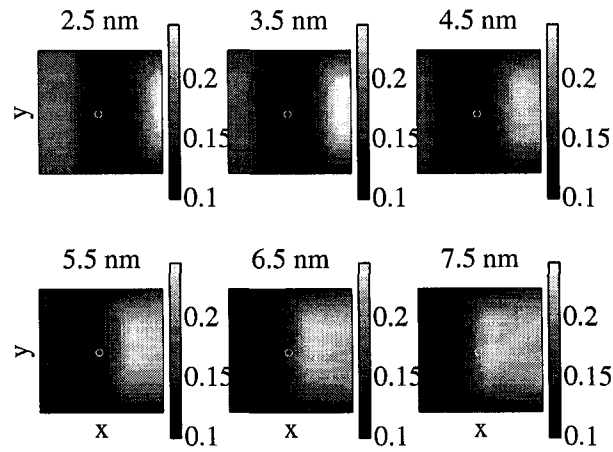


Figure 5.9: Spatial scan of intensity with different values of initial x placement on piezo stage (listed in title). The white circle (center) shows the location of the temporal scan for each placement. The bright areas in the image correspond to the copper wire. At the top and bottom of the copper wire in this image, there are darkened areas that correspond to the edges of aluminum mirrors on the nanocomposite. For some of these images the piezo stage has reached its scan limit in x , which results in repeating of the y scans for the edge areas.

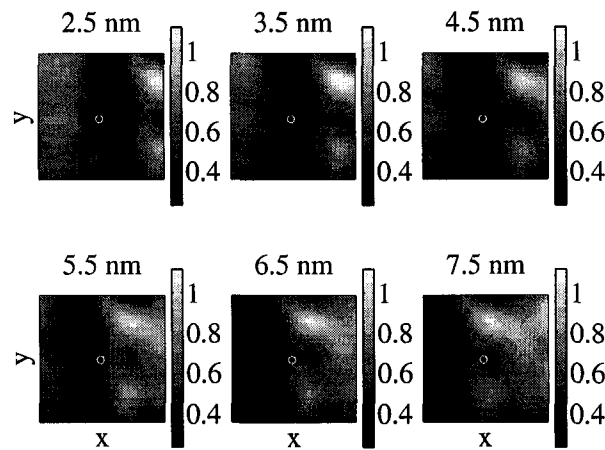


Figure 5.10: Spatial scan of Kerr signal with different values of initial x placement on piezo stage (listed in title). The white circle (center) shows the location of the temporal scan for each placement.

On examining the temporal scans, the rising edges of the responses can be seen to be almost identical in both shape and slope. The location of the peak, however, was found to shift in time as a function of position. The absolute position of the optical delay line was recorded using a sensitive rheostat so the time scale in Figure 5.8 is quite accurate: the error in recording resistivity is ± 0.001 Ohms, $dt/dR = 0.696715 \pm 0.000006$ ps/Ohm, so the error in time due to reading out the position of the rheostat is around 7×10^{-4} ps. The 20 ps shift in the time of the first peak is a real time shift that is brought about by a shift in the phase of the response, not a change in the pulse shape (the peak current as measured by the current probe was constant for all measurements indicating that alignment was optimized in all cases).

Midway between the wires the transient magnetic field should be entirely in the out-of-plane direction. Closer to the wires, the transient field gains an in-plane component in the $+x$ direction on one side, and in the $-x$ direction near the other wire. If the bias field is aligned precisely along the x -axis, this in-plane component of the transient field would be parallel to the bias field and would not have any effect on the resonance of the specimen. If, however, the field is not aligned along the x axis, there will be an in-plane component of the transient field that will influence the resonance. In the photoconductive switch experiments the static bias field was actually applied along the y axis for logistical reasons. It is believed, and will later be explored with simulations, that having an in-plane transient field applied perpendicular to the bias field should result in a phase change with position, which would explain both the variation in apparent rise time and the shift in the peak position.

5.3 AC Susceptibility as a function of temperature

Measurements of out-of plane AC magnetic susceptibility χ as a function of temperature were carried out using a modified version of the TR-SKEM system with a liquid helium cryostat.^{||} Instead of using a transmission wire to generate a transient field, a millimeter sized coil was used to generate a sinusoidally varying field with a frequency of 2.3 kHz. A waveform with the same frequency was also tied into the lock-in amplifier. The resulting

^{||}Measurements were carried out in collaboration with M. Roseman

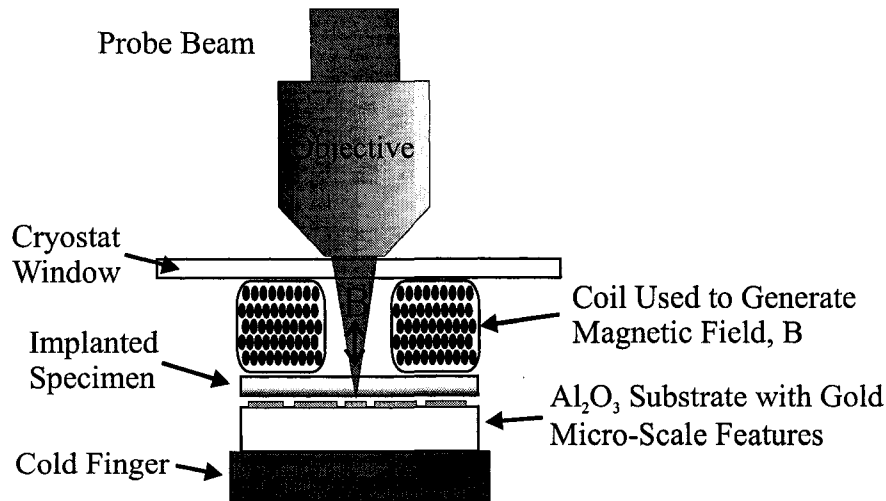


Figure 5.11: Diagram of the arrangement of the specimen and coil over a cold finger.

Kerr signal is then proportional to the AC susceptibility of the specimen. To convert to meaningful units the signal would have to be calibrated at a given temperature. Even without calibration, however, this setup provides a relative measure of the susceptibility as a function of temperature.

Figure 5.11 illustrates how the sample and magnet were positioned for these measurements. The coil was placed directly over the nanocrystal specimen, which was in turn placed over a patterned substrate. This apparatus was placed on top of a cold finger inside a cryostat. The probe beam is focused through the cryostat window and the nanocrystal specimen ($205 \pm 5 \mu\text{m}$ thick) onto the patterned substrate. The pattern was used to ensure that the beam is focused and that the measurements were made at the same physical location for all temperatures. Refocussing for every measurement was necessary to account for expansion and contraction of the cold finger on heating and cooling. Maintaining a constant $x - y$ position is important because the magnetic field generated by a coil will vary with position.

The coil used to generate the magnetic field for these experiments was constructed by winding a thin wire ($125 \mu\text{m}$ thick) around a template (a needle poked through two teflon cylinders). The coil was coated with epoxy and allowed to harden (Emerson & Cummings Stycast Epoxy 1267). Initial measurements were made down to liquid nitrogen temperature (went to around 80 K) with a coil that was approximately 1 mm thick, with an outer

diameter of 4.5 mm and an inner diameter of 0.8 mm (approximately 80 turns). A smaller, thinner coil was constructed for measurements down to liquid helium temperature (4 K): this coil had a 3.5 mm outer diameter, an 0.8 mm inner diameter and was $350 \pm 25 \mu\text{m}$ thick (approximately 12 turns). For the measurements, the amplitude of the sinusoidal driving current was selected such that the magnetic field measured 4 kA/m (50 Oe) peak-to-peak directly below the coil. For the larger coil, the RMS current was 165 mA (2.3 V RMS), while for the smaller current an RMS current of 410 mA (5.9 V RMS) was required.

Figure 5.12 shows the magneto-optical signal as a function of temperature for a Fe/SiO₂ nanocomposite (80 keV, 1.5×10^{17} ions/cm², as-implanted). The averages and standard deviations of the signal were taken over a mirrored area and non-mirrored area and both were normalized by the average intensity over the same area. The non-mirrored areas show a much stronger magneto-optical rotation but the mirrored areas are brighter and yield measurements with smaller uncertainties. The magneto-optical signal recorded here is proportional to the out-of-plane AC susceptibility.

These results indicate that there is very little change in χ between room temperature and 4 K. The out-of-plane hysteresis curve is similar to that of a paramagnetic material but a paramagnetic substance should exhibit a susceptibility proportional to $1/T$, which is not observed. The susceptibility may be slightly lower at low temperatures and slightly higher in magnitude approaching room temperature. The opposite trend has been observed for Fe/Al₂O₃ co-sputtered nanocomposites where a similar magneto-optical measure of the susceptibility showed a constant value below the blocking temperature and then a decrease in signal magnitude as a function of temperature above the blocking temperature [49,104]. A much flatter trend was obtained for the sample with the highest concentration, which was 85% by weight iron, which was attributed to the wide spread of particle sizes present in the sample, a trait that is shared with the nanocomposite examined here.

5.4 Effective medium approximation of magneto-optical rotation

When a material consists of a host with embedded particles that are small compared to the wavelength of incident light, the optical and magneto-optical properties can be described

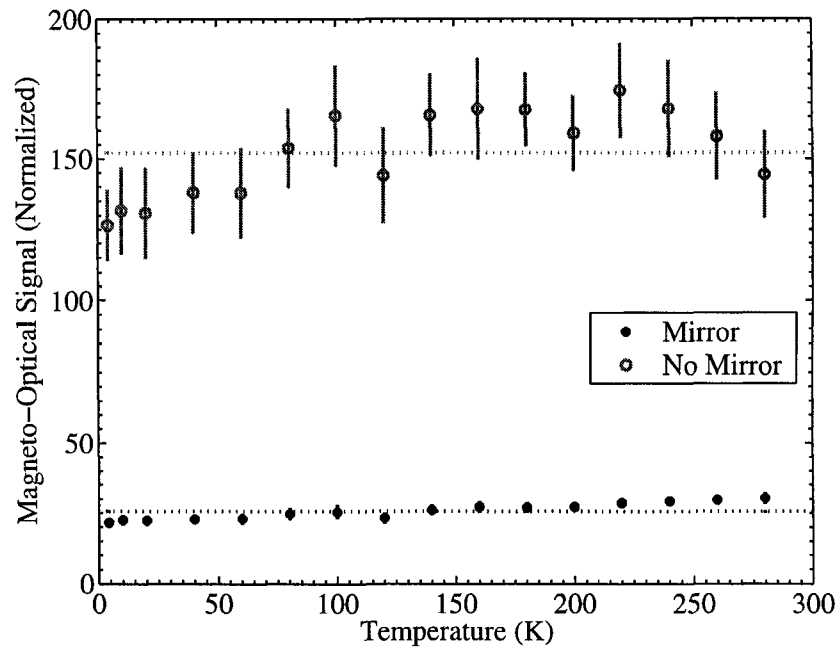


Figure 5.12: Intensity-normalized magneto-optical signal (proportional to AC susceptibility) as a function of temperature as measured from reflection from a mirror and from the nanocomposite (signal from the nanocomposite has been inverted). Dotted lines show the average signal over all temperatures.

in terms of effective material constants [18]. Effective medium approximations were used to estimate the index of refraction and the magneto-optical parameter for a SiO₂ host containing iron nanocrystals. These effective constants can then be used to calculate the expected Kerr or Faraday rotations for a given experimental configuration, which can then be compared to observations.

An order of magnitude estimation of the expected Faraday and Kerr rotation for the iron nanocomposite can first be made using the magneto-optical and optical constants for bulk Fe. In the limit of thin films ($d \ll \lambda/2\pi$ where d is the film thickness), the Kerr effect is thickness dependent [99]. According to Ref. [106], for a wavelength of 633 nm incident on a Fe thin film on Au, however, “thin” is less than 15 nm in practice, which is thinner than the nanocomposite. The expression for the polar Kerr rotation of a “thick” material is given by

$$\phi_K = -\Im \frac{\eta_o Q}{\eta_o^2 - 1} \quad (5.1)$$

where $Q = Q' + iQ''$ is the magneto-optical Voigt parameter (complex), and $\eta_o = n + ik$ is the complex index of refraction of the ferromagnetic film. These parameters are related to those in Equation 1.20 through the relations $Q = i\epsilon_2/\epsilon_1$ and $\eta_o = \epsilon_1^{1/2}$ (all parameters can be complex). For iron, these parameters are shown in Table 5.2. The Faraday rotation ϕ_F is

$$\phi_F = -\frac{\pi d}{\lambda} \Re(\eta_f Q) \quad (5.2)$$

where λ is the wavelength. A more careful treatment of the Kerr effect can be done following the method of Zak *et al.* [107]. This simple exercise, however, will give some insight into the expected signs and relative magnitudes of the two signals. The constants for iron and the expected magneto-optical rotation values can be found in Table 5.2. Using the parameters for bulk iron, the ratio of Faraday to Kerr rotation for a 62 nm thick film is found to be -3.2 and -4.8 for wavelengths of 532 and 800 nm, respectively, and the Faraday rotation is 8.42 mrad at 532 nm, which is 7.8×10^3 deg/mm, which is slightly larger than the measured value of $3.8 \pm 0.2 \times 10^3$ deg/mm.

A better estimate of the Faraday and Kerr rotation can be made by first using an effective medium approximation. For a composite material containing spherical nanoparticles, using the perturbative or Maxwell-Garnett approach, the effective dielectric constants are

5.4. EFFECTIVE MEDIUM APPROXIMATION

λ (nm)	η_o	ϵ_{xx}	γ	Q	ϕ_K (mrad)	ϕ_F (mrad)
532	2.65+3.34 <i>i</i>	-4.13+17.7 <i>i</i>	-0.258+0.330 <i>i</i>	0.0209+0.00969 <i>i</i>	2.64	-8.42
800	3.03+3.69 <i>i</i>	-4.44+22.4 <i>i</i>	0.00+1.27 <i>i</i>	0.0546-0.0108 <i>i</i>	10.4	-50.0

Table 5.2: Optical [108] and magneto-optical[109] parameters for bulk iron at wavelengths λ used in experiments.

[110]

$$\epsilon_{xx} = \epsilon_{yy} = \epsilon_{zz} = \epsilon_h + f(\epsilon_p - \epsilon_m)/[1 + (1 - f)(\epsilon_p - \epsilon_m)/(3\epsilon_m)] \quad (5.3)$$

$$\gamma = \gamma f/[1 + (1 - f)(\epsilon_p - \epsilon_m)/(3\epsilon_m)] \quad (5.4)$$

where f is the volume fraction of magnetic material, ϵ_p and ϵ_m are the dielectric constants for the particles and the host, respectively, ϵ_{ii} are the diagonal elements of the effective dielectric tensor, and $\pm i\hat{\gamma}$ occupy the off-diagonal xy and yx elements of the tensor (xy is positive, yx is negative). The parameter γ is related to the magneto-optical Voigt parameter Q through the relation $Q = \gamma/\epsilon_{xx}$.

In the self-consistent approximation, an alternate effective medium approach, the effective dielectric constants ϵ_e and γ_e can be found by solving [18,111,112]

$$\frac{(1 - f)(\epsilon_m - \epsilon_e)}{2\epsilon_e + \epsilon_m} + \frac{f(\epsilon_p - \epsilon_e)}{2\epsilon_e + \epsilon_p} = 0 \quad (5.5)$$

and [18]

$$\frac{(1 - f)(-\gamma_e)}{2\epsilon_e + \epsilon_m} + \frac{f(\gamma_p - \gamma_e)}{2\epsilon_e + \epsilon_p} = 0 \quad (5.6)$$

This approach has been found to describe experimental measurements made on iron nanoparticles with sizes of 5 nm and larger better than the perterbative approach [18].

Using the parameters for iron, the refractive index of SiO₂ ($\eta_m = 1.46$) and a volume fraction f of 0.40, the effective dielectric constants were determined and the Faraday and Kerr rotations were predicted for wavelengths of 800 and 532 nm (Table 5.3). The volume fraction of iron in the nanocomposite is not know precisely so the variation of the refractive index and the magneto-optical constant as a function of volume fraction was calculated using both methods (Figure 5.13). The magnitude of the Faraday rotation at a wavelength of 532 nm was calculated using the self-consistent values to be 6.9×10^3 deg/mm, which is slightly larger than the measured value for the as-implanted nanocomposite (at

5.4. EFFECTIVE MEDIUM APPROXIMATION

Method	λ (nm)	η	Q	ϕ_K (mrad)	ϕ_F (mrad)	ϕ_F/ϕ_K
Maxwell-	532	2.46+0.492i	0.0136+0.00763i	-1.75	-10.9	6.2
Garnett	800	2.49+0.395i	0.0372-0.00501i	5.98	-23.0	-3.8
Self-	532	2.03+1.09i	0.0102 + 0.0003i	-2.88	7.44	-2.6
Consistent	800	2.16+1.17i	0.0186 - 0.0131i	-9.61	-13.5	-1.4

Table 5.3: Values for the refractive index η , the magneto-optical Voigt parameter Q , and the Kerr and Faraday rotation, ϕ_K and ϕ_F , calculated using effective medium approximations.

incomplete saturation) of $3.8 \pm 0.2 \times 10^3$ deg/mm, but closer than the prediction made using the parameters for bulk iron.

The method of Zak *et. al.* [107] is a general approach for obtaining Kerr and Faraday rotation for arbitrary magnetization and incidence angles that is also capable of handling multilayers. This method was used, along with the values for η and Q found for the iron nanocomposite (62 nm thick) using the self-consistent approach (Figure 5.13), to calculate the expected rotation values for several experimental configurations. The in-plane hysteresis curves for the Fe/SiO₂ as-implanted sample (u1) were measured in both reflection and transmission. For s-polarized light ($\lambda = 532$ nm) incident at an angle of 22 degrees in the longitudinal configuration, the expected Kerr rotation is $\phi_{K_s} = -0.67$ mrad and $\phi_{F_s} = 1.5$ mrad with $\phi_{F_s}/\phi_{K_s} = -2.2$ for a volume fraction of 0.40. The variation of the Faraday and Kerr rotation as a function of volume fraction is shown in Figure 5.14a. Experimentally the Kerr rotation was larger in magnitude as compared to the Faraday rotation (although the Faraday *signal* was larger) by approximately a factor of 3, which is the reverse of the calculated ratio. Experimentally the rotations were opposite in sign, which is consistent with the prediction. The Faraday rotation at saturation was approximately 0.9 mrad, which is the same order of magnitude as the predicted value.

Measurements made using the TR-SKEM system were made on areas of the sample where the beam was reflected from the bare nanocomposite as well as from areas where a reflective mirror was present directly below the sample. In Section 5.1 the mirrors were made of aluminum, while in Section 5.3 the beam was reflected from gold. Using the self-consistent effective parameters in Table 5.14 for 800 nm, the Kerr rotation values expected for Fe/SiO₂ with and without an Al and Au underlayers ($\eta = 2.69 + 8.45i$ for aluminum and $\eta = 0.08 + 4.78i$ for gold [108]) were calculated for the polar configuration. For a

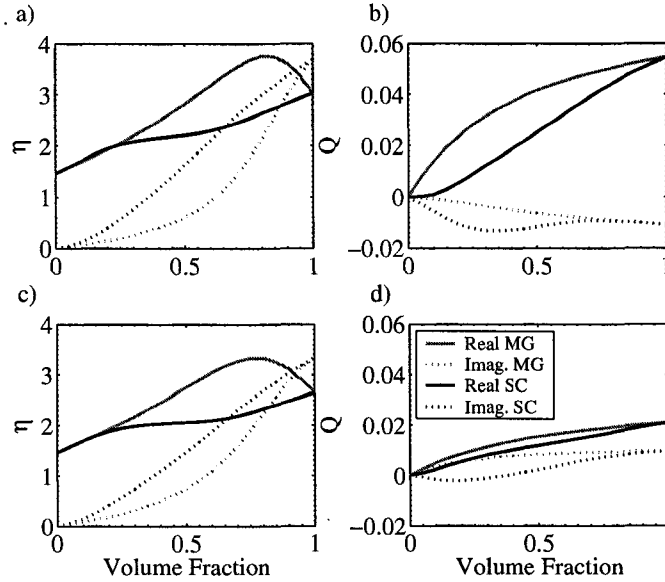


Figure 5.13: Effective medium approximation for the complex refractive indices and the magneto-optical Voigt parameter for Fe spheres in SiO_2 as a function of volume fraction of iron. Results of calculations made using both the perturbative or Maxwell-Garnet approach (MG) and the self-consistent approach (SC) are shown for wavelengths of 800 nm (a and b) and 532 nm (c and d).

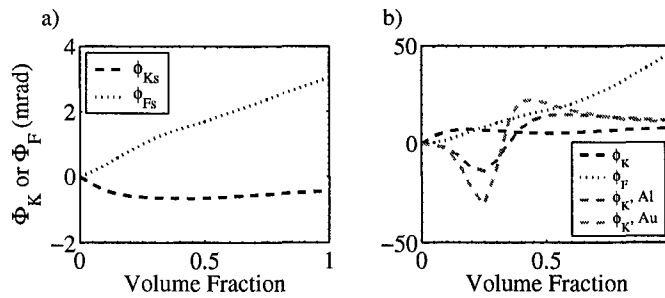


Figure 5.14: Kerr and Faraday rotation as a function of volume fraction of iron calculated using the parameters found using self-consistent approach for iron spheres in SiO_2 (shown in Figure 5.13). The rotation values are shown for a) the longitudinal configuration with an angle of incidence of 22° and a wavelength of 532 nm, and b) the polar configuration at normal incidence for a wavelength of 800 nm. In b), the predictions for the Kerr rotation from the bare nanocomposite as well as with an underlayer of Al and Au are shown.

volume fraction of 0.40, the ratio of mirrored to bare Kerr rotation for Al and Au mirrors were predicted to be 0.71 and 0.26, respectively. In both cases the sign of the Kerr rotation from the bare nanocomposite was the same as that from the mirrored areas.

These predictions are not consistent with experimental observations reported in Section 5.1 for aluminum mirrors or for the reflection from gold in Section 5.3. For the former, the signal over the mirrors is 4.5 a.u. as compared to -2.3 a.u. from the bare nanocomposite. After normalizing by the intensity, the ratio of rotation from the mirrored areas as compared to the bare was approximately -1.2 or -1.3. For the low temperature AC susceptibility measurements, this ratio was -0.17. The predicted ratios, however, vary considerably with volume fraction as shown in Figure 5.14b. The ratios of rotations for a volume fraction of 0.32 are actually much closer to the experimental observations both in magnitude and sign. The filling fraction for this sample was estimated to be 0.40, however, the estimation was very approximate so 0.32 is not an unrealistic value. Overall, the effective medium predictions are the same order of magnitude as the experimental observations but do not match exactly.

Chapter 6

Micromagnetics simulation results

Micromagnetic simulations are carried out using the Landau-Lifshitz Gilbert equation

$$\frac{d\vec{M}}{dt} = -\gamma\vec{M} \times \mu_0\vec{H}_{eff} + \frac{\alpha}{M_s}(\vec{M} \times \frac{d\vec{M}}{dt}) \quad (6.1)$$

where γ is the gyromagnetic field $\gamma = g|e|/(\mu_0 2m_e c)$. The spectroscopic splitting factor g is 2 for a free electron, e is the charge of an electron, m_e is the mass of an electron, and c is the speed of light, which yields a value of $\gamma = 1.76 \times 10^{11} \text{ Hz}\cdot\text{T}^{-1}$ ($1.76 \times 10^7 \text{ Hz}\cdot\text{Oe}^{-1}$). This value is often used for the 3d transition metals, which have g factors close to 2 (g varied for 4f ferromagnets) [71]. The dimensionless damping parameter α is around 0.008 for permalloy [21], and 0.0023 for iron [4]). The saturation magnetization M_s is $1.714 \times 10^6 \text{ A/m}$ (1714 emu/cm^3) for bulk iron [25]. The vector \vec{M} is the magnetization, t is time, and \vec{H}_{eff} is the effective magnetic field, which contains contributions from the external field, the demagnetization field, effective anisotropy fields, and exchange fields. A software package, the “LLG Micromagnetics Simulator” [25], was used.*

*Simulations were run on a Dell Workstation PWS450, Intel[®] Xeon[™] CPU 2.66 GHz, 2.00 GB of RAM, Microsoft Windows XP Professional Version 2002.

6.1 The models

Micromagnetics simulations have been carried out on simplified models of the nanocomposite system in order to gain insight into the origins of the response of the specimen to a transient magnetic field and the hysteresis curves. The sample was approximated as an array of ferromagnetic particles arranged on a plane. Cubic particles were used because the code operates on a regular, rectangular grid (much faster algorithms can be used); modeling similar sized arrays of three-dimensional spheres would require significantly more computational power. Cubic crystalline anisotropy was imposed with the anisotropy axes aligned along the principle axes of the cubes and the magnetic constants for bulk iron were used in the simulations ($M_s = 1.714 \times 10^6$ A/m, $K_1 = 4.7 \times 10^4$ J/m³, exchange energy 2.1×10^{-11} J/m [25]). The particles in the model were exchange-decoupled through physical separation but were close enough together that dipolar interactions remain important. All simulations were carried out at a temperature of 300 K to match experimental conditions unless otherwise indicated.

Several different models were used to approximate the nanocomposite specimen. The models that were explored can be divided into three groups:

Regular Arrays A variety of two-dimensional regular arrays of Fe cubes, usually 10 nm in diameter, with inter-particle separations ranging from 2.5 nm to 15 nm (and 200 nm in one case) were examined for a range of static bias fields. These masks represent filling factors of between 64 and 16% (and 0.23%). Figure 6.1a shows an array of 10 nm cubes separated by 5 nm, which corresponds to a filling factor of 44%. These models are efficient to run and ferromagnetic resonance results can be compared to the theory that was developed in Chapter 2. Grids of 128×128 elements with 5 nm cells (10 nm thick) were used for most simulations; grids of 256×256 were used to compare the effects of array size (5 nm cell size) and to allow finer granularity of inter-particle separations (2.5 nm cell size).

Irregular or Random Arrays The second model (Figure 6.1b) consists of 10 nm cubes randomly placed on a 256×256 element grid, where the individual cells are 2.5×2.5 nm in-plane and 10 nm thick. A minimum inter-particle separation of 2.5 nm was imposed to ensure that all of the particles were exchange-decoupled. The filling factor

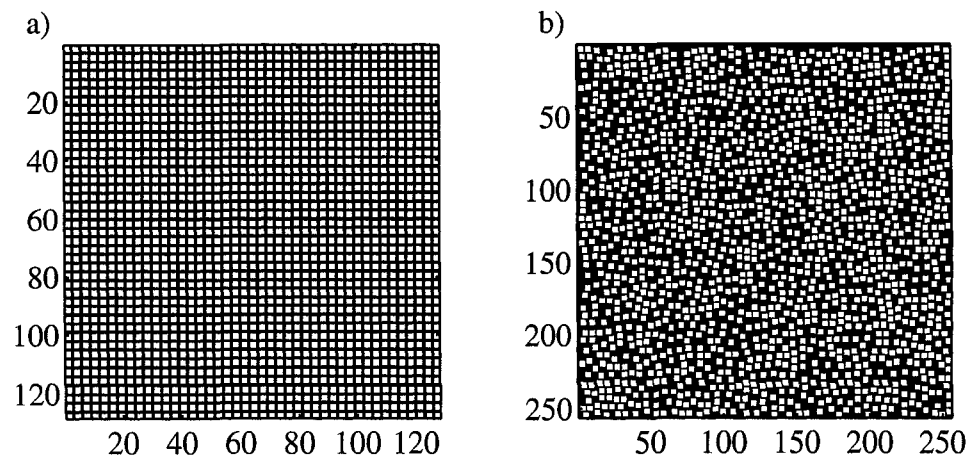


Figure 6.1: Illustration of two types of models used in to approximate the nanocomposite specimen: a) a regular array and b) an irregular array. The white areas are iron and the black cells are non-magnetic (except for the axis ticks that fall on white areas). The axis units are grid indices.

for this model was approximately 40%. This model captures the disordered nature of the specimen much better than the first.

Three-Dimensional Irregular Arrays More complicated models were used to represent the specimen to account for the fact that the nanocomposite is not made up of a single, two dimensional layer of nanoparticles. In this model, iron cubes were arranged on a $100 \times 100 \times 10$ grid with cells that were 2.5 nm on a side. Models with both randomly arranged 10 nm cubes (Model 3D a) and a distribution of sizes ranging from 2.5 to 17.5 nm, centered on 10 nm (Model 3D b), were constructed. Only a few simulations were carried out using these models due to the computational expense of running three-dimensional simulations.

For each simulation, a stable initial state was found by allowing the array of particles to relax to its equilibrium state from a “random state” – that is, a state where each grid cell is assigned a random magnetization orientation. Static bias magnetic fields of between zero and 800 kA/m (10,000 Oe) were applied in either the x (in-plane) or z (out-of plane) direction; in each case the initial state was found using the same bias magnetic field as used in the simulation. Convergence to a stable state was determined by exam-

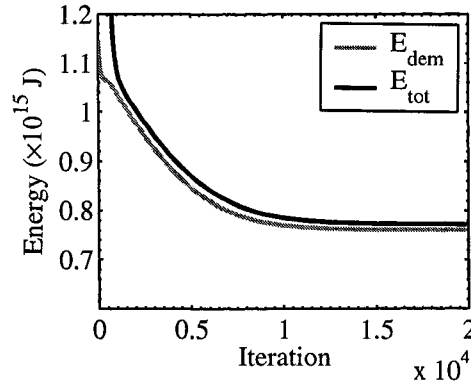


Figure 6.2: Total energy E_{tot} and demagnetization energy E_{dem} as a function of iteration for a regular array in zero bias field.

ining the energy of the model as a function of iteration number. The energy for a regular array model in zero bias field is shown in Figure 6.2. During the first 1000 or so iterations the exchange energy term dominates (initial total energy is 4.3×10^{-15} J). Once the magnetization vectors align within the cubes, the exchange energy remains relatively constant and the demagnetization energy E_{dem} takes over. The small difference between E_{dem} and the total energy E_{tot} is due to the exchange and the anisotropy energies. For this model, the energy starts to flatten out after 10,000 iterations and the magnetization state changes very little after this point.

To model the response to a transient field, the model in its initial state was subjected to a fast magnetic field pulse. Two different pulse types were used: pulses designed to approximate the output of the electronic pulse generator used in the experiments and pulses designed to approximate the output of the photoconductive switches. For the former, the fast edge rises from zero to the saturation level in 60 picoseconds, remains flat for 10 nanoseconds, and then drops to zero in 1 ns. For some simulations a 5 ns pulse duration was used to save on computational time. Pulses of up to 48 kA/m (600 Oe) in amplitude were considered, applied in the x (in-plane) and z (out-of-plane) directions. For the latter, the function $h(t) = h_{max}(1 - \exp(-t/\tau_r)) \exp(-t/\tau_c)$ was used to approximate the profile of the pulse generated by the photoconductive switch used in the experiments. A pulse rise time of $\tau_r = 1$ ps and a carrier lifetime of $\tau_c = 250$ ps were used in the simulations. Pulses of up to (32 kA/m) 400 Oe in amplitude (h_{max}) were considered, applied in the

z (out-of-plane) direction. In addition to the temporal response simulations, hysteresis curves were also mapped out by allowing the model to relax in sequentially applied static fields.

6.2 Initial states

The initial states for a regular array of 10 nm cubes separated by 5 nm are shown in Figures 6.3 and 6.4 for in-plane bias fields of 0 and 8 kA/m (100 Oe), respectively. The zero-field initial state (Figure 6.3) shows both large scale and small scale behaviour. On a small scale, stripes of alternating positive and negative magnetization states minimize the dipolar interaction energy. The individual stripes are generally between one and two rows wide. At a larger scale, domains containing x - and y - oriented stripes form with the stripes oriented such that they are parallel to the edges of the array. This minimizes the demagnetization energy at the edges of the array. If the array size is increased, the size of the domains increases.

As the in-plane bias field is increased, the striped pattern gives way to a uniform magnetization state where all of the magnetization vectors are aligned along the direction of the applied field. Figure 6.4 shows an example of a transitional state (bias field = 8 kA/m (100 Oe) in the negative x direction). As the in-plane bias field is increased from zero to the saturation field, the stripes oriented parallel to the direction of the applied field widen (e.g. two or more stripes along the field then one antiparallel) and the area of the model that is occupied by stripes that are perpendicular to the applied field decreases.

Figure 6.5 shows the zero-field initial state for the random array of 10 nm cubes. This initial state shows similarities to its regular array counterpart in that the magnetization is primarily in-plane and stripe-like patterns tend to form in both the x and y directions. Figure 6.6 shows the initial state for an in-plane bias field of 8 kA/m (100 Oe), applied in the negative x direction. At this bias field, the stripe-like patterns persist but the number of cubes aligned along the same direction as the applied field is greater than for the zero-field case. For this model, full alignment of the magnetization of all cubes along the direction of the applied field requires a larger magnetic field than that required to achieve saturation of the regular array. At a bias field of 60 kA/m (750 Oe), the array is approaching uniform

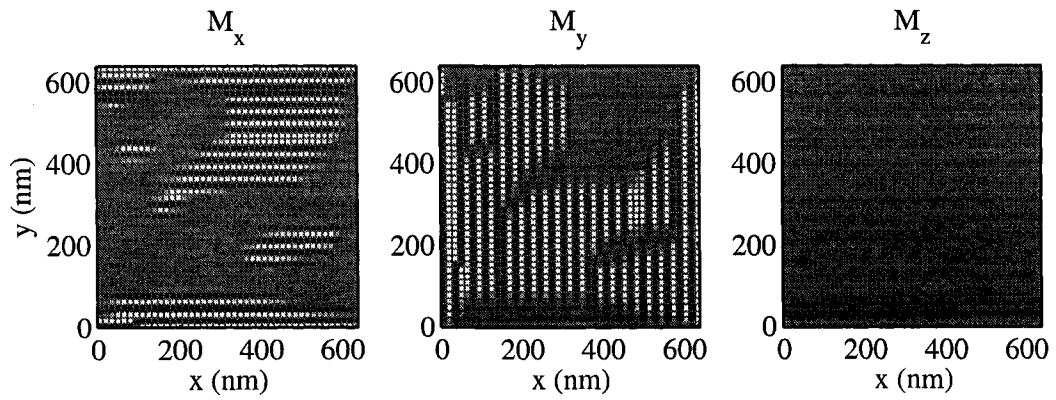


Figure 6.3: Initial state for a regular array of Fe cubes with no bias field. White represents positive values, black negative, and zero is grey.

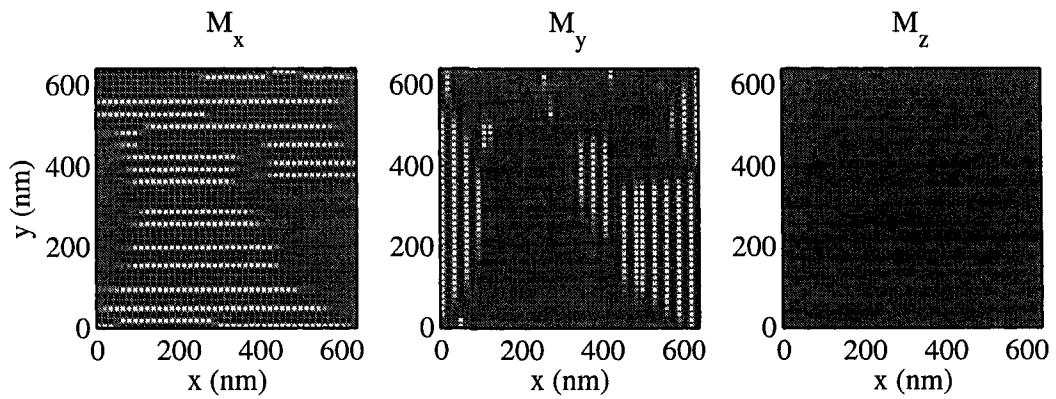


Figure 6.4: Initial state for a regular array of Fe cubes subject to an in-plane bias field of 8 kA/m (100 Oe).

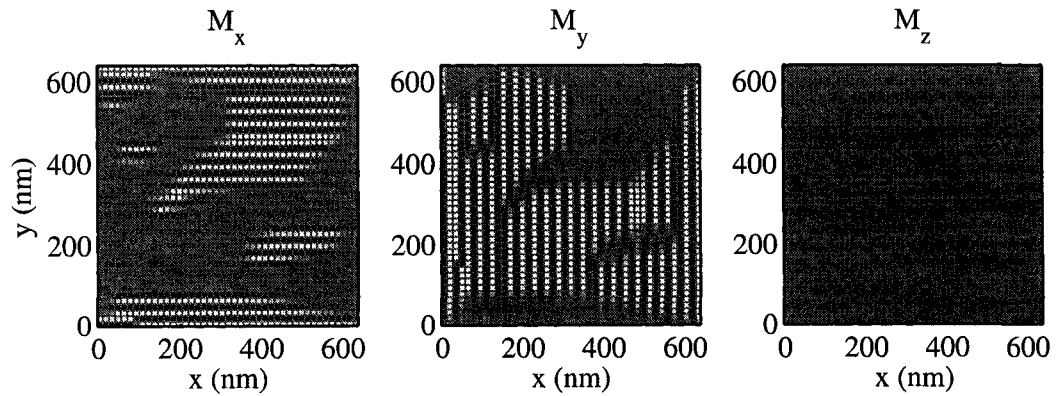


Figure 6.5: Initial state for a random array of Fe cubes with no bias field.

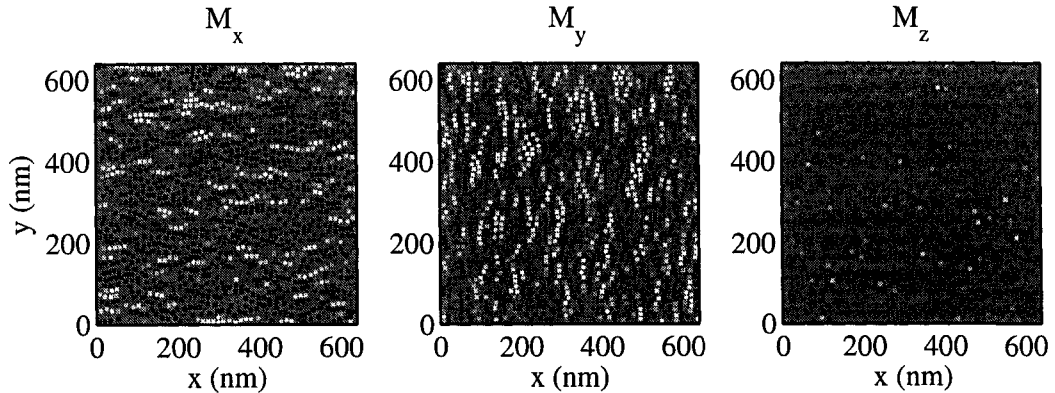


Figure 6.6: Initial state for a random array of Fe cubes subject to an in-plane bias field of 8 kA/m (100 Oe) in the negative x direction.

magnetization but even with an in-plane bias field as high as 140 kA/m (1750 Oe), some cubes still maintain a small y component of magnetization.

In addition to these two-dimensional arrays, two different three-dimensional models were examined, both in zero bias field. One model involves a number of 10 nm cubes randomly arranged on a $100 \times 100 \times 10$ grid (2.5 nm cell size) and the other model is comprised of cubes with a distribution of sizes ranging from 2.5 to 17.5 nm arranged on the same grid. The zero field initial states for these models are shown in Figures 6.7 and 6.8, respectively. The initial states are primarily in-plane, though not as strongly as for the two-dimensional models. Stripe-like patterns in x and y that are similar to those exhib-

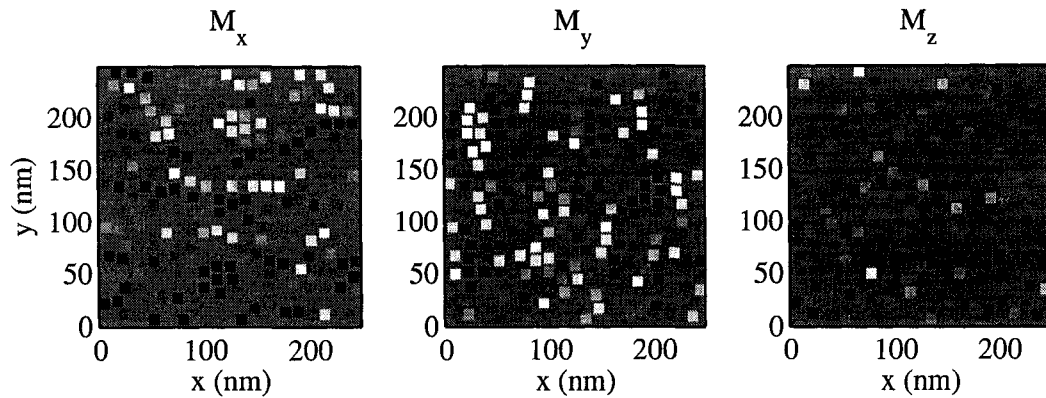


Figure 6.7: Initial state for a three dimensional random array of 10 nm Fe cubes subject to zero bias field. Only layer 5 of 10 is shown.

ited by the two-dimensional random array are observed.

6.3 Hysteresis

The hysteresis loops for a single 10 nm cube and for the two-dimensional regular and random arrays of 10 nm cubes have been simulated and will be compared. Figure 6.9 shows the hysteresis loop for a single 10 nm cube, modeled using $2 \times 2 \times 1$ elements. The crystalline anisotropy axes were aligned with those of the cube, as they are for the two-dimensional models. These curves were simulated with the magnetic field applied along the x -axis (easy axis of the cubes) and at an in-plane angle of 63° . The hysteresis loops are square in shape with coercivities of around 40 and 20 kA/m (500 and 250 Oe), respectively, for the two angles. The behaviour is Stoner-Wohlfarth-like in nature. Using this model, a coercivity of $2K_1/(\mu_0 M_s) = 43.6$ kA/m (548 Oe) for the x -axis hysteresis curve is predicted, which is close to the simulated value.

Simulated in-plane hysteresis curves for a regular array of 10 nm cubes with 5 nm separation are shown in Figure 6.10a. For this model, the coercivity is around 1.6 kA/m (20 Oe), which compares well with that of the unannealed Fe implanted SiO_2 (1.5×10^{17} ions/cm², 80 kV), which was found to have an in-plane coercivity of 1.8 ± 0.4 kA/m (23 ± 5 Oe). The biggest difference between the shape of the regular array hysteresis curves and the exper-

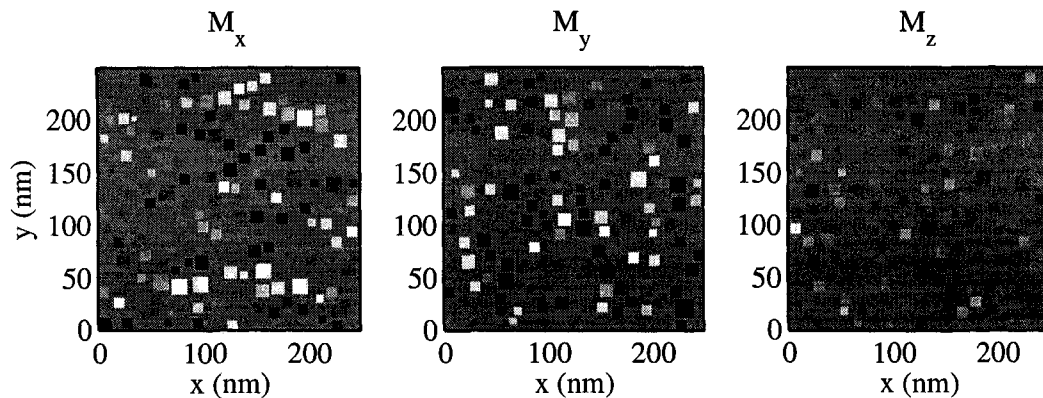


Figure 6.8: Initial state for a three dimensional random array of Fe cubes with sizes ranging from 2.5 to 17.5 nm subject to zero bias field. Only layer 5 of 10 is shown.

imental results is the “fattening” of the curve at higher fields, which may be related to the nucleation of the striped patterns.

Moving from models with a regular arrangement to random spatial positioning of the iron cubes has a significant effect on the shape of the hysteresis loop (Figure 6.10b). The rounded shape of these curves is closer to the shape of the experimental measurements for the nanocomposite specimens, although the coercivity of the model is much higher (39 kA/m or 490 Oe). There is only a very slight change in the hysteresis loop for an array of randomly-placed 10 nm cubes when the field is applied at an angle of 63° in-plane as compared to being applied in the x direction. In fact, the coercivities are identical.

Figure 6.11 shows the simulated out-of-plane hysteresis loop for the regular array of 10 nm cubes with 5 nm separation and for the random array. Both models require around 480 kA/m (6 kOe) to achieve saturation and the coercivity is less than 80 A/m (1 Oe). The random model shows a slightly smoother approach to saturation but otherwise the two curves are very similar. These hysteresis curves are also consistent with the experimentally measured out-of-plane hysteresis response for the as-implanted nanocomposite specimen.

For an array of particles, the coercivity is reduced as compared to the coercivity of a single particle, the curves are rounded rather than square, and the in-plane response is close to being isotropic. In these simulations, the crystalline anisotropy energy is almost two orders of magnitude smaller than the demagnetization energy, which helps to explain

the change from anisotropic to isotropic behavior. The demagnetization energy has contributions from the particle itself (which are similar to the energies observed for a single cube) and from the rest of the particles in the array. Due to the inter-particle interactions, the demagnetization energy for an array is correlated with the magnitude of the applied field and thus has a much stronger influence on the hysteresis behaviour than the smaller anisotropy energy. For the single cube simulations, the demagnetization energy is only from the cube itself so even though it is larger in magnitude, the anisotropy energy is actually of primary importance in determining the hysteresis behaviour.

A recent computational study on the effects of inter-particle interactions on the hysteresis of specimens containing cubic nanoparticles (fabricated using ion implantation) supports these findings [8]. The simulations were for models containing a distribution of particle sizes, with a mean particle diameter of 14 nm. This study showed that when inter-particle interactions are introduced there are three characteristic changes in the simulated hysteresis that occur: 1) rounding of the curve (less square), 2) out-of-plane hysteresis curve narrows significantly, and 3) the in-plane anisotropy is decreased (in other words, the shape of the in-plane hysteresis curve should be independent of the in-plane angle at which it is measured). In this study it was also noted that the saturation field is increased significantly and the coercivity is decreased when dipolar interactions are present. Volume fractions of 1.6% were found to exhibit some interaction effects and a volume fraction of 12.5% was sufficiently dense that in-plane isotropy of the hysteresis curves was induced. All of these findings are supported by the simulation results shown in this thesis.

6.3.1 Temperature dependence of AC Susceptibility

In Section 5.3, the AC susceptibility was measured as a function of temperature and found to remain relatively constant between liquid helium and room temperatures. Simulating the response to a 2.3 kHz sinusoidally varying field would be computationally quite intense (time steps are on the order of 0.1 ps), so instead, minor out-of-plane hysteresis loops for the random array model were simulated for magnetic fields ranging from -25 to 25 Oe. The results (Figure 6.12) are virtually identical for temperatures ranging from 0 to 300 K. The room temperature exchange constant actually ranges from 2.3 at low temperature to

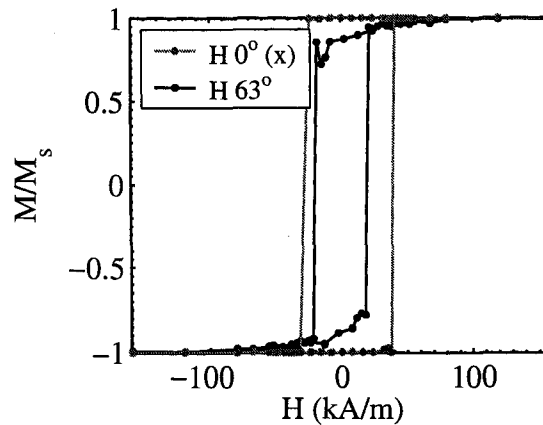


Figure 6.9: Simulations of the in-plane hysteresis curves along the x -direction (easy axis of the cube) and at an angle of 63° in-plane for a single 10 nm cube. The individual points show the actual simulation results while the connecting lines are meant as a guide to the eye.

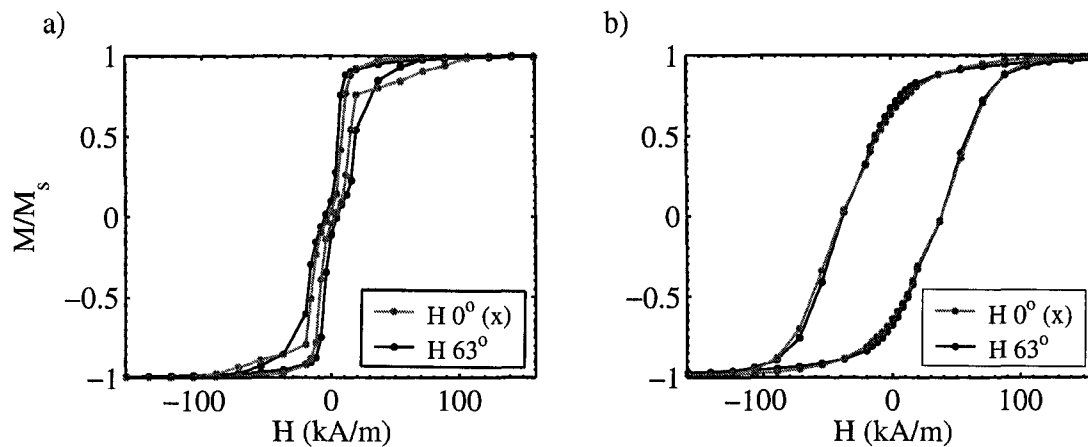


Figure 6.10: Simulations of the in-plane hysteresis curves along the x -direction (easy axis of cubes) and at an angle of 63° in-plane for a) a regular array with 5 nm separation (36% filling factor), and b) an irregular array of 10 nm cubes (40% filling factor).

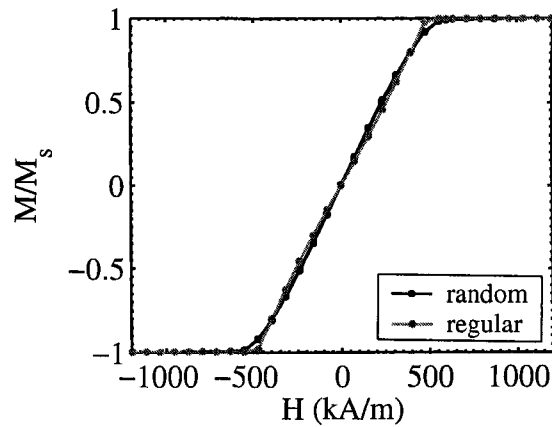


Figure 6.11: Simulations of the out-of-plane hysteresis curves for the same regular and random arrays as in Figure 6.10.

2.0 at 300 K [25] but the simulations shown here were actually run with an exchange constant of 2.1×10^{-6} erg/cm for all temperatures. The 0 K simulation was repeated using the low temperature exchange constant, which was found to have almost no effect on the outcome. The simulations, therefore, predict the flat trend of susceptibility as a function of temperature that was observed experimentally.

6.4 Temporal response to a square magnetic field pulse

6.4.1 In-plane transient field

Figure 6.13 shows the results from a regular array (10 nm cubes, 5 nm separation) as well as both two and three-dimensional random array simulations in response to a 48 kA/m (600 Oe) in-plane pulse, 5 ns in duration. The two-dimensional simulations were carried out both in zero bias field and for an in-plane bias field of 16 kA/m (200 Oe), while the three-dimensional simulations were only performed under zero bias field. The regular array simulations were repeated at a temperature of 400 K and the results were virtually identical to the 300 K results shown. Doubling the size of the regular array also did not cause an appreciable difference in the simulated behaviour. The overall shapes of the results for the two-dimensional models change very little with bias field and would be

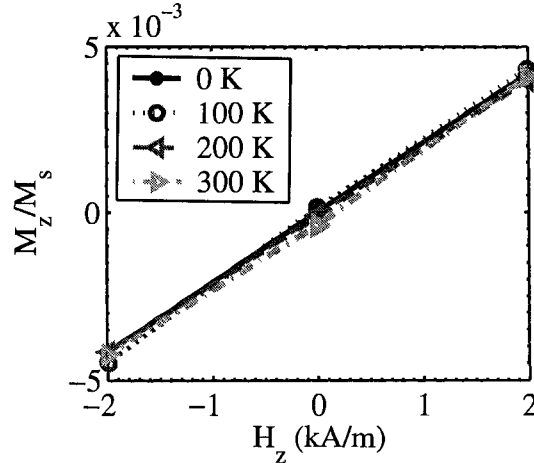


Figure 6.12: Simulations of the out-of-plane hysteresis curve over a smaller field range for temperatures ranging from 0 to 300 K.

expected to generate very similar TR-MOKE signals for both fields (recall that TR-MOKE probes the change in magnetization state rather than the magnitude). The simulation with the 16 kA/m (200 Oe) bias field did, however, show a slightly steeper approach to equilibrium on a relative scale. While the shape of the M_x response is not identical to the experimental results for any of these models, it is qualitatively similar for all of the models examined. The experimental data show exponential behaviour with two distinct time constants and the simulations show both fast and slow relaxation behaviour also. The time scales for the simulations, however, are much faster.

Figure 6.14 shows the in-plane magnetization response (M_x) as a function of time for the random model in zero bias field for a full 10 ns pulse. For these simulations, transient magnetic field pulses of 4.8 and 48 kA/m (60 and 600 Oe) were applied in the x -direction. The 4.8 kA/m (60 Oe) pulse simulations were scaled by a factor of 10 so that the shapes of the responses could be more easily compared on the same plot. The response to the 4.8 kA/m (60 Oe) pulse, which is significantly smaller than the coercivity of this model, is very similar to the observed out-of-plane response rather than to the in-plane response in that it mirrors the pulse shape. The response to the 48 kA/m (600 Oe) pulse, which is larger than the coercivity of the model, shows a smoother approach towards saturation with an initial fast response followed by a slower approach to saturation during the pulse.

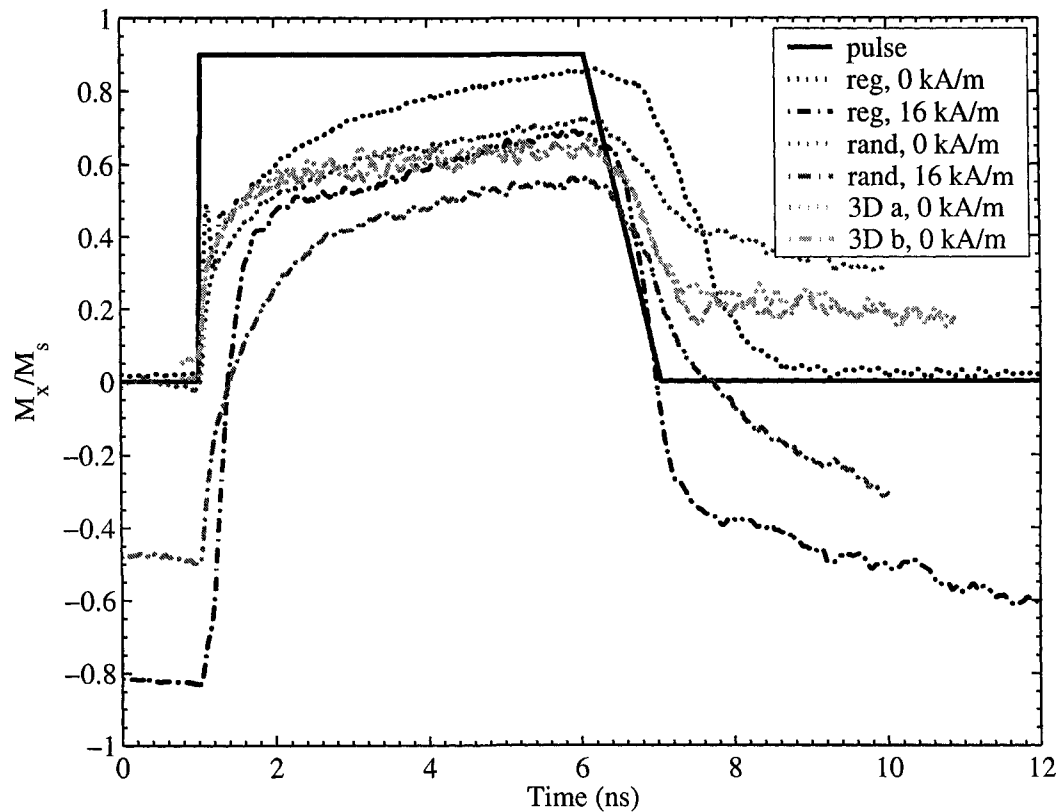


Figure 6.13: Magnetization as a function of time, x component, for a regular array of 10 nm cubes separated by 5 nm, a random array of 10 nm cubes, and both of the three-dimensional models. For the two-dimensional models, the results for both a zero bias field and an in-plane bias field of 16 kA/m (200 Oe) are shown while for the three-dimensional models only zero field results are displayed. The solid black line shows shape of the 48 kA/m (600 Oe) in-plane transient field.

6.4. TEMPORAL RESPONSE TO A SQUARE MAGNETIC FIELD PULSE

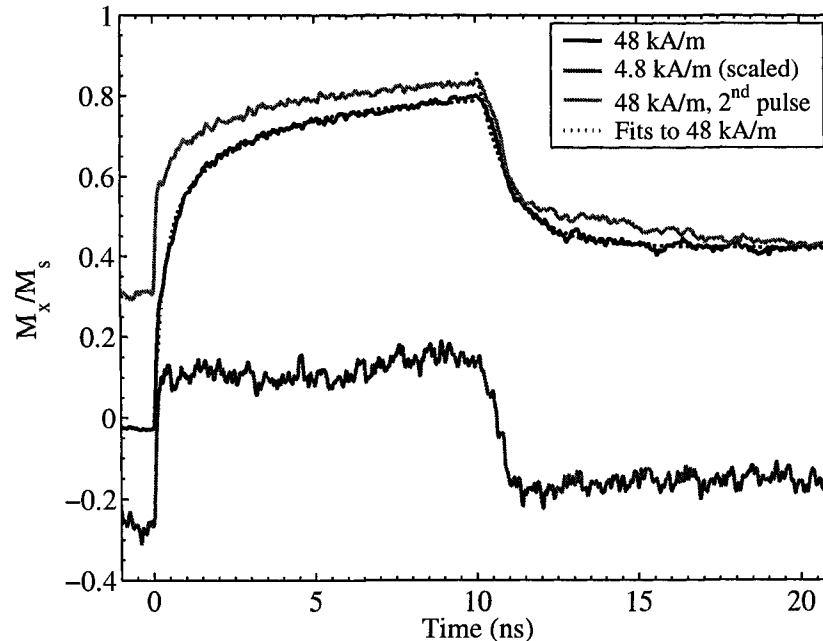


Figure 6.14: Average in-plane magnetization M_x as a function of time for the model in response to in-plane transient magnetic fields (x direction) of 4.8 and 48 kA/m (60 and 600 Oe). The curve labeled “48 kA/m, 2nd pulse” is the response of the final state in the 48 kA/m pulse simulation to a second pulse of the same magnitude. The 4.8 kA/m results have been scaled so that the shapes of the responses can be compared more easily. Two-exponential fits to the 48 kA/m simulation results during and after the pulse are also shown.

The time-resolved measurements rely on repetition of the excitation. To explore the effect of having a non-equilibrium initial state, these simulations were repeated using the final state ($t = 21$ ns) from each simulation as the initial state in an identical simulation, which yielded very similar response shapes for both the 4.8 and 48 kA/m (60 and 600 Oe) pulse amplitudes.

Qualitative features of the 48 kA/m (600 Oe) random simulations in particular are in agreement with the experiment. The simulations yield a fast initial response followed by a slower approach to saturation during the pulse. Similarly the relaxation to the initial state after the pulse shows a fast initial fall in M_x followed by a slower approach to equilibrium. Both responses are, however, much faster than observed experimentally. In fact, the experimental data taken over the full duration of the pulse were found to be well de-

6.4. TEMPORAL RESPONSE TO A SQUARE MAGNETIC FIELD PULSE

	τ_1	τ_2	A_1/A_2
During Pulse:	0.336 ± 0.001	3.03 ± 0.02	1.706 ± 0.005
After Pulse:	1.022 ± 0.006	430.7 ± 0.9	0.937 ± 0.007

Table 6.1: Exponential fit parameters for simulated response to a 48 kA/m (600 Oe) in-plane transient magnetic field. Uncertainties represent a 95% confidence interval on the fitting parameters.

scribed by a single exponential function, which is believed to be analogous to the faster initial response of the model. The same exponential function used to fit the data also describes the simulation results well (dotted lines in figure). The parameters found for fits to the results obtained during and after the pulse are shown in Table 6.1. The fit to the trailing edge is not as good as the fit during the pulse because the initial fall of the simulation is actually limited by the 900 ps fall time of the pulse. The fit parameters for the results during and after the pulse are different, especially for τ_2 . If the pulse fall time is limited to 60 ps then τ_1 for the fall is comparable to τ_1 during the pulse, which is consistent with the experimental observations. The time constants from the simulations are all faster than those obtained from the experiment with the exception of τ_2 from the falling edge, which is the same order of magnitude as τ_2 from the experiment. The amplitude ratios are greater than 1 or slightly less than 1 for the simulations and equal to or slightly less than 1 for the experiment.[†]

The two exponential terms could be related to either two separate populations that relax with separate time constants, or two separate behaviors that dominate at different time scales. The amplitude ratio would represent the relative sizes of the populations in the first case and would be related to the cross-over point in the second. In the simulations there is evidence that the states oriented initially along the positive or negative y directions respond more quickly at the onset of the pulse and level off at a lower mean M_x value. The states oriented initially along the x axis, in contrast, are slower to respond initially and show a steeper M_x slope towards the end of the pulse. The behaviors of the two

[†]For a well constrained fit, examining $\sum_i (M_x(t_i) - M_{x,predicted}(t_i))^2$ will show that the solution is located in a minimum when each parameter is varied. For the four-parameter fit used here, however, this is not observed, which suggests that there are correlations between the parameters and that the amplitude and time constant parameters are not completely independent. The uncertainties listed for the parameters do not reflect the fact that there are other parameter combinations that will describe the data equally as well.

6.4. TEMPORAL RESPONSE TO A SQUARE MAGNETIC FIELD PULSE

populations, however, are not different enough from each other to match the individual terms of the exponential fit. It is thus thought to be more likely that the exponential terms are related to different processes rather than different populations. At fast time scales, the onset or removal of the pulse triggers large-angle rotations of the magnetization. At longer time scales, the array exhibits smaller angle oscillations as it settles into a more stable magnetization state.

Examining the behaviour of the individual cubes in the regular array simulations yields additional insight into the origins of the fast and slow relaxation behaviour. Figure 6.15 shows the x component of the magnetization as a function of time for twenty randomly-selected individual cubes from the regular array simulation with no bias field. This particular simulation was carried out at a temperature of 0 K in order to eliminate thermal fluctuation effects to make it possible to focus on the dynamic behaviour caused only by the transient magnetic field. Throughout the simulations, the magnetization remains predominantly in-plane so when the x component of the magnetization is zero, the cube in question will be magnetized in the positive or negative y direction. The cubes initially magnetized in the y direction become aligned along the direction of the pulsed magnetic field very quickly after the onset of the transient field. The cubes that are initially oriented in the negative x direction change direction very quickly when they do switch (< 200 ps) but they do not necessarily switch right away. In all cases, the individual cubes show oscillatory behaviour. The y oriented cubes are switched more easily and the x oriented cubes have a smaller probability of switching over a given length of time. For this simulation it appears that the presence of fluctuations that are damped over a much longer period of time contributes to the incomplete saturation of the model both during and after the pulse.

The model presented here represents the physical specimen very qualitatively. The grid spacings used here are comparable to the particle sizes, which results in discrete rather than smooth variations of inter-particle spacing. Also, the models shown here, with the exception of one of the three-dimensional models, contain particles of uniform size while the specimen contains a distribution. The true shapes of the nanoparticles are also not well represented in the models. The in-plane magnetization change may be a manifestation of a more complex three dimensional switching scenario.

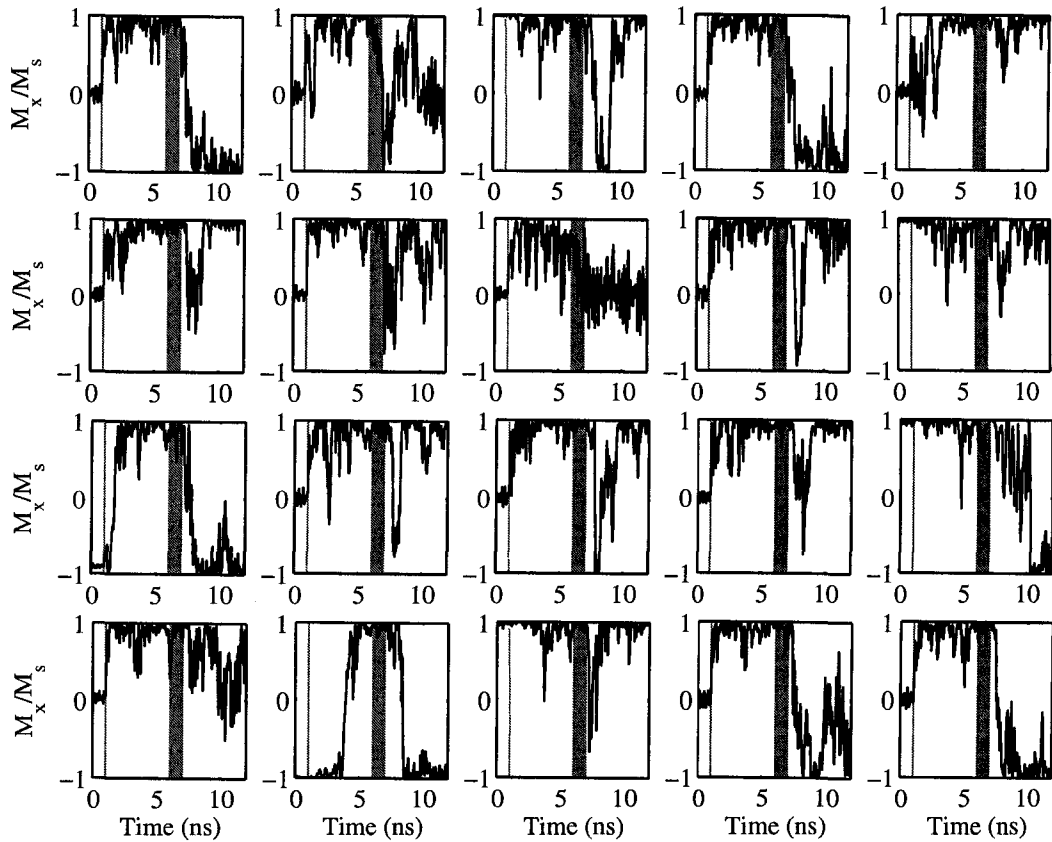


Figure 6.15: Magnetization as a function of time, x component, for randomly selected individual cubes in a regular array in response to a 48 kA/m (600 Oe) in-plane transient field with zero bias field. The shaded areas show the rise and fall of the 5 ns transient field pulse.

6.4.2 Out-of-plane transient field

The response to an out-of-plane square pulse, 5 ns in duration, was simulated for a regular array of 10 nm cubes separated by 5 nm and also for the two and three-dimensional random arrays of 10 nm cubes. The results for all of these models at zero bias field and the two-dimensional models for an in-plane bias field of 16 kA/m (200 Oe) are shown in Figure 6.16. In all cases, the M_z response follows the profile of the transient field pulse (with small fluctuations superimposed). These simulation results agree with experimental observations for the nanocomposite specimens. The regular array simulations run at a temperature of 400 K resulted in the same overall M_z response. Simulations were also run on the regular array under zero bias field with a 16 kA/m (200 Oe) pulse applied in the x direction simultaneously with a 16 kA/m (200 Oe) out-of-plane pulse. If an in-plane component is added to the transient pulse, the out-of-plane response for this model remains the same. The fast out-of-plane response is observed for simulations carried out on a variety of models involving small, densely packed magnetic elements arranged on a plane. These results also indicate that the in-plane response is decoupled from the more easily reproducible fast out-of-plane response.

To verify the importance of the interactions in producing this fast response, the separation between cubes in the regular array was increased to 200 nm (volume fraction 0.22%). The initial state for this model shows no significant in-plane anisotropy in zero-field. In the presence of a 16 kA/m (200 Oe) in-plane bias field, coherent oscillations were observed for an out-of-plane pulse, similar to what would be expected for a single particle. The simulation does follow the pulse profile but the rise time is slower and the magnetization is highly oscillatory at close to a single (low) frequency. The interactions do have a significant effect both on the initial state and on the out-of-plane response to a transient magnetic field.

6.5 Temporal response to a photoconductive switch pulse

The two-dimensional regular and random arrays of 10 nm iron cubes were subjected to conditions similar to those under which the time-resolved experimental measurements with the photoconductive switches were made. The regular array model was used to

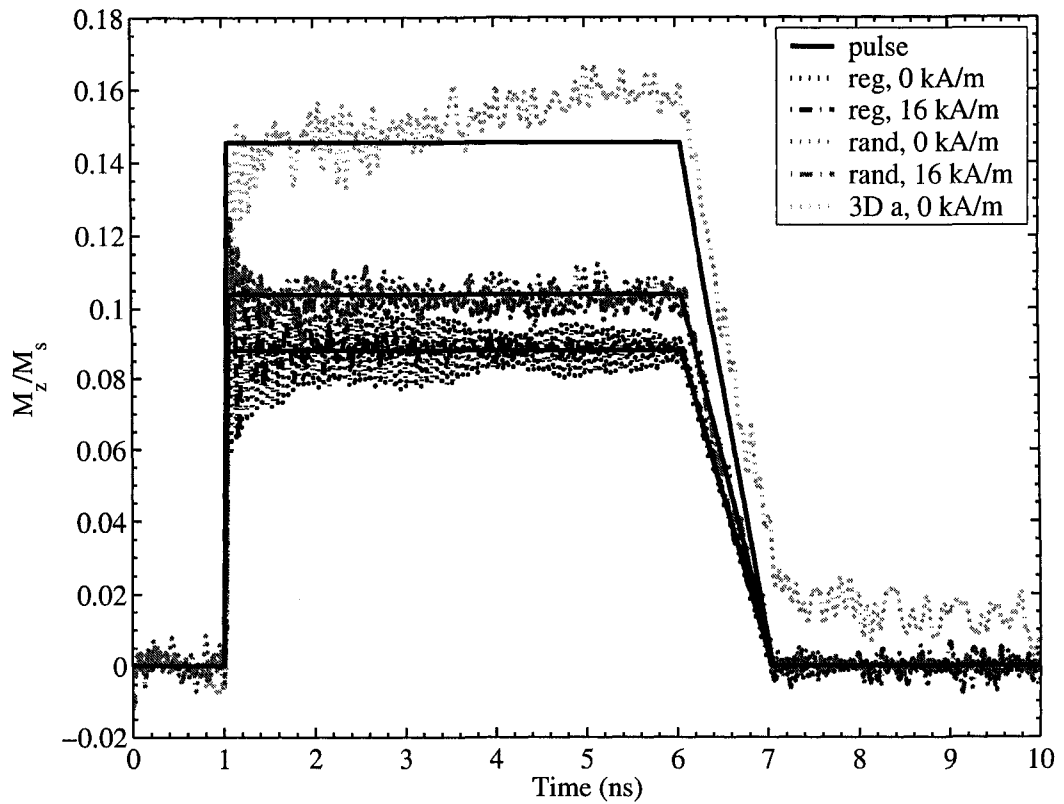


Figure 6.16: Magnetization as a function of time, z component, for a regular array of 10 nm cubes separated by 5 nm, and both two and three-dimensional random arrays of 10 nm cubes. The responses of the two-dimensional models subjected to zero bias field and an in-plane bias field of 16 kA/m (200 Oe) are shown, while only the zero-field results for the three-dimensional model are included. The solid black line shows the shape of the 48 kA/m (600 Oe) out-of-plane transient field.

further explore the effects of parameters such as out-of-plane bias field, angle of applied pulse, model scale, array density, and in-plane bias field.

6.5.1 Regular array response as a function of in-plane bias field

The response of the regular array of 10 nm cubes with 5 nm separation to a transient magnetic field meant to approximate that of a photoconductive switch is shown in Figure 6.17 for in-plane bias fields ranging from 0 to 140 kA/m (1750 Oe). At this time-scale and for this model, the out-of-plane response is no longer a direct map of the current pulse. The overall response still follows the pulse shape but also shows strong, coherent oscillations in the z component of the magnetization. The rise time is limited by the material response, not by the rise time of the transient field. At low bias fields, there is no significant M_y response but at high fields, oscillations that are shifted by $\pi/2$ with respect to those of the M_z component are observed. This suggests that any oscillations in y of the individual particles are such that they cancel out at low fields but at high fields the oscillations in the magnetization are coherent.

An interpolated view of the same simulation results (Figures 6.18) reveals that there is a smooth variation of resonance frequencies over most of the range that was examined but at low fields there is a fairly sharp transition to a much higher frequency resonance; the frequencies are roughly doubled on the low-field side of the transition point. The bias field at which this transition takes place, which is around 20 kA/m (250 Oe), corresponds to the bias for which the initial state changes from predominantly striped in nature to mostly uniform (see figures in Section 6.2).

The rise time and peak frequencies have been extracted from the simulations and plotted as a function of in-plane bias field (Figure 6.19). The rise times are fast at low fields, with a sharp increase around the transition point followed by a slow decrease with increasing bias field. The peak frequency trend is the opposite. The theoretical predictions for the resonance frequency and rise times have been superimposed on Figure 6.19. The equations and constants used for the theory lines on this plot can be found in Appendix A. This appendix also includes an explanation of the relationship between the predicted rise times and resonance frequencies.

A slight correction to the theory was made to account for the fact that there is a discrep-

6.5. TEMPORAL RESPONSE TO A PHOTOCONDUCTIVE SWITCH PULSE

ancy between the method used to calculate the field generated by a cube for the theoretical derivation and the simulation code. The theory treats the cubes as ideal dipoles, which is an excellent approximation for large separations but can lead to an overestimation of the true magnetic field generated by a cube when separations are small. Micromagnetics simulations generally treat the demagnetization problem through a volume-averaging method, designed to accommodate cubic or rectangular array elements. A correction value was determined by choosing a small array (13×13 particles) from the interior of the regular array model and calculating the effective magnetic field for each particle due to the others using first the dipole approximation and second a standard method for evaluating the demagnetization field for a cube [83]. The calculation for magnetic bias fields of 0, 100, 250 and 1500 Oe yielded discrepancies of $92.7 \pm 2.4\%$, $93.7 \pm 4.9\%$, $96.1 \pm 3.7\%$, and $96.0 \pm 3.6\%$, respectively, where the uncertainty is the standard deviation. To properly compare the theoretical predictions to the simulation results, the weighted average of the discrepancies was rounded to the nearest percentage (94%) and the dipolar approximation in the theory was reduced by replacing the particle volume V by an effective volume $V_{eff} = 0.94V$.

The predictions for the resonance frequencies match very well with those observed in the simulations (Figure 6.19). The low-bias field simulation results have frequencies close to the predicted zero-field value while the high-field observed frequencies agree well with the high-field theory. Notice that some of the high-field results also agree with the Larmor prediction but the overall behaviour is described much better by the proper theory for an array of nanoparticles.

The rise time predictions are quite good at zero bias field and at high bias fields. At transitional fields, however, the rise times observed in the simulations are faster than those predicted by theory. The cause for this discrepancy can best be understood by examining the distribution of local magnetic fields experienced by the individual particles in the array. Histograms of these values for in-plane bias fields of 0, 8, 20, and 120 kA/m (0, 100, 250, and 1500 Oe) are shown in Figure 6.20 (estimated using the dipolar approximation). For zero and high bias fields, the effective field histograms are relatively sharp and the peak of the histogram is very close to the highest effective field. For transitional initial states, however, the distributions are broadened and contain effective fields above

6.5. TEMPORAL RESPONSE TO A PHOTOCONDUCTIVE SWITCH PULSE

the peak. These distributions are expected to be reflected in the simulation results in that a broader distribution of effective fields should result in a broader frequency distribution and higher effective fields should make it possible to have faster rise times than what would be expected based on the peak frequency.

The change of magnetization with time for individual cubes in the model can be examined more closely. Focusing on a section of the model in zero bias field that is initially magnetized in a striped configuration parallel to the x axis, the y and z components of the magnetization (Figure 6.21) show that the cubes that are part of positive x stripes oscillate in-phase, as do those that make up the negative x stripes. The z components of the oppositely oriented stripes are identical while the y components are mirror images of each other. This explains why the overall M_z response shows oscillations while the M_y response is zero at low bias fields. At high bias fields, examination of the individual cubes reveals that all of the cubes oscillate in phase with each other, resulting in both M_z and M_y signals.

6.5.2 Regular array response as a function of inter-particle separation

The effects of varying inter-particle separation were examined for regular arrays of 10 nm cubes. Inter-particle separations (between the edges of the particles) of 2.5, 5, 10, and 15 nm were investigated for zero bias field and for a bias field of 120 kA/m (1500 Oe). A uniformly magnetized initial state (negative x direction) was used to save on computational time for the latter simulations. The results are shown in Figure 6.22, scaled by the peak M_z value so that the rise times can be compared more easily. The zero-field data for the as-implanted nanocomposite sample have also been included for comparison with the zero bias field simulation results. The shape traced out by the initial rise of data is very similar to that of the simulation results and the overall appearance of the data is also quite similar, although the oscillations are less pronounced than for the simulations. The experimentally observed rise time is slightly faster as compared to the model with 10 nm inter-particle separation and slightly slower than that of the model with 5 nm inter-particle separation.

The rise times and peak frequencies are plotted as a function of inter-particle separation s in Figure 6.23. In general, the rise time increases and the frequency decreases with

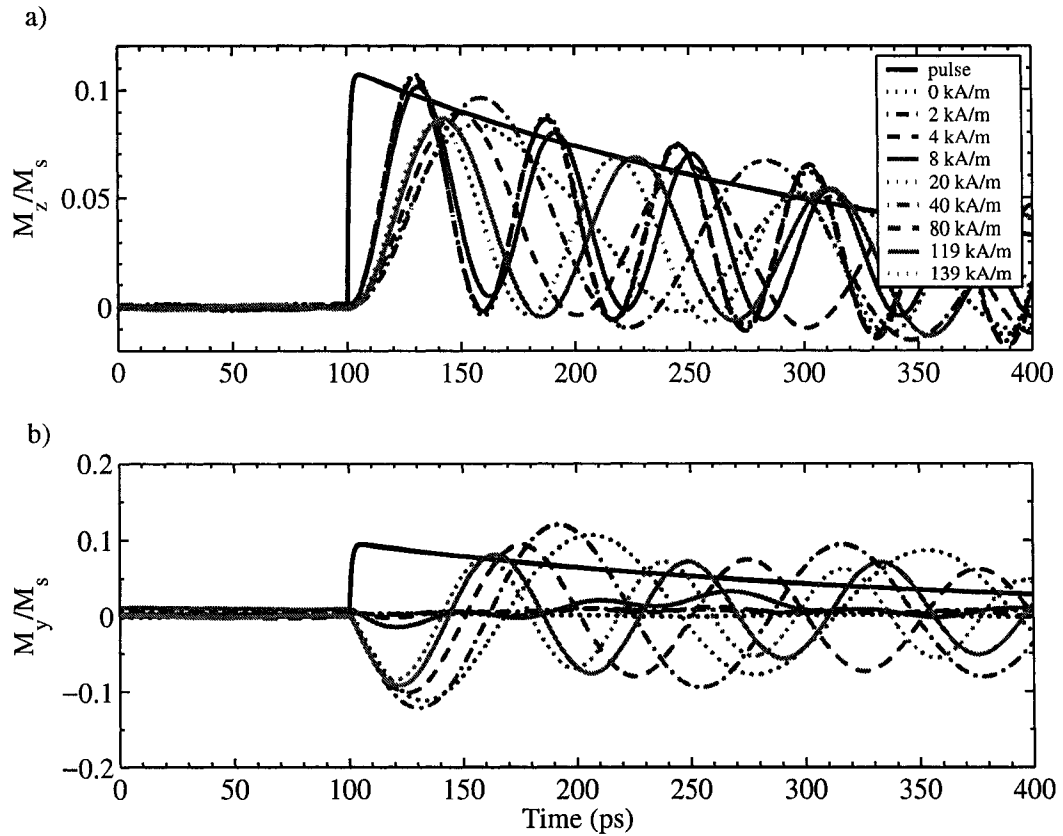


Figure 6.17: Magnetization as a function of time for a regular array of cubes subjected to a transient out-of-plane magnetic field in the presence of an in-plane bias. Figure a) shows the z -component while b) shows the y -component.

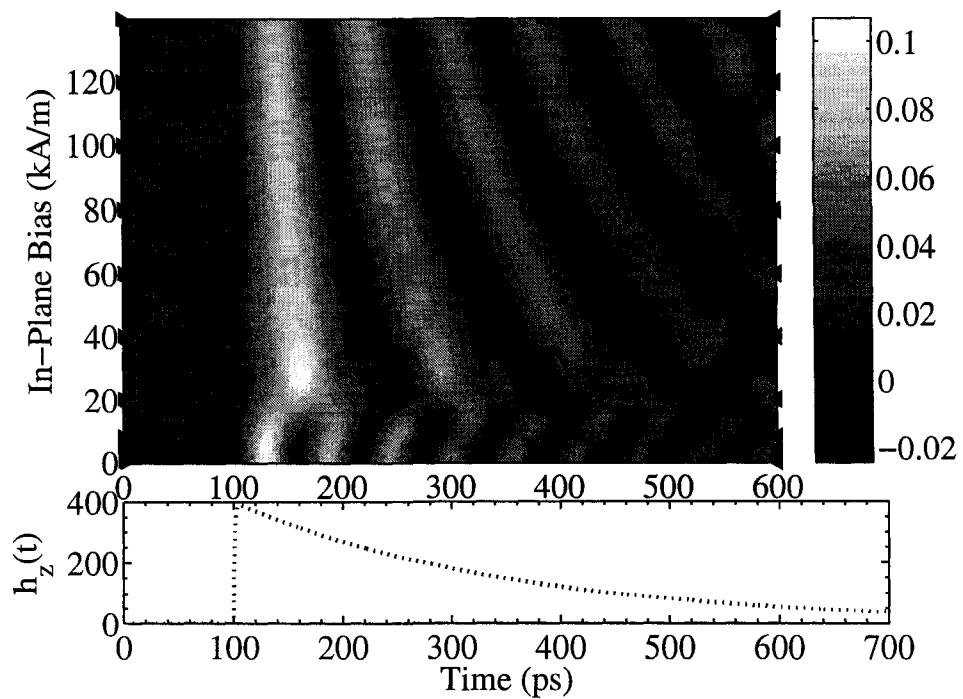


Figure 6.18: Interpolated image of the magnetization (z component) as a function of time and in-plane bias field for a regular array of cubes subjected to a transient out-of-plane magnetic field (shown in lower plot). The triangular markers indicate the bias fields for which simulations were carried out.

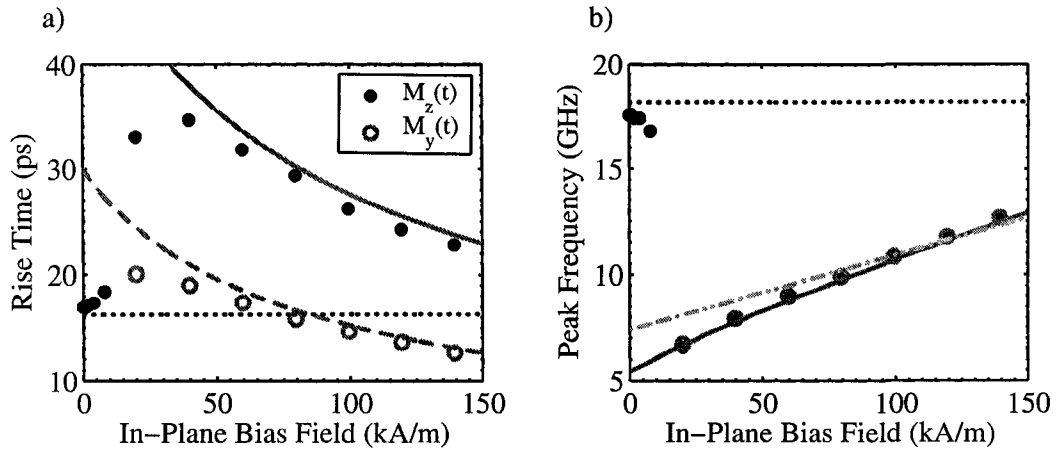


Figure 6.19: a) Rise time and b) resonance frequency as a function of out-of-plane bias field for a regular array of Fe cubes. In both plots, the dotted line shows the zero-field resonance frequency and its corresponding M_z rise time. In b), the solid line shows the predicted high-field resonance frequency and the dash-dotted line is the high-field Larmor frequency prediction. In a), the solid line shows the corresponding prediction for the high-field M_z rise time while the dashed line shows the predicted M_y rise time. Both predictions are based on the high-field resonance frequency.

increasing separation for both zero bias field and high bias field (120 kA/m). The predicted behaviour (solid lines) matches the simulation results reasonably well in both cases. These predictions are based on equation 2.46 for the zero-field case and equation 2.53 for the high bias field simulations with $a = s + d$, where d is the width of a cube. An effective volume of $0.94V$ was used. Although this value was found for an inter-particle separation of 5 nm, it provides a reasonable fit for the separations that were investigated. For larger separations, the dependence of the resonance frequency on the demagnetization term is reduced. For a separation of 2.5 nm, however, the the dipole approximation should overestimate the dipolar interactions even more than for a separation of 5 nm so it is not unexpected that the peak frequencies observed in the simulations are smaller than predicted. An effective volume of closer to $0.75V$ for this case would provide much better agreement for both the zero and 120 kA/m (1500 Oe) bias field simulations.

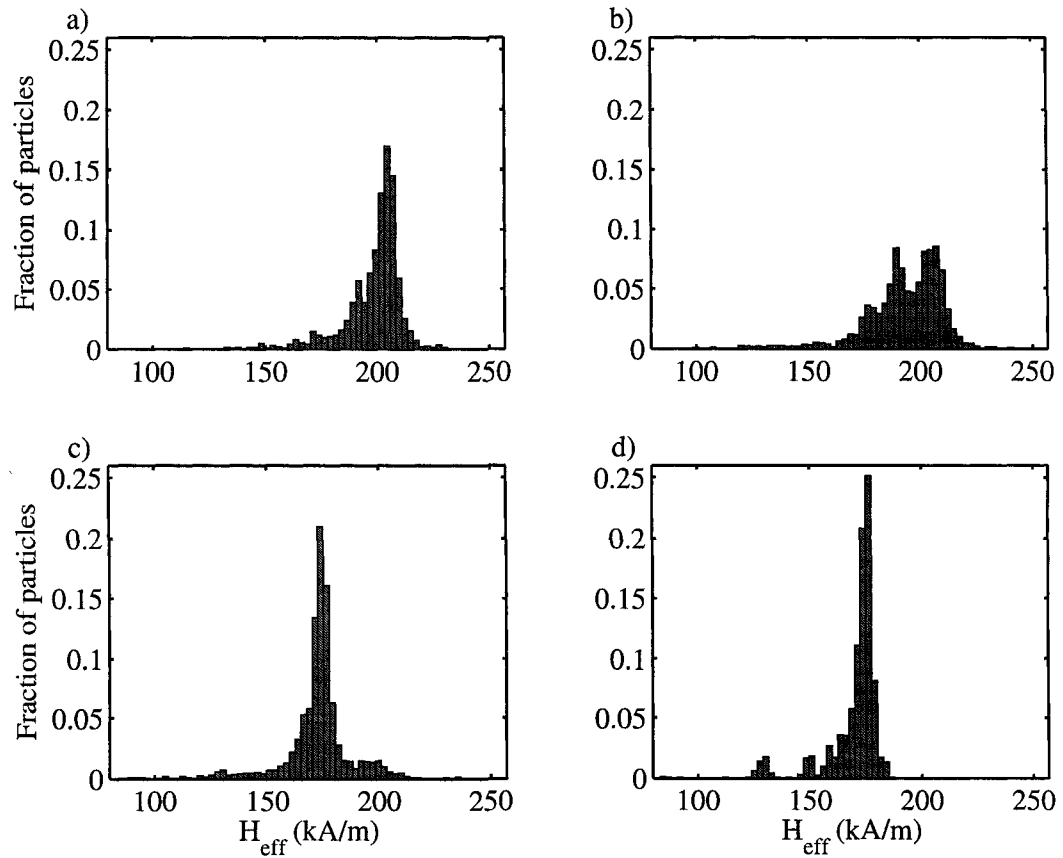


Figure 6.20: Histograms of local effective fields at each cube due to the dipolar fields of all of the other cubes in the model. Calculations are based on initial states for in-plane bias fields of a) 0 Oe, b) 8 kA/m, c) 20 kA/m, and d) 120 kA/m.

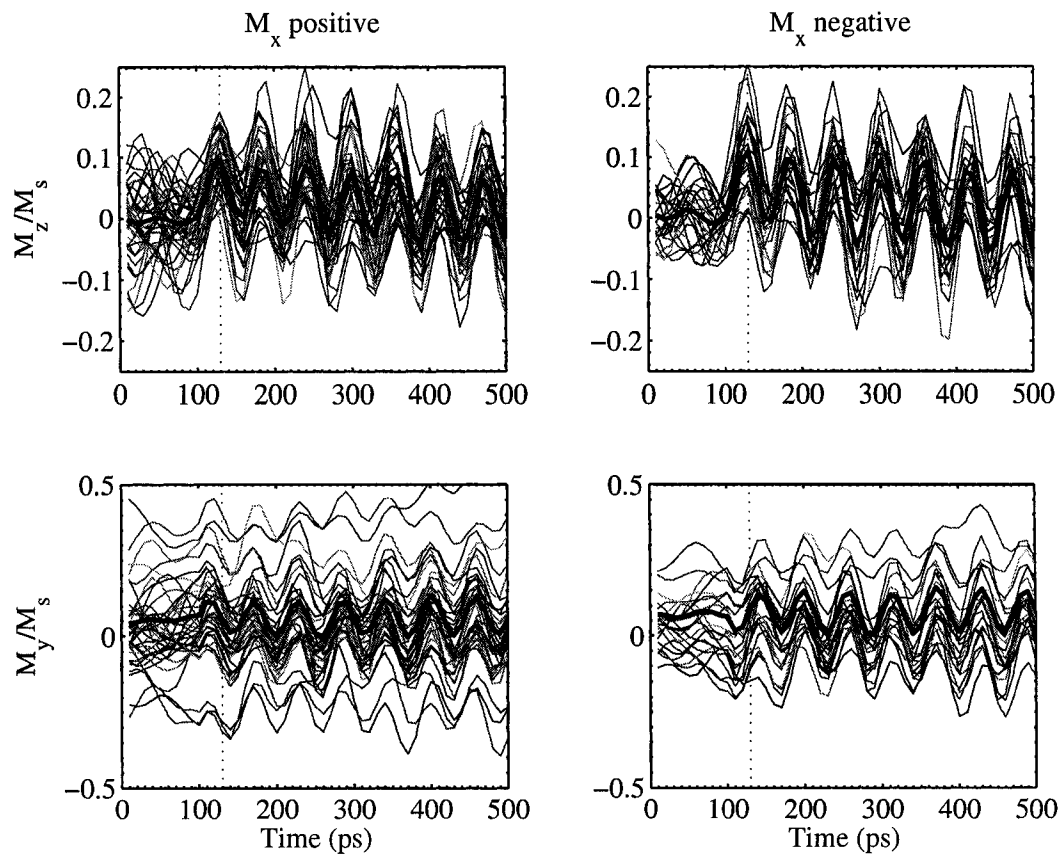


Figure 6.21: Magnetization as a function of time, y and z components, for a single cube from an area with stripes parallel to the x axis. The thick black line shows the average magnetization for each of the plots and the vertical dotted line marks the time of the first M_z peak. The cubes oscillate such that the y components of the magnetization are mirror images of each other and the z components are identical for the oppositely oriented stripes.

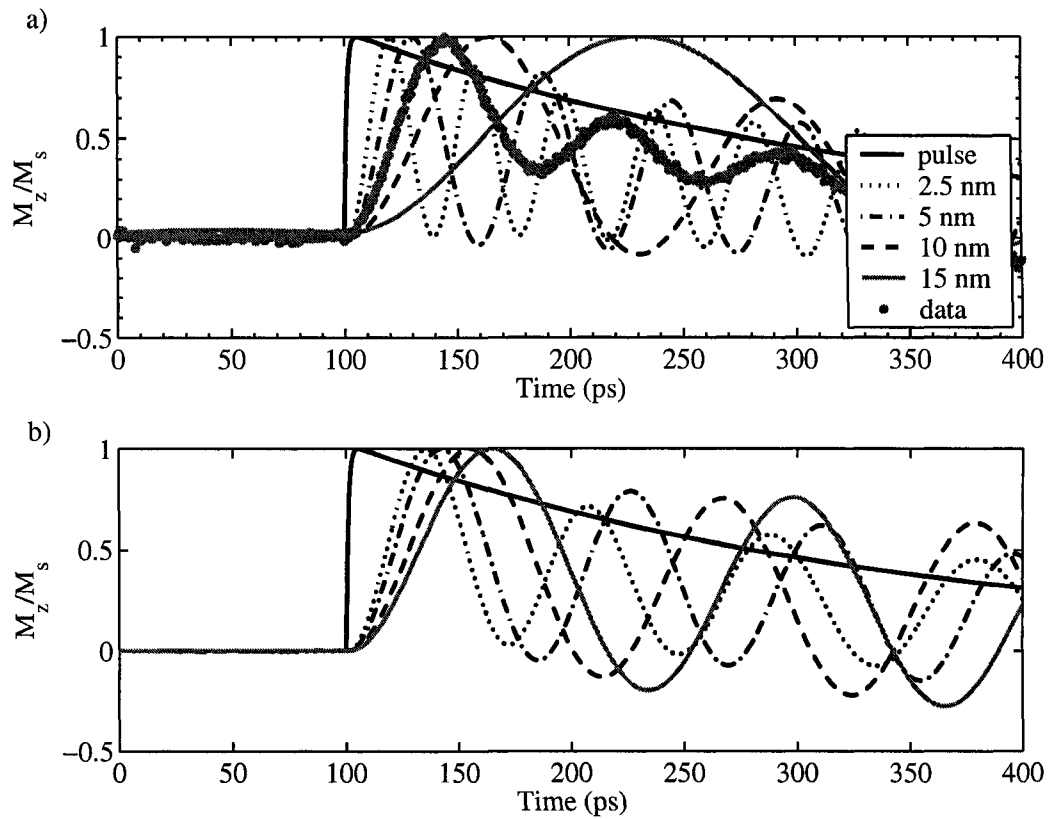


Figure 6.22: The z component of the magnetization for a regular array of Fe cubes for inter-particle separations ranging from 2.5 to 15 nm in a) zero bias field and b) a 120 kA/m (1500 Oe) in-plane bias field. The zero bias field data for the as-implanted sample (dots) are also shown in a).

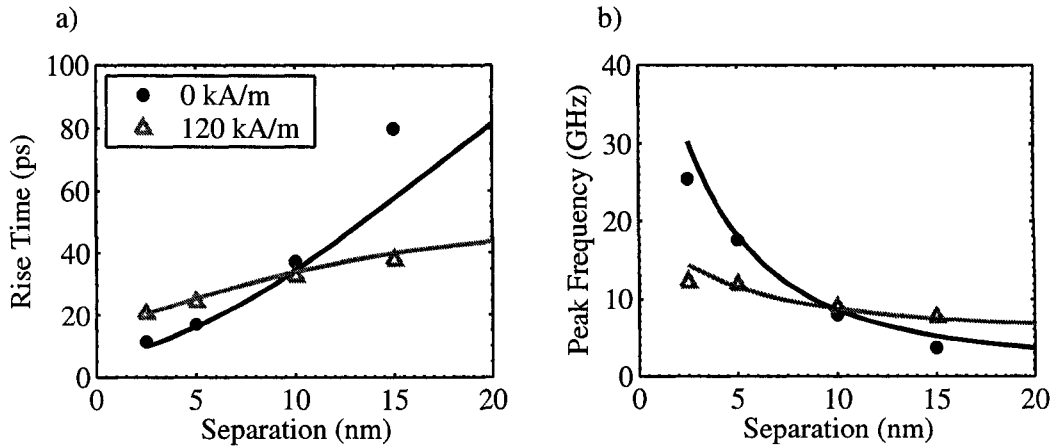


Figure 6.23: a) Rise times and b) peak frequencies measured from the M_z response for regular array simulations carried out at zero bias field (black asterisks) and an in-plane bias field of 120 kA/m (1500 Oe) (grey triangles) as a function of inter-particle separation. Solid lines of the same shade show the respective theoretical predictions.

6.5.3 Regular array response as a function of scale

The effects of length scale on the regular array model was also investigated. A model with cubes of 2 cells by 2 cells, separated by a single cell was used, with 128×128 cells in the full array. Cell sizes ranging from 1 nm to 10 nm were investigated with the thickness of the array chosen to maintain cubic nanoparticles. The initial states found in zero-field are very similar to that shown in Figure 6.3 for cell sizes of 3 nm and larger. For a cell size of 2 nm the initial state is more random but stripes are still visible (Figure 6.24) and with 1 nm cells, the initial state is almost entirely random and even deviates from in-plane magnetization (Figure 6.25). With the smaller particle sizes, thermal fluctuations are strong compared to other contributions to the total energy, which results in these more random initial states.

Figure 6.26 shows the z and y components of the magnetization as a function of time. The curves are virtually identical, with the exception of the models with 1 and 2 nm sized cells. The volume and separation are present in the theoretical prediction (equation 2.46) as a ratio V/a^3 , where V is the volume of a cube and a is the center to center separation between cubes. For this array, this ratio is $(2c)^3/(3c)^3$, where c is the cell size. The actual value for the cell size cancels out in this ratio so the resonance frequency is predicted to be the same for this model independent of the length scale. At large length scales this will

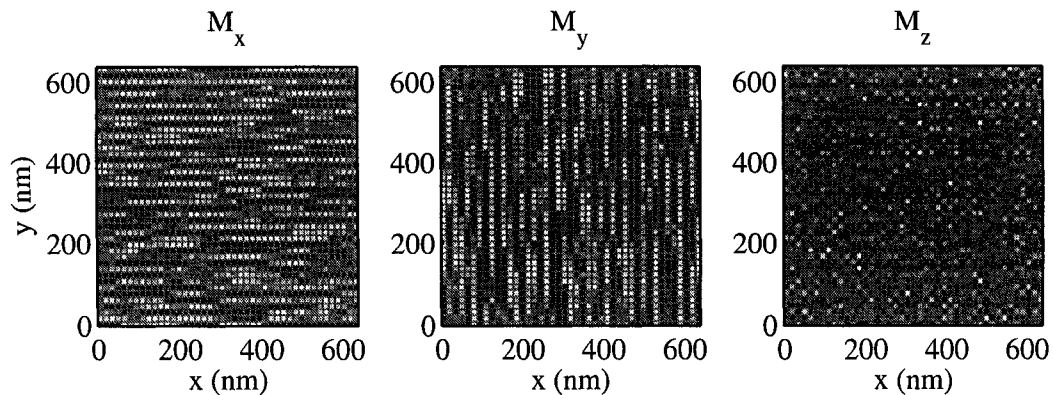


Figure 6.24: Initial state for a regular array of cubes, 2×2 cells, separated by 1 cell, cell size 2 nm.

break down when the individual nanoclusters become large enough that they no longer support the single domain state. At small length scales, thermal fluctuations will become important, as they do at cell sizes of 1 and 2 nm, and the initial state will no longer support the striped patterns assumed in the derivation. The same simulations were carried out for an in-plane bias field of 80 kA/m (1000 Oe) and again, the behaviour of the models with 1-nm and 2-nm cells deviates from the rest.

6.5.4 Regular array response as a function of pulse angle

In Section 5.2.3, the temporal response of a nanocomposite specimen was measured at different locations between the wires. The details of the response shape were different, as was the rise time, depending on the location at which the measurement was made for an in-plane bias field of 140 kA/m (1750 Oe). At the mid-point between the two wires, the transient magnetic field is entirely out-of-plane. Near the edges of the wires, however, there is also an in-plane component to the transient field. The experiment is designed such that the in-plane bias field is applied in a direction perpendicular to the wires (parallel to the in-plane transient field). If the experiment is well aligned then the in-plane transient field should have no effect on the resonance frequency observed. If, however, the bias field is slightly misaligned, there will be a small in-plane component to the transient field that is perpendicular to the bias field.

6.5. TEMPORAL RESPONSE TO A PHOTOCONDUCTIVE SWITCH PULSE

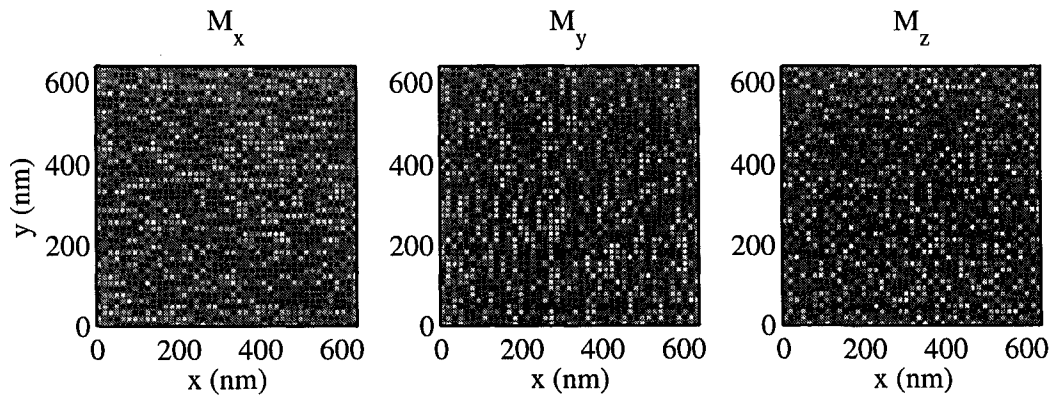


Figure 6.25: Initial state for a regular array of cubes, 2×2 cells, separated by 1 cell, cell size 1 nm.

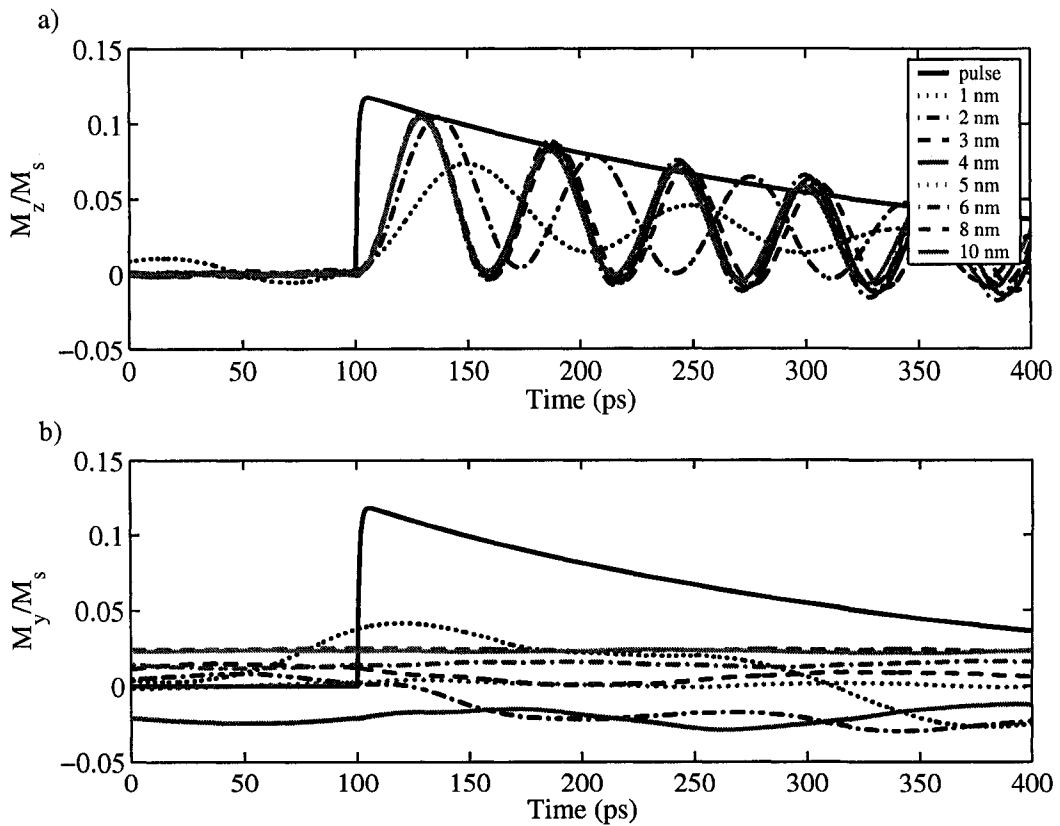


Figure 6.26: The a) z , and b) y components of the magnetization for a regular array of Fe cubes with cell sizes ranging from 1 to 10 nm where the cubes are made up of 2×2 cells and are separated by 1 cell. No bias field was applied for these simulations.

6.5. TEMPORAL RESPONSE TO A PHOTOCONDUCTIVE SWITCH PULSE

Simulations were designed to test the effects of the presence of this in-plane transient field. The in-plane bias field was applied to the regular array along the negative x direction and the transient field was applied at various angles θ in the $y - z$ plane, where a 90° angle represents the positive z direction. Figure 6.27 shows the results of these simulations for an in-plane bias field of 140 kA/m (1750 Oe). A phase shift is introduced depending on the angle of the transient field. The oscillatory part of the M_z response is proportional to $\sin(\theta_{shift} + \omega t)$ and M_y to $\sin(\theta_{shift} + \omega t - \pi/2)$. The phase shift angle θ_{shift} should be equal to θ when the pulse is in the z direction and close to but not necessarily equal to θ for other angles.

The important result here is that introducing a y component to the pulse results in a phase shift, the direction of which is related to the direction of this y component. This will have a direct impact on experimental rise time measurements. In order for valid statements to be made concerning experimental rise-time trends, care should be taken both in achieving optimal alignment of the bias field and in ensuring that measurements are made as close to the mid-point between the transmission wires as possible.

6.5. TEMPORAL RESPONSE TO A PHOTOCONDUCTIVE SWITCH PULSE

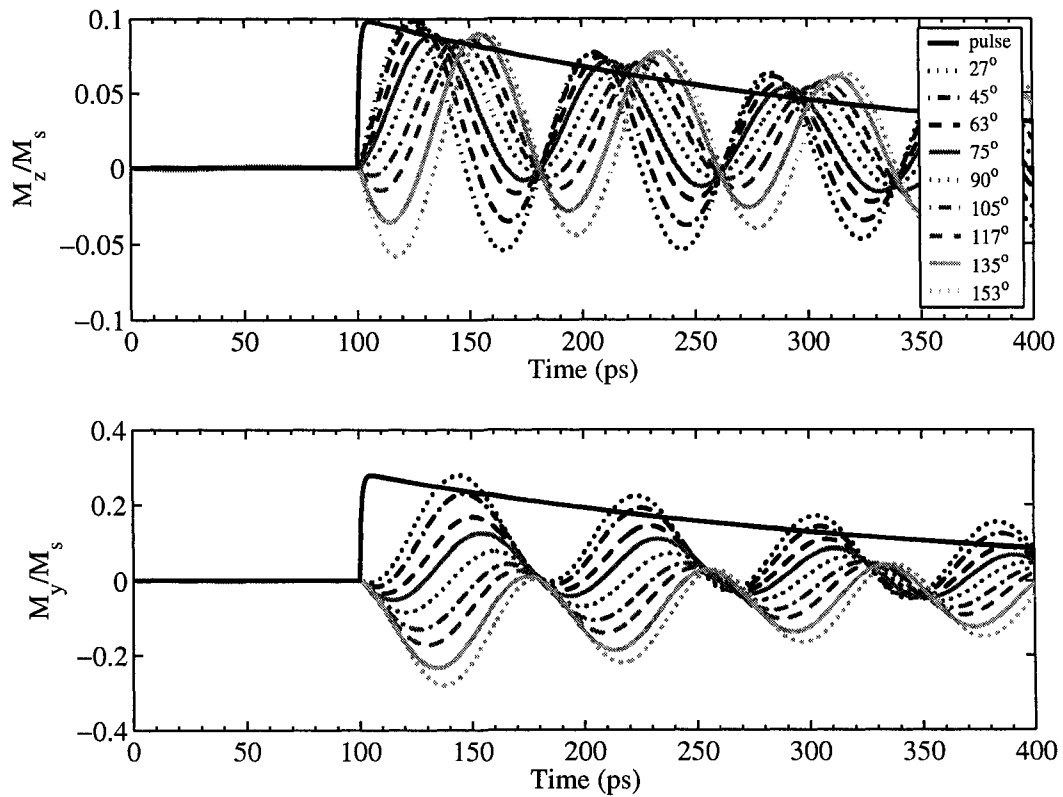


Figure 6.27: Magnetization, y and z components, as a function of time for a regular array of cubes subjected to a transient magnetic field in the presence of an in-plane bias field of 140 kA/m (1750 Oe) applied in the x direction. The angle of the transient field is varied in the $y - z$ plane, which results in a phase shift in the magnetization response.

6.5.5 Regular array response as a function of out-of-plane bias field

The effects of an out-of-plane bias field were explored for a regular array of 10 nm iron cubes with 5 nm separation. The initial states were found by starting from a random state and allowing the system to relax to a stable state in the presence of an out-of-plane bias field. Recall that for zero bias field, striped patterns were present but a larger scale vortex-like pattern, made up of areas with x and y oriented stripes, was also apparent (Figure 6.3). Figure 6.28 shows the initial state for a 320 kA/m (4 kOe) out-of-plane bias field. At this field, the striped arrangement is still dominant but the magnetization vectors for all of the cubes gain an out-of-plane component. The stripes in this case are almost all oriented in the same direction. At out-of-plane bias fields ≥ 560 kA/m (7 kOe), the magnetization vectors for all of the cubes align along the direction of the applied field.

The temporal simulations are shown in Figure 6.29. In Figure 6.29a, the bias fields are insufficient to result in a saturated initial state. In response to a transient pulse applied in the out-of-plane direction, the z components of the magnetization vectors oscillate in-phase, whereas the in-plane components of the stripes of opposing magnetization oscillate such that they cancel each other out. When the bias field is higher than that required to saturate the model, the cubes oscillate coherently about the z -axis, provided that the transient pulse is applied in the in-plane direction (Figure 6.29b). In all cases, oscillations are observed, but the frequency is very different depending on the magnitude of the bias field.

Figure 6.30 shows plots of rise time and peak frequency as a function of the magnitude of the out-of-plane bias field. At very low fields, the striped pattern dominates, at high fields the individual clusters precess all in the same direction about the out-of-plane axis, and at intermediate fields a more complicated version of the theory must be used. The dotted line in Figure 6.30b shows this more complicated theory, valid only below the saturation point (around 480 kA/m) (discussed in Section 2.4.2). The solid line shows the analytic high-field solution, which is valid at and above the saturation point (Equation 2.64). The particle volume V was replaced by an effective volume $V_{eff} = 0.94V$ to account for the discrepancy between the magnetic field from a cube calculated using dipole approximation as compared to the standard method used in micromagnetics simulations [83]. To match the smaller array size, $C = -8.76$ was used. The rise time theoretical curves

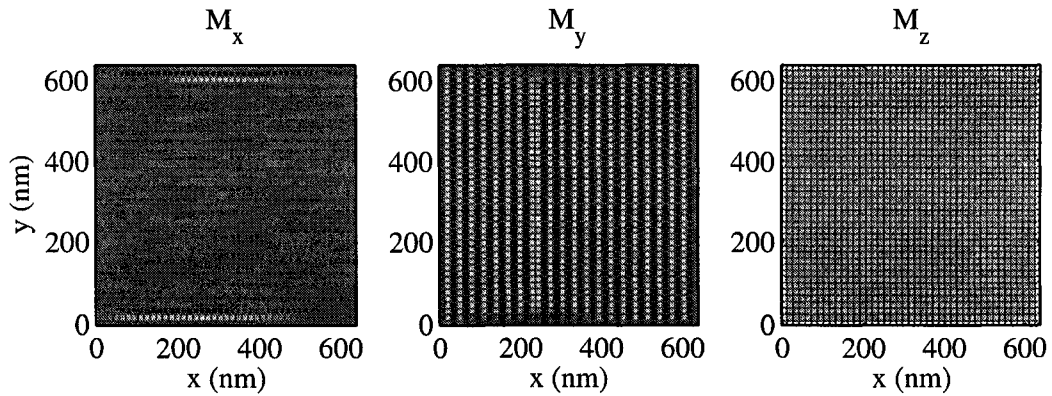


Figure 6.28: Initial state for a regular array of Fe cubes subject to a 320 kA/m (4 kOe) out-of-plane bias field.

are derived from the predicted frequencies through the relation $t_{rise} = \sin^{-1}(0.8)/(\pi f)$. The crossover from striped to uniform theory occurs at 480 kA/m (6 kOe), at which point the frequency is at a minimum of around 0.9 GHz and the rise time reaches a maximum of 330 ps.

6.5.6 Irregular array response as a function of in-plane bias field

The response of the random array of 10 nm cubes to an ultrafast transient magnetic field was simulated for in-plane bias fields ranging from 0 to 140 kA/m (1750 Oe) (Figure 6.31). The simulation conditions were identical to those for the regular array as a function of in-plane bias field and the results from Section 6.5.1 will be compared to those for the random array. As for the regular array simulations, the rise time is limited by the material response, not by the rise time of the transient field. The overall response follows the pulse shape and the oscillations in the z component of the magnetization are significantly lower in amplitude than for the regular array simulations. At low bias fields, there is no significant M_y response but at high fields, oscillations that are damped significantly after half a period are observed. The M_z response of the random array is closer to that of the nanocomposite specimens than the regular array response.

Figure 6.32 shows the rise times and frequencies for the random array simulations as a function of in-plane bias field. In this figure, the rise times are much more accurate than

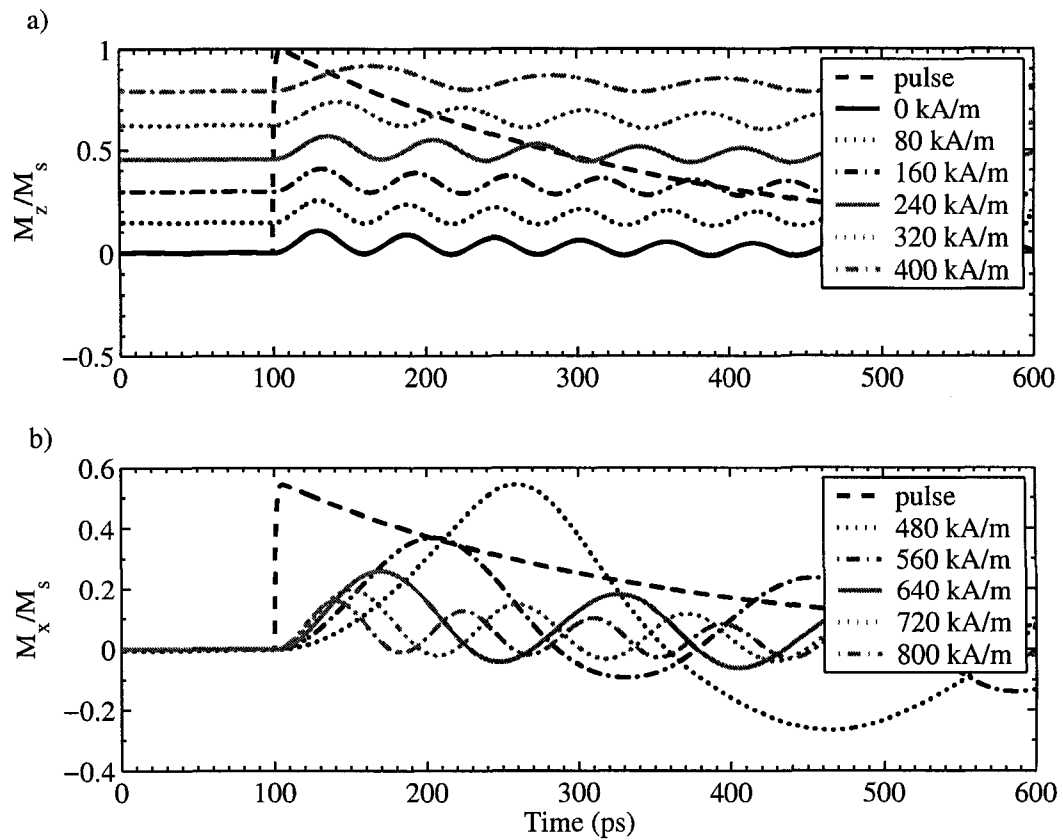


Figure 6.29: a) Magnetization (z -component) as a function of time for a regular array of cubes subjected to a transient out-of-plane magnetic field in the presence of an out-of-plane bias fields below the saturation field. b) Similar plots where the out-of-plane bias field is sufficient to saturate the magnetization of the specimen. In this case the transient field is applied in the x direction.

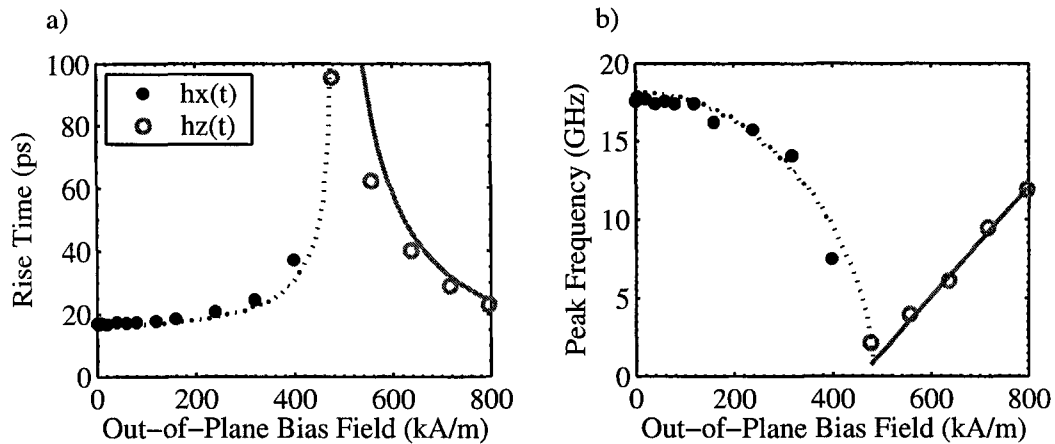


Figure 6.30: a) Rise time and b) resonance frequency as a function of out-of-plane bias field for a regular array of Fe cubes. The solid line represents the high-field theory and the dotted line represents the low-field theory. The legend indicates the direction of the transient field.

the frequencies. The simulation results contain a wide range of frequencies, whereas the rise times can be accurately determined from the M_z response in the temporal domain. The rise time plot shows a trend similar to that observed in both the experimental measurements and the regular array simulations. Rise times are slowest for mid-level bias fields where saturation of the model is incomplete. The rise times increase with in-plane bias field, which is not unexpected, but also increase as the in-plane bias field is decreased towards zero, where the initial state is stripe-like in nature.

The theoretical predictions for a regular array with an inter-particle separation $a = 12.5$ nm are superimposed on Figure 6.32. This separation value was chosen because it provides a reasonable fit to the high-field rise times. It also corresponds to the minimum inter-particle separation. The mean separation corresponds to $a = 15.8$ nm for this model. The theory is expected to describe the simulation results better in the high-field region where the assumption of uniform magnetization is met. The initial states at low bias fields are stripe-like in nature but the pattern is not as strong as for the regular array.

The shape of the theory at high fields is similar to the results. The striped array theory, however, underestimates the zero-field rise time using the same separation parameter. Another factor contributing to the underestimation of this rise time is that these formulae

6.5. TEMPORAL RESPONSE TO A PHOTOCONDUCTIVE SWITCH PULSE

were developed assuming that the magnetization is aligned close to an easy axis (i.e., the full anisotropy field is included). For the zero-field random array this will not necessarily be the case, thus the rise time is expected to be underestimated by the zero-field formula for the regular array. The zero-field frequency observed is still higher than the Larmor prediction based on the mean effective field, which is approximately 9 GHz. The zero field frequency (14.1 GHz) corresponds to an effective field of 360 to 400 kA/m (4.5 kOe to 5 kOe), depending on the magnitude of the anisotropy contribution, using the Larmor equation. Effective fields of this magnitude are present in this model (Figure 6.32a) but only for a small fraction of the particles. Overall, the random arrangement of cubes provides a moderating effect as compared to the regular array. The transition from striped behaviour to uniform is much more gradual, as is the rise-time trend. The zero-field rise time is also not enhanced as much as for the regular array simulations.

Histograms of the local effective fields found at each of the cubes in the irregular array model are shown in Figure 6.33 for in-plane bias fields of 0, 8, 20, and 120 kA/m (0, 100, 250, and 1500 Oe). These histograms are quite broad in comparison to those for the regular array (Figure 6.20). Note that the overall effective fields are slightly less at high bias fields than at low bias fields, a result which is also observed for the regular array. The averaged resonance behaviour for the irregular array was found to be closer to the overall shape of the pulse than the regular array results. This suggests that the frequency response of the irregular array is broadened for all in-plane bias fields as a result of the wide range of effective dipolar fields present in the array. The oscillations of the individual particles at different frequencies would result in the cancellation of the majority of the oscillations, which in turn would explain the rapid damping of the M_y response and the tendency of the M_z response to follow the pulse shape.

6.5.7 Comparison of data and simulations

Figure 6.34a shows the polar Kerr rotation from both the as-implanted and annealed nanocomposite specimens (u1 and u2) along with selected regular and random array simulations for zero bias field. Both models show a response that follows the pulse profile with oscillations superimposed. These oscillations are stronger for the regular array and suppressed in the random simulation, which is qualitatively closer to the experimental re-

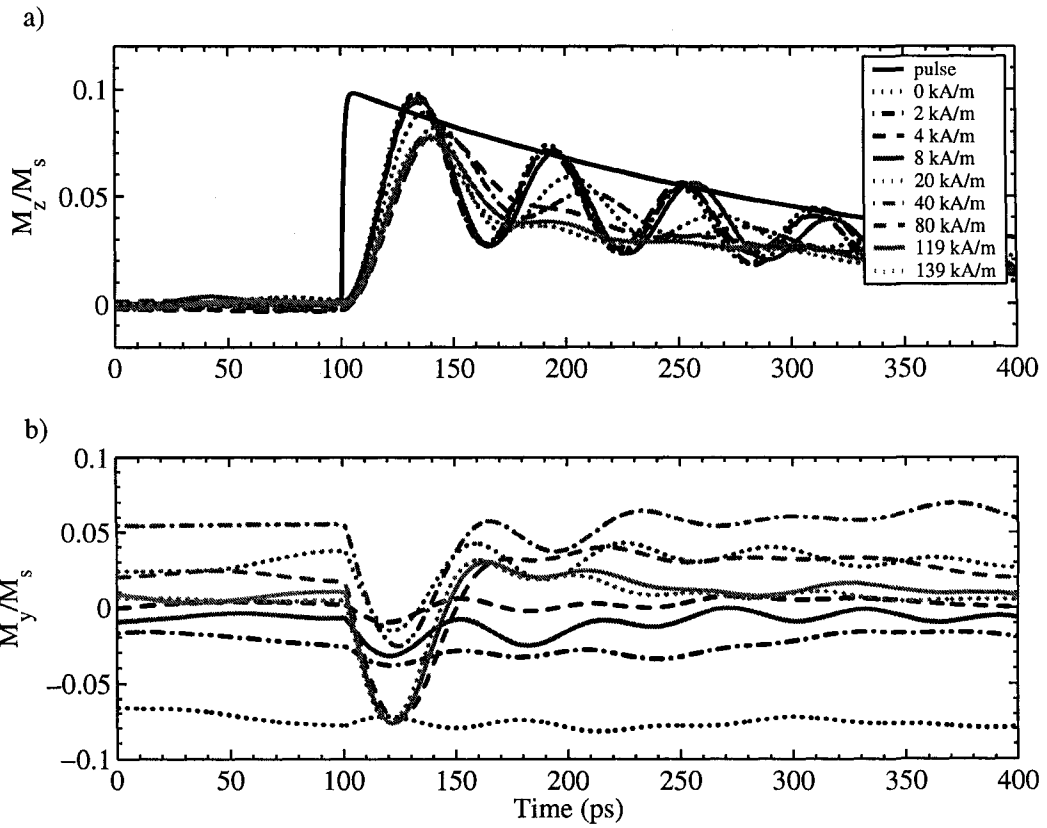


Figure 6.31: The a) z and b) y components of magnetization as a function of time for a random array of cubes subjected to a transient out-of-plane magnetic field in the presence of a range of in-plane bias fields.

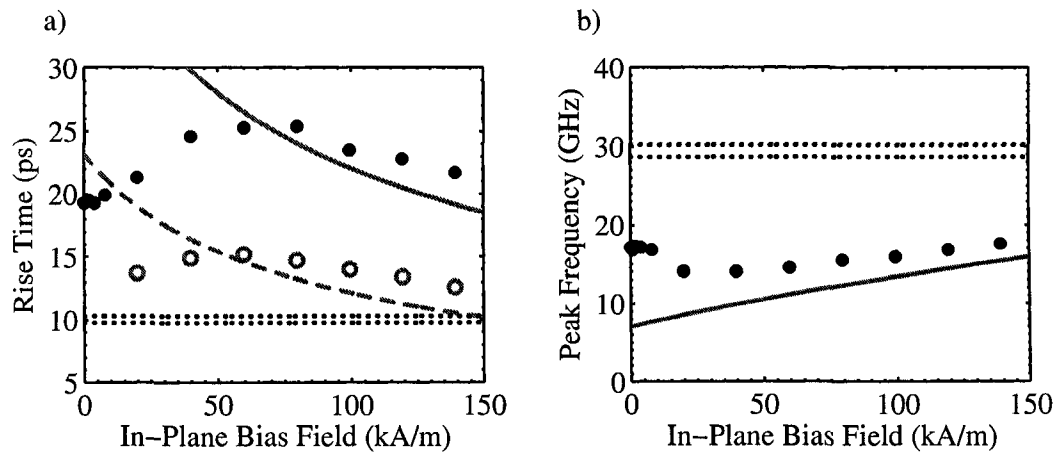


Figure 6.32: a) Rise time and b) resonance frequency as a function of in-plane bias field for a random array of Fe cubes. Solid dots represent the rise time and frequencies measured from the z component of the simulated response, while the open circles show the rise times for the y component. Solid line represents the high-field theory for a regular array where the value of $a = 12.5$ nm was used; dotted lines represent the zero-field theory, with and without anisotropy contributions, for the same a value. The dashed line in a) shows the high-field prediction for the rise time of the y component of the magnetization.

sults. The regular array rise times are comparable to the data at high bias fields, especially for sample u2, however, the zero-field enhancement is not observed to the same degree for the nanocomposites. The smoother rise time trend and smaller increase in zero-field rise time observed for the random array are closer to the experimental measurements (Figure 6.34b). The rise times are slightly faster for the simulations as compared to the experiments, which is to be expected as the models are relatively crude approximations of the sample. These results indicate that the dipolar interactions play an important role in the dynamics densely packed nanocomposites. In addition, the presence of a wide range of effective fields was found to be a significant factor in determining the shape of the response and the rise time trend. In the sample a range of effective fields is expected due to both the random particle placement and to the distribution of particle sizes.

6.5. TEMPORAL RESPONSE TO A PHOTOCONDUCTIVE SWITCH PULSE

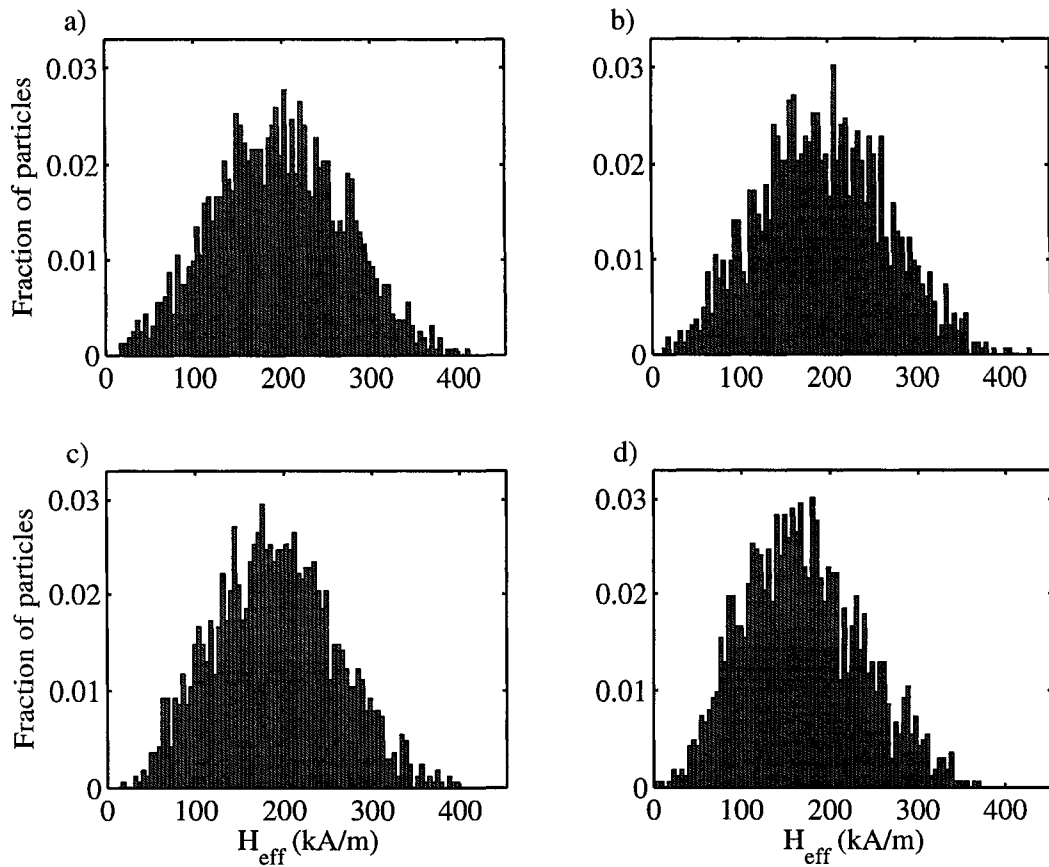


Figure 6.33: Histograms of local effective fields at each cube due to the dipolar fields of all of the other cubes in the model. Calculations are based on initial states for in-plane bias fields of a) 0 kA/m, b) 8 kA/m, c) 20 kA/m, and d) 120 kA/m for an irregular array model.

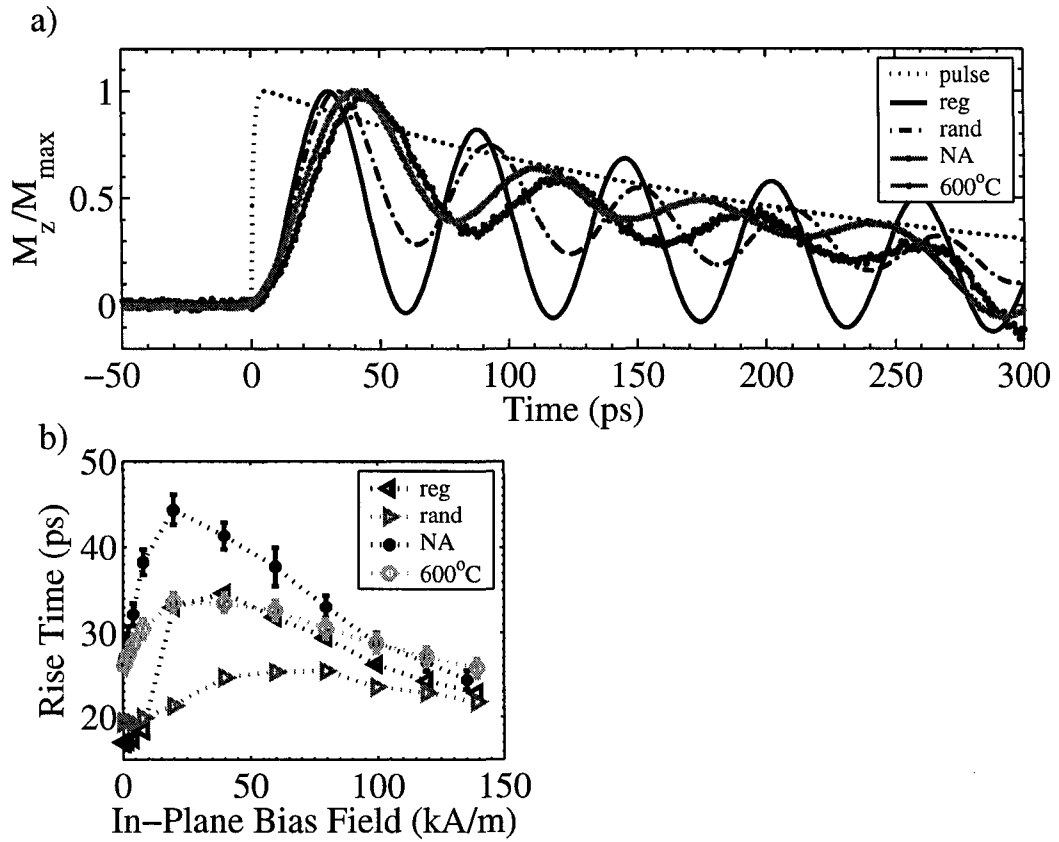


Figure 6.34: Comparison of simulations and data measured using a photoconductive switch showing a) M_z as a function of time for zero bias field and b) rise time as a function of bias field. The points are connected as a guide to the eye.

Chapter 7

Discussion

7.1 Comparison of experimental and simulation results

The simulations indicated that for a collection of closely spaced single domain iron nanoparticles, the dipolar interactions between the particles have a strong influence on both the static and dynamic properties of the ensemble. The particles do not interact through exchange as they have no nearest-neighbor contact and are chemically isolated by the SiO₂ matrix in the real sample. Based on the simulations, an illustration of the expected initial state for the specimen is shown in the top portion of Figure 7.1. The magnetization vectors of the spherical nanocrystals are expected to lie in-plane such that the net in-plane magnetization sums to zero. The magnetizations lie mainly in-plane for the same reason that thin-films are magnetized in-plane, that is, to reduce the overall demagnetization energy of the specimen. This interpretation is supported by the out-of-plane hysteresis loops, where fields of greater than 480 kA/m (6 kOe) are required to saturate the 80 kV iron implanted specimens, indicating the presence of a strong in-plane anisotropy and also by the simulations where very little out-of-plane magnetization is observed for the initial states.

The in-plane directions of the individual particles are influenced by the crystalline anisotropy and the dipolar interactions between particles. Ordered arrays of cubes tend to exhibit (in-plane) stripe formation to minimize dipolar energy, a phenomenon that is also

7.1. COMPARISON OF EXPERIMENTAL AND SIMULATION RESULTS

observed to a limited degree in more random arrangements of cubes. In the presence of an in-plane bias field, the nanocrystals reorient preferentially along the field and the initial state is still predominantly in-plane. A field of several tens of kA/m (hundred Oersteds), however, is required to cause all of the nanocrystals to align (the in-plane hysteresis curves in Fig. 4.10 show that these nanocomposites generally require a field much higher than the coercive field to achieve full saturation).

The strong interactions between the nanocrystals are believed to play a role in the slow in-plane switching of the nanocomposite. Although the agreement between simulations and experiment is not complete, some qualitative features are similar. The switching dynamics can be described by two time constants – a fast time constant (10 ns experimentally), which is thought to correspond to large-angle rotations of the magnetization of nanocrystals that are relatively free to re-orient along the direction of the field, and a slower time constant (300 ns experimentally) that corresponds to slower switching of particles that are pinned through dipolar interactions as well as the overall resettling of the magnetization of the composite into a new equilibrium through smaller-angle oscillations of the individual particles. Models that more closely resemble the specimen may be required to reproduce the in-plane dynamic response more accurately.

Micromagnetic simulations were able to qualitatively reproduce the ultrafast response to a 10 ns out-of-plane transient magnetic field pulse. The interpretation of this response is illustrated in the bottom of Figure 7.1. The z (out-of-plane) component of the magnetization follows the pulse shape almost exactly as the nanocrystals collectively tilt out-of-plane by a small amount in response to the transient field. The individual nanocrystals oscillate about the direction of the effective field at that location. The oscillations of the collection average out such that only a M_z signal is observed, which follows the shape of the pulse. The distribution of in-plane magnetization directions of the individual nanocrystals remains constant. At the end of the transient pulse the nanocrystals relax back into the initial state as quickly as they tilted out-of-plane.

To visualize the fast out-of-plane response, first consider a single domain, spherical magnetic nanoparticle aligned along a magnetic field in the x direction. When a transient field is applied in the z direction, there is suddenly an angle between the magnetic moment of the particle and the direction of the net effective field at that particle. The particle

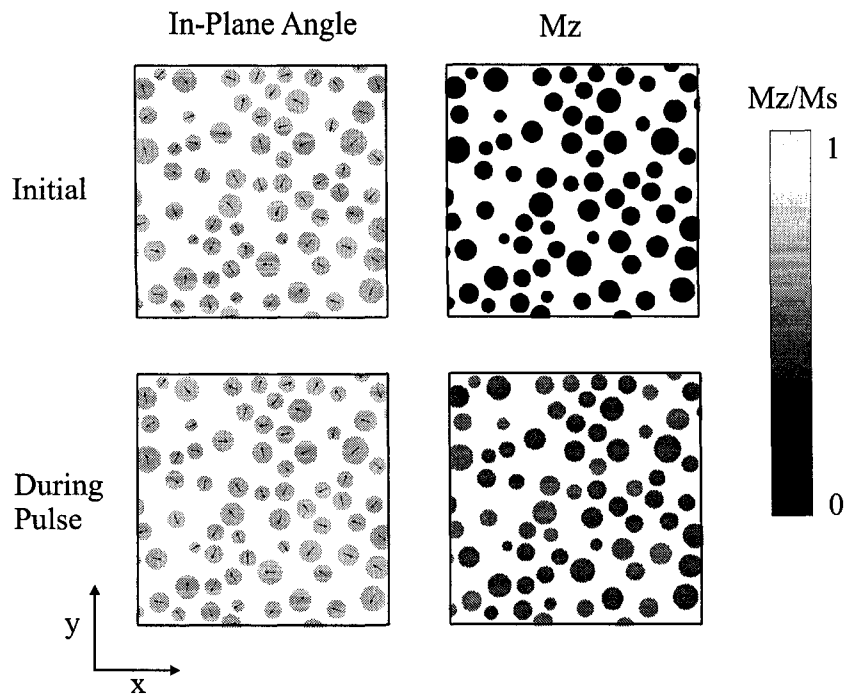


Figure 7.1: Diagram showing how the nanoparticles respond to a transient out-of-plane field. Initially the single domain nanoclusters are magnetized in-plane such that the overall magnetization of the specimen sums to zero. The arrows illustrate the direction of in-plane magnetization while the colour in the right panel represents the out-of-plane magnetization component. In response to a transient out-of-plane pulse, the magnetic moments of the particles gain a small z component on average. At the end of the pulse the magnetization reverts to its initial in-plane state. The individual particles oscillate about the local effective field but on average the oscillations cancel out resulting in only a net response in the z direction that follows the shape of the transient field.

7.1. COMPARISON OF EXPERIMENTAL AND SIMULATION RESULTS

will begin to precess around the direction of the effective field H_{eff} at a frequency ω_o proportional to its magnitude $\omega_o = \gamma\mu_o H_{eff}$, where γ is the gyromagnetic ratio for an electron spin (note: expression differs for non-spherical particles[72]). For an ensemble of non-interacting particles in this same bias field, the result should be the same – oscillations of the particles, all at the same frequency.

In the case of a collection of magnetic nanoparticles with strong dipolar interactions, the effective field experienced by a given particle is the sum of the external field and the fields generated by all of the particles in the ensemble. With the exception of very high external fields, there will be a range of effective fields present in the nanocomposite as well as a range of initial in-plane orientations. Having a range of frequencies will cause the oscillations to cancel out (on average), yielding a measure of the average magnetization for all three components. The in-plane components average to zero while the z component follows the shape of the out-of-plane transient field.

The out-of-plane dynamics of two nanocomposite specimens were explored in more detail using photoconductive switches to generate current pulses with rise times on the order of a few picoseconds. The iron nanocomposites that were examined contain similarities and differences in terms of their microstructural, optical and hysteresis properties. These samples contain spherical iron nanocrystals in the bcc crystalline form. Both specimens should contain close to the same amount of iron, although it is possible that a small amount is lost on annealing. The nanocrystals are generally slightly larger for the annealed sample (up to 25 nm in diameter as compared to 20 nm or less for the as-implanted samples) and are also distributed over a thicker layer (70 to 80 nm compared to 62 nm), with a few isolated nanocrystals more than twice as deep as the others. The in-plane and out-of-plane hysteresis curves for both specimens are very similar except that the in-plane coercivity of the annealed specimen is higher and the Faraday rotation is smaller.

Micromagnetic simulations were able to qualitatively reproduce both the ultrafast response to an out-of-plane transient pulse and the rise-time trend observed for the data taken using photoconductive switches. Similar rise-time trends were observed in both the experimental measurements and for the regular and random array simulations. Rise times were found to be slowest for mid-level bias fields and increased as a function of both increasing and decreasing in-plane bias field from this point. The simulations in-

7.1. COMPARISON OF EXPERIMENTAL AND SIMULATION RESULTS

dicating that ordered arrays of cubes tend to exhibit in-plane stripe formation to minimize dipolar energy, a phenomenon that is also observed to a limited degree in more random arrangements of cubes. This stripe formation is directly linked to the increased zero bias field rise times and it has been shown both theoretically and in simulations to lead to an enhancement of the resonance frequency by more than a factor of two over that expected from the magnetostatic dipolar fields alone. For the simulations, the slowest rise times, which were observed for mid-level bias fields, corresponded to incomplete saturation of the model and weakening of the stripe-like patterns. At higher bias fields, the models approach or reach saturation and the magnitude of the external field becomes the most important factor in determining the resonance frequencies and rise times.

Overall, the results for the random array simulations were more similar to the measurements on the nanocomposites than the regular array responses, suggesting that having a distribution of inter-particle spacings, and hence a distribution of effective magnetic fields, is an important factor in suppressing stronger oscillations in the temporal response. Zero field enhancement of the resonance frequency is still observed but to a lesser degree. The exact shape of the particles (only symmetric particles were examined) and the directions of the crystalline anisotropy axes has a lesser influence on the dynamic behaviour of the system. The random arrangement of cubes provides a moderating effect as compared to the regular array. The transition from striped behaviour to uniform is much more gradual, as is the rise-time trend. The zero-field rise time is also not enhanced as much as for the regular array simulations.

The two nanocomposites showed very similar rise-time trends. For the experimental measurements, the rise times for the two nanocomposites agree within error at zero field and high fields. At intermediate fields, however, the rise times were faster for the annealed sample and slower for the as-implanted sample. In other words, the overall rise-time trend is less pronounced for the annealed sample as compared to the as-implanted one. The slowest rise time for the as-implanted specimen was also observed to occur at a slightly lower field. This is consistent with the hysteresis measurements in that the as-implanted specimen showed both a smaller coercivity and a lower saturation field as compared to the annealed specimen. The lowering of the rise time peak could indicate that the annealed sample contains a broader range of effective fields for these bias fields.

7.1. COMPARISON OF EXPERIMENTAL AND SIMULATION RESULTS

The nanocrystals were observed to be less compactly packed overall in cross-sectional electron micrographs of the annealed specimen. This specimen, however, contains larger particles as compared to the as-implanted specimen that are close together, which would generate higher local effective fields and explain the faster rise times observed for intermediate bias fields.

The importance of dipolar interactions in understanding the magnetic properties of collections of nanoparticles has often been overlooked in the past. In interpreting magnetic hysteresis curves in particular, non-interacting models have been favored for their simplicity. It is only very recently [8,26] that the inter-particle interactions have been shown to be necessary for a full understanding of the hysteresis curves for these types of materials and have also been shown to lead to dipolar-based anisotropy effects depending on detailed arrangement of nanoparticles [27].

The role of dipolar interactions in determining the dynamics of ferromagnetic nanostructures is a topic that has gained attention even more recently. One study examined the ferromagnetic resonance of periodic arrays of lithographically patterned submicron sized permalloy disks [113]. They report finding a number of ferromagnetic resonance peaks, in contrast to the single peak expected for a continuous film, that they associate with coupled exchange and dipolar spin-wave modes. Their experiment differs significantly from the nanostructures examined here in that the individual patterned structures are not small enough to be single domain. It does, however, confirm that dipolar interactions are important in determining the dynamic behaviour of collections of small magnetic structures. A study examining the ferromagnetic resonance of iron implanted SiO₂ (100 keV, 0.1, 1.7, and 2.8×10^{17} ions/cm²) showed that the angular dependence, from out-of-plane to in-plane, of the results can be fit using the resonance equation for a thin film, the agreement with which was attributed to the dipolar interactions in the specimens [58]. The form of the Kittel formula for a thin film is the same as that for a uniformly magnetized array of nanoparticles in both the in-plane and out-of-plane directions (Chapter 2 or Appendix A), which is consistent with this interpretation. The results presented in these studies and in this thesis indicate that the interactions are not only important in determining the static magnetic properties but also play a role in defining the characteristics of the dynamic response of magnetic nanocomposite materials.

The results presented here (and in Refs. [56] and [57]), supported further by more recent measurements made by another member of the same group [93], support the belief that this fast out-of-plane response should be observed for collections of magnetic elements that meet the following criteria:

- The individual particles are single domain,
- The particles are exchange decoupled through physical separation but close enough together that inter-particle interactions are important (i.e., the dipolar magnetic fields experienced by the individual particles are higher than the effective anisotropy field), and
- The material must be thin enough that the demagnetization energy will favour an in-plane equilibrium magnetization state.

In addition, particles with a random component to the arrangement should follow the shape of an out-of-plane pulse more closely than a regular array because a wide range of frequencies will be excited. For a regular array coherent oscillations are expected at fast time-scales.

7.2 Technological implications

7.2.1 Ultrafast current probe

An iron nanocomposite has been found to exhibit “giant” Faraday rotation, which is an important property for magneto-optical applications. In addition to the large Faraday rotation, the material also exhibits unusually fast magnetic relaxation, a property that is of immediate technological interest. Specifically, these types of materials may be useful for measuring the profile of current pulses with bandwidth upwards of 14 GHz with submicron spatial resolution [114]. Combining ion implantation with existing solid immersion lens technology could further enhance the spatial resolution of this probe. It should be straightforward to extend the resolution to several hundred nanometers by implanting a solid immersion lens made of a high-refractive-index glass. This would provide higher spatial resolution than any previous magneto-optical probe, which would be important

for characterizing ultra-large-scale integration (ULSI) circuits (more than one million circuit elements on a single chip). Furthermore, it should be possible to extend the spatial resolution of this probe down to several tens of nanometers, if the Fe nanocrystals can be formed in a suitable host material possessing a higher refractive index than fused quartz ($n = 1.46$). In addition to being useful in high-speed current probe applications these nanocomposite magnetic materials may also be useful for other magneto-optical applications such as all-optical switches, or optical modulators.

This material exhibits unusually fast magnetic relaxation in response to an out-of-plane transient magnetic field. This fast relaxation response is maintained over a range of in-plane bias fields including zero in-plane bias, a feature that is unusual and represents a significant advantage over materials used at present for current sensing applications. Previously the profiles of fast current pulses have been mapped magneto-optically using yttrium iron garnet. The main disadvantage to this technique is that in order to achieve similar temporal resolution to that exhibited by the nanocomposite, an in-plane bias field of almost 3 Tesla must be applied to raise the resonance frequency high enough above the bandwidth of the current pulse [115]. Using the Fe/SiO₂ nanocomposite, the profile of a fast current pulse with a rise time of less than 26 ps can be resolved easily with an excellent signal-to-noise ratio, without the need for applying any in-plane bias field. Therefore, compared to existing materials, this Fe/SiO₂ nanocomposite has some very attractive properties for fast magneto-optic sensing (no need for extra bias fields, extremely fast response times, large Faraday rotation).

One particularly interesting implementation of this magnetic nanocomposite is through the implantation of a solid immersion lens. Solid immersion lenses (SIL) are usually hemispheres or aplanatic hemispheres made of transparent materials [116]. The SIL is positioned between the objective and the sample with the flat side of the lens positioned a distance of less than a wavelength (of light) away from the sample surface. The higher index of refraction of the SIL allows for a sharper focus and the close proximity allows for near-field optical coupling between the SIL and sample. Spatial resolution of around 100 nm can theoretically be achieved using a solid immersion lens made of high index glass. Terris *et al.* (1994) [117] report a spot size of 317 nm with 780 nm light using a glass SIL ($n = 1.83$); a spot size of 125 nm is expected using blue light.

There are two possible ways of further improving the spatial resolution of the proposed high-speed current probe. The first involved the use of higher index of refraction materials. If Fe nanoclusters can be formed successfully in higher index of refraction materials such as rutile or high bandgap semiconductors such as ZnS, spatial resolution of tens of nm could, in theory, be achieved. The second involves using the masking technique to create very small implanted areas. The contact mask technique for creating micron-scale patterned nanocomposite arrays discussed earlier in this thesis and in Ref. [55] should be easy to adapt to obtain smaller sizes. For a 50-nm-wide opening in a contact mask, which could be fabricated using electron-beam lithography, an implanted area approximately 80-90 nm wide would be expected (implanted area is larger due to lateral straggling). The ultimate resolution is also affected by the thickness of the magneto-optical layer. Large Faraday rotation is observed from a nanocomposite layer only 60 nm thick, which would permit excellent spatial resolution.

Standard solid immersion lenses have already been demonstrated to be useful in time-resolved magneto-optical applications [118] but to date there have been no reports of coating or implanting the lenses with magneto-optical materials for measuring fast electrical currents. This implementation would improve the overall resolution beyond current capabilities as well as overcoming the need to attach a magneto-optic film directly to the circuit of interest.

Micromagnetics simulations, as well as ferromagnetic resonance theory, suggest that the resonance frequency of the material may be tunable, i.e., that the properties of magnetic nanocomposites could be customized to suit a particular application, which would extend the usefulness of this type of material. Simulations carried out to date agree qualitatively very well with experimental measurements, indicating that computational studies can be used to direct future experiments to minimize trial and error in developing the magnetic nanocomposite materials for current probe or other applications.

To summarize, the Fe/SiO₂ nanocomposite material described in this thesis exhibits giant Faraday rotation and ultrafast magnetic relaxation - properties that make it immediately useful as an ultrafast magneto-optical current probe (see Figure 7.2 for an illustration of how it would be incorporated into a magneto-optical measurement system for measuring currents). The opportunity exists to extend the spatial resolution to a few hundred

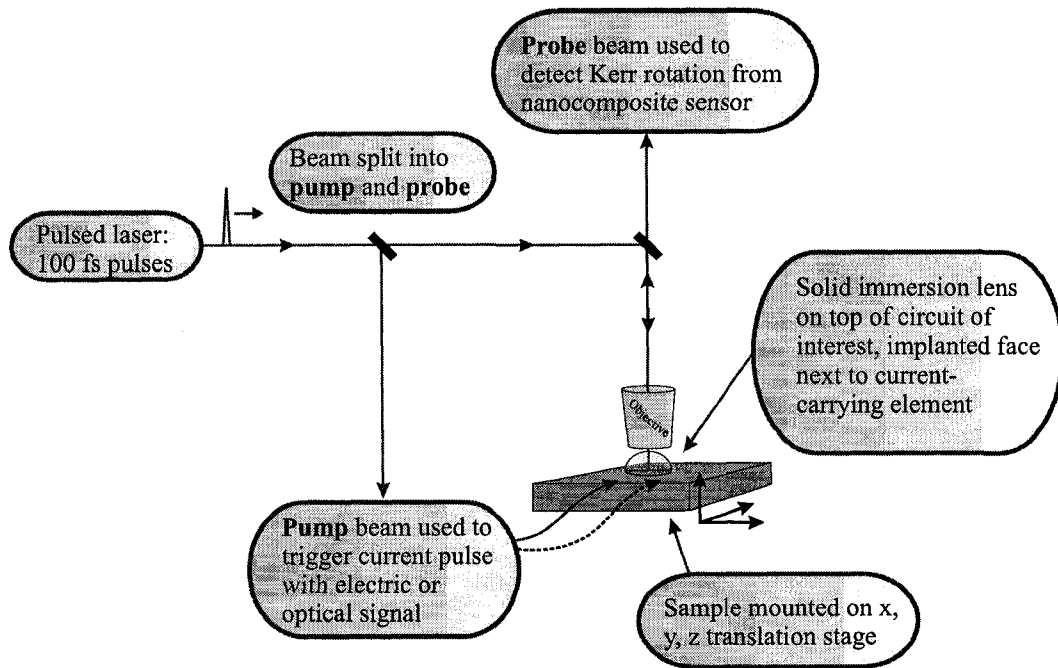


Figure 7.2: Illustration of how an ion implanted SIL lens can be used as an ultrafast current probe.

nanometers, possibly a few tens of nanometers, by creating an implanted solid immersion lens. An alternate implantation protocol that could be more convenient in certain applications would be to create fiber optic current probe through the implantation of the end of a fiber optic cable. In addition, this material also has the potential to be useful for other magneto-optical applications such as Faraday isolators, or all optical switches and modulators.

7.2.2 Considerations in MRAM development

There is currently great interest in magnetic random access memory (MRAM) devices. In fact, IBM announced in June 2003 that they anticipate having MRAM ready for production as early as 2005 [119]. A recent article reports on efforts in exploring the limits on the speed of magnetic reading and writing in the context of magnetic storage media [3]. Ferromagnetic resonance frequencies were measured for magnetic microstructures using a configuration similar to that used for the photoconductive switch measurements reported

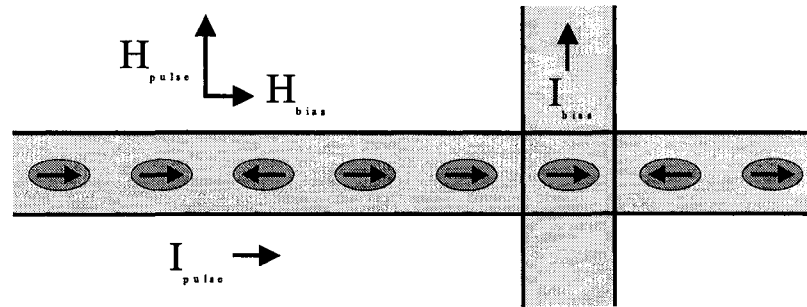


Figure 7.3: Diagram illustrating a possible plan for precession-limited fast MRAM [3].

in the previous chapter and they also explore the limits of coherent, precessional magnetic reversal for single micron-sized permalloy elements. Frequencies of up to 4 GHz were reported for magnetic element $10\ \mu\text{m}$ wide by $20\ \mu\text{m}$ long, and $16\ \text{nm}$ thick that are well described by Kittel formula predictions. To explore switching through coherent rotation, two photoconductive switches were used to generate a pulse with a fast rise time and an equally sharp fall-time. The pulse was used to induce a torque, which causes the magnetization to reverse through large-angle precession. The timing between the two pulses was carefully chosen so that the pulse was terminated at half the precessional period, which is theoretically the fastest that a magnetic element can be switched. Precession-limited switching was then demonstrated using a small static magnetic field ($0.8\ \text{kA/m}$ or $10\ \text{Oe}$) applied along the long axis of an elliptical element ($8\ \text{nm}$ thick, lateral dimensions 10 by $20\ \mu\text{m}$) to ensure uniform magnetization and a larger transient field, a $6\ \text{kA/m}$ ($70\ \text{Oe}$) pulse applied in the direction perpendicular to the static field (but still in-plane), to switch the magnetization of the element.

The coherent rotation results of the study detailed above [3] were discussed in the context of a magnetic random access memory (MRAM) device. Figure 7.3 illustrates their suggested arrangement for ultrafast MRAM. In this design, a bias field is applied to a given element using a current through a vertical wire while the transient field is applied through the horizontal wire (bit line). The small bias field alone will not produce any torque so other elements along the vertical wire will not switch. The elements along the horizontal wire may, however, require some stabilization. At this size-scale, the interactions between the elements are not very large. Nevertheless, at smaller scales and

with higher packing densities the dipolar interactions could become significant. The results presented in this thesis indicate that for high packing densities, dipolar interactions could affect the resonance frequencies of the individual elements and that they may be an important design consideration in the development of high-density, high-speed MRAM devices.

The magnitude of the dipolar interactions effects can be estimated by comparing the predicted resonance frequencies for the lowest energy (highest field parallel to magnetization vector) state and the highest energy (highest field antiparallel to magnetization vector) state. For a regular array on a square lattice the former is the striped state ($H_{dipolar} = M_s V / (4\pi a^3) A$, with $A = 5.0989$) while the latter corresponds to the striped pattern with the magnetization vectors rotated by an angle of 90 degrees ($\hat{m}_{ij} = (-1)^i \hat{j}$, $H_{dipolar} = M_s V / (4\pi a^3) B$ where $B = -6.0343$ is defined in Chapter 2). The dipolar approximation is strictly only valid for spheres or else when the distance is large with respect to the element size. Nevertheless, it provides an order of magnitude estimate for the field due to inter-particle interactions. The precessional frequencies for the elements in Ref. [3] were well described by

$$\omega = \gamma \mu_o [(H_{ext} + M_s + H_{sx})(H_{ext} + H_{sx})]^{1/2} \quad (7.1)$$

where $H_{sx} = 160$ A/m (2 Oe) is the experimentally determined effective anisotropy field. Since only one element at a time is meant to be excited, the dipolar fields from the other elements can be considered as static external fields. Replacing H_{ext} with $|H_{ext} + H_{dipolar}|$ and using $M_s = 8 \times 10^5$ A/m (or 800 emu/cm³ for permalloy), the percentage difference in frequency for the maximum and minimum dipolar energy configurations $df = 1 - f_{min}/f_{max}$ can be determined for a given separation a . This calculation predicts that a 1% change in frequency will occur for a centre-to-centre separation of 39 μm .

Chapter 8

Conclusions

Iron nanocomposite materials containing a thin layer of strongly interacting Fe nanoparticles were fabricated by implanting Fe⁺ ions into a SiO₂ host material to a fluence of 1.5×10^{17} ions/cm². A patterning technique involving lithographic masking was developed to work in conjunction with the implantation process. This technique has proven useful for creating patterned magnetic nanocomposites for TR-SKEM applications [56] and micro-pixelated luminescent arrays of silicon nanoparticles [86].

The 80 kV as-implanted specimen was found to contain spherical, randomly oriented nanocrystals concentrated in a layer 62 ± 2 nm thick. The majority of the nanocrystals were around 10 nm in diameter with clusters as large as 20 nm present. Annealing the sample at 600°C resulted in an increase in both particle diameter and layer thickness. Particles ranging in size up to 25 nm in diameter were found in the top 70 to 80 nm of the specimen. The addition of a 200 nm coating was found to result in a slight increase the particle sizes for the samples annealed at 600°C as well as the nanocrystals being arranged through a larger depth range (from 140 to 320 nm from the surface of the coating).

Hysteresis curves were measured in both the in-plane and out-of-plane configurations for Fe/SiO₂ samples implanted at 80 and 150 kV to a fluence of 1.5×10^{17} ions/cm². The properties of samples annealed at 600, 800 and 1000°C for 1 hour were compared and contrasted with the as-implanted specimens. In general, coercivity (and particle size) were found to increase with annealing temperature. The 80 kV as-implanted was found

to have an in-plane coercivity of 1.8 ± 0.2 kA/m (22 ± 2 Oe) while the coercivity of the 600°C annealed sample was 3.7 ± 0.4 kA/m (46 ± 6 Oe). The coercivity of its coated counterpart was slightly higher at 4.9 ± 0.6 kA/m (61 ± 7 Oe). The increase in coercivity corresponds to a trend of increasing particle sizes present in the samples. The hysteresis curves for the 80 kV samples showed strong in-plane anisotropy, which is believed to be a consequence of strong inter-particle interactions, while the interactions were found to be weaker for the 150 kV specimens (Chapter 4).

The 80 kV as-implanted nanocomposite material was found to exhibit extremely large magneto-optical Faraday/Kerr rotation under both transmission and reflection. The Verdet constant is 7.9 ± 0.5 deg/A (6.3 ± 0.4 deg/cm/Oe), which for an applied field of 480 kA/m (6 kOe) yields a minimum Faraday rotation of 3,800 deg/mm (because the applied field is below the saturation field of the specimen, an even larger effect can, in principle, be expected for higher applied fields) [56]. Annealed samples from the same series were found to exhibit Faraday rotations that were significantly smaller (by approximately a factor of 4), which could indicate that the annealed samples possess a smaller amount of magnetic iron due to either diffusive losses, the formation of oxidized shells, or both (Chapter 4).

The dynamic properties of both the as-implanted 80 kV sample and the sample annealed at 600°C for an hour were successfully probed using time-resolved Kerr effect microscopy. The in-plane and out-of-plane switching dynamics were found to be quite different for the as-implanted sample. The in-plane response showed an almost linear change throughout the duration of the pulse followed by a slow relaxation that is well described by a two-exponential function with time constants of around 10 ns and 300 ns. The faster time constant also provides an excellent fit to the data obtained during the pulse. Micromagnetics simulations on simplified models of the nanocomposite were able to qualitatively reproduce the shape of the response and were also well described by a two-exponential fit.

An extremely fast response to an out-of-plane transient magnetic field was observed. Using an electronic pulser in conjunction with an optical delay line, the out-of-plane response time was determined to be at least 150 ps, limited by the measurement apparatus. The M_z signal was found to follow the shape of the transient field pulse throughout the measurement [56]. Simulations in this case were able to reproduce the expected response

for in-plane bias fields ranging from zero to 140 A/m (1.75 kOe) for a variety of simplified models.

This fast out-of-plane was explored in greater detail by using photoconductive switches to generate a transient magnetic field pulses with faster rise times. Response times as fast as 26 ps were recorded for the Fe/SiO₂ as-implanted sample as well as the sample annealed at 600°C [57]. A trend in the rise time and peak frequency of the response was observed experimentally; fast rise times were observed at very low bias fields (< 8 kA/m), slower rise times occur at intermediate fields, and the rise time increases again with the magnitude of the in-plane bias field up to 140 A/m (1.75 kOe), the maximum field applied (Chapter 5). Experimentally the rise-time trend for the annealed specimen is less pronounced, which indicates that there are higher effective fields present at intermediate bias fields as compared to the as-implanted specimen, which is consistent with the observation of larger particles that are close together in this specimen.

Micromagnetic simulations on simplified arrays of cubes show similar trends in both rise time and peak frequency, providing insight into the cause for these trends (Chapter 6). The trend for a regular array of iron cubes agrees well with the theoretical predictions developed in Chapter 2. For a regular two-dimensional array of nanoparticles, strong dipolar interactions promote the formation of a striped initial state that has been shown theoretically to enhance the low field resonance frequency by more than a factor of two over that predicted based on static dipolar fields. Randomized arrays show similar behaviour but to a lesser degree. These simulations indicate that the dipolar interactions between single domain nanoparticles play an important role in influencing the dynamic responses observed and that the exact particle size and shape (note that only particles with in-plane symmetry were considered) are not as important as the magnitude of the dipolar field. Other arrays of strongly interacting nanoparticles are expected to exhibit similar behavior. This ultrafast magnetic response may find use in technological applications, for example as an ultrafast current probe [114], as discussed in Chapter 7, and may also be an important consideration in the development of dense, precession limited magnetic storage devices.

There are a number of directions that could be taken in expanding on the research presented here. It would be informative to examine the specimens using electron holography

to determine how closely the low bias field initial states are represented by the random array simulations. In terms of simulations, there is certainly progress that could be made in the development of more efficient modeling techniques for collections of interacting nanocrystals. In addition to exploring models that provide a more realistic representation of the specimen, it would also be very interesting to examine the dynamic properties of specimens that match the simulations more closely. In particular, theoretical predictions for the resonance frequencies have been made for a regular array of magnetic nanocrystals that could be tested systematically as a function of in-plane and out-of-plane bias fields, as well as, the magnitude of the dipolar interactions (through adjusting spacing, volume, or M_s). The prediction for zero-field resonance enhancement for regular arrays could also be investigated.

Appendix A

FMR equation summary

Summary of ferromagnetic resonance equations for a regular array of dipoles.

Zero field: Initial state – striped.

$$\omega_o = \gamma\mu_o ((H_a + H_c(A - C))(H_a + H_c(A - B)))^{\frac{1}{2}} \quad (\text{A.1})$$

High in-plane bias field: Initial state – saturated in-plane.

$$\omega_o = \gamma\mu_o ((H_a + H_{ext})(H_a + H_{ext} + H_c(A_U - C)))^{\frac{1}{2}} \quad (\text{A.2})$$

Low out-of-plane bias field: Initial state – stripes in-plane, all dipoles tilted out-of-plane.

Use method of Smit and Beljers [76], modified to include demagnetization energy of the array. See Section 2.4.2.

High out-of-plane bias field: Initial state – saturated out-of-plane.

$$\omega_o = \gamma\mu_o (H_a + H_{ext} + H_c(C - A_U))^{1/2}, \quad (\text{A.3})$$

which is only valid when $H_{ext} > -H_a + -H_c(C - A_U)$.

The variables and constants are defined as follows:

-
- $\gamma = 1.76 \times 10^{11} \text{ Hz}\cdot\text{T}^{-1}$
 - $H_a = 2K_1/(\mu_o M_s)$, with $\mu_o = 4\pi \times 10^{-7} \text{ N/A}^2$, $K_1 = 4.7 \times 10^4 \text{ J/m}^3$, and $M_s = 1.714 \times 10^6 \text{ A/m}$ for iron.
 - $H_c = M_s V/(4\pi a^3)$, where V is the volume of an individual dipole, and a is the distance between the centers of adjacent dipoles in the array.
 - The constants are $A = 5.0989$, $B = -6.0343$, $C = -9.03362$, and $A_U = 4.51681$ for an infinite array. For an array size similar to that used in simulations, C is closer to -8.76 and A_U is closer to 4.38 .

To compare rise-times to theory, relationships between the rise-time and frequency can be developed. For an out-of-plane excitation, the initial rise of the z component of the magnetization can be described as $M_z(t)/M_{max} = 1/2(\sin(\omega t) + 1)$. The 10/90% rise-time t_{rise} , that is, the time difference between a points at 10 and 90% of the maximum pulse amplitude, is then related to the resonance frequency $f_o = \omega_o/(2\pi)$ by

$$t_{rise} = \frac{1}{\pi f_o} \sin^{-1}(0.8). \quad (\text{A.4})$$

The initial rise of the y component of the magnetization can be described as $M_y(t)/M_{max} = \sin(\omega t)$. The 10/90% rise-time for the y component is then

$$t_{rise} = \frac{1}{2\pi f_o} (\sin^{-1}(0.9) - \sin^{-1}(0.1)). \quad (\text{A.5})$$

If the transient excitation has an in-plane component perpendicular to the static bias field then this will modify the phase of the initial rise, which will in turn affect the rise-time.

The majority of the regular array simulations were carried out for an array of dipoles with $V = (10 \text{ nm})^3$ and $a = 15 \text{ nm}$. When comparing this theory to simulations, recall that the cubes are close enough together that the approximating them as a dipole actually results in an overestimate of the magnetic field they generate. The particle volume V can be replaced by a reduced effective volume V_{eff} to compensate for this discrepancy. For this particular regular array, the effective magnetic field for each particle due to the others was calculated using first the dipole approximation and second a standard method used in micromagnetics simulations for evaluating the demagnetization field for a cube [83], which yielded an effective volume of $V_{eff} = 0.94V$ (see Section 6.5.1).

Appendix B

Details of patterning technique

Implantation substrates were patterned with 5-10 μm Cu pillars or else to contain holes in a Mo or Cr film ranging from 0.5 μm to 10 μm in diameter. A diagram of the mask used to generate the second pattern is shown in Figure B.1. It was designed for use with either 1 inch circular wafers, as high purity SiO_2 substrates of this size are readily available, or 1 cm^2 square wafers, which is a more common size for single crystal host such as Al_2O_3 , MgO , or $\text{Y-Zr}_2\text{O}_3$. All masks were created using deep UV lithography at the University of Alberta Nanofab using standard processes. Thin films of Cu films were grown by thermal evaporation, while the Mo and Cr films were sputtered. Copper films were etched using a solution of ferric chloride (PC Board Etch), Mo was etched using H_2O_2 , and Cr was etched using a Chromium etchant.

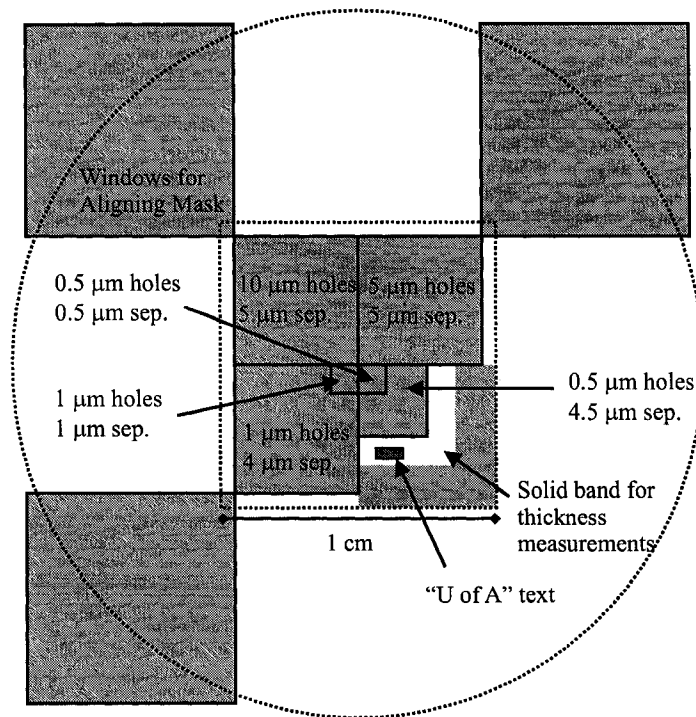


Figure B.1: Design of mask for optical lithography. Minimum feature size is $0.5\ \mu\text{m}$. Shaded areas will be entirely clear or else contain holes. The dotted lines show the outline of a 1 inch diameter circular wafer and a $1\ \text{cm}^2$ square wafer.

Appendix C

Magneto-optical hysteresis loop measurements

Instructions for a typical run

The basic optical set-up used in measuring hysteresis curves was introduced (Chapter 3). Here some additional details of the system will be discussed and instructions for a typical measurement run will be provided.

The components of the system are hooked into a DAQ card for computer control and data storage. A Labview program* is used to control the magnetic field of the electromagnet via a voltage programmable power supply (Kepco BOP 100-2M). For the in-plane configuration, a pole piece separation of 1.1 cm was used, yielding a maximum field of ~ 760 kA/m (9.5 kOe). The out-of-plane configuration requires a slightly larger pole piece separation distance, typically 2 cm, which resulted in a maximum field of ~ 480 (6 kOe). The two photodetectors in the set up (matched pair of PIN-10DP/SB photovoltaic detectors from UDT Sensors Inc.) are connected to a differential amplifier (Stanford Research

*Current version of Labview program is `hysteresis.k.vi`, which can be found on the computer *Vortex* in directory `c:/usr/kristen/`.

Systems Model SR560 Low-Noise Preamplifier[†]). The signal photodetector is connected in through input A while the reference is connected to input B. The differential signal from the amplifier (50 Ohm output) is then read in by Labview through the DAQ card (analog input channel 3). The magnitude of the magnetic field generated by the magnet is measured simultaneously using a gaussmeter (Walker Scientific MG-3D Precision Hall Effect Gaussmeter[‡]) and also recorded using the DAQ card (analog input channel 2).

Procedure for a typical run:

- Insert sample so that the beam hits a clean area not too close to the edge. A neutral density filter can be used to reduce the beam intensity for this step. Sample should be aligned using the flat edges of the sample holder so that the sample face is either parallel or perpendicular to the direction of the magnetic field, depending on the type of measurement to be made. Alignment to within 1 or 2° is possible. Visually check to make sure that the beam profile at the signal detector is clean and well aligned with the detector.
- Angle of incidence: For out of plane measurements, normal incidence is desired, which can be achieved by adjusting the angle of the first small mirror until the reflected spot from the sample comes close to retracing its path. For in-plane measurements the angle of incidence should be recorded once for a given configuration of the beam and magnet. To measure the angle of incidence, ensure that the sample is lined up such that its face is parallel to the magnetic field of the electromagnet. First note the angle rotation on the sample holder in the in-plane position, then rotate the sample while watching the position of the reflected spot until the normal incidence is achieved. Record this second angle, and take the difference between the two angles is the angle of incidence.
- Check (and record) the angle on the second polarizer. For samples where the rotation is not too large an angle of 2° from extinction works well. Smaller angles tend to give better signal to noise as long as they are not too close to extinction.
- Measure the beam intensity at the signal detector with no applied magnetic field.

[†]Typical operating parameters: 30 kHz, 6 dB/octave low pass filter, A-B, 100-500 times gain, and high dynamic reserve.

[‡]Some measurements were made using an FW Bell Model 6010 Hall Effect Gaussmeter.

This can be done using an oscilloscope connected to the output of the amplifier (50 Ohm) with the amplifier set to *A* and gain of 1, being sure to subtract off the ground level. The detector signal is linear in beam intensity up to a saturation point, which for the current set-up is around 300 mV. Care should be taken to not exceed this intensity at any point.

- After measuring the intensity of the signal beam, the reference beam should be balanced to the same intensity (choose *B* on amplifier) using the variable attenuator and any necessary neutral density filters.
- Select and record the appropriate scale on the gaussmeter.
- Choose run parameters in the Labview program. Typical run parameters are: either 10 V maximum voltage with 200 mV steps or 1 V maximum voltage with 10 mV steps, X max of 2.5 V, Y max is chosen based on maximum output from amplifier (0.1, 0.25, 0.5, 1, 2.5, 5, and 10 V are threshold values for DAQ card), 1 ms wait time, 10-30 runs, drift correction off, and 1 average/run. Maximum voltage and voltage steps can be varied to record hysteresis loops over any desired range (max. 10 V). To slow the looping speed, increase the wait time between measurements.
- The data are saved into two files. The .d00 file contains 4 rows: average hall probe voltage, average differential signal, and the standard deviations of each. The .dat file contains the data for all runs stored in $2 \times n$ columns, where n is the number of runs. The first n columns contain the hall probe voltages for each run and the remaining n columns contain the corresponding differential signals.
- If sample heating is believed to be an issue, a small thermocouple can be attached to the sample as close to the incident beam as possible. The DAQ card has an input channel designed for a thermocouple and the Labview code has been designed to monitor this channel for temperature.
- Note that the magnet is not cooled at present so check periodically to make sure that it is not too hot to touch. If it gets hot the resistance goes up and the field for a given applied voltage goes down.

-
- For measurements made in transmission, a reference sample should also be measured so that the Faraday rotation from the substrate can be subtracted from the data.

Appendix D

Preparation of photoconductive switches

Design of wire/photoconductive switches

The design for the transmission wire/photoconductive switched used in the fast time-resolved MOKE measurements is shown in Figure D.1. Versions of this design were fabricated with narrow transmission wires with widths/spacings of $5/5\ \mu\text{m}$, $10/10\ \mu\text{m}$, and $20/20\ \mu\text{m}$. The wires connecting the narrow transmission wire area to the photoconductive switches were designed to be either 2 mm (short) or 6.4 mm (long), resulting in a total of six variations on the initial design. It is desirable to have the photoconductive switch as close to the sample area as possible in order to minimize the effects of dispersion on the current pulse. The design with the longer connection wires provides more space for placing the sample and for getting higher resolution objectives, even oil immersion lenses, closer to the sample without interfering with the beam that triggers the photoconductive switch.

A two-layer design was used for the photoconductive switches based on the design described by Gerrits[92,40]. A 10 nm thick under-layer of copper is used along with a

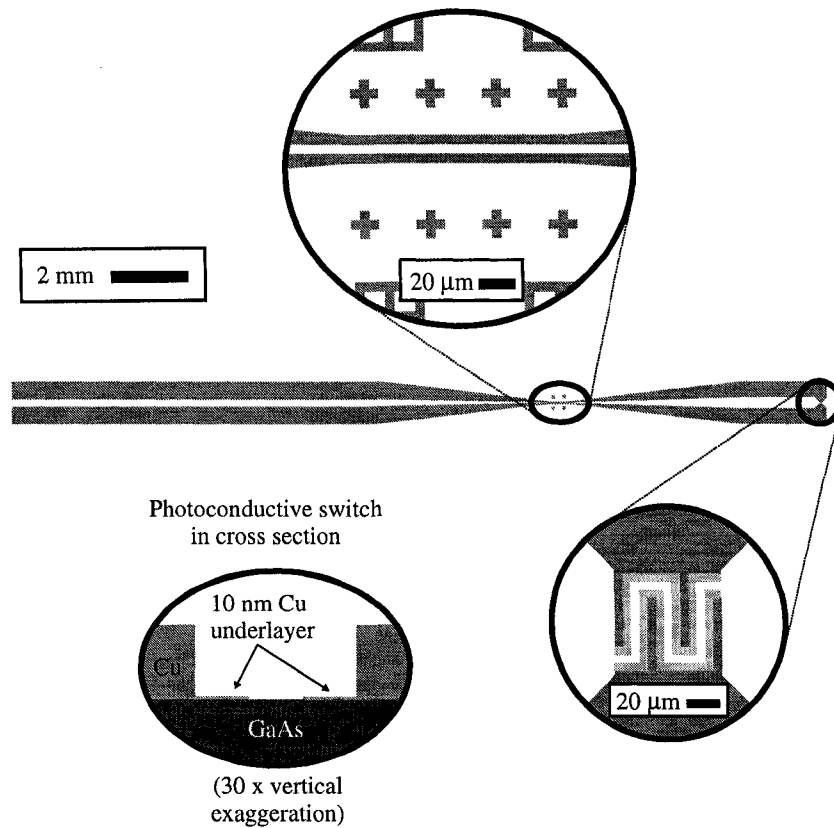


Figure D.1: Diagram (to scale) showing the design of the wires with photoconductive switches. Some of the important dimensions are: the leads are 14 mm long and the distance from the end of the region containing the narrow transmission wires to the beginning of the photoconductive switch is 6.4 mm. A second design has the photoconductive switch placed only 2 mm from the narrow wire region. The transmission wires in the sample region are $10\ \mu\text{m}$ wide and $10\ \mu\text{m}$ apart, 0.5 mm long. Similar structures were designed with $20\ \mu\text{m}$ width and spacing (1 mm long) and $5\ \mu\text{m}$ width and spacing (0.25 mm long). In all cases, the bottoms of the cross-shaped alignment marks, designed for e-beam lithography, are $25\ \mu\text{m}$ above the top of the upper wire and the tops of the alignment marks are $50\ \mu\text{m}$ below the bottom of the lower wire. The photoconductive switch, shown both from the top and in cross-section, consists two layers of copper on GaAs. The lower layer is 10 nm thick and the upper is 250 nm thick.

thicker (250 nm) copper layer. The under-layer is expected to improve the efficiency of the switches. It is thick enough that the conduction layer is extended if the beam is incident on the switch at an angle to avoid shadowing effects. It is also thin enough that carriers can still be excited under the layer in areas where there is no shadowing.

Process for fabricating photoconductive switches

The detailed processing steps for fabricating the photoconductive switch structures are detailed out below. A lift-off process was used involving two masks - one for the 10 nm copper under-layer and the other for the 250 nm copper over-layer on a GaAs substrate. In both cases a two-layer resist system was used. The top layer is a standard lithographic imaging resist and the bottom layer is a resist designed specifically for lift-off[120].

1. Clean the wafer using the "HCl dip" method:

- Prepare a 50:50 35% HCl: H₂O solution
- Dip wafer in the solution for 1 minute, rinse with DI water (making sure to flush acid from beneath tweezers)
- Blow dry with nitrogen

2. Spin on lift off resist (LOR)

- Use Microchem LOR 0.5A (use ~10 mL)
- Coating parameters: spread at 500 RPM for 5 s, spin at 3000 RPM for 45 s
- Bake resist in convection oven for 10 min. at 190°C

3. Spin on imaging resist

- Use HP504 photoresist (use ~10 mL)
- Coating parameters: spread at 500 RPM for 10 s, spin at 4000 RPM for 40 s
- Bake on hotplate under vacuum for 90 s at 115°C

4. Expose first layer

- Use mask labeled "wafer 2", designed for the 10 nm copper under-layer *
- Be sure that all alignment marks are on the wafer with the major flat of the wafer more or less centered in the large window of the mask
- Expose for 4 s

*Gerrit's design incorporates a SiO₂ layer to electrically isolate the GaAs from the copper layer. This layer was included in the mask design as "wafer 1" but never incorporated into the process.

5. Develop imaging resist

- Develop resist for 20-24 s in developer 354
- Rinse well in DI water and dry with nitrogen

6. Develop LOR

- Develop resist for ~20 s in developer CD-26
- Rinse well in DI water, dry with nitrogen

7. Deposit Cu

- Use e-beam evaporation[†] to deposit 10 nm of copper
- Parameters used – rate: ~1 Å/s, base pressure ~ 4×10^{-6} Torr

8. Lift off

- Use Remover PG at 70°C (measure the temperature with a thermometer; the hotplate display may not be accurate)
- It works well to have the wafer sitting in a petri dish and rock it gently back and forth
- This step generally only takes about a minute for completion

9. Spin on LOR

- For this step, use LOR 5B (~10 mL)
- Coating parameters: spread at 500 RPM for 5 s, spin at 3000 RPM for 45 s
- Bake resist in a convection oven for 10 min. at 190°C

10. Spin on imaging resist

- Use HP504 resist (~10 mL)
- Coating parameters: spread at 500 RPM for 10 s, spin at 4000 RPM for 40 s

[†]E-beam evaporation is preferable to sputtering for lift-off processes because deposition is more directional. Thermal evaporation would also work for copper but the source to substrate distance is quite close in the available system (around 20 cm), which would result in uneven coverage for a 3 inch wafer. For the e-beam evaporation system this distance is closer to 60 cm.

-
- Bake resist on a hotplate under vacuum for 90 s at 115°C

11. Align and expose second mask

- Use mask entitled "wafer3", which is designed for the 250 nm copper top layer
- Align the wafer in the mask aligner such that the major flat is under the main window in the mask.
- Carefully position the wafer under the mask, moving the crosses such that they fit exactly into the boxes. A mask aligner with proper illumination and video cameras attached makes this process much easier. Good alignment is critical for the performance of the switches.
- It is much easier to achieve good alignment with a full wafer as compared to smaller pieces. If smaller pieces are to be used, it is strongly recommended that the under-layer be omitted altogether.
- Expose for 4 s

12. Develop imaging resist

- Develop for 24 s in developer 354
- Rinse well in DI water, dry with nitrogen

13. Develop LOR

- Recommended developer is MF-319; MF-321 was used instead for a slightly shorter time of 24 s
- Sometimes undercut can be observed under an optical microscope
- Rinse well in DI water, dry with nitrogen

14. Deposit Cu

- Deposit 250 nm of copper by e-beam evaporation †
- Parameters used – rate: 5-7.5 Å/s, pressure $\sim 7-8 \times 10^{-6}$ Torr

†For the switches used in the most recent round of measurements, the Cu film grown with the e-beam system in Rm. 101 was 250 nm thick according to the thickness monitor (close to but not exactly at the same height as the wafer) and 290 ± 5 nm thick according to profilometer measurements.

15. Lift-off

- Use Microchem "Remover PG" heated on a hotplate to 60 to 70°C
- The copper is much thicker in this case so the lift-off process takes longer (usually around 45 min but it can take as long as 90 min). Several techniques were used to gently assist the process:
 - Gravity assistance: use a Teflon holder, much like for cleaning, to suspend the wafer upside down in a large beaker of the solvent
 - Rocked and twist holder back and forth
 - Apply short bursts of ultrasound

A note on mask fabrication

The masks used to make the photoconductive switches were made at the University of Alberta Nanofabrication facility. The mask writer used had two modes of operation for high and low resolution. The high resolution mode would have been the best mode for writing these masks but would have taken > 100 hours to write each of the 3 inch masks, which was considered to be too long. The low resolution mode, on the other hand, was able to produce each mask in under 12 hours.

The theoretical resolution limit of the low resolution lens is 5 μm , which is also the smallest feature size on this mask. In practice, some adjustments to the size of the smaller features on the mask had to be made in order to achieve the desired feature sizes. A mask containing a series of switches with different finger widths was written to test the accuracy of the low resolution mode in reproducing small features. A plot of actual versus expected feature sizes is shown in Figure D.2. It was found that distances between the centers of different features are preserved but line-widths are affected. This calibration curve was used to design a template that would produce masks with the proper feature sizes.

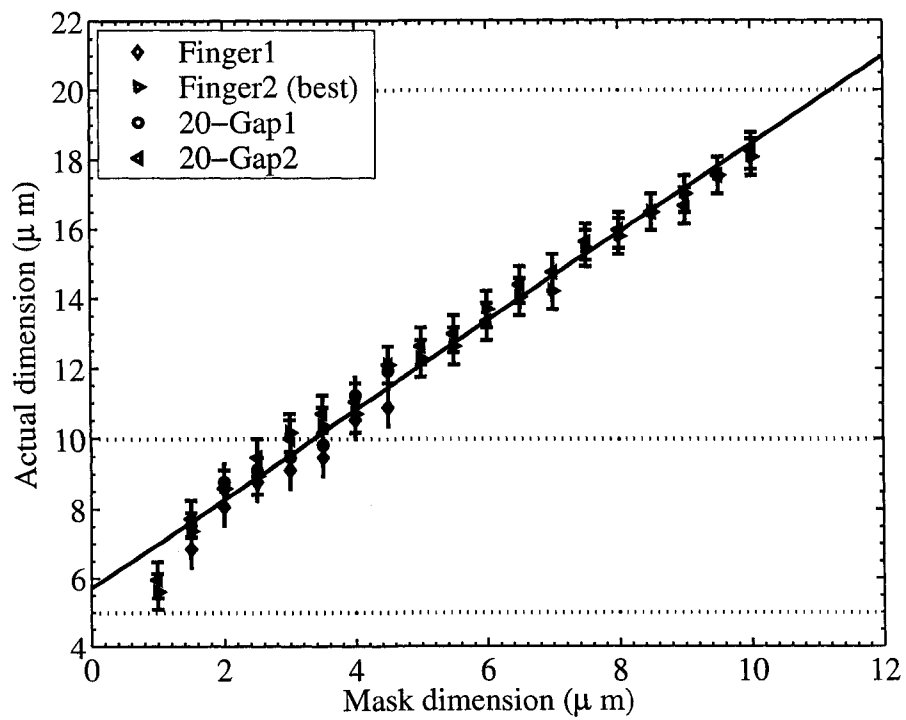


Figure D.2: Calibration curve for Nanofab mask writer (July, 2002).

Bibliography

- [1] J. F. Ziegler, J. P. Biersack, and U. Littmark, *Stopping and range of ions in solids*, Pergamon Press, 2003.
- [2] B. D. Cullity, *Introduction to Magnetic Materials*, Addison Wesley, 1972.
- [3] T. Rasing, H. van den Berg, T. Gerrits, and J. Hohlfeld, *Topics Appl. Phys.* **87**, 213 (2003).
- [4] J. F. Cochran, J. M. Rudd, W. B. Muir, G. Trayling, and B. Heinrich, *J. Appl. Phys.* **70**, 6545 (1991).
- [5] C. Ross, *Ann. Rev. Mat. Res.* **31**, 203 (2001).
- [6] Seagate, <http://www.seagate.com/newsinfo/about/milestones/>.
- [7] K. D. Sorge et al., *IEEE Trans. Magn. Magn. Mater.* **37**, 2197 (2001).
- [8] T. C. Schulthess et al., *J. Appl. Phys.* **89**, 7594 (2001).
- [9] R. P. Cowburn and M. E. Welland, *Science* **287**, 1466 (2000).
- [10] Q. Chen, A. J. Rondinone, B. C. Chakoumakos, and Z. J. Zhang, *J. Magn. Magn. Mater.* **194**, 1 (1999).
- [11] A. H. Morrish, *The Physical Principles of Magnetism*, Wiley, 1965.
- [12] A. Meldrum, R. F. J. Haglund, Jr., L. A. Boatner, and C. W. White, *Adv. Mater.* **13**, 1431 (2001).
- [13] S. Honda et al., *Mater. Res. Soc. Symp. Proc.* **581**, 71 (2000).
- [14] S. Honda et al., *Appl. Phys. Lett.* **77**, 711 (2000).
- [15] V. G. Kravets, A. K. Petford-Long, and A. F. Kravets, *J. Appl. Phys.* **87**, 1762 (2000).
- [16] Z. S. Jiang et al., *J. Appl. Phys.* **78**, 439 (1995).
- [17] B. Sepulveda, Y. Huttel, C. Boubeta, A. Cebollada, and G. Armelles, *Phys. Rev. B* **68**, 64401 (2003).
- [18] J. L. Menendes et al., *Phys. Rev. B* **65**, 205413 (2002).
- [19] J. P. Castera, *Encyclopedia of Applied Physics* **9**, 157 (1994).
- [20] M. Freeman and B. C. Choi, *Science* **294**, 1484 (2001).
- [21] W. K. Hiebert, *Ultrafast Magnetization Reversal by TR-SKEM*, PhD thesis, University of Alberta, 2001.
- [22] W. K. Hiebert, A. Stankiewicz, and M. R. Freeman, *Phys. Rev. Lett.* **79**, 1134 (1997).
- [23] B. Choi, M. Belov, W. Hiebert, G. Ballentine, and M. R. Freeman, *Phys. Rev. Lett.* **86**, 728 (2001).
- [24] A. Aharoni, *Introduction to the Theory of Ferromagnetism*, Oxford University Press, Inc., 1996.
- [25] M. R. Scheinfein, Landau Lifshitz Gilbert LLG Micromagnetic Simulator TM.
- [26] K. R. Heim, G. G. Hembree, K. E. Schmidt, and M. R. Scheinfein, *Appl. Phys. Lett.* **67**, 2878 (1995).
- [27] A. Sugawara and M. R. Scheinfein, *Phys. Rev. B* **56**, 8499 (1997).
- [28] E. Cattaruzza et al., *Appl. Phys. Lett.* **73**, 1176 (1998).
- [29] F. C. Fonseca et al., *Phys. Rev. B* **66**, 104406 (2002).
- [30] F. Luis et al., *J. Appl. Phys.* **93**, 7032 (2003).
- [31] G. F. Goya et al., *J. Appl. Phys.* **93**, 6531 (2003).
- [32] J. L. Dormann, L. Bessai, and D. Fiorani, *J. Phys. C* **21**, 2015 (1988).

-
- [33] M. Mansuripur, *Classical Optics and its Applications*, Cambridge University Press, 2002.
- [34] Merriam-Webster, *Merriam Webster's collegiate dictionary*, Merriam-Webster, 2003.
- [35] E. Hecht, *Optics*, Addison-Wesley Publishing Company, 1987.
- [36] M. J. Freiser, IEEE Trans. Magn. **MAG-4**, 152 (1968).
- [37] K. Tanaka, N. Tatehata, K. Fujita, and K. Hirao, J. Appl. Phys. **89**, 2213 (2001).
- [38] H. Kim, A. Grishin, and K. V. Rao, J. Appl. Phys. **78**, 439 (2001).
- [39] C. E. Vallet et al., J. Appl. Phys. **92**, 6200 (2002).
- [40] T. Gerrits et al., J. Appl. Phys. **89**, 7648 (2001).
- [41] T. Gerrits, H. A. M. van den Berg, J. Hohlfeld, L. Bär, and T. Rasing, Nature **418**, 509 (2001).
- [42] B. Koopmans, M. van Kampen, and W. J. M. de Jonge, J. Phys.:Condens. Matter **15**, S723 (2003).
- [43] B. Koopmans, Topics Appl. Phys. **87**, 253 (2003).
- [44] T. Kampfrath et al., Phys. Rev. B **65**, 104429 (2002).
- [45] G. Ju et al., Phys. Rev. B **57**, R700 (1998).
- [46] J. P. van der Ziel, P. S. Pershan, and L. D. Malmstrom, Phys. Rev. Lett. **15**, 190 (1965).
- [47] F. Dumestre, B. Chaudret, C. Amiens, P. Renaud, and P. Fejes, Science **303**, 821 (2004).
- [48] S. Sun, C. Murray, D. Weller, L. Folks, and A. Moser, Science **287**, 1989 (2000).
- [49] J. L. Dormann, D. Fiorani, F. Giammaria, and F. Lucari, J. Appl. Phys. **67**, 5894 (1990).
- [50] N. M. Dempsey et al., J. Appl. Phys. **90**, 6268 (2001).
- [51] G. T. Fei et al., J. Phys. D: Appl. Phys. **35**, 916 (2002).
- [52] G. T. Kraus et al., J. Appl. Phys. **82**, 1189 (1997).
- [53] R. P. Cowburn, J. Magn. Magn. Mater. **242**, 505 (2002).
- [54] E. Alves et al., Surfaces and Coatings Technology **128-129**, 434 (2000).
- [55] K. S. Beaty et al., Mater. Res. Symp. Soc. Proc. **703**, 331 (2002).
- [56] K. S. Buchanan, A. Krichevsky, M. R. Freeman, and A. Meldrum, Phys. Rev. B (submitted).
- [57] K. S. Buchanan, M. R. Freeman, and A. Meldrum, Phys. Rev. Lett. (in preparation).
- [58] D. L. Griscom, J. J. Krebs, A. Perez, and M. Treilleux, Nucl. Instrum. Meth. B **32**, 272 (1988).
- [59] G. W. Arnold, G. D. Marchi, P. Mazzoldi, and G. Battaglin, Nucl. Instrum. Meth. B **116**, 364 (1996).
- [60] N. Hayashi, I. Sakamoto, H. Wakabayashi, T. Toriyama, and S. Honda, J. Appl. Phys. **94**, 2597 (2003).
- [61] A. Meldrum, L. A. Boatner, and K. Sorge, Nucl. Instr. Meth. B **207**, 36 (2003).
- [62] C. W. White et al., Mater. Res. Soc. Symp. Proc. **704**, 187 (2002).
- [63] C. W. White et al., Nucl. Instrum. Methods B **191**, 437 (2002).
- [64] SII NanoTechnology Inc., http://www.siint.com/en/products/ion_beam_microscope.html.
- [65] Orsay Physics, <http://www.orsayphysics.com/sommaire.htm>.
- [66] J. W. Mayer, L. Eriksson, and J. A. Davies, *Ion Implantation in Semiconductors*, Academic Press, 1970.
- [67] C. Chappert et al., Science **280**, 1919 (1998).
- [68] D. N. Lambeth, E. M. T. Velu, G. H. Bellesis, L. L. Lee, and D. E. Laughlin, J. Appl. Phys. **79**, 4496 (1996).
- [69] D. J. Griffiths, *Introduction to Electrodynamics*, Prentice-Hall Canada, Inc., 1989.
- [70] J. D. Jackson, *Classical Electrodynamics*, John Wiley & Sons, Inc., 1999.
- [71] C. Kittel, *Introduction to Solid State Physics*, John Wiley & Sons, Inc., 1986.
- [72] C. Kittel, Phys. Rev. **73**, 155 (1948).
- [73] B. Lax and K. J. Button, *Microwave Ferrites and Ferrimagnetics*, McGraw-Hill Book Company, Inc., 1962.
-

-
- [74] J. H. Van Vleck, *Phys. Rev.* **78**, 266 (1950).
- [75] O. Kohomoto, *J. Magn. Magn. Mater.* **262**, 280 (2003).
- [76] J. Smit and H. G. Beljers, *Philips Res. Rep.* **10**, 113 (1955).
- [77] Y. Zhai et al., *J. Appl. Phys.* **93**, 7622 (2003).
- [78] O. Kohomoto, *J. Phys. D.: Appl. Phys.* **30**, 546 (1997).
- [79] M. Mansuripur, *J. Appl. Phys.* **63**, 5809 (1988).
- [80] G. E. Ballentine, *Comparison of Time-Resolved Micromagnetic Dynamics Experiments with Permalloy and Landau-Lifshitz-Gilbert Micromagnetic Simulation*, PhD thesis, University of Alberta, 2002.
- [81] Z. Liu, *Micromagnetic simulations on Ni₈₀Fe₂₀ thin film microstructures*, 2003.
- [82] N. W. Ashcroft and N. D. Mermin, *Solid State Physics*, Saunders Company, 1976.
- [83] H. Fukushima, Y. Nakatani, and N. Hayashi, *IEEE Trans. Magn.* **34**, 193 (1998).
- [84] R. H. Kodama, A. E. Berkowitz, E. McNiff, and S. Foner, *Phys. Rev. Lett.* **77**, 394 (1996).
- [85] R. H. Kodama, A. E. Berkowitz, E. McNiff, and S. Foner, *J. Appl. Phys.* **81**, 5552 (1997).
- [86] A. Meldrum, K. S. Buchanan, A. Hryciw, and C. W. White, *Adv. Mater.* **16**, 31 (2004).
- [87] J. Haber, http://www.chem.ualberta.ca/~joelhaber/Template_frames.htm.
- [88] A. P. Li, F. Muller, A. Birner, K. Nielsch, and U. Gosele, *Adv. Mater.* **11**, 483 (1999).
- [89] M. R. Freeman and J. F. Smyth, *J. Appl. Phys.* **79**, 5898 (1996).
- [90] M. R. Freeman, R. W. Hunt, and G. M. Steeves, *Appl. Phys. Lett.* **77**, 717 (2000).
- [91] M. R. Freeman, Dept. of Physics, University of Alberta: Personal Communication.
- [92] T. Gerrits, *Precession dynamics in micron sized magnetic thin films caused by ultra-short magnetic field pulses*, 2000.
- [93] X. Zhu, Dept. of Physics, University of Alberta: Personal Communication.
- [94] T. Gerrits et al., *IEEE Trans. Magn. and Magn. Mater.* **38**, 2484 (2002).
- [95] J. C. Pivin, G. Roger, M. A. Garcia, F. Singh, and D. K. Avasthi, *Nucl. Instrum. Meth. B* **215**, 373 (2004).
- [96] A. Meldrum et al., *J. Mater. Res.* **14**, 4489 (1999).
- [97] X. Ding et al., *J. Appl. Phys.* **86**, 2550 (1999).
- [98] O. Kononchuk, K. G. Korablev, N. Yarykin, and G. A. Rozgonyi, *Appl. Phys. Lett.* **73**, 1206 (1998).
- [99] A. K. Zvezdin and V. A. Kotov, *Modern magneto-optics and magneto-optical materials*, Institute of Physics Publishing, 1997.
- [100] P. Auric, J. S. Micha, O. Proux, L. Giacomoni, and J. R. Regnard, *J. Magn. Magn. Mater.* **217**, 175 (2000).
- [101] E. I. Il'yashenko, V. P. Klin, A. D. Nickolsky, and A. G. Solovjov, *J. Appl. Phys.* **75**, 7104 (1994).
- [102] L. P. Fu, T. Schmiedel, A. Petrou, J. Warnock, and B. T. Jonker, *Appl. Phys. Lett.* **60**, 583 (1991).
- [103] T. Tepper et al., *J. Appl. Phys.* **93**, 6948 (2003).
- [104] J. L. Dormann, D. Fiorani, F. Giammaria, and F. Lucari, *J. Appl. Phys.* **69**, 5130 (1991).
- [105] J. R. Taylor, *An Introduction to Error Analysis*, University Science Books, 1982.
- [106] E. R. Moog, S. D. Bader, and J. Zak, *Appl. Phys. Lett.* **56**, 2687 (1990).
- [107] J. Zak, E. R. Moog, C. Liu, and S. D. Bader, *Phys. Rev. B* **43**, 6423 (1991).
- [108] D. R. Lide, *CRC Handbook of Chemistry and Physics*, CRC Press, 2003.
- [109] G. S. Krinchik and V. A. Artem'ev, *Sov. Phys. JETP* **26**, 1080 (1968).
- [110] M. Abe and M. Gomi, *Japanese J. Appl. Phys.* **23**, 1580 (1984).
- [111] J. S. Ahn et al., *Phys. Rev. B* **52**, 15244 (1995).
- [112] D. Stroud, *Phys. Rev. B* **12**, 3368 (1975).
-

-
- [113] S. Jung, B. Watkins, L. DeLong, J. B. Ketterson, and V. Chandrasekhar, *Phys. Rev. B* **66**, 132401 (2002).
- [114] K. S. Buchanan, A. Krichevsky, M. R. Freeman, and A. Meldrum, Report of Invention and Assignment (2003).
- [115] A. Y. Elezzabi and M. R. Freeman, *Appl. Phys. Lett.* **68**, 3546 (1996).
- [116] S. M. Mansfield and G. S. Kino, *Appl. Phys. Lett.* **57**, 2615 (1990).
- [117] B. D. Terris, H. J. Mamin, and D. Rugar, *Appl. Phys. Lett.* **65**, 388 (1994).
- [118] J. A. H. Stotz and M. R. Freeman, *Rev. Sci. Instr.* **68**, 4468 (1997).
- [119] IBM, IBM, Infineon develop most advanced MRAM technology to date, <http://www.research.ibm.com/resources/news/20030610.mram.shtml>.
- [120] Microchem, LOR Resists, <http://www.microchem.com/products/lor.htm>.